frontiers | Research Topics

Transformation optics and its frontier branches

Edited by
Fei Sun, Shuomin Zhong, Yichao Liu and Shuai Zhang

Published in
Frontiers in Materials
Frontiers in Nanotechnology
Frontiers in Physics

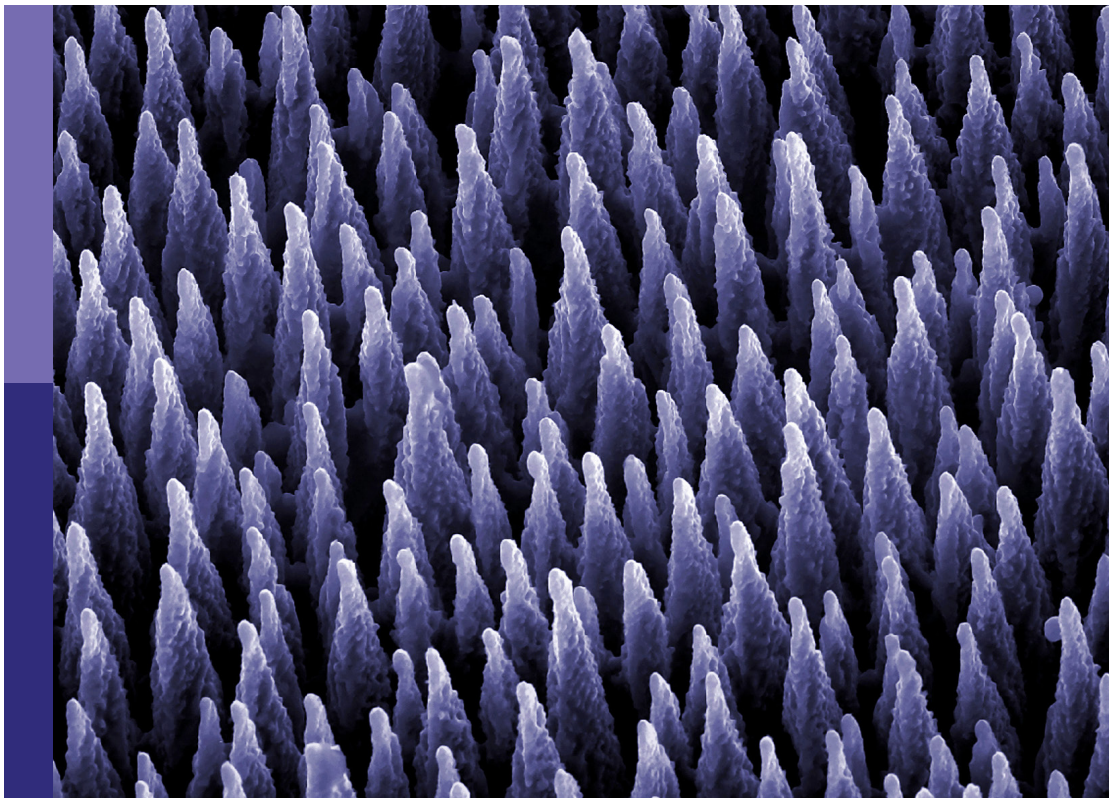

ISSN 1664-8714
ISBN 978-2-8325-3885-2
DOI 10.3389/978-2-8325-3885-2

About Frontiers

Frontiers is more than just an open access publisher of scholarly articles: it is a pioneering approach to the world of academia, radically improving the way scholarly research is managed. The grand vision of Frontiers is a world where all people have an equal opportunity to seek, share and generate knowledge. Frontiers provides immediate and permanent online open access to all its publications, but this alone is not enough to realize our grand goals.

Frontiers journal series

The Frontiers journal series is a multi-tier and interdisciplinary set of open-access, online journals, promising a paradigm shift from the current review, selection and dissemination processes in academic publishing. All Frontiers journals are driven by researchers for researchers; therefore, they constitute a service to the scholarly community. At the same time, the *Frontiers journal series* operates on a revolutionary invention, the tiered publishing system, initially addressing specific communities of scholars, and gradually climbing up to broader public understanding, thus serving the interests of the lay society, too.

Dedication to quality

Each Frontiers article is a landmark of the highest quality, thanks to genuinely collaborative interactions between authors and review editors, who include some of the world's best academicians. Research must be certified by peers before entering a stream of knowledge that may eventually reach the public - and shape society; therefore, Frontiers only applies the most rigorous and unbiased reviews. Frontiers revolutionizes research publishing by freely delivering the most outstanding research, evaluated with no bias from both the academic and social point of view. By applying the most advanced information technologies, Frontiers is catapulting scholarly publishing into a new generation.

What are Frontiers Research Topics?

Frontiers Research Topics are very popular trademarks of the *Frontiers journals series*: they are collections of at least ten articles, all centered on a particular subject. With their unique mix of varied contributions from Original Research to Review Articles, Frontiers Research Topics unify the most influential researchers, the latest key findings and historical advances in a hot research area.

Find out more on how to host your own Frontiers Research Topic or contribute to one as an author by contacting the Frontiers editorial office: frontiersin.org/about/contact

Transformation optics and its frontier branches

Topic editors

Fei Sun — Taiyuan University of Technology, China
Shuomin Zhong — Ningbo University, China
Yichao Liu — Taiyuan University of Technology, China
Shuai Zhang — Aalborg University, Denmark

Citation

Sun, F., Zhong, S., Liu, Y., Zhang, S., eds. (2023). *Transformation optics and its frontier branches*. Lausanne: Frontiers Media SA. doi: 10.3389/978-2-8325-3885-2

Table of contents

frontiers | Frontiers in Materials

TYPE Editorial
PUBLISHED 23 October 2023
DOI 10.3389/fmats.2023.1310326

OPEN ACCESS

EDITED AND REVIEWED BY
Huanyang Chen,
Xiamen University, China

*CORRESPONDENCE
Fei Sun,
sunfei@tyut.edu.cn
Yichao Liu,
liuyichao@tyut.edu.cn
Shuomin Zhong,
zhongshuomin@nbu.edu.cn
Shuai Zhang,
sz@es.aau.dk

RECEIVED 09 October 2023
ACCEPTED 16 October 2023
PUBLISHED 23 October 2023

CITATION
Sun F, Liu Y, Zhong S and Zhang S (2023), Editorial: Transformation optics and its frontier branches.
Front. Mater. 10:1310326.
doi: 10.3389/fmats.2023.1310326

Editorial: Transformation optics and its frontier branches

Fei Sun[1]*, Yichao Liu[1]*, Shuomin Zhong[2]* and Shuai Zhang[3]*

[1]Key Lab of Advanced Transducers and Intelligent Control System, Ministry of Education and Shanxi Province, College of Electronic Information and Optical Engineering, Taiyuan University of Technology, Taiyuan, China, [2]School of Information Science and Engineering, Ningbo University, Ningbo, China, [3]Department of Electronic Systems, Aalborg University, Aalborg, Denmark

KEYWORDS

transformation optics, metamaterials, metasurfaces, optical illusions, null medium, micro-nanostructures

Editorial on the Research Topic
Transformation optics and its frontier branches

Since transformation optics was first proposed to design invisibility cloaking in 2006, it has gradually emerged as a novel optical design method and has been widely applied in various fields. In recent years, in order to realize novel optical devices designed by transformation optics, various artificial materials such as metamaterials/metasurfaces and photonic crystals have also rapidly developed. Up to the present, the theoretical design methods of coordinate transformation have extended from the initial electromagnetic/optical domain to encompass other physical fields such as temperature fields, acoustic fields, quantum fields, and even the simultaneous control of multiple physical fields. This Research Topic covers the latest developments in the application of transformation optics and research on new materials. In this Research Topic, the latest research on transformation optics primarily involves the following aspects:

- One of the main application areas of transformation optics is for achieving various optical illusions, such as invisibility, deformation, and shrinking. Sadeghi has designed an electromagnetic expander, which can directly "amplify" the electromagnetic field distribution inside a scatter without disturbing the external scattering field (Sadeghi).
- Another major application of transformation optics is the ability to change the shape and size of optical devices while keeping their functionality unchanged, such as reshaping the focal surface of a lens and modifying the shape of electromagnetic antenna/cavity. Eskandari uses transformation optics to design an elliptical half Maxwell fish-eye lens, which can perform as a collimator for dual-polarized electromagnetic waves (Eskandari). Zang et al. use transformation optics to design a bi-dimensional compressed Luneburg lens, which can be applied to wide-angle beam steering (Zang et al.). Compared to uncompressed Maxwell fish-eye lens and Luneburg lens, the compressed lenses proposed in these two works can maintain the functionality of Maxwell fish-eye lens and Luneburg lens while obtaining a flattened, compact geometric structure, making them more suitable for on-chip integration.
- A future branch of development in transformation optics is the simultaneous control of multiple physical fields using coordinate transformation methods. Wu et al. propose the double-physical-field null medium by a metal plate array to achieve a double-

physical-field focusing lens, which can focus electromagnetic waves and acoustic waves simultaneously (Wu et al.).

In this Research Topic, the latest research on artificial materials primarily involves the following aspects:

- Micro-nanostructures, such as metal nanowires, nanorods, and nanospheres, are a common type of metamaterial in the optical range. They can be used for enhanced Raman spectroscopy, super-resolution imaging, optical illusions, and so on. In recent years, the fabrication techniques and synthesis processes of micro-nanostructures have been continuously improved. Link et al. conduct research on antimony telluride nanoplates by leveraging screw dislocation-driven growth, which can be used as a viable chemical route to realize spiral-type nanplate (Link et al.). Usman et al. propose a method to achieve large-scale ordered assembly of gold nanorods by controlling the droplet evaporation mode on hydrophobic substrates (Usman et al.).
- Metasurfaces were initially used to create specific phase gradients at interfaces, thereby verifying the general Snell's law. In recent years, metasurfaces have gradually evolved towards multi-functionality and intelligence. Li et al. have integrated many distinct functions within a single metasurface unit, which enables simultaneous color control and phase manipulation for pseudo-color nanoprinting and holographic image display (Li et al.). Additionally, Zhu et al. propose an intelligent tunable metasurface optimized by a generic algorithm, which can generate false electromagnetic targets in different scenarios (Zhu et al.).
- One direction of metamaterial development is to move from metallic metamaterials to all-dielectric metamaterials with low loss and large bandwidth. Cai et al. propose dielectric metamaterials based on ceramic cuboid units and apply them to achieve broadband extraordinary electromagnetic transmission (Cai et al.). Nonlinear metamaterials are also a branch of metamaterial research that can be used for frequency conversion devices. Shao et al. Propose a modified high-sensitivity optical nonlinear measurement method to characterize weak nonlinear refractive indices by a wide-band phase object (Shao et al.).

In summary, after more than 15 years of development, the applications of transformation optics are constantly expanding, and in the future it will be cross-developed with other theories and techniques, which may breed new branches including: multi-physical-field metamaterials and artificial intelligence transformation optics design. Its application domains will be further expanded from single function and single physical field to multi-functional and multi-physical field.

Author contributions

FS: Conceptualization, Funding acquisition, Writing–original draft, Writing–review and editing. YL: Conceptualization, Funding acquisition, Writing–review and editing. SoZ: Conceptualization, Funding acquisition, Writing–review and editing. SaZ: Conceptualization, Funding acquisition, Writing–review and editing.

Funding

The author(s) declare financial support was received for the research, authorship, and/or publication of this article. This work is supported by the National Natural Science Foundation of China (Nos 61971300, 12274317, 12374277, and 61905208), Natural Science Foundation of Zhejiang Province (LY22F010001), DFF-Research Project 1 (2035-00152B), Natural Science Foundation of Ningbo (2022J098), the Fundamental Research Funds for the Provincial Universities of Zhejiang, and 2022 University Outstanding Youth Foundation in Taiyuan University of Technology.

Conflict of interest

The authors declare that the research was conducted in the absence of any commercial or financial relationships that could be construed as a potential conflict of interest.

Publisher's note

frontiers | Frontiers in Materials

ORIGINAL RESEARCH
published: 22 June 2022
doi: 10.3389/fmats.2022.937437

Radar Cross Section Approach in Illusion Effects of Transformation Optics-Based Expander

Mohammad Mehdi Sadeghi *

Department of Physics, Jahrom University, Jahrom, Iran

In this paper, analytical calculation has been provided to show illusion perception in electromagnetics expander. For this end, a precise analytical solution has been done for a scattered wave from the expander including an object in the core medium. Also, this analytical calculation has been done for a bare transformed object with different size and constitute parameters (CPs). Illusion perception, in the far field, can be illustrated by comparing the calculated scattered field patterns (SFP) of the object placed inside the expander with SFP of the bare transformed object. Moreover, the same calculation and comparison has been done for nearfield SFP. In continuation, for precise deduction, radar cross sections (RCSs) of both objects have been calculated and plotted using MATLAB. Well functionality in illusion perception has been obtained using comparisons in both analytical SFPs parts and RCSs parts.

Keywords: illusion optics, radar cross section, electromagnetics wave expander, scattering theory, transformation optics

OPEN ACCESS

Edited by:
Fei Sun,
Taiyuan University of Technology, China

Reviewed by:
Shuomin Zhong,
Ningbo University, China
Yichao Liu,
Taiyuan University of Technology, China

***Correspondence:**
Mohammad Mehdi Sadeghi
Sadeghi@jahromu.ac.ir

Specialty section:
This article was submitted to Metamaterials, a section of the journal Frontiers in Materials

Received: *06 May 2022*
Accepted: *06 June 2022*
Published: *22 June 2022*

Citation:
Sadeghi MM (2022) Radar Cross Section Approach in Illusion Effects of Transformation Optics-Based Expander. Front. Mater. 9:937437. doi: 10.3389/fmats.2022.937437

INTRODUCTION

Transformation optics theory (Leonhardt, 2006; Pendry et al., 2006) was introduced in 2006, and since then it has attracted a great deal of scientific attention in theoretical and experimental (Schurig et al., 2006; Chen and Chan, 2007; Chen et al., 2008; Kwon and Werner, 2008; Luo et al., 2008; Rahm et al., 2008; Yan et al., 2008; Chen et al., 2009; Cheng et al., 2009; Lai et al., 2009; Narimanov and Kildishev, 2009; Roberts et al., 2009; Chen et al., 2010a; Chen et al., 2010b; Jiang et al., 2010; Jiang et al., 2011; Li et al., 2011; Mei et al., 2011; Li et al., 2013; Jiang et al., 2014; Sadeghi et al., 2014; Sadeghi et al., 2015a; Sadeghi et al., 2015b; Xu and Chen, 2015; Forouzeshfard and Hosseini Farzad, 2018; Liu et al., 2019; Sadeghi, 2020; Zhao et al., 2022) aspects. This theory applies coordinate transformation and metamaterials to provide desired form variations for the CP to manipulate electromagnetic waves path and direct it in the chosen manner. Hence, this theory provides a great ability to design and construct new composite artificial devices using metamaterials with various extraordinary applications. Among all these different devices, some of them also exhibit interesting illusory optical properties (Lai et al., 2009; Jiang et al., 2010; Li et al., 2011; Forouzeshfard and Hosseini Farzad, 2018; Liu et al., 2019; Sadeghi, 2020; Zhao et al., 2022). In this paper we use analytical calculation for illusion perception in transformation-based expander. For this purpose, in next section we present a transformation function to create and design a wave expander. Next, we provide a close solution in wave expansion form for SFP of an object that has been placed in the core medium of transformation-based expander. In order to show the illusion effect of this device, we compare this SFP of the object inside the expander with the SFP of a transformed bare object. Also, to illustrate the illusion effect more precisely, we provide a comparison in RCSs of both objects. Finally, we provide the conclusion in the end.

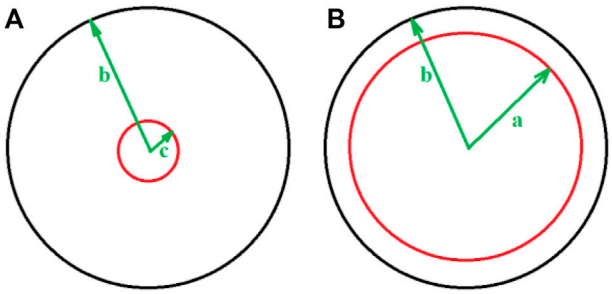

FIGURE 1 | schematic functionality of transformation function that expand **(A)** virtual region [0, c] to **(B)** real space [0, a].

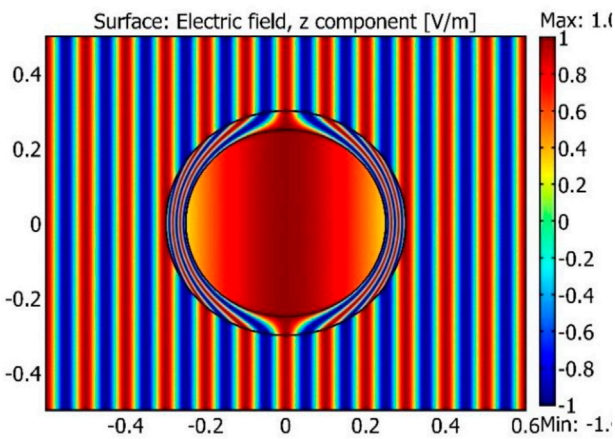

FIGURE 2 | field distribution of a TE incident wave with working frequency 1GHZ, $a = 0.25\,m$, $b = 0.3m$ and $c = 0.02m$.

General Preliminarily

We start with a transformation function that expands the region $[0, c]$ of virtual space into region $[0, a]$ of real space as shown in **Figure 1**. This function can be provided as follow,

$$r = \begin{cases} \dfrac{a-b}{c-b}r' + b\dfrac{c-a}{c-b} & for \;\; c \le r' \le b \\ \dfrac{a}{c}r' & for \;\; 0 \le r' \le c \end{cases} \tag{1}$$

Where r and r' show the real and virtual space respectively.

According transformation optics theory we have CP of core medium i.e., $[0, a]$ of wave expander as follow,

$$\varepsilon_{core} = \mu_{core} = \begin{bmatrix} 1 & 0 & 0 \\ 0 & 1 & 0 \\ 0 & 0 & \left(\dfrac{c}{a}\right)^2 \end{bmatrix} \tag{2}$$

Likewise, for surrounding shell i.e., $[a, b]$, of wave expander we have,

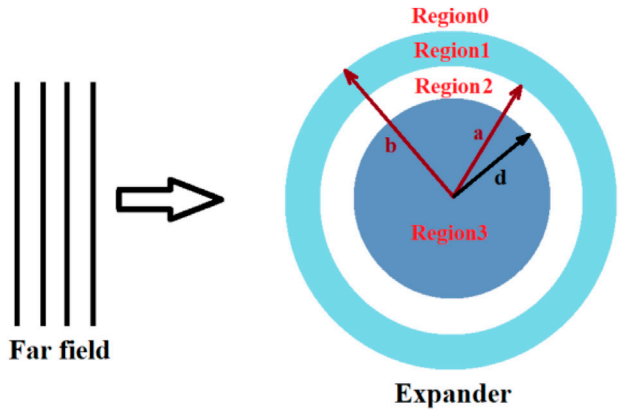

FIGURE 3 | Schematic plan for a cylindrical sample with radius d. ε_{sample} and μ_{sample} are the CP of the object that placed in core medium of expander and illuminated by planewave.

$$\varepsilon_{shell} = \mu_{shell} = \begin{bmatrix} \left(\dfrac{a-b}{c-b}\right)\dfrac{r'}{r} & 0 & 0 \\ 0 & \left(\dfrac{c-b}{a-b}\right)\dfrac{r}{r'} & 0 \\ 0 & 0 & \left(\dfrac{c-b}{a-b}\right)\dfrac{r'}{r} \end{bmatrix} \tag{3}$$

Now with these core and shell parameters and using an incidenting TE-z plane wave, the functionality of the device can be plotted as shown in **Figure 2**. The field distribution pattern of a TE incident plane wave with working frequency 1 GHZ, $a = 0.25\,m$, $b = 0.3m$ and $c = 0.02m$ has been plotted in **Figure 2** the device remains invisible and the wave expands in the core medium. However, this device can be used to create an illusion that has been presented in the next section.

RCS APPROACH

In this section we focus on illusion perception using exact solutions in the wave equation of scattering waves. For this end we put a cylindrical object with radius $d = 0.1m$ and relative CP, $\varepsilon = \varepsilon_{sample}$ and $\mu = \mu_{sample}$ in core medium in order to see the field pattern. Noteworthy we choose the sample in cylindrical shape to provide an exact analytical solution in the wave equation. In the following, we provide a solution in illusion scattering for far field and near field separately.

Consider a TE plane wave propagating in x direction as shown in **Figure 3**. Hence, we can present wave expansion outside and inside the device using boundary condition (BC). This TE plane wave can be formulated as below,

$$E = \mathcal{E}e^{ik_0 x - i\omega t} \tag{4}$$

Where k_0 and ω are the wave number and frequency of incidenting waves in the host, respectively. also $\mathcal{E}$, is the amplitude of incidenting wave. We calculate the total field in all regions using general wave equation as below:

For the electric field outside the device i.e., region0 or $\rho > b$, we have incidenting wave and scattering wave as below,

$$E_0 = \mathcal{E} \sum_{n=-\infty}^{n=\infty} [i^{-n} J_n(k_0\rho) + C_{0,n} H_n^1(k_0\rho)] e^{in\varphi} \quad (5)$$

Where J_n and H_n^1 are Bessel and Hankel function of first kind, respectively. $C_{0,n}$ is the unknown expansion coefficients of scattered part of the total field outside the device. Also, inside the device in shell region i.e., region1, we can present,

$$E_1 = \mathcal{E} \sum_{n=-\infty}^{n=\infty} [A_{1,n} J_n(k_1\rho) + C_{1,n} H_n^1(k_1\rho)] e^{in\varphi} \quad (6)$$

For the core medium i.e., region2, we have the wave as follow,

$$E_2 = \mathcal{E} \sum_{n=-\infty}^{n=\infty} [A_{2,n} J_n(k_2\rho) + C_{2,n} H_n^1(k_2\rho)] e^{in\varphi} \quad (7)$$

And finally, for inside the sample i.e., region3, that has been inserted inside the core medium we have,

$$E_3 = \mathcal{E} \sum_{n=-\infty}^{n=\infty} [A_{3,n} J_n(k_3\rho)] e^{in\varphi} \quad (8)$$

Where in **Eqs 9–11** A and C are unknown expansion coefficients. Also k_1, k_2 and k_3 are the wave vectors in corresponding regions. Now by matching of the boundary condition (BC) for continuity of electric and magnetic field at all interfaces we calculate the unknown coefficients. For three interfaces, as shown in **Figure 3**, we can provide three equations for continuity of electric field and three equations for continuity of magnetic field using $H_\varphi = \frac{1}{i\omega\mu} \frac{\partial E_z}{\partial \rho}$.

For continuity of electric fields at $\rho = b$,

$$A_{0,n} J_n(k_0 b) + C_{0,n} H_n^1(k_0 b) = A_{1,n} J_n(k_1 b) + C_{1,n} H_n^1(k_1 b) \quad (9)$$

For continuity of electric fields at $\rho = a$,

$$A_{1,n} J_n(k_1 a) + C_{1,n} H_n^1(k_1 a) = A_{2,n} J_n(k_2 a) + C_{2,n} H_n^1(k_2 a) \quad (10)$$

And for continuity of electric fields at boundary of object inside the core medium, $\rho = d$,

$$A_{2,n} J_n(k_2 d) + C_{2,n} H_n^1(k_2 d) = A_{3,n} J_n(k_3 d) \quad (11)$$

We use similar BCs for continuity of magnetic fields at all boundaries.

For continuity of magnetic fields at $\rho = b$,

$$\frac{k_0}{\mu_0}\left(A_{0,n} J'_n(k_0 b) + C_{0,n} H_n^{1'}(k_0 b)\right) = \frac{k_1}{\mu_1}\left(A_{1,n} J'_n(k_1 b) + C_{1,n} H_n^{1'}(k_1 b)\right) \quad (12)$$

For continuity of magnetic fields at $\rho = a$,

$$\frac{k_1}{\mu_1}\left(A_{1,n} J'_n(k_1 a) + C_{1,n} H_n^{1'}(k_1 a)\right) = \frac{k_2}{\mu_2}\left(A_{2,n} J'_n(k_2 a) + C_{2,n} H_n^{1'}(k_2 a)\right) \quad (13)$$

And for continuity of magnetic fields at boundary of object inside the core medium, $\rho = d$,

$$\frac{k_2}{\mu_2}\left(A_{2,n} J'_n(k_2 d) + C_{2,n} H_n^{1'}(k_2 d)\right) = \frac{k_3}{\mu_3}\left(A_{3,n} J'_n(k_3 d)\right) \quad (14)$$

Finally, we can obtain the unknown coefficients in all regions with recursive procedure (Cheng et al., 2009) using MATLAB code. Hence, we can plot the electric field in all regions as shown in **Figure 4A**. Moreover, we can achieve $C_{0,n}$, the scattering coefficient of wave in the host medium in **Eq. 5**, in order to plot RCS in the end of this paper.

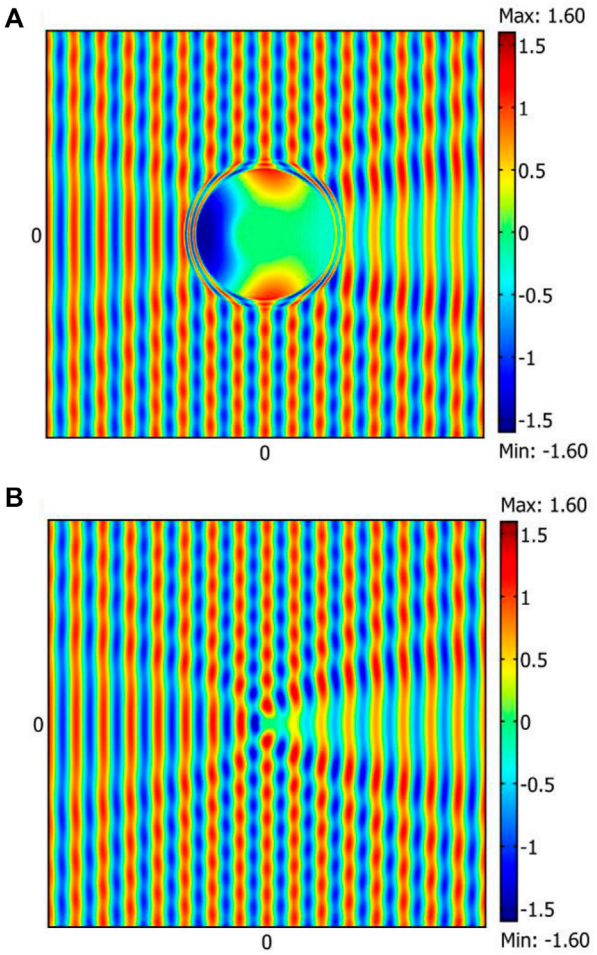

FIGURE 4 | (A) SFP of object placed in core medium of expander illuminated by far field, with $b = 0.3m$, $a = 0.25m$ and $c = 0.05m$ and $d = 0.1m$ as object radius. The object here is PEC. $\varepsilon_{sample} = -10000$ and $\mu_{sample} = 1$ **(B)** SPF of bare transformed object illuminated by far field, with radius $d' = dc/a$. In both plot working frequency is 1 GHZ.

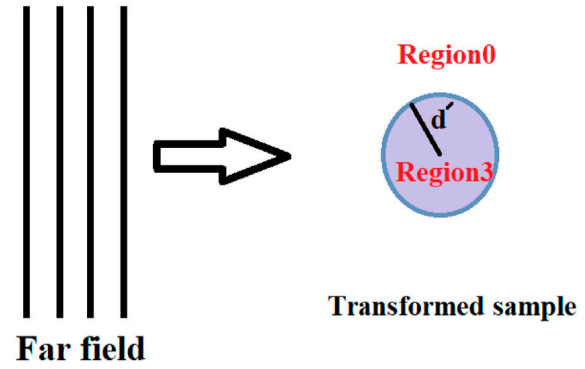

FIGURE 5 | Schematic plan for bare transformed cylinder with radius d'. $\varepsilon' = \varepsilon_{sample}c/a$ and $\mu' = \mu_{sample}c/a$ are the CP of the bare transformed object that illuminated by planewave.

Now to comprehend and understand the illusion perception, similar to the scattering calculation for the expander device, we also provide the same calculation for SFP of bare transformed cylinder as shown in **Figure 5** with transformed size and CP. For the transformed case we use a bare cylinder with radius $d' = (c/a)d$ and CP, $\varepsilon' = \varepsilon_{sample}\,(c/a)^2$ and $\mu' = \mu_{sample}$ illuminate by TE plane wave. We can provide the wave expansion outside of sample $\rho > d'$,

$$E_0 = \mathcal{E}\sum_{n=-\infty}^{n=\infty}\left[A_{0,n}\,J_n(k_0\rho) + C^t_{0,n}H^1_n(k_0 r)\right]e^{in\varphi} \tag{15}$$

Where $C^t_{0,n}$ is the scattering coefficient of wave in region0. And for inside the sample $\rho < d'$,

$$E_3 = \mathcal{E}\sum_{n=-\infty}^{n=\infty}\left[A_{3,n}\,J_n(k_3\rho)\right]e^{in\varphi} \tag{16}$$

In this case we have only one interface and for continuity of electric field and magnetic field we can derive matching boundary condition as follow.

For the electric fields at the boundary $r = d'$,

$$A_{0,n}\,J_n(k_0 d') + C_{0,n}H^1_n(k_0 d') = A_{3,n}\,J_n(k_3 d') \tag{17}$$

And for magnetic fields at the boundary $r = d'$,

$$\frac{k_0}{\mu_0}\left(A_{0,n}\,J'_n(k_0 d') + C_{0,n}H^{1'}_n(k_0 d')\right) = \frac{k_3}{\mu_3}\left(A_{3,n}\,J'_n(k_3 d')\right) \tag{18}$$

Similar to calculations in the expander case we calculate the unknown coefficients using recursive code and plot the electric inside and outside of the object as shown in **Figure 4B**. Illusion perception can be understood by comparing SFP in **Figure 4A** and SFP in **Figure 4B** in region $\rho > b$. In region $\rho > b$ SFP of both cases are the same as each other. Hence, we can say qualitatively, the expander creates the same illusion as a bare transformed object with transformed size and CP parameters.

Now for more consideration we also provide the same calculation for illusion perception using near field source. For

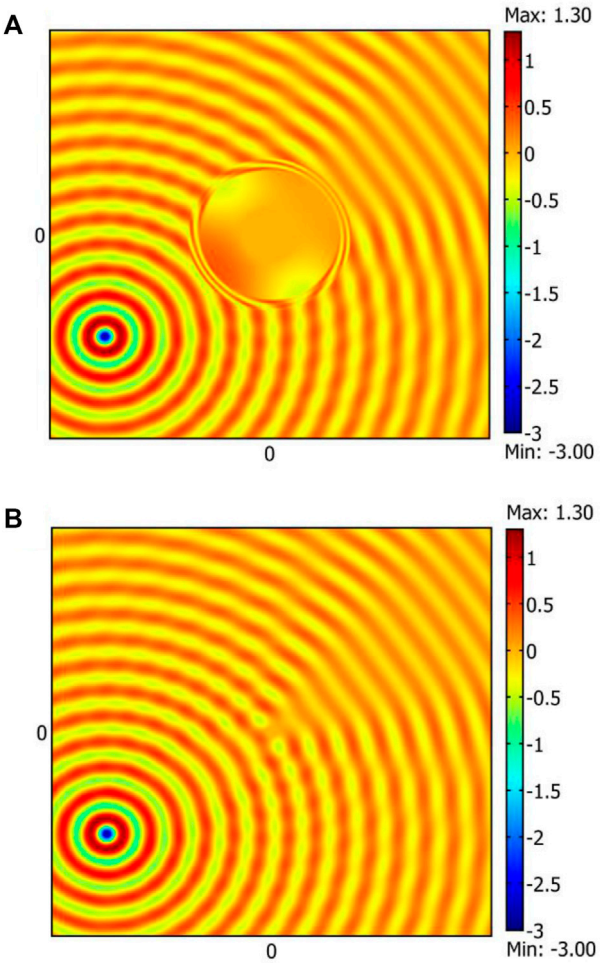

FIGURE 6 | (A) SFP of object placed in core medium of expander and illuminated by nearfield with $b = 0.3m$, $a = 0.25m$ and $c = 0.05m$ and $d = 0.1m$ as object radius. The object here is PEC. $\varepsilon_{sample} = -10000$ and $\mu_{sample} = 1$ **(B)** SPF of bare transformed object and illuminated by nearfield with radius $d' = dc/a$. In both plot working frequency is 1 GHZ and the point source located in.$\rho' = -0.6i - 0.4j$

this part we illuminate both the expander and bare transformed object by a point source located near the device (ρ') with working frequency 1 GHZ. Hence, we provide the total electric field in all regions.

For the expander calculation, outside of device, we can derive total electric field as follow.Where $C_{0,n}$ is the scattering parameter in region0. For electric field in surrounding shell region, $a < \rho < b$,

$$E_0(\rho,\varnothing) = \hat{a}_z\mathcal{E}\times\begin{cases}\sum_{n=-\infty}^{\infty}\left[J_n(k_0\rho)H^{(2)}_n(k_0\rho') + C_{0,n}H^{(2)}_n(k_0\rho)\right]e^{in(\varphi-\varphi')} & b\le\rho\le\rho'\\ \sum_{n=-\infty}^{\infty}\left[J_n(k_0\rho') + C_{0,n}\right]H^{(2)}_n(k_0\rho)e^{in(\varphi-\varphi')} & \rho\ge\rho'\end{cases} \tag{19}$$

$$E_1(\rho,\varphi) = \hat{a}_z\mathcal{E}\sum_{n=-\infty}^{\infty}\left\{\alpha^{C1}_n J_n(k_1\rho) + \beta^{C1}_n H^{(1)}_n(k_1\rho)e^{in(\varphi-\varphi')}\right\} \tag{20}$$

For core region, $d < \rho < a$,

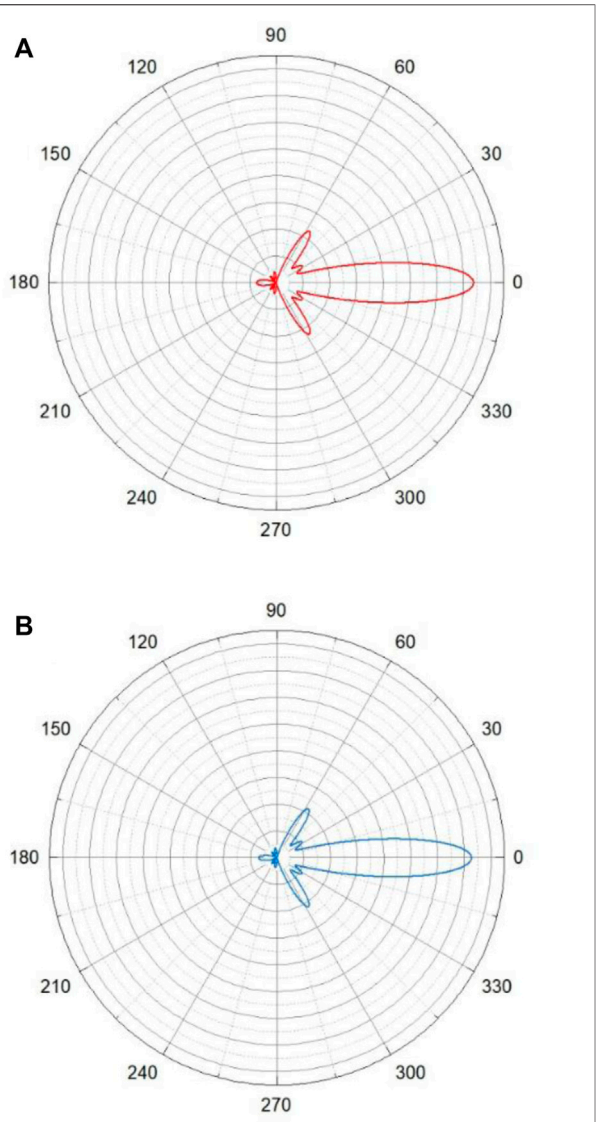

FIGURE 7 | (A) RCS (scale of 0.1 m) of a cylinder placed in expander **(B)** RCS (scale of 0.1 m) of bare transformed cylinder.

$$E_2(\rho,\varphi) = \hat{a}_z \mathcal{E} \sum_{n=-\infty}^{\infty} \left\{ \alpha_n^{C2} J_n(k_2\rho) + \beta_n^{C2} H_n^{(1)}(k_2\rho) e^{in(\varphi-\varphi')} \right\} \quad (21)$$

And finally, for inside the object, $\rho < d$,

$$E_3(\rho,\varphi) = \hat{a}_z \mathcal{E} \sum_{n=-\infty}^{\infty} \left\{ \alpha_n^{C3} J_n[k_3\rho] e^{in(\varphi-\varphi')} \right\} \quad (22)$$

Similar to far field calculation we use BC for continuity of electric and magnetic field at all interfaces and using recursive method (Cheng et al., 2009) we can derive all unknown parameters and plot the electric field in all regions as showed in **Figure 6A**.

Likewise, to understand and comprehend the illusion effect we have the same calculation for the bare transformed cylinder that is illuminated by point source. we can calculate the wave outside the cylinder as follow.Where $C_{0,n}^t$ is the coefficient parameter of the scattering wave and ρ' is the location of the point source. Also, for inside the cylinder we can present the following equation,

$$E_0(\rho,\varnothing) = \hat{a}_z \mathcal{E} \times \begin{cases} \sum_{n=-\infty}^{\infty} \left[J_n(k_0\rho) H_n^{(2)}(k_0\rho') + C_{0,n}^t H_n^{(2)}(k_0\rho) \right] e^{in(\varphi-\varphi')} & b \le \rho \le \rho' \\ \sum_{n=-\infty}^{\infty} \left[J_n(k_0\rho') + C_{0,n}^t \right] H_n^{(2)}(k_0\rho) e^{in(\varphi-\varphi')} & \rho \ge \rho' \end{cases} \quad (23)$$

$$E_3(\rho,\varphi) = \hat{a}_z \mathcal{E} \sum_{n=-\infty}^{\infty} \left\{ \alpha_n^{C3} J_n[k_3\rho] e^{in(\varphi-\varphi')} \right\} \quad (24)$$

Similar to far field derivation we use **a** recursive method to calculate unknown parameters and plot the field inside and outside the cylinder as shown in **Figure 6B**. Also, illusion perception can be understood by comparing SFP in **Figure 6A** and **Figure 6B** i.e., the SFPs in the region $\rho \ge b$ show the same pattern in both cases qualitatively.

For more precise consideration we provide a qualitative approach. RCS is an indicator of far field scattering, SO, we use RCS plot to compare the both scattering far fields to prove the perfect illusion perception. we use scattering parameters of both object in far field to plot RCS of both scatterers using scattering formula,

$$\xi(\theta) = 4 \Big/ k_0 \left| \sum_{n=-\infty}^{+\infty} C_n e^{in\theta} \right|^2 \quad (25)$$

We plot the RSCs in **Figures 7A, B** for expander and bare transformed cylinder, respectively. Both RSCs of samples illustrate the same scattering effects and hence, perfect illusion can be realized.

CONCLUSION

Although the wave expander transformation optic-base manipulates electromagnetic wave propagation to expand the wave in core medium, it has some illusory effects that can change the radar cross section of objects. In this paper we used scattering theory to provide full calculations and close solutions to show illusion effects of this device. For this end we compared the scattered waves from both the bare transformed object and object placed in the expander. Moreover, we provided a comparison in RCS for both objects. The results, RCSs and SFPs for both objects, confirmed the perfect illusion effects. Expander illustrates perfect illusion perception in the size of objects.

DATA AVAILABILITY STATEMENT

The raw data supporting the conclusion of this article will be made available by the authors, without undue reservation.

AUTHOR CONTRIBUTIONS

MMS conceived the idea and did the theoretical calculations and the numerical simulations. MMS wrote and revised the manuscript.

REFERENCES

Chen, H., Chan, C. T., and Sheng, P. (2010). Transformation Optics and Metamaterials. *Nat. Mater* 9, 387–396. doi:10.1038/nmat2743

Chen, H., and Chan, C. T. (2007). Transformation Media that Rotate Electromagnetic Fields. *Appl. Phys. Lett.* 90, 241105. doi:10.1063/1.2748302

Chen, H., Hou, B., Chen, S., Ao, X., Wen, W., and Chan, C. T. (2009). Design and Experimental Realization of a Broadband Transformation Media Field Rotator at Microwave Frequencies. *Phys. Rev. Lett.* 102, 183903. doi:10.1103/physrevlett.102.183903

Chen, H., Luo, X., Ma, H., and Chan, C. T. (2008). The Anti-cloak. *Opt. Express* 16, 14603–14608. doi:10.1364/oe.16.014603

Chen, H., Miao, R.-X., and Li, M. (2010). Transformation Optics that Mimics the System outside a Schwarzschild Black Hole. *Opt. Express* 18, 15183–15188. doi:10.1364/oe.18.015183

Cheng, Y., Xu, J. Y., and Liu, X.-J. (2009). Broadband Acoustic Cloak with Multilayered Homogeneous Isotropic Materials. *Piers Online* 52, 177–180.doi:10.2529/piers080901204601

Forouzeshfard, M. R., and Hosseini Farzad, M. (2018). Illusion Optics by Single and Twin Cylindrical Cavity Cloaks. *Optik* 156, 1007–1013. doi:10.1016/j.ijleo.2017.12.053

Jiang, W. X., Ma, H. F., Cheng, Q., and Cui, T. J. (2010). Illusion Media: Generating Virtual Objects Using Realizable Metamaterials. *Appl. Phys. Lett.* 96, 121910. doi:10.1063/1.3371716

Jiang, X., Liang, B., Zou, X.-Y., Yin, L.-L., and Cheng, J.-C. (2014). Broadband Field Rotator Based on Acoustic Metamaterials. *Appl. Phys. Lett.* 104, 083510. doi:10.1063/1.4866333

Jiang, Z. H., Gregory, M. D., and Werner, D. H. (2011). Experimental Demonstration of a Broadband Transformation Optics Lens for Highly Directive Multibeam Emission. *Phys. Rev. B* 84, 1–6. doi:10.1103/physrevb.84.165111

Kwon, D.-H., and Werner, D. H. (2008). Polarization Splitter and Polarization Rotator Designs Based on Transformation Optics. *Opt. Express* 16, 18731–18738. doi:10.1364/oe.16.018731

Lai, Y., Ng, J., Chen, H., Han, D., Xiao, J., Zhang, Z.-Q., et al. (2009). Illusion Optics: the Optical Transformation of an Object into Another Object. *Phys. Rev. Lett.* 102, 253902. doi:10.1103/physrevlett.102.253902

Leonhardt, U. (2006). Optical Conformal Mapping. *Science* 312, 1777–1780. doi:10.1126/science.1126493

Li, C., Liu, X., Liu, G., Li, F., and Fang, G. (2011). Experimental Demonstration of Illusion Optics with "External Cloaking" Effects. *Appl. Phys. Lett.* 99, 084104. doi:10.1063/1.3629770

Li, L., Huo, F., Zhang, Y., Chen, Y., and Liang, C. (2013). Design of Invisibility Anti-cloak for Two-Dimensional Arbitrary Geometries. *Opt. Express* 21, 9422–9427. doi:10.1364/oe.21.009422

Liu, Y., Guo, S., and He, S. (2019). Illusion Optics: Disguising with Ordinary Dielectric Materials. *Adv. Mater* 316, e1805106.

Luo, Y., Chen, H., Zhang, J., Ran, L., and Kong, J. A. (2008). Design and Analytical Full-Wave Validation of the Invisibility Cloaks, Concentrators, and Field Rotators Created with a General Class of Transformations. *Phys. Rev. B* 77, 125127. doi:10.1103/physrevb.77.125127

Mei, Z. L., Bai, J., and Cui, T. J. (2011). Experimental Verification of a Broadband Planar Focusing Antenna Based on Transformation Optics. *New J. Phys.* 13, 1367–2630. doi:10.1088/1367-2630/13/6/063028

Narimanov, E. E., and Kildishev, A. V. (2009). Optical Black Hole: Broadband Omnidirectional Light Absorber. *Appl. Phys. Lett.* 95, 041106. doi:10.1063/1.3184594

Pendry, J. B., Schurig, D., and Smith, D. R. (2006). Controlling Electromagnetic Fields. *Science* 312, 1780–1782. doi:10.1126/science.1125907

Rahm, M., Schurig, D., Roberts, D. A., Cummer, S. A., Smith, D. R., and Pendry, J. B. (2008). Design of Electromagnetic Cloaks and Concentrators Using Form-Invariant Coordinate Transformations of Maxwell's Equations. *Photonics Nanostructures - Fundam. Appl.* 6, 87–95. doi:10.1016/j.photonics.2007.07.013

Roberts, D. A., Kundtz, N., and Smith, D. R. (2009). Optical Lens Compression via Transformation Optics. *Opt. Express* 17, 16535–16542. doi:10.1364/oe.17.016535

Sadeghi, M. M. (2020). Illusion Properties in Perfect Cylindrical Devices. *Plasmonics* 153, 709–715. doi:10.1007/s11468-019-01088-4

Sadeghi, M. M., Li, S., Xu, L., Hou, B., and Chen, H. (2015). Transformation Optics with Fabry-Pérot Resonances. *Sci. Rep.* 5, 8680. doi:10.1038/srep08680

Sadeghi, M. M., Nadgaran, H., and Chen, H. (2014). Perfect Field Concentrator Using Zero Index Metamaterials and Perfect Electric Conductors. *Front. Phys.* 9, 90–93. doi:10.1007/s11467-013-0374-0

Sadeghi, M. M., Xu, L., Nadgaran, H., and Chen, H. (2015). Optical Concentrators with Simple Layered Designs. *Sci. Rep.* 5, 11015. doi:10.1038/srep11015

Schurig, D., Mock, J. J., Justice, B. J., Cummer, S. A., Pendry, J. B., Starr, A. F., et al. (2006). Metamaterial Electromagnetic Cloak at Microwave Frequencies. *Science* 314, 977–980. doi:10.1126/science.1133628

Xu, L., and Chen, H. (2015). Conformal Transformation Optics. *Nat. Phot.* 9, 15–23. doi:10.1038/nphoton.2014.307

Yan, M., Yan, W., and Qiu, M. (2008). Cylindrical Superlens by a Coordinate Transformation. *Phys. Rev. B* 78, 125113. doi:10.1103/physrevb.78.125113

Zhao, P., Cai, G., and Chen, H. (2022). Exact Transformation Optics by Using Electrostatics. *Sci. Bull.* 673, 246–255. doi:10.1016/j.scib.2021.09.017

Conflict of Interest: The authors declare that the research was conducted in the absence of any commercial or financial relationships that could be construed as a potential conflict of interest.

frontiers | Frontiers in Nanotechnology

TYPE Original Research
PUBLISHED 17 August 2022
DOI 10.3389/fnano.2022.973348

OPEN ACCESS

EDITED BY
Georgios Veronis,
Louisiana State University, United States

REVIEWED BY
Lei Zhang,
Xi'an Jiaotong University, China
Shuyuan Xiao,
Nanchang University, China

*CORRESPONDENCE
Zile Li,
lizile@whu.edu.cn
Guoxing Zheng,
gxzheng@whu.edu.cn

SPECIALTY SECTION
This article was submitted to Nanophotonics, a section of the journal Frontiers in Nanotechnology

RECEIVED 20 June 2022
ACCEPTED 26 July 2022
PUBLISHED 17 August 2022

CITATION
Li J, Zhou Z, Li Z and Zheng G (2022), Single-sized metasurface for simultaneous pseudo-color nanoprinting and holographic image display.
Front. Nanotechnol. 4:973348.
doi: 10.3389/fnano.2022.973348

Single-sized metasurface for simultaneous pseudo-color nanoprinting and holographic image display

Jiaxin Li[1], Zhou Zhou[1], Zile Li[1,2]* and Guoxing Zheng[1,2,3,4]*

[1]Electronic Information School, Wuhan University, Wuhan, China, [2]Peng Cheng Laboratory, Shenzhen, China, [3]Wuhan Institute of Quantum Technology, Wuhan, China, [4]Hubei Luojia Laboratory, Wuhan, China

Metasurfaces provide a novel platform for multifunctional devices due to their incomparable competence for the manipulation of different optical properties. Recently, many works have emerged to merge distinct functions into a single metasurface, which effectively increase the information density and capacity of meta-devices. In this work, combining the dual-wavelength polarizer and the orientation degeneracy of the Malus law, we further exploit the design degree of freedom of the metasurface, and realize color control and phase manipulation simultaneously with single-sized nanostructures. We experimentally demonstrate our concept by integrating the function of pseudo-color nanoprinting and holographic image display together. Our research can effectively improve the functionalities of metasurface and promote advanced research of multimode displays, information encryption, optical multiplexing, and many other related fields.

KEYWORDS

metasurface, single size, multifunctional device, color control, dual-wavelength polarizer

1 Introduction

Benefiting from the incomparable capability of manipulation for optical properties such as phase (Hao et al., 2021; Wang et al., 2021; Zhang H. et al., 2022; Cheng et al., 2022; Ma et al., 2022; Ming et al., 2022; Tao et al., 2022), polarization (Ouyang et al., 2021; Xu et al., 2021; Deng J. et al., 2022; Zhang S. et al., 2022; Kim et al., 2022; Zhou et al., 2022) and amplitude (Li Z. et al., 2021; Ren et al., 2021; Zheng et al., 2021; Deng L. et al., 2022; Chen et al., 2022; Yang et al., 2022), metasurface has emerged as a powerful platform for implementing multifunctional devices (Deng J. et al., 2020; Deng L. et al., 2020; Chen et al., 2020; Dai et al., 2020; Li et al., 2020; Li J. et al., 2021). By dividing the metasurface into different parts, the segmenting metasurfaces have showcased their ability to integrate different functions, e.g., imaging and nanoprinting (Chen et al., 2020) or near- and far-field display together (Dai et al., 2020). However, these works simply hybrid the single-function by spaces and sacrifice the device size to increase the functionality, in which the information density is not increased in essential. Another

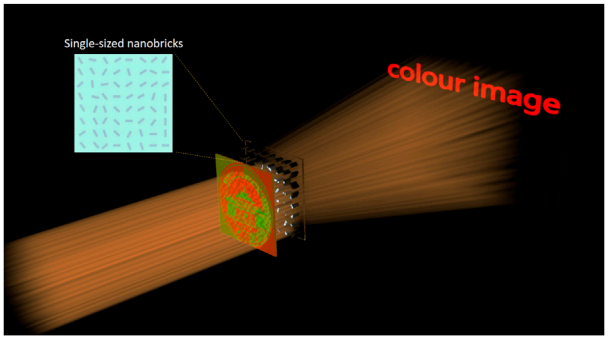

FIGURE 1
Schematic illustration of the single-sized metasurface for pseudo-color control and holographic image display. The metasurface can display a pseudo-color nanoprinting in the near-field under the illumination of incident beam with red (620 nm) and green (510 nm) light, and a Fourier holographic image in the far-field when the wavelength of incident beam is 620 or 510 nm.

attempt to realize multifunction is employing the nanostructure with distinct dimensions, i.e., combining the geometric and propagation phase to realize different functions (Li et al., 2020; Li J. et al., 2021), which decreases the crosstalk between different functions and improves the information density. Nevertheless, the complicated design and fabrication process hamper the wide applicability of the metasurface. To settle this issue, the orientation degeneracy hidden in the Malus law is proposed and the multimode gray-scale image display is realized (Deng J. et al., 2020; Deng L. et al., 2020). Such approaches, however, only work for one single wavelength and the chromatic images display is still elusive.

Herein, we employ the dual-wavelength polarizer and successfully achieve the Fourier holographic and pseudo-color nanoprinting images display based on single-sized nanostructures, as shown in Figure 1. Specifically, the proposed metasurface works as polarizer arrays at two distinct wavelengths (i.e., 510 and 620 nm) with orthogonal polarization direction, and the mixture of these two colors with different ratio can be realized merely by rotating the orientation angle of the nanostructure. More importantly, employing the orientation degeneracy, the phase manipulation can be simultaneously implemented by selecting the nanostructure orientations through the simulated annealing algorithm (SAA) (Deng L. et al., 2020), without influencing the color modulation. As a result, the pseudo-color control and phase manipulation can be fulfilled at the same time. The present research provides an exciting opportunity to advance our knowledge of multifunctional devices based on a single-sized metasurface, and can make major contribution to fields such as image display, optical anticounterfeiting, information encryption, and etc.

2 Materials and methods

2.1 Working principle for simultaneous color control and phase manipulation

To realize pseudo-color control with the single-sized nanostructures, each unit-cell of the metasurface is supposed to modulate the polarization direction of incident beam at two wavelengths, i.e., each nanostructure acts as dual-wavelength nano-polarizer. Herein we employ the silver nanobricks sitting on the fused silica to implement the proposed function. Figures 2A, B show the diagram of a unit-cell, in which the orientation angle θ is defined as the angle between the x-axis and the long axis of nanobrick. Here, CST Microwave Studio software is used to simulate the optical response of the nanobricks. After careful optimization, each nanobrick is designed with length L of 140 nm, width W of 85 nm, unit-cell dimension CS of 340 nm, and H of 70 nm. Figure 2C shows the simulated reflectivities and transmissivities with incident beam polarized along the long (r_l and t_l) and short (r_s and t_s) axes of the nanobrick. We can see that at the working wavelength of 510 nm, r_s reaches 69.93% and t_s is 3.98%; while at the working wavelength of 620 nm, r_l reaches 90.9% and t_l is 0.3%, which demonstrates that the nanobrick works as polarizer at two designed wavelengths. According to the Malus law, when the incident light beam polarized along the x-axis and with wavelength of 510 nm or 620 nm passes through the nanobrick, the transmitted beam's intensity can be expresses as:

$$I_{510} = I_0 \cdot cos^2\theta \tag{1}$$

or

$$I_{620} = I_0 \cdot sin^2\theta \tag{2}$$

where I_0 represents the intensity of the incident beam, I_{510} and I_{620} are the intensity of the output light at wavelength of 510 and 620 nm, respectively. As a result, when the incident beam is with two wavelengths of 510 and 620 nm, the ratio of the red (620 nm) and green (510 nm) components $I_{620/510}$ in the output beam can be adjusted by changing the orientation angle of the nanobrick:

$$I_{620/510} = tan^2\theta \tag{3}$$

Consequently, the color between red and green can be modulated, and this is the basic principle of pseudo-color manipulation.

Further, due to the orientation degeneracy of the trigonometric function, each nanobrick has two angles (θ or π-θ) to generate the same output color, as shown in Figure 2D of the blue line. And it's known that when the circularly polarized light passes through an anisotropic structure, the output light with opposite chirality will carry

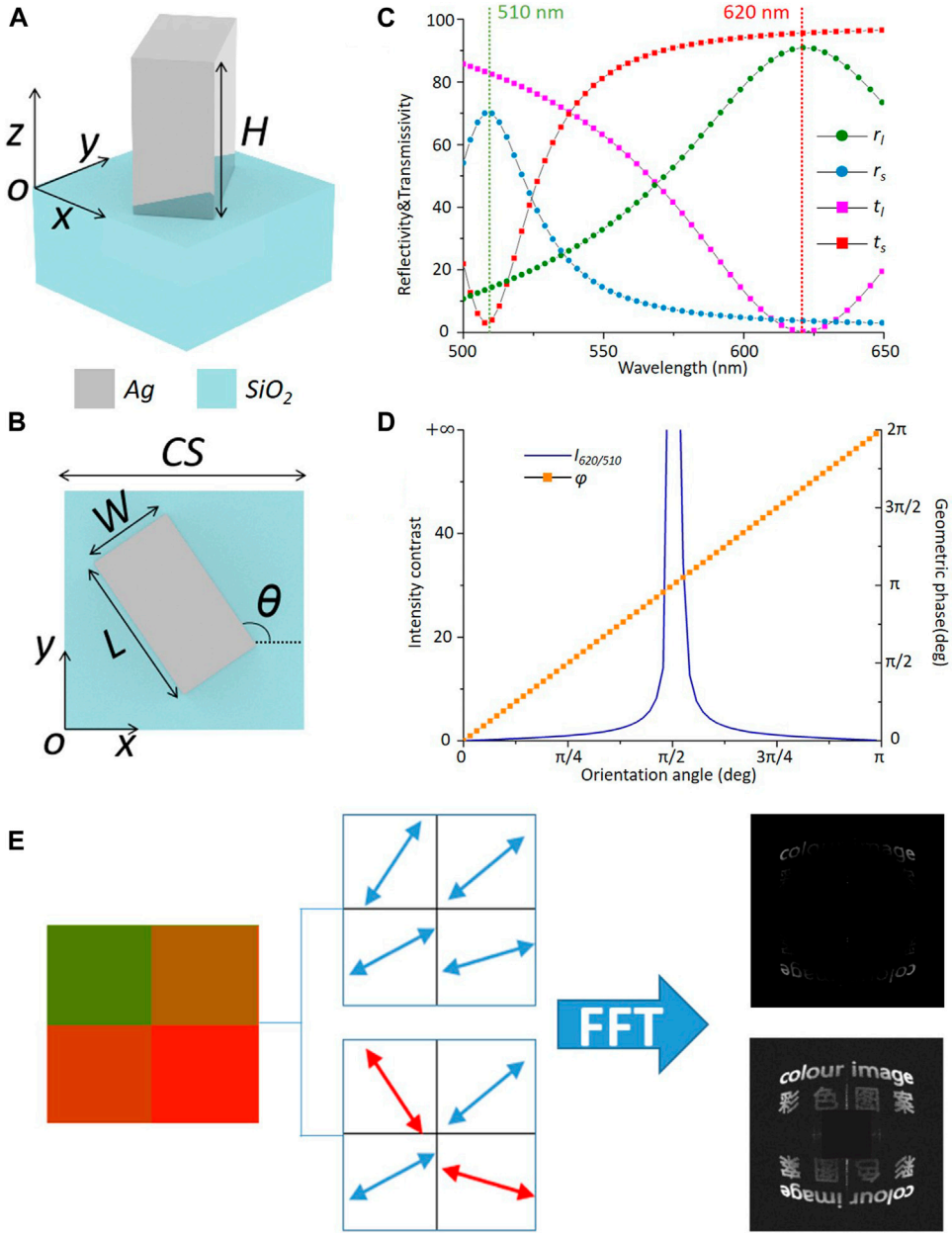

FIGURE 2
(A) The space and **(B)** top views of a unit-cell consisting of *Ag* nanobrick and SiO_2 substrate. **(C)** Simulated reflectivity and transmissivity of the nanobricks when illuminated by light polarized along the long (r_l, t_l) and short axes (r_s, t_s), which shows that the nanobrick works as a dual-wavelength polarizer with orthogonal polarization direction at the wavelengths of 510 and 620 nm. **(D)** Calculated intensity contrast ($I_{620/510}$) and geometric phase φ as the function of orientation angle θ, from which we can see that there are always two orientation angles to produce the same pseudo-color but different geometric phase. **(E)** The optimization process to determine the orientation arrays. There are different orientation arrays producing the same pseudo-color nanoprinting, the FFT to which will obtain holographic images with different correlation coefficient. And the SAA is employed to select the orientation angle pixel by pixel until the correlation coefficient finally satisfies the requirement.

the geometric phase $\varphi = \pm 2\theta$, the sign of which is positive for the left-handed circularly polarized (LCP) light and negative for the right-handed circularly polarized (RCP) light (Li et al., 2018; Fu et al., 2020; Zheng et al., 2022). Herein we employ the LCP light as the incidence and the calculated geometric phase is shown in Figure 2D of the orange line. It can be seen that there are always two angles that correspond to the same color but different geometric phase. Consequently, combining the dual-wavelength polarizer and orientation degeneracy hidden in the Malus law, the proposed metasurface can manipulate

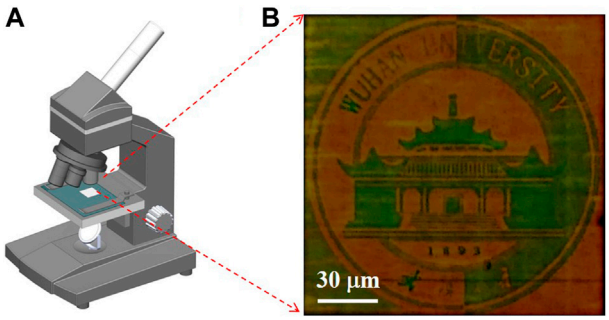

FIGURE 3
(A) The diagram of the optical microscope for observing the pseudo-color image recording by the metasurface. **(B)** The captured images when a polarizer with polarization directions of 0° is inserted before the metasurface. Scale bar: 30 μm.

the color and 2-step phase of the output beam at the same time.

The SAA is employed to select the orientation angle of the nanobrick. As shown in Figure 2E, for one pixel of the nanobrick arrays, there are two angles generating the same color, which is presented by the blue and red arrows, respectively. And these two angle arrays will generate PB phase with different value in the above-mentioned pixel. Subsequently, the fast Fourier transform (FFT) to the PB phase will obtain different calculated images, and we employ the correlation coefficient between the calculated and target images to select the orientation angle of a single nanobrick, the definition of which is given as:

$$CC(I,\ M) = \frac{cov(I,M)}{\sqrt{Var(I)}\sqrt{Var(M)}} \tag{4}$$

where I and M represent the calculated and target image, $cov(I,M)$ is the covariance of I and M, $Var(I)$ and $Var(M)$ represent the variances of I and M, respectively. This operation is implemented pixel by pixel to optimize the orientation array, which is finally determined until the correlation coefficient satisfies the requirement. Herein the final correlation coefficient between the calculated and the target images reaches 0.864. In this way, the obtained dual-wavelength polarizer with elaborately designed orientation can control the pseudo-color and phase of the output light simultaneously.

2.2 Sample fabrication

Firstly, we employ the spin coater to spin and coat a polymethyl methacrylate (PMMA) film and a conducting layer on the SiO_2 substrate. Subsequently, the electron beam lithography (EBL) is utilized to pattern the nanobrick structures. Then the conducting layer is washed away by the deionized water, and the exposed resist is developed in a mixture of methyl isobutyl ketone (MIBK) and isopropyl alcohol (IPA) with the ratio of 1/3 for 80 s, dipped in IPA for 30 s and blown dry by the nitrogen. Next, electron beam evaporator is employed to deposit a layer of chromium (3 nm) to increase the adhesion and a 70 nm silver film. Finally, we obtain the designed silver metasurface structure through lift-off process in hot acetone with temperature of 85°C.

3 Results

To demonstrate our concept, we design and fabricate a metasurface with 500 × 500 pixels (150 × 150 μm) to implement the near-field pseudo-color encoding and the far-field Fourier holographic images display. Firstly, the function of pseudo-color image display is characterized. Figure 3A displays the optical microscope (Motic BA310Met) for observing the nanoprinting image. In the experimental process, a polarizer is employed to decode the image right at the metasurface plane. Figure 3B shows the captured transmitted image when a polarizer with polarization angle of 0° is placed before the metasurface, which possesses ultra-high resolution of 75 k dpi (dots per inch) and the scale bar is 30 μm. We can see the images with color changing from red to green clearly, which demonstrates that the proposed metasurface can realize pseudo-color control merely by changing the orientation angle of the single-sized nanobrick.

Next, the function of the far-field holographic image display is demonstrated. As shown in Figure 4A of the optical setup, the light source is a linearly polarized super-continuum laser (YSL SC-pro), which is modulated to be LCP by a quarter-wave plate (QWP) after passing through an iris, and the far-field holographic image can be observed after the metasurface being illuminated by the incident LCP light. The inset is the scanning electron microscope (SEM) image of the nanobricks, the scale bar of which is 600 nm. The experimentally observed images at the working wavelengths of 510 and 620 nm are shown in Figures 4B,C, respectively, from which we can recognize the words clearly. Because the correction of geometric distortion is performed at the wavelength of 620 nm, the captured image at 510 nm shows slight distortion. These experiment results effectively prove that the metasurface can display a pseudo-color nanoprinting in the near-field and a Fournier holographic image in the far-field.

Subsequently, to explore the broadband characteristic of the metasurface, we change the wavelength of the incident light beam from 490 nm to 640 nm with a step of 30 nm. The experimentally captured holographic images are shown in Figures 5A–F, which display the designed words clearly although they show different sizes and geometric distortion versus the wavelength due to different diffraction angles. These experimental results prove

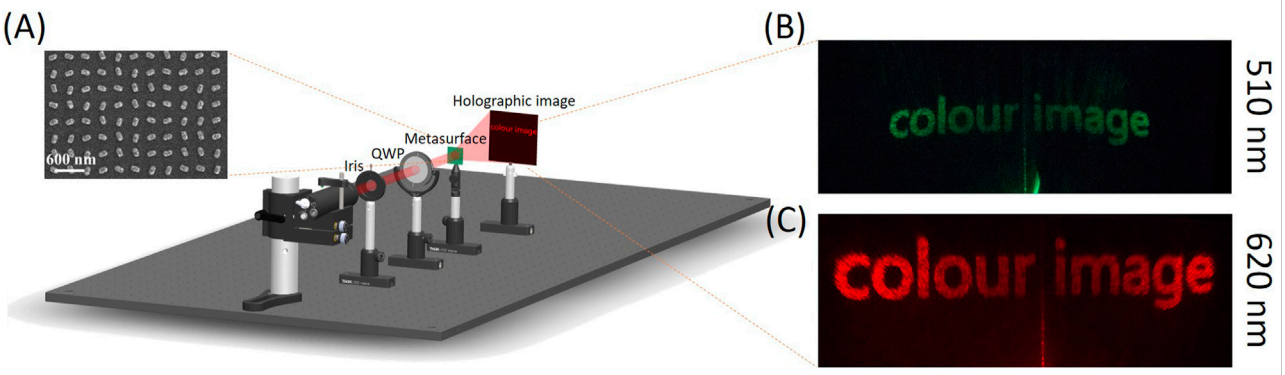

FIGURE 4
(A) Schematic illustration of the optical setup to decode far-field holographic image. The light source is a linearly polarized super-continuum laser. A QWP before the metasurface is employed to modulate the laser beam to be LCP, and the transmitted holographic image can be obtained in the far-field when the incident beam illuminates the metasurface. The inset shows partial view of the SEM image of the metasurface with the scale bar of 600 nm. **(B)** Experimental Fourier holographic images under LCP light illumination at 510 nm and **(C)** 620 nm.

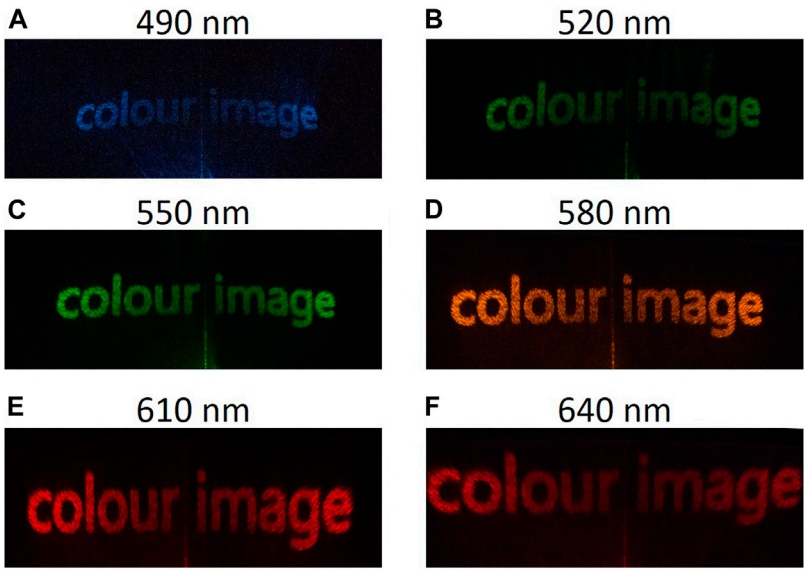

FIGURE 5
(A-F) Experimentally captured holographic meta-images from 490 to 640 nm with steps of 30 nm.

that the proposed metasurface possesses broadband characteristic for displaying holographic images.

4 Discussion

In conclusion, combining the dual-wavelength polarizer and orientation degeneracy hidden in the Malus law, a general platform for simultaneous pseudo-color control and phase manipulation is proposed. The employment of the dual-wavelength polarizer effectively converts the gray scale to pseudo color. On this basis, the employment of the orientation degeneracy allows the metasurface to further control the phase of the output light, thus realizing the holographic image and chromatic nanoprinting image display at the same time. In addition, benefiting from the single-sized strategy, our work effectively simplifies the process of design and fabrication. This study provides new insights into the multifunctional devices design based on the metasurface, and can be applied in fields such as optical anticounterfeiting, image display, information encryption, and etc.

Data availability statement

The original contributions presented in the study are included in the article/supplementary material, further inquiries can be directed to the corresponding authors.

Author contributions

ZL and GZ proposed the idea and initiated the project. ZL and JL conducted the metasurface design and numerical simulations. JL fabricated the samples. ZZ and JL performed the experimental characterization. GZ and ZL analyzed the experimental data. GZ, ZL, JL, and ZZ co-wrote the paper. GZ and ZL supervised the project. The manuscript was discussed and corrected by all authors.

Funding

The authors would like to acknowledge the support from the National Key Research & Development Program of China (2021YFE0205800), National Natural Science Foundation of China (11904267, 12174292, 91950110), Natural Science Foundation of Hubei Province (ZRMS2021000211), and the Fundamental Research Funds for the Central Universities (2042021kf0018, 2042022kf0024, 2042022kf1013 and 2042022kf1011).

Conflict of interest

The authors declare that the research was conducted in the absence of any commercial or financial relationships that could be construed as a potential conflict of interest.

Publisher's note

All claims expressed in this article are solely those of the authors and do not necessarily represent those of their affiliated organizations, or those of the publisher, the editors and the reviewers. Any product that may be evaluated in this article, or claim that may be made by its manufacturer, is not guaranteed or endorsed by the publisher.

References

Chen, K., Xu, C., Zhou, Z., Li, Z., Chen, P., and Zheng, G. (2022). Multifunctional liquid crystal device for grayscale pattern display and holography with tunable spectral-response. *Laser Phot. Rev.* 16, 2100591. doi:10.1002/lpor.202100591

Chen, R., Zhou, Y., Chen, W., Chen, R., Iqbal, N., and Ma, Y. (2020). Multifunctional metasurface: Coplanar embedded design for metalens and nanoprinted display. *ACS Photonics* 7, 1171. doi:10.1021/acsphotonics.9b01795

Cheng, J., Sha, X., Zhang, H., Chen, Q., Qu, G., Song, Q., et al. (2022). Ultracompact orbital angular momentum sorter on a CMOS chip. *Nano Lett.* 22, 3993. doi:10.1021/acs.nanolett.2c00572

Dai, Q., Guan, Z., Chang, S., Deng, L., Tao, J., Li, Zhong., et al. (2020). A single-celled tri-functional metasurface enabled with triple manipulations of light. *Adv. Funct. Mat.* 30, 2003990. doi:10.1002/adfm.202003990

Deng, J., Deng, L. G., Guan, Z., Tao, J., Li, G. F., Li, Z., et al. (2020a). Multiplexed anticounterfeiting meta-image displays with single-sized nanostructures. *Nano Lett.* 20, 1830. doi:10.1021/acs.nanolett.9b05053

Deng, J., Gao, F., Yuan, P., Li, Y., and Yan, B. (2022a). Bidirectional nanoprinting based on bilayer metasurfaces. *Opt. Express* 30, 448136. doi:10.1364/OE.448136

Deng, L., Deng, J., Guan, Z., Tao, J., Chen, Y., Yang, Y., et al. (2020b). Malus-metasurface-assisted polarization multiplexing. *Light-Sci. Appl.* 9, 101. doi:10.1038/s41377-020-0327-7

Deng, L., Li, Z., Zhou, Z., He, Z., Zeng, Y., Zheng, G., et al. (2022b). Bilayer-metasurface design, fabrication, and functionalization for full-space light manipulation. *Adv. Opt. Mat.* 10, 2102179. doi:10.1002/adom.202102179

Fu, R., Deng, L., Guan, Z., Chang, S., Tao, J., Li, Z., et al. (2020). Zero-order-free meta-holograms in a broadband visible range. *Photonics Res.* 8, 723. doi:10.1364/PRJ.387397

Hao, Z., Liu, W., Li, Z., Li, Z., Geng, G., Wang, Y., et al. (2021) Full complex-amplitude modulation of second harmonic generation with nonlinear metasurfaces. 15, 2100207. doi:10.1002/lpor.202100207

Kim, J., Jeon, D., Seong, J., Badloe, T., Jeon, N., Kim, G., et al. (2022). Photonic encryption platform via dual-band vectorial metaholograms in the ultraviolet and visible. *ACS Nano* 16, 3. doi:10.1021/acsnano.1c10100

Li, J., Wang, Y., Chen, C., Fu, R., Zhou, Z., Li, Z., et al. (2021a). From lingering to rift: Metasurface decoupling for near- and far-field functionalization. *Adv. Mat.* 33, 2007507. doi:10.1002/adma.202007507

Li, Z., Chen, C., Guan, Z., Tao, J., Chang, S., Dai, Q., et al. (2020). Three-Channel metasurfaces for simultaneous meta-holography and meta-nanoprinting: A single-cell design approach. *Laser Phot. Rev.* 14, 2000032. doi:10.1002/lpor.202000032

Li, Z., Dai, Q., Mehmood, M., Hu, G., Yanchuk, B., Tao, J., et al. (2018). Full-space cloud of random points with a scrambling metasurface. *Light-Sci. Appl.* 7, 63. doi:10.1038/s41377-018-0064-3

Li, Z., Deng, L., Deng, J., He, Z., Tao, J., Zheng, G., et al. (2021b). Metasurface-enabled three-in-one nanoprints by multifunctional manipulations of light. *iScience* 24, 103510. doi:10.1016/j.isci.2021.103510

Ma, Q., Gao, W., Xiao, Q., Ding, L., Gao, T., Zhou, Y., et al. (2022). Directly wireless communication of human minds via non-invasive brain-computer-metasurface platform. *eLight* 2, 11. doi:10.1186/s43593-022-00019-x

Ming, Y., Intaravanne, Y., Ahmed, H., Kenney, M., Lu, Y., and Chen, X. (2022). Creating composite vortex beams with a single geometric metasurface. *Adv. Mat.* 34, 2109714. doi:10.1002/adma.202109714

Ouyang, X., Xu, Y., Xian, M., Feng, Z., Zhu, L., Cao, Y., et al. (2021). Synthetic helical dichroism for six-dimensional optical orbital angular momentum multiplexing. *Nat. Photonics* 15, 901. doi:10.1038/s41566-021-00880-1

Ren, R., Li, Z., Deng, L., Shan, X., Dai, Q., Guan, Z. Q., et al. (2021). Non-orthogonal polarization multiplexed metasurfaces for tri-channel polychromatic image displays and information encryption. *Nanophotonics* 10, 2903. doi:10.1515/nanoph-2021-0259

Tao, J., You, Q., Li, Z., Luo, M., Liu, Z., Qiu, Y., et al. (2022). Mass-manufactured beam-steering metasurfaces for high-speed full-duplex optical wireless-broadcasting communications. *Adv. Mat.* 34, 2106080. doi:10.1002/adma.202106080

Wang, Y., Fan, Q., and Xu, T. (2021). Design of high efficiency achromatic metalens with large operation bandwidth using bilayer architecture. *Opto-Electron. Adv.* 4. 200008. doi:10.29026/oea.2021.200008

Xu, P., Tian, H., Jiang, W., Chen, Z., Cao, T., Qiu, C.-W., et al. (2021). Phase and polarization modulations using radiation-type metasurfaces. *Adv. Opt. Mat.* 9, 2100159. doi:10.1002/adom.202100159

Yang, B., Ma, D., Liu, W., Choi, D.-Y., Li, Z., Cheng, H., et al. (2022). Deep-learning-based colorimetric polarization-angle detection with metasurfaces. *Optica* 9, 217. doi:10.1364/OPTICA.449893

Zhang, H., Sha, X., Chen, Q., Cheng, J., Ji, Z., Song, Q., et al. (2022a). All-dielectric metasurface-enabled multiple vortex emissions. *Adv. Mat.* 34, 2109255. doi:10.1002/adma.202109255

Zhang, S., Huang, L., Geng, G., Li, J., Li, X., and Wang, Y. (2022b). Full-Stokes polarization transformations and time sequence metasurface holographic display. *Photonics Res.* 10, 1031. doi:10.1364/PRJ.450354

Zheng, P., Dai, Q., Li, Z., Ye, Z., Xiong, J., Liu, H., et al. (2021). Metasurface-based key for computational imaging encryption. *Sci. Adv.* 7, eabg0363. doi:10.1126/sciadv.abg0363

Zheng, P., Li, J., Li, Z., Ge, M., Zhang, S., Zheng, G., et al. (2022). Compressive imaging encryption with secret sharing metasurfaces. *Adv. Opt. Mat.* 2200257. doi:10.1002/adom.202200257

Zhou, Z., Wang, Y., Chen, C., Fu, R., Guan, Z., Li, Z., et al. (2022). Multifold integration of printed and holographic meta-image displays enabled by dual-degeneracy. *Small* 18, 2106148. doi:10.1002/smll.202106148

frontiers | Frontiers in Physics

TYPE Original Research
PUBLISHED 29 September 2022
DOI 10.3389/fphy.2022.1012470

OPEN ACCESS

EDITED BY
Ben-Xin Wang,
Jiangnan University, China

REVIEWED BY
Yan-Feng Wang,
Tianjin University, China
Rujiang Li,
Xidian University, China

*CORRESPONDENCE
Yongzhong Zhu,
bsbs1980@sina.com

SPECIALTY SECTION
This article was submitted to Optics and Photonics,
a section of the journal
Frontiers in Physics

RECEIVED 05 August 2022
ACCEPTED 12 September 2022
PUBLISHED 29 September 2022

CITATION
Zang Y, Zhu Y, Xie W, Yang Y, Bu L and Liu X (2022), A bi-dimensional compressed Luneburg lens antenna for miniaturization based on transformation optics.
Front. Phys. 10:1012470.
doi: 10.3389/fphy.2022.1012470

A bi-dimensional compressed Luneburg lens antenna for miniaturization based on transformation optics

Yadan Zang, Yongzhong Zhu*, Wenxuan Xie, Yufei Yang, Lijun Bu and Xiaoyu Liu

School of Information Engineering, Engineering University of PAP, Xi'an, China

Transformed Luneburg lens has been widely employed to provide aberration-free imaging and high-gain antenna system, but whose focal plane and beam scanning range decrease correspondingly. In this paper, a two-dimensional compressed elliptical cylindrical Luneburg lens is presented based on transformation optics (TO) to achieve miniaturization and wide-angle beam steering. The Jacobian matrix and the permittivity tensor are calculated after supposing formulas to compress the focal plane, while maintaining the lens' inherent performance. The gradient permittivity is achieved by two ring-type periodic unit cells on the basis of the Equivalent Medium Theory. The lens is then attached between a pair of parallel metal plates to further improve its gain and lower the side lobe level (SLL). To demonstrate this assumption, a prototype of this Luneburg lens is manufactured by isotropic material and 3D printing technique. The antenna operates at 3.3–5 GHz with a peak gain of 16.1/15.9 dBi. A 2D beam scanning range of $\pm 50^{\circ}$ and $\pm 20^{\circ}$ can be implemented by merely five feeds, the side lobe level keeping less than -16.3/-16 dB. Measured results coincide well with theoretical predictions, offering a beneficial transformation mapping to both microwaves and optics.

KEYWORDS

transformation optics, Luneburg lens, lens antenna, multi-beam antenna, gradient index lenses

1 Introduction

Lens antenna system, a classic example of aperture array antennas, has the ability to regulate the propagation of electromagnetic waves from the perspective of the electromagnetic field. A typical representative is the Luneburg lens system. The Luneburg lens is originally an inhomogeneous dielectric spherical lens with a continuous refractive index [1], which is capable of converting the spherical wavefront into a planar wavefront and is widely applied in multi-beam and high gain scenario [2]; [3]; [4]. Despite the advantage of beam coherence, the sphere with large scale limits its wider application. With the advent of transformation optics (TO) [5]; [6] and quasi-conformal transformation optics (QCTO) [7], a Luneburg lens can be transformed

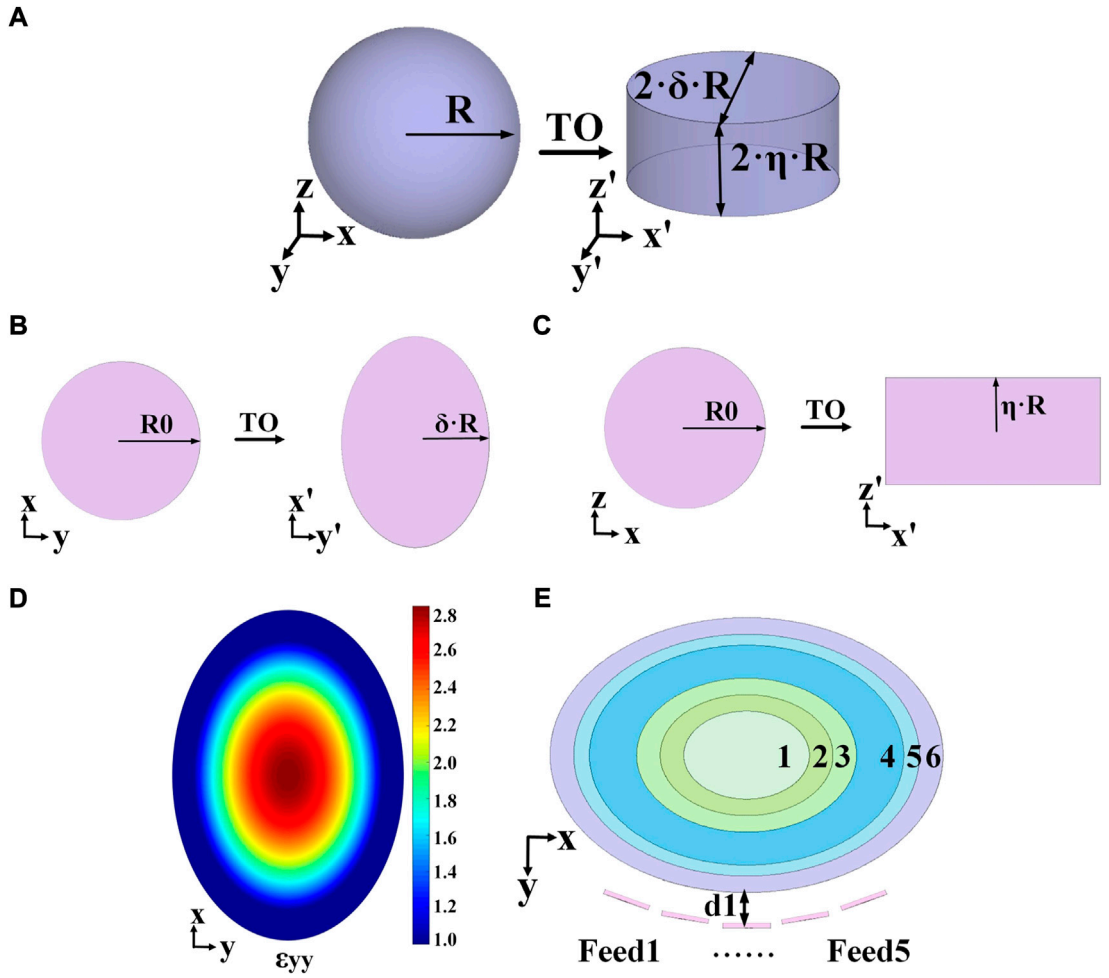

FIGURE 1
Transformation schematic of the Luneburg lens. **(A)** The proposed approach of transformation. **(B)** Compression of the y-coordinate. **(C)** Compression of the z-coordinate. **(D)** Distribution of the ε_{yy} component. **(E)** Shells and feeds.

TABLE 1 Gradient permittivity and dimensions.

Shell	1	2	3	4	5	6
ε_r	2.85	2.6	2.3	2	1.6	1.45
lx	0.36R	0.44R	0.6R	0.84R	0.92R	R
ly	0.252R	0.308R	0.42R	0.588R	0.644R	0.7R

to a lower and more conformal profile for the sake of better matching with feeds, while original performances of the lens are practically reserved.

Recently, profile reduction and miniaturization of the Luneburg lens have been widely investigated, the typical cases of which are truncated lens [8]; [9]; [10]; [11], hemispherical lens [12]; [13], ellipsoidal lens [14,15], discus lens [16,17]; [18], diffuse lens [19] and flat lens [20]; [21]; [22,23]; [24]; [25]; [26]. The key of all the aforementioned miniaturization is to assign new formulas to a particular coordinate or a group of boundary conditions of the sphere in one specific plane, and then apply it to lower the profile and propose a transformed lens. However, the beam scanning range and aperture efficiency would be lowered owing to the focal plane of the lens being minished. In order to radiate a wider scanning coverage and accommodate more feeds, [11] enlarged the focus surface to be extend-flattened based on QCTO. [14] proposed an lens array composed of two ellipsoidal Luneburg lenses, simultaneously enhancing its aperture efficiency and reducing the amount of feeds by introducing the local-beam shifting method. Alternatively, [26] increased its scanning angle *via* a transmission line made of two metallic surfaces, which can be regarded as a parallel-plate waveguide. In addition, the fabrication process of transformed Luneburg lens is fairly complicated due to the employment of

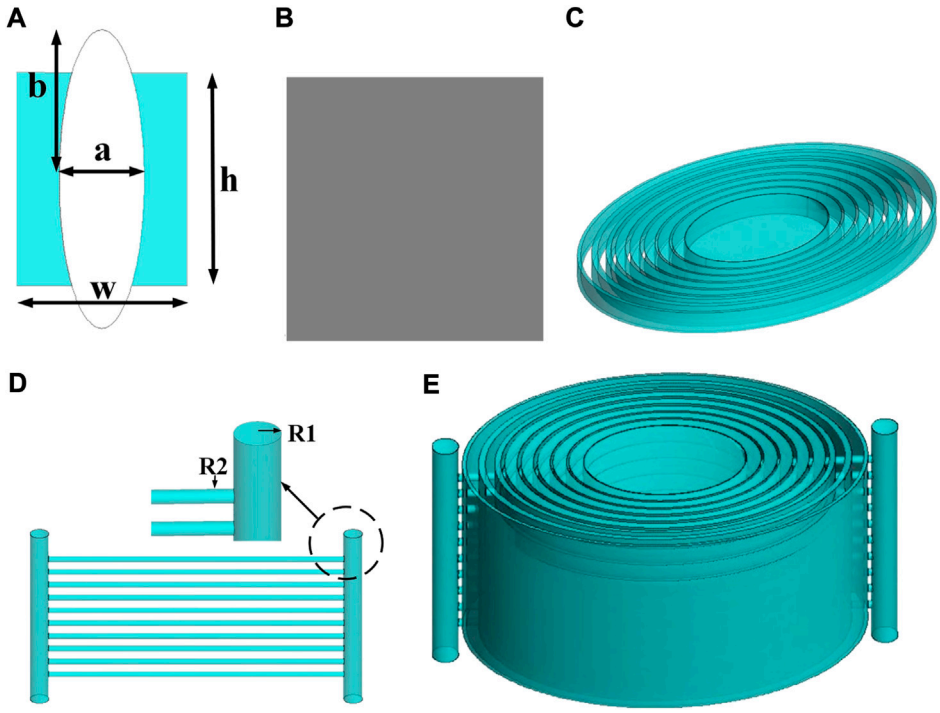

FIGURE 2
Schematic of the proposed Luneburg lens. **(A)** The ellipse ring-type unit. **(B)** The rectangle ring-type unit. **(C)** The single layer lens composed of periodic unit cells. **(D)** The supporting frame. **(E)** The elliptical Luneburg lens.

TABLE 2 Parameters of ring-type units.

Periodic unit cells	The ellipse ring-type unit				The rectangle Ring-type unit	
a/mm	0	1.6	3.6	5.6	4.6	5.2
ε_r	2.85	2.6	2.3	2	1.6	1.45

multiple dielectric materials [16,17]; [18]; [20]; [25] or metamaterials [8]; [9]; [13]; [15]; [22,23]; [24].

This paper argues that the effective aperture of the lens can be adjusted while maintaining a wide scanning angle and high aperture efficiency. This is possible by simultaneously changing two coordinates. In this paper, an elliptical cylindrical Luneburg lens is proposed based on the transformation mapping, which is a novel scheme for miniaturization. The spherical Luneburg lens is transformed from two orthogonal directions, and the continuously spatially variable permittivity is then determined, approximated, discretized, and optimized. Additionally, one single material can be set with specified permittivity and implemented by 3D printing based on the Equivalent Medium Theory. Two ring-type periodic unit cells composed of photosensitive resin are created in order to obtain the gradient permittivity. Experiments reveal that the proposed lens for antenna applications can achieve an impedance bandwidth of 41% (3.3–5 GHz), a peak gain of 16.1/15.9 dBi, and a beam coverage of 100° in the H-plane and 40° in the E-plane with five feed antennas, with beam steering performance of ± 50° with only 1.2 dBi reduction in peak gain.

2 Theoretical analysis on transformation and antenna design

2.1 Analysis of anisotropic tensors

Figure 1A illustrates the novel scheme of bi-dimensional transformation. Set coordinates for a spherical lens are (x, y, z) in

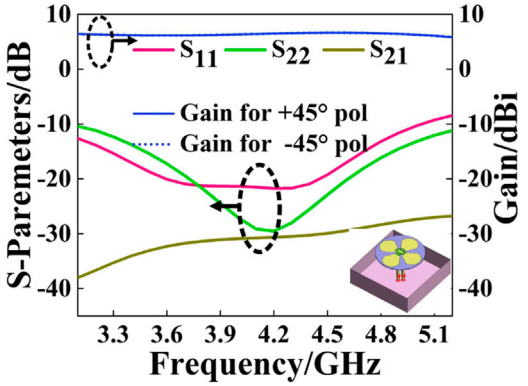

FIGURE 3
Simulated results of the feed antenna.

the virtual space, while those for an elliptical cylindrical lens are (x', y', z') in the physical space. Suppose the spherical has a radius of R, the compression factor for the y-coordinate is δ, and it for the z-coordinate is η. Both δ and η take any real number between 0 and 1.

In the transformation, the y-coordinate transformation is introduced to directly reduce the curvature of the lens profile and change the circular arc into an elliptical arc. And the z-coordinate transformation is proposed to change the original circular surface which is not easily conformable into a rectangle with straight upper and lower boundaries. The transformations of the y- and z-coordinate are all compressed, while the transformation of the x-coordinate are essentially expanded, so that the long axis of the ellipse can be controlled to be R.

A spherical lens can be regarded as an infinite number of planar circles, where the radius of each circle is a function of the

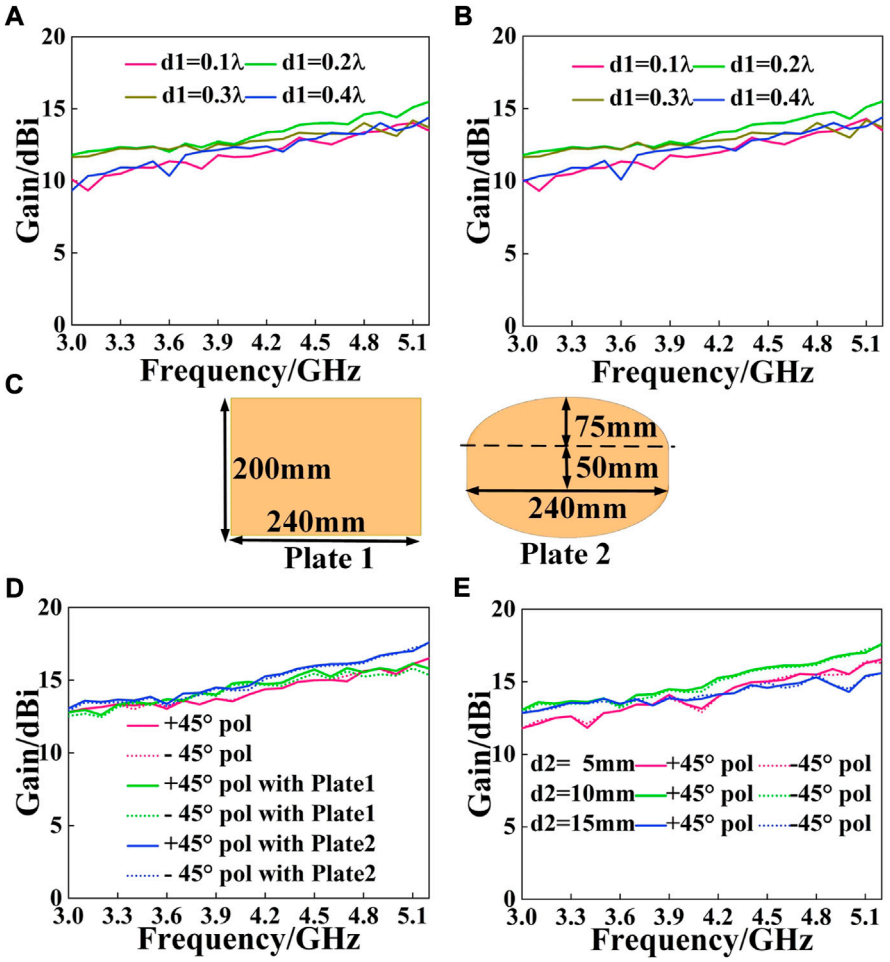

FIGURE 4
Gain performance of the proposed Luneburg lens antenna. **(A)** Gain for +45° pol with different *d1*. **(B)** Gain for -45° pol with different *d1*. **(C)** Two type of plates. **(D)** Gain with two plates. **(E)** Gain with different *d2*.

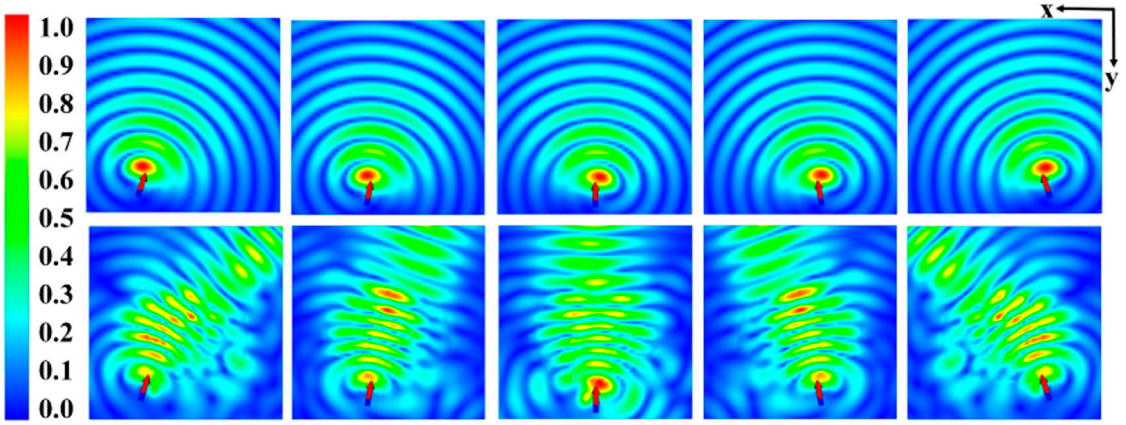

FIGURE 5
Normalized electric field distribution.

coordinates of a point on the circumference as the independent variable. Take a point (x0,y0,z0) as an example. Let the radius of its circle be *R0*, as shown in Figures 1B,C.

Through coordinate transformation, the circle can be changed into an ellipse with long axis *2R* and short axis $2\eta R$ in the H- plane, as illustrated in Figure 1B. And Figure 1C shows that this circle is changed to be a rectangle with length *2R* and width $2\delta R$ in its orthogonal E- plane. The transformations are namely two-dimensional compression.

The equation of the permittivity of the spherical lens is:

$$\varepsilon(r) = 2 - \frac{x^2 + y^2 + z^2}{R^2}, u(r) = 1 \tag{1}$$

The transformation formulas can be defined as:

$$x' = \frac{R}{\sqrt{R^2 - z^2}}x \quad y' = \delta y \quad z' = \frac{\eta \cdot R}{\sqrt{R^2 - y^2}}z \tag{2}$$

For singularities in Formula 2, note x' = x = 0 in the case of z = ±R, and z' = z = 0 in the case of y = ±R. In the subsequent analysis, the effect of the 4 singularities is neglected. The Jacobian transformation matrix, the permittivity tensor and the permeability tensor are calculated in the following equations:

$$\Lambda = \begin{bmatrix} 1 & 0 & xB/\eta \\ 0 & \delta & 0 \\ 0 & \eta yzA^3/R^2 & \eta B \end{bmatrix} \tag{3}$$

$$\begin{aligned} \overline{\overline{\varepsilon'}} &= \frac{\Lambda\bar{\varepsilon}\Lambda^T}{\det\Lambda} \\ &= \frac{\varepsilon(r)\sqrt{(R^2 - z^2)(R^2 - y^2)}}{\delta\eta R^2} \\ &\quad \cdot \begin{bmatrix} R^2(R^2 - z^2)^{-1} + x^2B^2 & 0 & xAB \\ 0 & \delta^2 & \delta yB \\ xAB & \delta yB & \eta^2A^2 + y^2B^2 \end{bmatrix} \end{aligned} \tag{4}$$

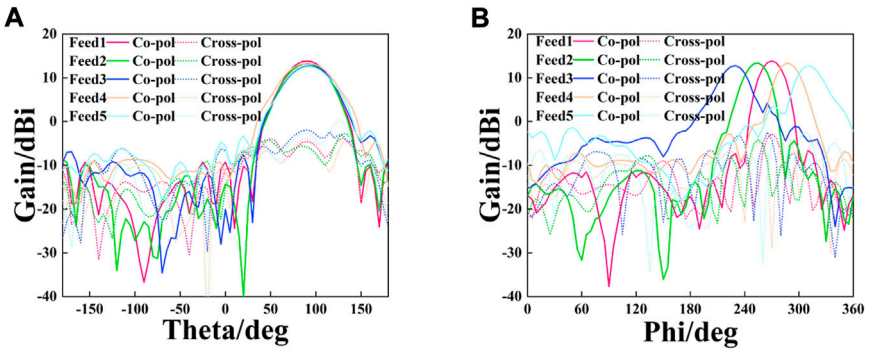

FIGURE 6
Simulated radiation patterns for +45° pol at 3.3 GHz. **(A)** E-plane. **(B)** H-plane.

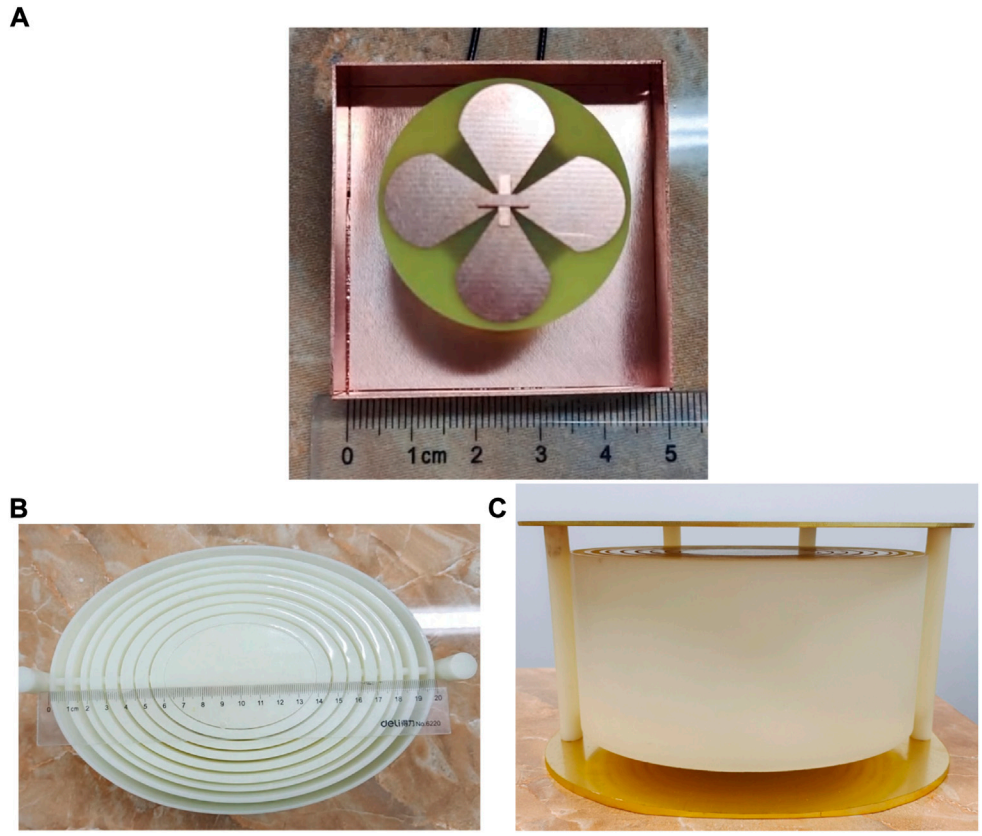

FIGURE 7
The elliptical cylindrical Luneburg lens. **(A)** The feed antenna. **(B)** The 3-D printed lens. **(C)** The overall structure.

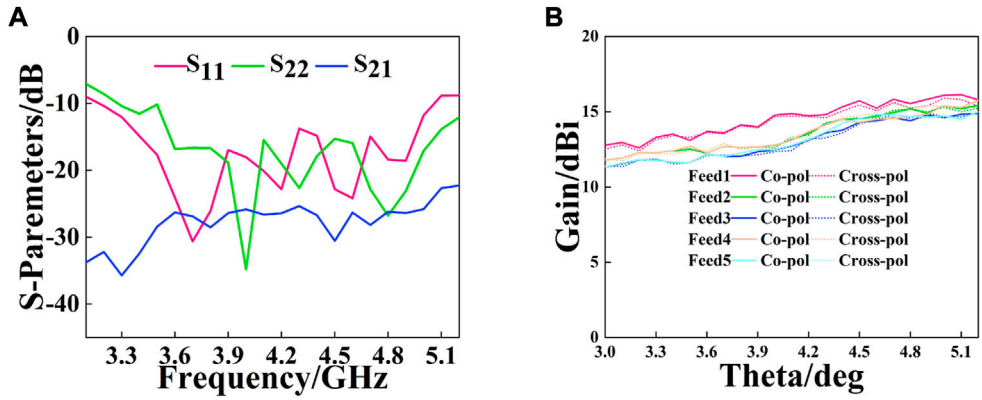

FIGURE 8
Measured results of the proposed Luneburg lens. **(A)** S-Parameters. **(B)** Gain performance.

$$\overline{\overline{\mu'}} = \frac{\Lambda\bar{\mu}\Lambda^T}{\det\Lambda} = \begin{bmatrix} R^2\left(R^2 - z^2\right)^{-1} + x^2B^2 & 0 & xAB \\ 0 & \delta^2 & \delta yB \\ xAB & \delta yB & \eta^2A^2 + y^2B^2 \end{bmatrix} \quad (5)$$

where $A = \frac{R}{\sqrt{R^2-y^2}}$, and $B = \frac{R\eta z}{\sqrt[3/2]{R^2-Z^2}}$.

According to Formulas 4, 5, the elliptical Luneburg lens' constitutive parameters possess significant anisotropy on

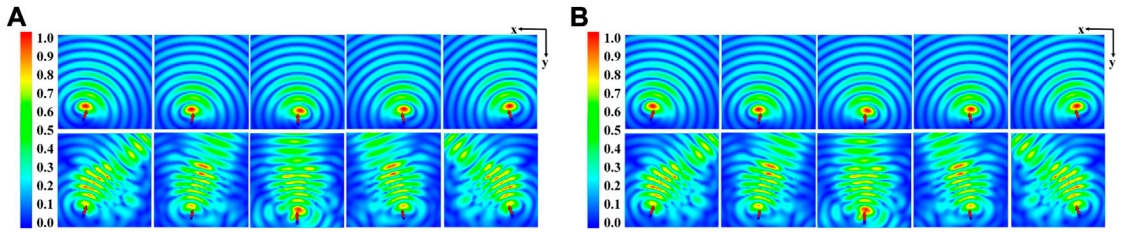

FIGURE 9
The measured normalized electric field distribution. **(A)** +45° pol. **(B)** -45° pol.

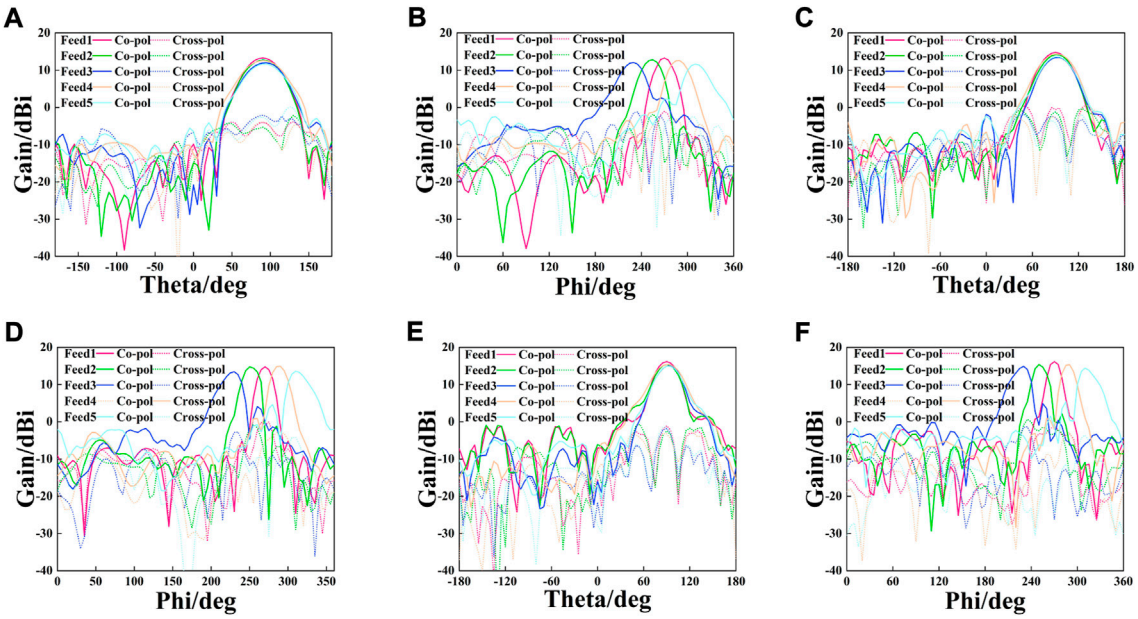

FIGURE 10
Measured radiation patterns for +45° pol. **(A)** E-plane at 3.3 GHz. **(B)** H-plane at 3.3 GHz. **(C)** E-plane at 4.2 GHz. **(D)** H-plane at 4.2 GHz. **(E)** E-plane at 5.0 GHz. **(F)** H-plane at 5.0 GHz.

account of non-diagonal tensor components. As a result, the permittivity tensor's numerical value should be processed before being applied to next step.

Most researchers are inclined to deal with the permittivity tensor firstly, and then fabricate Luneburg lens with isotropic materials. There are four representative methods. Method 1: Change the non-diagonal tensor to be a diagonal one by eigenvalues, and then set components of the tensor which are less than one [20] or insensitive to the lens performance to be one [13]. Method 2: For the diagonal tensor, calculate the plane wave dispersion equation and determine a component with the greatest value in the tensor as the permittivity value [14]. Method 3: Designate a component in the diagonal tensor that most affects the lens performance and then directly assume and approximate the numerical value of the permittivity [15]; [16,17]; [18]; [19]; [22,23]. Method 4: Directly rotate the transformed coordinate system x'y'z' by an angle ϕ, then adjust ϕ to make the non-diagonal elements in the tensor become 0. The element with the greatest influence on wave propagation is specified to be the permittivity value [21]; [27].

Firstly, in order to fully utilize the lens's focusing capabilities, the xoz plane with the largest section area is chosen as the focal plane. The electromagnetic waves radiated from the feed will be nearly perpendicular to the xoz plane and relatively parallel to the y-axis direction. As a result, the ε_{yy} component of $\overline{\overline{\varepsilon'}}$ has the biggest impact on the lens performance. Secondly, the function of

TABLE 3 Comparison between the proposed Luneburg lens and references.

Reference	Geometry	L*W*H (λ^3)	Fre. (GHz)	BW	Gain (dBi)	Feed antennas	Beam scanning range
13	Hemisphere	4*4*2.2	10	15.1%	15.7	3 Patch Antennas	±41°
15	Ellipsoid	3.2*1.6*1.6	10	NA	18.4 dB	8 Patch Antennas	±42°
18	Discus	2*3.5*3.5	84	37.8%	22	8 Open-Ended Waveguides	±30°
23	Slab	3.14*3.14*0.5	10	20%	13.2	7 Patch Antennas	±54°
This work	Elliptical Cylinder	2.76*1.94*1.38	4.1	41%	16.1/15.9	5 Dual-DipoleAntennas	± 50 and ±20°

ε_{yy} is more stable and modest than others', which is benign for the following research. On the basis of the above analysis, the amplitude of ε_{yy} is set to be the permittivity of this dielectric lens. In addition, the permeability is directly appointed to be one in order to avoid using magnetic materials [15]; [18].

Define R = 100 mm, δ = 0.7, and η = 0.5. This compression reduces the size of the lens from $4\pi R^3/3$ to $2\pi\eta\delta R^3$, a volumetric reduction of 47.5%. Meanwhile, the focal plane (the xoz plane) is reduced from πR^2 to $4\eta R^2$, an areal reduction of 36.3%. Obviously, the focal plane realizes a relative expansion in comparison with the volume, promising a broader steering angle. Furthermore, the curvature of the lens becomes smaller (from $1/R$ to δ/R), which is favorable for matching with more feed sources. Figure 1D is the numerical distribution of ε_{yy} calculated in MATLAB, varying from 1 to 2.86. The gradient permittivity and the size of each layer are listed in Figure 1E; Table 1 in accordance with the gain optimization approach of multishell Luneburg lenses in [28]. The variables lx and ly respectively denote the long and short axes of the elliptical cylinder.

2.2 Implementation of gradient index

Periodic unit cells are often employed to actualize the gradient permittivity distribution of Luneburg lens, and the common forms include the ring-type units [3], the cubical lattices [4,8], and the hole-type units [29]. Compared with other unit cells, the ring-type units are less sensitive to the angle of incidence and more conducive to beam consistency, hence being employed to realize gradient permittivity. The design of ring-type units is on the basis of the A-BG formula of the Equivalent Medium Theory [30], which actually involves mixing dielectric materials within a cell to obtain equivalent electromagnetic properties. It is widely used in the design of the aforementioned periodic unit cells. The formula is as follows:

$$\frac{\varepsilon_i - \varepsilon_{eff}}{\varepsilon_i - \varepsilon_h} = (1-p)\left(\frac{\varepsilon_{eff}}{\varepsilon_h}\right)^{\frac{1}{3}} \tag{6}$$

The equivalent permittivity of the cell ε_{eff} can be calculated based on the permittivity of the substrate material ε_h, the permittivity of the insert material ε_i and the volume fraction of the insert material to the whole p. From the perspective of easy preparation, the substrate material is photosensitive resin (ε_r = 2.85, tanδ = 0.005), a common material for 3D printing technology. Furthermore, the photosensitive resin material is stable, which means its refractive index and permittivity slightly vary with the frequency increasing. It hardly affects the performance of the antenna. The insert material is air (ε_r = 1, tanδ = 0). Relative permittivity of Shell 1 can be directly attained by resin, and that of Shells 2–6 can be attained by resin with periodic unit cells, which are shown in Figures 2A,B with b = 7 mm, w = 8 mm and h = 10 mm. White for air, blue for photosensitive resin. The volume fraction p in the ring-unit with different inclusions is in the following equation:

$$p_i = \begin{cases} 0, & i = 1 \\ \dfrac{(lx_i + lx_{i-1}) \cdot (2 + \pi - 2\delta) \cdot 4\int_0^{\frac{b a_i}{2}} \sqrt{1 - \frac{y^2}{b^2}}\, dy}{\pi\delta h \cdot (lx_i^2 - lx_{i-1}^2)}, & i = 2,3,4 \\ \dfrac{(\pi + 2 - 2\delta)(2lx_i - w + a)(w - a)h}{\pi\delta h \cdot (lx_i^2 - lx_{i-1}^2)}, & i = 5,6 \end{cases} \tag{7}$$

Values of a and permittivity are calculated based on Formulas 6, 7, as listed in Table 2. The combination schematic of the two periodic unit cells is in Figure 2C. To ensure the robustness of the lens, a support structure is introduced. The support structure of the lens is also made of photosensitive resin with two vertical cylinders of radius $R1$ = 6.5 mm and 10 horizontal cylinders of radius $R2$ = 2 mm, as illustrated in Figure 2D. The assembled elliptical lens is in Figure 2E.

2.3 Performance simulation and optimization

The feed antenna is a dual-polarized dipole antenna, consisting of two orthogonal modified bowtie dipoles, parasitic elements and a cavity [31]. Parameters of the antenna is modified to operate at 3.3–5 GHz. The simulations are performed in Altair FEKO (2021.2), and the gain, S11, S22, S21 of the feed are shown in Figure 3.

The gain of the proposed lens antenna is optimized below. According to [24], transformation mapping would cause the

focal point's initial placement on the lens' surface to move to the exterior of the lens. As a result, the optimal distance between the feed source and the lens needs to be investigated. The feed antenna is positioned at four distinct points during simulations, with *d1* standing for the distance between the feed and the lens surface. Results are summarized in Figures 4A,B. It is obvious that the gain is prime at $d1 = 0.2\lambda$ for 14.5/14.3 dBi. The antenna is fixed between two parallel metal plates in order to further improve gain and decrease side lobe level [26]; [32]. Figure 4C depicts two plate shapes, both of which are 1.5 mm thick. Gain curves for the lens antenna are shown in Figures 4D,E, where *d2* denotes the separation between the plates and the lens. With Plate 2 and *d2* = 10mm, it is discovered that the gain reaches its maximum of 16.9/16.8dBi.

Further investigation into multi-beam properties of the proposed lens is operated. Only results of +45° polarization are shown for simplicity. Figure 5 contrasts the normalized electric field distribution, where the five subjacent plots are under the circumstance of beams passing through the proposed lens. As can be observed from Figure 5, the relative phase of the propagating fields is rebuilt and then the necessary wave-transformation functions to enhance gain and turn the original spherical wavefront to be planar, conforming to the inherent characteristics of Luneburg lens. Figure 6 depicts radiation patterns in the E- and H-plane at 3.3 GHz. It can be seen from the pattern that the cross-polarization level of multiple beams is higher than 18.5dB, and the SLL is lower than -19 dB. Since the beamwidth in H-plane is smaller than it in E-plane, multiple feeds must be put in H-plane, so as to achieve a wide beam coverage. The beamwidth is the sole factor that is affected by the differing lens diameters in the E- and H-plane, while dual-linear polarization remain unchanged.

3 Measured results and discussion

The feed antenna is depicted in Figure 7A. The proposed elliptical cylindrical Luneburg lens in Figures 7B,C is fabricated by Stereo Lithography Apparatus, a technique of 3D printing. Figure 8A is the measured result, indicating S-parameters of the feed. In 3.3–5 GHz, S11 is less than -10 dB and S21 is less than -30 dB, hence the impedance bandwidth reaches up to 41%. The measured result coincides well with its simulation. Both processing accuracy and measurement error contribute to the slight performance degradation. Contrast of gain curves are shown in Figure 8B, with the maximum value of 16.1/15.9 Bi. Electromagnetic beams radiated from the feed antennas are focused by the transformed lens, thus greatly narrowing beams and enhancing the gain. As can be seen in Figure 8B, gain curves with lens are not consistent, which is common for transformed lenses. Because the transformation mapping applied in this letter is longitudinally parallel to the y- and *z*-direction, instead of radial mapping, which changes the original radial refractive index distribution and intrinsical rotational symmetry of the spherical lens. Besides, the placement of feed antennas in Figure 1A can also produce different convergences of beams, inevitably resulting in slight diversities and degradation in the final gain. Figure 9 is the measured normalized electric field distribution, which coincides with the simulated results. The different half power bandwidths (HPBW) in Figure 10 strongly prove that the elliptic cylindrical lens can not only independently control the beam in different planes, but also assure its multi-beam performance. And the wider beamwidths in the E-plane can reduce the number of feeds in the same plane. Dual-polarization is achieved by the dipole feed antenna, with cross-polarization level of 17/16.8 dB and the SLL of -16.3/-16 dB.

A comparison between the proposed Luneburg lens and other reported Luneburg lenses based on TO is summarized in Table 3. After the compression in the y-dimension and z-dimension, the antenna has a more miniaturized scale than other lenses that are merely transformed in one dimension. In addition, the flat structure of the elliptical cylinder makes it more conformal and allows for a wider range of practical applications. The proposed two-dimensional coordinate transformation compresses the geometry of the Luneburg lens, making its electrical size is smaller than that in [13, 18]. And the gain of the proposed antenna is superior to antennas in [13, 23]. The different beamwidths in the E- and H-plane enable the proposed antenna to achieve two-dimensional beam coverage with five feed antennas, and produce a wider beam coverage than that in [15, 18].

4 Conclusion

Based on the analysis of transformed lenses in antenna applications, this paper presents a novel bi-dimensional transformation mapping to minimize the geometry of Lunebueg lens. Through compression, the lens changes from a sphere to an elliptical cylinder, reducing its volume by 47.5%. Meanwhile, since the vertical section of the lens in the xoz plane has the largest profile, it is identified as the focal plane. It contributes to matching with more feeds and steering in a wide angle. Both transformed permittivity tensor and permeability tensor are anisotropic, and they are modified to be isotropic following approximation and discretization. In order to implement the inhomogeneous lens, two ting-type periodic unit cells are designed to achieve the presumptive permittivity. The gain can be further improved through the gain optimization method and a pair of parallel metal elliptical plate, eventually reaching up to 16.1/15.9 dBi. The elliptical cylindrical Luneburg lens is fabricated with photosensitive resin. By reasonably adjusting the position of feed antennas, merely five beams can achieve a two-dimensional beam coverage of 100° in the H-plane and 40° in the E-plane.

Data availability statement

The original contributions presented in the study are included in the article/supplementary material, further inquiries can be directed to the corresponding author.

Author contributions

YZ designed the structure and then performed the experiments. The final manuscript was written by YZ and YZ. The numerical calculation was finished by WX and LB. YY and XL fabricated the sample. All authors contributed to the manuscript.

Funding

National Natural Science foundation of China (61771490), the Natural Science Foundation of Shaanxi Province, China (2018JM6055), Basic research Foundation of Engineering University of PAP (WJY201908) and Excellent Postgraduate Training Program of Engineering University of PAP (XYYJS01).

Conflict of interest

The authors declare that the research was conducted in the absence of any commercial or financial relationships that could be construed as a potential conflict of interest.

Publisher's note

All claims expressed in this article are solely those of the authors and do not necessarily represent those of their affiliated organizations, or those of the publisher, the editors and the reviewers. Any product that may be evaluated in this article, or claim that may be made by its manufacturer, is not guaranteed or endorsed by the publisher.

References

1. Luneburg RK, Max H. *Mathematical Theory of optics mathematical theory of optics* (1964).

2. Liu K, Zhao C, Qu S-W, Chen Y, Hu J, Yang S. A 3-d-printed multibeam spherical lens antenna with ultrawide-angle coverage. *IEEE Antennas Wirel Propag Lett* (2021) 20:411–5. doi:10.1109/LAWP.2021.3054042

3. Li Y, Ge L, Chen M, Zhang Z, Li Z, Wang J. Multibeam 3-d-printed luneburg lens fed by magnetoelectric dipole antennas for millimeter-wave mimo applications. *IEEE Trans Antennas Propag* (2019) 67:2923–33. doi:10.1109/TAP.2019.2899013

4. Guo Y, Li Y, Wang J, Ge L, Zhang Z, Chen M, et al..A 3d printed nearly isotropic luneburg lens antenna for millimeter-wave vehicular networks. *IEEE Trans Veh Technol* (2022) 71:1145–55. doi:10.1109/TVT.2021.3134703

5. Pendry JB, Schurig D, Smith DR. Controlling electromagnetic fields. *science* (2006) 312:1780–2. doi:10.1126/science.1125907

6. Leonhardt U. Optical conformal mapping. *science* (2006) 312:1777–80. doi:10.1126/science.1126493

7. Li J, Pendry JB. Hiding under the carpet: A new strategy for cloaking. *Phys Rev Lett* (2008) 101:203901. doi:10.1103/physrevlett.101.203901

8. Ma HF, Cui TJ. Three-dimensional broadband and broad-angle transformation-optics lens. *Nat Commun* (2010) 1:124–7. doi:10.1038/ncomms1126

9. Biswas S, Mirotznik M. High gain, wide-angle qcto-enabled modified luneburg lens antenna with broadband anti-reflective layer. *Sci Rep* (2020) 10:12646–13. doi:10.1038/s41598-020-69631-6

10. Driscoll T, Lipworth G, Hunt J, Landy N, Kundtz N, Basov DN, et al.Performance of a three dimensional transformation-optical-flattened lüneburg lens. *Opt Express* (2012) 20:13262–73. doi:10.1364/oe.20.013262

11. Li Y, Zhu Q. Luneburg lens with extended flat focal surface for electronic scan applications. *Opt Express* (2016) 24:7201–11. doi:10.1364/oe.24.007201

12. Weily AR, Nikolic N. Dual-polarized planar feed for low-profile hemispherical luneburg lens antennas. *IEEE Trans Antennas Propag* (2011) 60:402–7. doi:10.1109/tap.2011.2167941

13. Xu R, Chen ZN. A hemispherical wide-angle beamsteering near-surface focal-plane metamaterial luneburg lens antenna using transformation-optics. *IEEE Trans Antennas Propag* (2022) 70:4224–33. doi:10.1109/tap.2021.3138554

14. Wang B, Wang C, Zhu Q. An ellipsoidal luneburg lens antenna for gain enhancement and beam scanning. 2021 7th International Conference on Computer and Communications (ICCC). IEEE (2021). 10-13 December 2021. Chengdu, China p. 2149–53.

15. Wang C, Xia Y, Guo G, Nasir M, Zhu Q. Ellipsoidal luneburg lens binary array for wide-angle scanning. *IEEE Trans Antennas Propag* (2020) 68:5702–7. doi:10.1109/tap.2020.2969875

16. Demetriadou A, Hao Y. Slim luneburg lens for antenna applications. *Opt Express* (2011) 19:19925. doi:10.1364/oe.19.019925

17. Demetriadou A, Hao Y. A grounded slim luneburg lens antenna based on transformation electromagnetics. *IEEE Antennas Wirel Propag Lett* (2011) 10:1590–3. doi:10.1109/lawp.2011.2180884

18. Giddens H, Andy AS, Hao Y. Multimaterial 3-d printed compressed luneburg lens for mm-wave beam steering. *IEEE Antennas Wirel Propag Lett* (2021) 20:2166–70. doi:10.1109/lawp.2021.3109591

19. Quevedo-Teruel O, Hao Y. Directive radiation from a diffuse luneburg lens. *Opt Lett* (2013) 38:392–4. doi:10.1364/ol.38.000392

20. Mateo-Segura C, Dyke A, Dyke H, Haq S, Hao Y. Flat luneburg lens via transformation optics for directive antenna applications. *IEEE Trans Antennas Propag* (2014) 62:1945–53. doi:10.1109/tap.2014.2302004

21. Guo G, Nasir M, Zhu Q. Subtracted flat generalized luneburg lens for high gain and low profile applications. 2019 IEEE 5th International Conference on Computer and Communications (ICCC) (IEEE) (2019). 06-09 December 2019. Chengdu, China p. 685–9.

22. Su Y, Chen ZN. A flat dual-polarized transformation-optics beamscanning luneburg lens antenna using pcb-stacked gradient index metamaterials. *IEEE Trans Antennas Propag* (2018) 66:5088–97. doi:10.1109/tap.2018.2858209

23. Su Y, Chen ZN. A radial transformation-optics mapping for flat ultra-wide-angle dual-polarized stacked grin mtm luneburg lens antenna. *IEEE Trans Antennas Propag* (2019) 67:2961–70. doi:10.1109/tap.2019.2900346

24. Xu R, Chen ZN. A transformation-optics-based flat metamaterial luneburg lens antenna with zero focal length. *IEEE Trans Antennas Propag* (2022) 70:3287–96. doi:10.1109/tap.2021.3137528

25. Kundtz N, Smith DR. Extreme-angle broadband metamaterial lens. *Nat Mater* (2010) 9:129–32. doi:10.1038/nmat2610

26. Marin JG, Hesselbarth J. Lens antenna with planar focal surface for wide-angle beam-steering application. *IEEE Trans Antennas Propag* (2019) 67:2757–62. doi:10.1109/tap.2019.2894336

27. Schurig D. An aberration-free lens with zero f-number. *New J Phys* (2008) 10:115034. doi:10.1088/1367-2630/10/11/115034

28. Fuchs B, Le Coq L, Lafond O, Rondineau S, Himdi M. Design optimization of multishell luneburg lenses. *IEEE Trans Antennas Propag* (2007) 55:283–9. doi:10.1109/tap.2006.889849

29. Ansari M, Jones B, Zhu H, Shariati N, Guo YJ. A highly efficient spherical luneburg lens for low microwave frequencies realized with a metal-based artificial medium. *IEEE Trans Antennas Propag* (2020) 69:3758–70. doi:10.1109/tap.2020.3044638

30. Merrill WM, Diaz RE, LoRe MM, Squires MC, Alexopoulos NG. Effective medium theories for artificial materials composed of multiple sizes of spherical inclusions in a host continuum. *IEEE Trans Antennas Propag* (1999) 47:142–8. doi:10.1109/8.753004

31. Yang Z, Zhang C, Yin Y-Z, Wang Y. A wideband dual-polarized modified bowtie antenna for 2g/3g/lte base-station applications. *PIER Lett* (2016) 61:131–7. doi:10.2528/pierl16052504

32. Liu P, Zhu X-W, Zhang Y, Jiang ZH, Wang X, Hong W, et al..A novel e-plane-focused cylindrical luneburg lens loaded with metal grids for sidelobe level reduction. *IEEE Trans Antennas Propag* (2019) 68:736–44. doi:10.1109/tap.2019.2943438

frontiers | Frontiers in Materials

TYPE Original Research
PUBLISHED 20 October 2022
DOI 10.3389/fmats.2022.963775

OPEN ACCESS

EDITED BY
Mingliang Tian,
Hefei Institutes of Physical Science (CAS), China

REVIEWED BY
Deepak K. Pandey,
KICVentures Group - The LES Institute, United States
Xue Liu,
Anhui University, China

*CORRESPONDENCE
David Carroll,
carroldl@wfu.edu

SPECIALTY SECTION
This article was submitted to Quantum Materials, a section of the journal Frontiers in Materials

RECEIVED 07 June 2022
ACCEPTED 03 October 2022
PUBLISHED 20 October 2022

CITATION
Link R, Marcus G and Carroll D (2022), Solvothermal growth of moiré superlattices in antimony telluride spiral-type nanoplates.
Front. Mater. 9:963775.
doi: 10.3389/fmats.2022.963775

Solvothermal growth of moiré superlattices in antimony telluride spiral-type nanoplates

Robert Link, Gabriel Marcus and David Carroll*

Center for Nanotechnology and Molecular Materials, Department of Physics, Wake Forest University, Winston-Salem, NC, United States

The study of moiré superlattices (MSLs) has surged in recent years, as they have been found to host several emergent quantum phenomena associated with high electron correlations. In this study, we put forward a viable chemical route to the formation of moiré patterns in antimony telluride (Sb_2Te_3) nanoplates by leveraging screw dislocation-driven growth. These Sb_2Te_3 MSLs are synthesized using a scalable, one-pot, colloidal solution-liquid-solid (SLS) procedure. We report twist angles up to 0.52° (estimated using a combination of transmission electron microscope (TEM) image analysis and computer simulation). We investigate the early growth stages of Sb_2Te_3 spiral-type nanoplates under TEM, and we detail the growth of Sb_2Te_3 spiral-type nanoplates that feature a central nanopore, caused by tandem growth with nanorods. We hope that these methods will facilitate future investigation into the electronic properties of Sb_2Te_3 MSLs.

KEYWORDS

moiré pattern, chalcogenide, topological insulator, quantum material, one pot synthesis, twistronics, screw dislocation, van der waals materials

1 Introduction

Moiré superlattices (MSLs) are created when two or more heterogeneous or homogeneous atomically thin layers of van der Waals (vdW) material are stacked with a relative twist angle, creating periodic long-range changes in stacking order (Cao, Fatemi, Demir, et al., 2018; Liu et al., 2019). Since the discovery of superconducting and correlated insulating phases in "magic angle" twisted bilayer graphene, MSLs have become a central focus of materials research, spawning the new and promising subfield of twistronics (Cao, Fatemi, Demir, et al., 2018; Cao, Fatemi, Fang, et al., 2018). MSLs of several 2D vdW materials have since been fabricated and studied, notably uncovering Wigner crystal states and provisional evidence for other highly correlated behaviors such as nematicity, quantum anomalous Hall and quantum spin Hall states, ferromagnetism, and superconductivity in transition metal dichalcogenide heterobilayers (Hennighausen et al., 2019; Li et al., 2021; Lau et al., 2022).

One key challenge that persists within the development of this research is the difficulty of fabricating MSLs, especially small twist angle MSLs. MSLs are commonly prepared using a process called the vdW transfer method. This method typically involves exfoliating a monolayer of vdW material, non-destructively transferring it onto a silicon substrate,

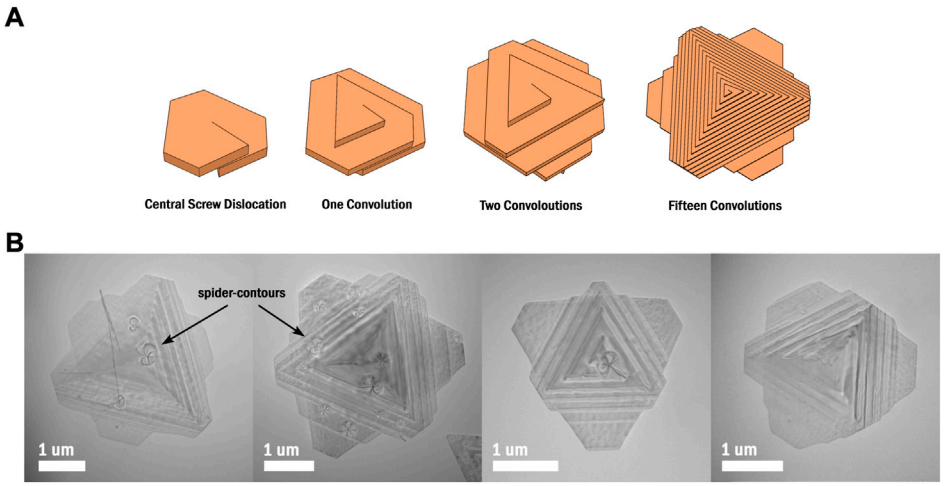

FIGURE 1
(A) An illustration of the growth process of spiral Sb_2Te_3 nanoplates. **(B)** A selection of TEM images showing spiral Sb_2Te_3 nanoplates of slightly different sizes and morphologies, some with spider-contours.

lifting a portion of that monolayer off of the substrate with a polymer stamp layered with hexagonal boron nitride, adjusting the angle of the substrate, and then lifting the remaining portion of monolayer off of the substrate and onto the polymer stamp (He et al., 2021). This process does allow for careful control of the resulting twist angle between layers; however, it is not a simple or particularly scalable process.

While many vdW materials can be formed into MSLs, the literature is primarily focused on bilayer graphene. In fact, graphene's often favorable properties as a conductor can render it unsuitable for applications in nanoelectronic devices that require a band gap. Thus, recent research has moved towards studying the properties of MSLs formed from semiconducting vdW materials. Among other class V-VI semiconductors, antimony telluride (Sb_2Te_3) has garnered significant attention for its large thermoelectric effect; for its properties as a topological insulator; and for its layered structure, held together by vdW interaction. Numerous synthesis methods exist for Sb_2Te_3 and similar chalcogenides, including chemical vapor deposition, exfoliation, and molecular-beam epitaxy. Colloidal solution-liquid-solid (SLS) chemistry is another method that can achieve effective synthesis of Sb_2Te_3 and offers several significant advantages when compared to other methods. First, the synthesis set-up is inexpensive and does not require specialized laboratory equipment. Second, the reactions and associated steps required are straightforward and provide high purity yield of product. Third, SLS chemistry is highly versatile; by using one general procedure, a researcher can produce a wide array of materials and subsequently achieve edge modulation doping (Dun et al., 2017). Lastly, and perhaps the most important benefit of this approach, is that tweaking several reaction parameters can lead to a variety of morphological and structural changes in the final material. A striking example of such a change is screw dislocation-driven growth in nanoplates, wherein the presence of a screw dislocation creates a 3D spiral structure instead of a simple 2D nanoplate. This growth pattern is general and has been observed in a wide range of materials including such vdW materials as SnSe, WSe_2, BiOCl, Bi_2Se_3, and Sb_2Te_3 (Morin et al., 2011; Chen et al., 2014; Zhuang et al., 2014; Liu et al., 2016, 2019; Dun et al., 2017). Interestingly, in each of these cases, vdW gaps are located between the steps formed during dislocation-driven growth (Figure 1A). In the case of BiOCl, this structure has been leveraged to grow spiral nanosheets with a moiré pattern (Liu et al., 2019).

Growth of spiral Sb_2Te_3 nanoplates by SLS method was first achieved in a recent paper by Dun et al. (2017), which serves as a foundational work for this study. In their paper, Dun et al. not only grew these topologically complex nanoplates, but further used the dangling tellurium bonds on the active nanoplate edges as heterogeneous nucleation sites, growing small silver (Ag) nanoparticles. The resulting Ag-decorated spiral nanoplates were then used to construct flexible thermoelectric thin films that remarkably saw a decoupled electrical conductivity and Seebeck effect. These thin films were measured to have a power factor of 371 $\mu W\ m^{-1}\ K^{-2}$ and a figure of merit ZT of 0.23.

The present study further develops the synthesis procedure put forth by Dun et al. (2017) in order to produce Sb_2Te_3 spiral nanoplate MSLs. We additionally detail a procedure that produces spiral nanoplates with a central nanopore, caused by tandem growth with nanorods. Emphasis is given to modifications of the typical reaction procedure that lead to visible and controllable changes in the resulting nanocrystals. The crystal growth process and conditions necessary for the screw dislocation-driven growth of Sb_2Te_3 are also explored in this

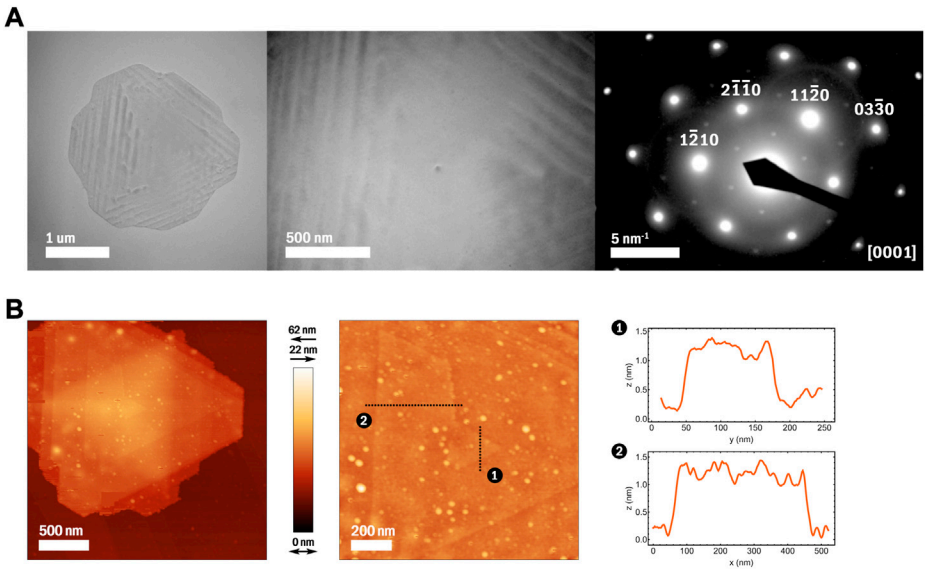

FIGURE 2
(A) TEM images and corresponding SAED pattern of an Sb_2Te_3 spiral nanoplate with a visible core. **(B)** AFM images and height profile plots of an Sb_2Te_3 spiral nanoplate showing the crystal steps to be 1 nm thick.

study. We propose that further research could yield a synthesis procedure for Sb_2Te_3 MSLs with a twist angle that is controlled by tuning reaction parameters. Such a development could allow large scale production of Sb_2Te_3 MSLs, ready for use in electronic systems.

2 Materials and methods

2.1 Synthesis of Sb_2Te_3 spiral-type nanoplates

The reaction that creates Sb_2Te_3 spiral-type nanoplates (Figure 1B and Figure 2) takes place in one three-necked flask under reflux. Reactants 9 mmol of tellurium oxide (TeO), 6 mmol of antimony chloride ($SbCl_3$), 1.46 g of sodium hydroxide (NaOH), and 800 mg of Polyvinylpyrrolidone (PVP) are dissolved into 70 ml of ethylene glycol (EG) one by one. Air is evacuated from the flask and replaced with argon gas. The flask is heated with a heating mantle to 130°C and held at this temperature for 10 min. In this time, the solution should turn black. Then, 8 ml hydrazine hydrate (N_2H_4) is pumped into the flask at a pace of 2.5 ml per minute. The solution is then left to stir at 130°C for 3 hours before it is further heated to 160°C and left for an additional 15 h. In this time, the solution should lighten a bit to an opaque gray. Heating is then stopped, and the flask is left to cool.

At this stage, the nanoplates have formed and are well-coated with PVP, much of which must be washed away for successful edge doping, imaging, or other applications. Once the flask is cool, the solution is divided into four centrifuge tubes. These tubes are then filled with acetone, and the nanoplates are collected into pellets by centrifugation at 5000 rpm for 20 min. The supernatant is discarded, after which the pellets are dispersed into 20 ml of ethanol by crushing with a glass stir rod, by vortexing, and by bath sonicating in water. This process is repeated by again by filling the tubes with acetone, followed by centrifugation. In this manner, the nanoplates are washed three to six times.

2.2 Synthesis of hexagonal Sb_2Te_3 nanoplates

The reaction that creates hexagonal Sb_2Te_3 nanoplates (Figure 3) is identical to that of Section 2.1 with one exception. The 8 ml of N_2H_4 is added at a rapid, unregulated pace before heating begins.

2.3 Synthesis of Sb_2Te_3 spiral-type nanoplates with moiré patterns

The reaction that creates Sb_2Te_3 spiral-type nanoplates with moiré patterns (Figure 4) uses two three-necked flasks, joined with a distillation adapter. One flask is placed under reflux (Flask A). In Flask A, the same reactants as listed in Section 2.1 are dissolved into 70 ml of EG. An additional 1.5 ml of EG is placed in the remaining flask (Flask B). Air is then evacuated from the

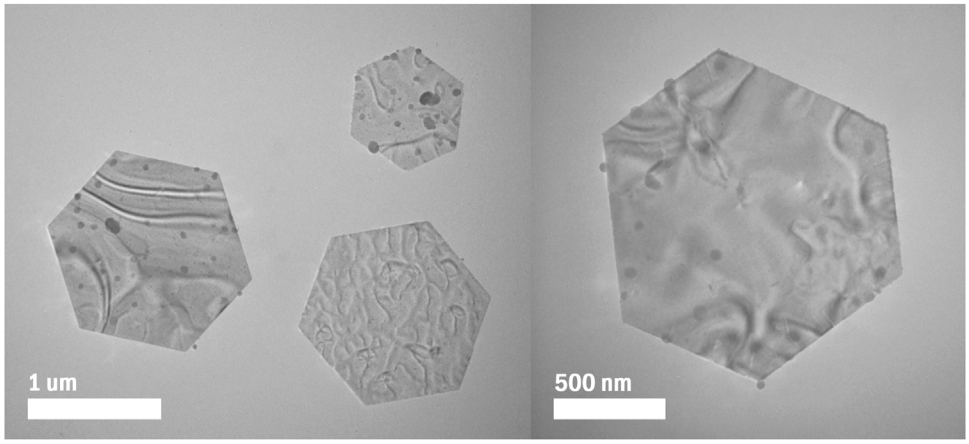

FIGURE 3
TEM images of flat, hexagonal Sb_2Te_3 nanoplates.

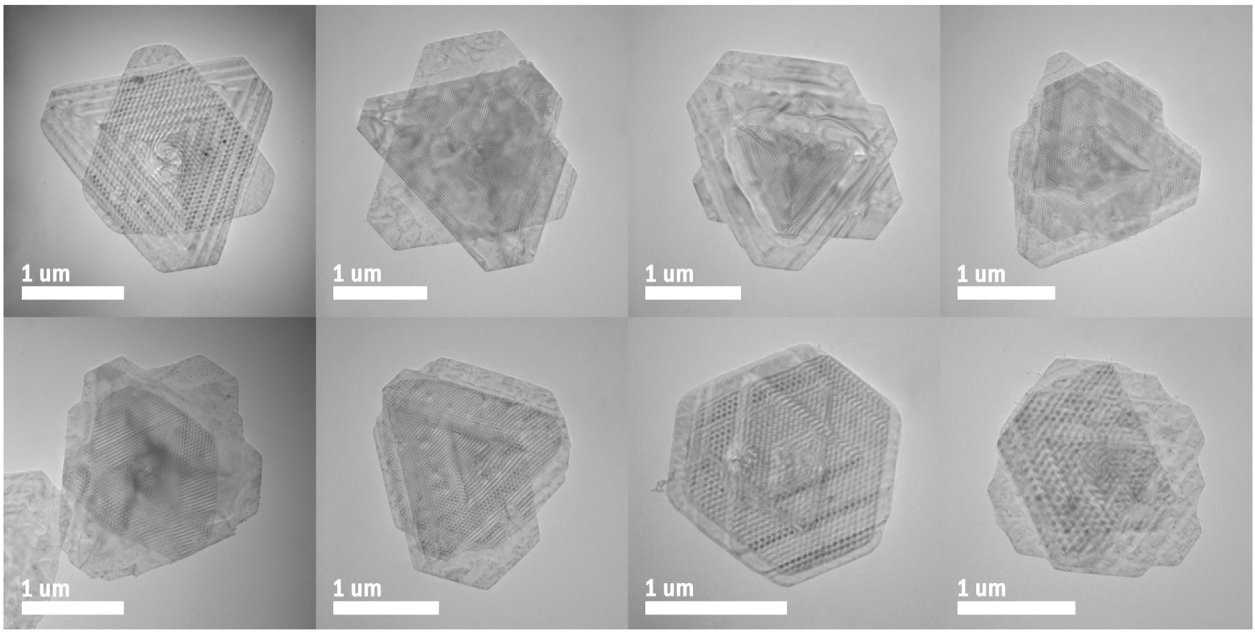

FIGURE 4
TEM images of Sb_2Te_3 spiral nanoplates, each with a visible moiré pattern.

setup and replaced with argon gas. Both flasks are heated simultaneously to 130°C. Then, 8 ml of N_2H_4 is pumped into Flask B, such that it begins to vaporize and is slowly delivered as a vapor into Flask A. The solution is then left to stir at 130°C for 3 hours before it is further heated to 160°C and left for an additional 15 h. The heating is then stopped, the flasks are left to cool, and the resulting nanoplates are collected and washed as described in Section 2.1.

2.4 Synthesis of Sb_2Te_3 spiral-type nanoplates with central nanopores

The reaction that creates Sb_2Te_3 spiral-type nanoplates with central nanopores (Supplementary Figure S1B) is identical to that of Section 2.3 with one exception. Into Flask B is added 30 ml of EG instead of 1.5 ml. This is done to further slow the rate of addition of N_2H_4 into Flask A.

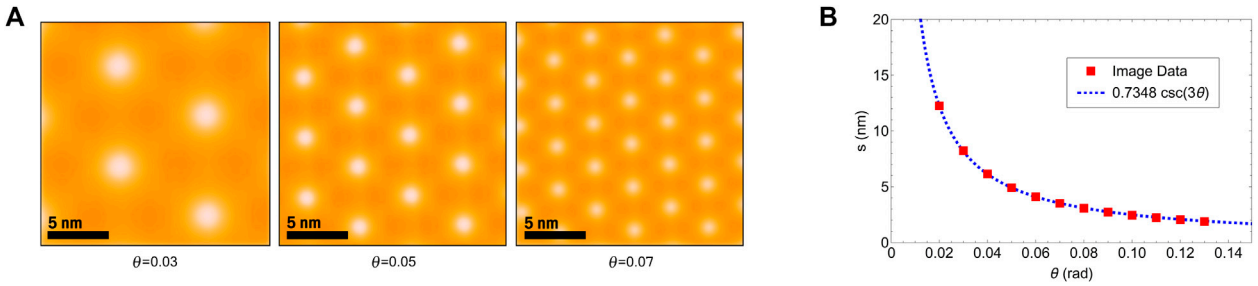

FIGURE 5
(A) Three simulated Sb_2Te_3 moiré patterns at increasing twist angles. **(B)** Plot showing both the simulated image data and the best-fit curve.

2.5 Sample characterization methods

Analysis of results from various reactions is performed by thorough examination of material sample images captured using a JEOL 1200-EX TEM equipped with a SIA-L3 camera. SAED analysis is also performed with the same machine. SAED image analysis was performed in CrysTBox. The AFM analysis in this study was performed by a Veeco Nanoscope IIIa Multimode in tapping mode. AFM image analysis was performed in Gwyddion. Moiré pattern simulation was performed by custom code written in Wolfram Mathematica, and TEM direct image analysis was performed using ImageJ.

3 Results and discussion

3.1 Spiral characterization results

Synthesized as described in Section 2.1; Figure 1B shows a selection of Sb_2Te_3 spiral-type nanoplates. The growth of these nanoplates is driven by a central screw dislocation, causing the typically many-layered structure of Sb_2Te_3 to instead form one continuous layer that spirals into a third dimension (Dun et al., 2017). Figure 1A illustrates how one screw dislocation is integral to this structural change. Given our colloidal synthesis method, and thus lack of substrate, the spiral-type nanoplates grow similarly on both sides, with a morphology like that of a trigonal bipyramid. Spider-contours are visible on many of these nanoplates (Figure 1B), often positioned at their center, which likely result from the strain field caused by screw dislocations (Morin et al., 2011). These nanoplates have been measured to range between 4μm^2 and 10 μm^2 in area. Selected area electron diffraction (SAED) analysis of Sb_2Te_3 spiral-type nanoplates (Figure 2A) reveals an interplanar spacing of 0.213 nm for planes $(11\bar{2}0)$, $(\bar{1}2\bar{1}0)$, and $(\bar{2}110)$, while a spacing of 0.123 nm was measured for $(03\bar{3}0)$. These values match accepted values for Sb_2Te_3 exactly to three decimal places. AFM analysis (Figure 2B) has revealed that the crystal steps of our spiral-type nanoplates are 1 nm in height, corresponding to one five-atom layer of Sb_2Te_3 (Dun et al., 2017). This supports the notion that our vdW gap is located between spiral steps. The total height of this sample was measured to be 25 nm (Supplementary Figure S1).

Careful and deliberate modification of synthesis procedures revealed that the quantity and rate of N_2H_4 addition greatly impacts the morphology of the resulting nanomaterials. Without N_2H_4, only nanorods form. When N_2H_4 is added with the other reactants, all at once before heating, screw dislocation-driven growth is not observed. Instead, flat hexagonal Sb_2Te_3 nanoplates with a typical area of about 1.5 μm^2 are formed (Figure 3). The slower addition of N_2H_4 as a vapor, described in Section 2.3, frequently produces spiral nanoplates that exhibit moiré patterns (Figure 4). We propose that the presence of these patterns is due to increased strain within the central screw dislocation, resulting in a relative twist angle between spiral steps. While each spiral has many vdW gaps, observed moiré patterns are typically characteristic of a twist across only one gap, allowing interpretation of these patterns to be consistent with those produced by twisted bilayer Sb_2Te_3.

We performed a simulation in order to characterize the relationship between relative twist angle (θ) and moiré fringe spacing in bilayer Sb_2Te_3. A custom code was written that directly plots two lattices with a relative twist angle using graphics objects. Each lattice represents Sb_2Te_3's five atomic sheet structure as seen from the [0001] zone axis. The scale of this plot is determined using the accepted values for the lattice constants of Sb_2Te_3. The resulting moiré pattern is then made more pronounced with careful use of uniform image filtering (Figure 5A). An isometric grid is fit to the set of brightest pixels within this plot, from which nearest neighbor spacing (s) was measured. This process was repeated for several values of θ, and from the resulting data was found the following best-fit equation with a root-mean-square error (RSME) of 0.032 nm (Figure 5B).

$$s = \left| \frac{0.7348}{sin(3\theta)} \right|$$

With a choice of $0 < \theta < \pi/6$, this best-fit equation is easily inverted to estimate the twist angle of the Sb_2Te_3 MSLs observed

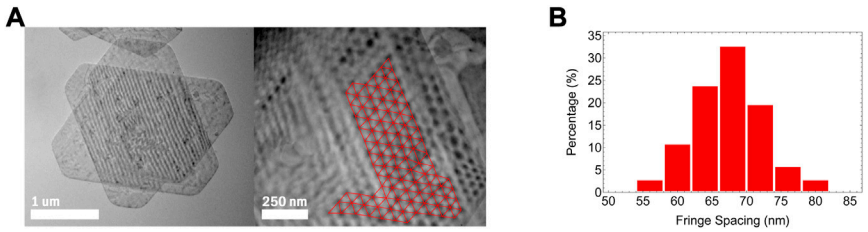

FIGURE 6
(A) TEM images of an Sb_2Te_3 nanoplate with a visible moiré pattern. A nearest-neighbor grid is marked in red. **(B)** A histogram showing the distribution of side lengths in this nearest-neighbor grid. A fringe spacing of 67.60 ± 0.05 nm is determined from this data, and thus an estimated twist angle of 0.2074 ± 0.0003°.

with TEM. Moiré fringe spacing was measured from TEM images in agreement with our simulation: by fitting a nearest-neighbor grid to the dark spots of an MSL (Figure 6A). From this grid is produced a distribution of lengths (Figure 6B), from which is extracted an average value for s and its error. Using our equation obtained from simulation, θ values are then estimated. Twenty MSLs were analyzed in this manner; between nanoplates, θ values ranged from 0.14° to 0.52° and measurement error never exceeded 0.2%. Additional detail is provided in the Supplementary Materials. Twist angles in vdW materials have also been effectively measured using SAED pattern analysis (Liu et al., 2019). In our case, the reported twist angles are too small to be properly quantified using this method (Supplementary Figure S6).

To observe the nanoplate growth process directly, samples were extracted from early stages of synthesis and examined with TEM. Minutes after heating begins, nanorods form in solution, turning the solution black. Nanoplates then nucleate and grow at the tips of these nanorods in the following few hours of heating (Supplementary Figure S4). Interestingly, this process is analogous to the vapor-phase snowflake growth performed by Libbrecht (2005), wherein the growth phases of ice were manipulated to form plate-like crystals at the tips of ice needles. By the time heating is switched off in the syntheses described in Sections 2.1–2.3, these nanorods have mostly redissolved into solution. However, in the synthesis described in Section 2.4, these nanorods instead persist and thicken as shown in Supplementary Figure S1A. During this synthesis, nanoplates frequently become separated from the thickened nanorods, often leaving the nanoplate with a central nanopore as seen in Supplementary Figure S1B. These nanopores are typically circular and range from 20 to 25 nm in diameter.

4 Conclusion

In this study, we have demonstrated a viable chemical route to the formation of moiré materials based on multilayer 2D chalcogenides by leveraging screw dislocation-driven growth. We observed twist angles up to 0.52° utilizing high-resolution microscopy and simulation. We suggest that the presence of moiré patterns in Sb_2Te_3 spiral-type nanoplates is due to increased strain within the central screw dislocation, and that this strain has been modulated by changes to the rate and method of N_2H_4 addition during synthesis. Further exploration may lead to precise chemical control over the resulting twist angle. Given that the syntheses put forward in this study are simple and scalable, we believe that this approach to moiré patterns in spiral-type Sb_2Te_3 nanoplates could represent an exciting new way to create twistronic systems, ready for use in electronic devices.

Data availability statement

The raw data supporting the conclusion of this article will be made available by the authors, without undue reservation.

Author contributions

RL wrote the manuscript, performed computations, and created the figures. RL and GM developed synthesis methods. DC coordinated the project. All authors have discussed the results, contributed to manuscript revision, and have approved the submitted version.

Funding

The Carroll lab was provided by Streamline Automation: U.S. Department of Defense/Air Force under Grant No. GR-00000327.

Acknowledgments

We would like to thank Martin Guthold and Stephen Baker for allowing us access to their equipment and for their work gathering AFM data.

Conflict of interest

The authors declare that the research was conducted in the absence of any commercial or financial relationships that could be construed as a potential conflict of interest.

Publisher's note

All claims expressed in this article are solely those of the authors and do not necessarily represent those of their affiliated organizations, or those of the publisher, the editors and the reviewers. Any product that may be evaluated in this article, or claim that may be made by its manufacturer, is not guaranteed or endorsed by the publisher.

Supplementary material

The Supplementary Material for this article can be found online at: https://www.frontiersin.org/articles/10.3389/fmats.2022.963775/full#supplementary-material

References

Cao, Y., Fatemi, V., Demir, A., Fang, S., Tomarken, S. L., Luo, J. Y., et al. (2018). Correlated insulator behaviour at half-filling in magic-angle graphene superlattices. *Nature* 556 (7699), 80–84. doi:10.1038/nature26154

Cao, Y., Fatemi, V., Fang, S., Watanabe, K., Taniguchi, T., Kaxiras, E., et al. (2018). Unconventional superconductivity in magic-angle graphene superlattices. *Nature* 556 (7699), 43–50. doi:10.1038/nature26160

Chen, L., Liu, B., Abbas, A. N., Ma, Y., Fang, X., Liu, Y., et al. (2014). Screw-dislocation-driven growth of two-dimensional few-layer and pyramid-like WSe_2 by sulfur-assisted chemical vapor deposition. *ACS Nano* 8 (11), 11543–11551. doi:10.1021/nn504775f

Dun, C., Hewitt, C. A., Li, Q., Xu, J., Schall, D. C., Lee, H., et al. (2017). 2D chalcogenide nanoplate Assemblies for thermoelectric applications. *Adv. Mat.* 29 (21), 1700070. doi:10.1002/adma.201700070

He, F., Zhou, Y., Ye, Z., Cho, S. H., Jeong, J., Meng, X., et al. (2021). Moiré patterns in 2D materials: A review. *ACS Nano* 15 (4), 5944–5958. doi:10.1021/acsnano.0c10435

Hennighausen, Z., Lane, C., Buda, I. G., Mathur, V. K., Bansil, A., and Kar, S. (2019). Evidence of a purely electronic two-dimensional lattice at the interface of TMD/Bi_2Se_3 heterostructures. *Nanoscale* 11 (34), 15929–15938. doi:10.1039/C9NR04412D

Lau, C. N., Bockrath, M. W., Mak, K. F., and Zhang, F. (2022). Reproducibility in the fabrication and physics of moiré materials. *Nature* 602 (7895), 41–50. doi:10.1038/s41586-021-04173-z

Li, H., Li, S., Regan, E. C., Wang, D., Zhao, W., Kahn, S., et al. (2021). Imaging two-dimensional generalized Wigner crystals. *Nature* 597 (7878), 650–654. doi:10.1038/s41586-021-03874-9

Libbrecht, K. G. (2005). The physics of snow crystals. *Rep. Prog. Phys.* 68 (4), 855–895. doi:10.1088/0034-4885/68/4/R03

Liu, J., Huang, Q., Qian, Y., Huang, Z., Lai, F., Lin, L., et al. (2016). Screw dislocation-driven growth of the layered spiral-type SnSe nanoplates. *Cryst. Growth & Des.* 16 (4), 2052–2056. doi:10.1021/acs.cgd.5b01708

Liu, L., Sun, Y., Cui, X., Qi, K., He, X., Bao, Q., et al. (2019). Bottom-up growth of homogeneous Moiré superlattices in bismuth oxychloride spiral nanosheets. *Nat. Commun.* 10 (1), 4472. doi:10.1038/s41467-019-12347-7

Morin, S. A., Forticaux, A., Bierman, M. J., and Jin, S. (2011). Screw dislocation-driven growth of two-dimensional nanoplates. *Nano Lett.* 11 (10), 4449–4455. doi:10.1021/nl202689m

Zhuang, A., Li, J., Wang, Y., Wen, X., Lin, Y., Xiang, B., et al. (2014). Screw-dislocation-driven bidirectional spiral growth of Bi2Se3 nanoplates. *Angew. Chem. Int. Ed.* 53 (25), 6425–6429. doi:10.1002/anie.201403530

frontiers | Frontiers in Materials

TYPE Original Research
PUBLISHED 08 December 2022
DOI 10.3389/fmats.2022.1079809

OPEN ACCESS

EDITED BY
Yichao Liu,
Taiyuan University of Technology, China

REVIEWED BY
Bo Hou,
Soochow University, China
Fei Sun,
Taiyuan University of Technology, China

*CORRESPONDENCE
Hossein Eskandari,
Hossein.skandari@gmail.com

SPECIALTY SECTION
This article was submitted to Metamaterials, a section of the journal Frontiers in Materials

RECEIVED 25 October 2022
ACCEPTED 14 November 2022
PUBLISHED 08 December 2022

CITATION
Eskandari H (2022), A reflectionless compact elliptical half Maxwell fish-eye lens designed by transformation optics. *Front. Mater.* 9:1079809.
doi: 10.3389/fmats.2022.1079809

A reflectionless compact elliptical half Maxwell fish-eye lens designed by transformation optics

Hossein Eskandari*

Department of Electrical Engineering, Ferdowsi University of Mashhad, Mashhad, Iran

A two-dimensional half Maxwell fish-eye lens is compressed using a linear transformation that maps a half circle to a half ellipse. The focusing property of the lens is preserved while making the device more compact. The boundary reflections, investigated for both TE and TM polarizations, were suppressed for beams directed toward the optical axis of the lens. A designed prototype provided a scanning range of ±20° with negligible reflections. The design's functionality was verified using COMSOL multiphysics.

KEYWORDS

half Maxwell fish-eye lens, linear transformation, lens compression, transformation optics, optical axis

1 Introduction

Graded index (GRIN) devices are presently in the spotlight thanks to recent developments in manufacturing technology. A GRIN lens implemented in dielectric provides a wideband, cost-effective solution. Among the well-known classical GRIN lenses with rotational symmetry and aberration-free performance are the Luneburg lens (Luneberg, 1964) and the Maxwell fish-eye lens (MFEL) (Maxwell, 1854). The Luneburg lens offers scanning directive beams and has an excellent refractive index profile in terms of realizability. When a point is excited on the boundary of the lens, it creates a directive beam on the opposite side. This characteristic, along with its rotationally symmetrical structure, has made the Luneburg lens superb for direction finding, beam scanning, and wide-angle large RCS generation. The MFEL, on the other hand, provides stigmatic imaging (Tyc et al., 2011). The refractive index of the lens is given by:

$$n(r) = \frac{2n_0}{1 + (r/R)^2}, \tag{1}$$

where $r = \sqrt{x^2 + y^2}$ is the radial distance from the lens center and R is the lens radius. Taking the background refractive index $n_0 = 1$ leads to a lens that is index-matched to the vacuum at its rim $r = R$. The MFEL images a point source located at position $\mathbf{r}$ to the point $-\mathbf{r}R^2/r^2$. Hence, if a point is excited at the lens rim, MFEL

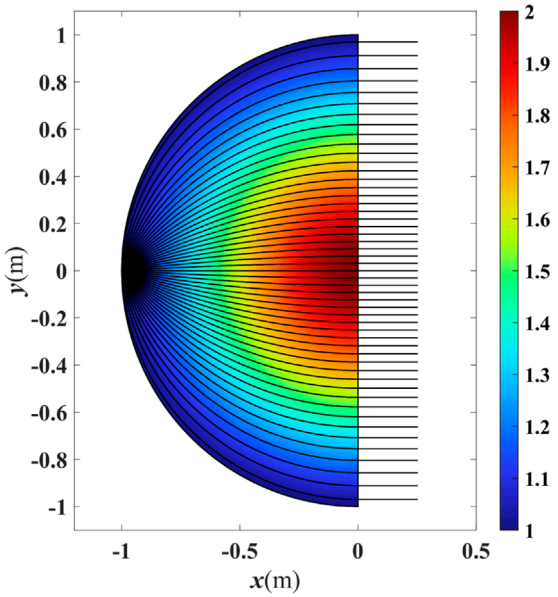

FIGURE 1
Ray trajectories and refractive index of an HMFEL. Parameters $n_0 = 1$ and $R = 1$ are considered in **Eq. 1**.

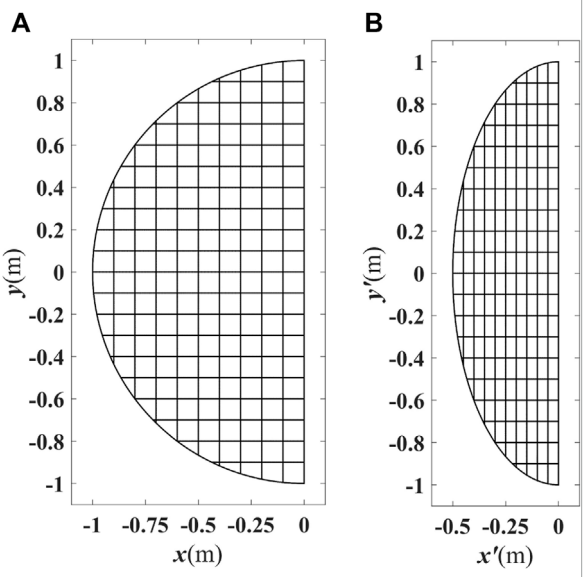

FIGURE 2
Schematic of the underlying transformation between **(A)** the half circle with radius of one and **(B)** a half ellipse with semi-minor axis of $\delta = 0.5$ and semi-major axis of one. The x-constant and y-constant lines in virtual space are plotted as well as their mapped version in physical space.

symmetrically focuses the rays to a mirrored point on the rim. If the lens is sliced in half, it produces a single directive beam in the opposite direction of the source. This sliced lens is called a half Maxwell fish-eye lens (HMFEL). The HMFEL has a refractive index mismatch at its aperture and is often used to produce a single directive beam (Fuchs et al., 2006, 2007; Huang et al., 2014; Xu et al., 2014; Shi et al., 2015). The focusing property is best when the excitation is at the center of the circular rim, and the performance degrades as the excitation point moves along the rim. However, it has been demonstrated that the HMFEL can provide some scanning capabilities (Fuchs et al., 2007). The refractive index profile of an HMFEL with $n_0 = 1$ and $R = 1$ and the ray trajectories for 51 rays launched from the $(-1, 0)$ coordinate are depicted in **Figure 1**.

The MFEL and Luneburg lens have been actively studied in the transformation optics (TO) discipline. A connection between the deformation of space and the medium is made possible by TO, based on the form invariance of Maxwell's equations under a coordinate transformation. This notion gained popularity following the publication of early research on the invisibility cloak by Pendry (2006) and Leonhardt (2006) who asserted that a carefully calculated transformation medium could reproduce the attributes of a deformed space. Having a specific virtual space where wave propagation properties are known, a carefully-selected space deformation could be employed to manipulate the waves' behavior. It was demonstrated that the hypothetical deformation could be embodied into a material within a physical space using the TO method. TO has been used to create various devices with unique functions, including beam expanders (Rahm et al., 2008; Emiroglu and Kwon, 2010), polarization splitters and transformers (Kwon and Werner, 2008; Mousavi et al., 2017; Eskandari et al., 2018), waveguide couplers (García-Meca et al., 2011; Markov et al., 2012; Eskandari et al., 2017b,a, 2019b; Eskandari and Tyc, 2019), and directivity enhancers (Eskandari et al., 2021a,b; Schmiele et al., 2010; Yao and Jiang, 2011; Gu et al., 2012; Aghanejad et al., 2012; Wu et al., 2013; Giddens and Hao, 2020; Eskandari, 2022; Kadera et al., 2022; Nazarzadeh and Heidari, 2022).

For a virtual space described in Cartesian coordinates (x, y, z), with ϵ and μ as relative permittivity and permeability, the constitutive parameters of the physical space described by the Cartesian coordinates (x', y', z') can be calculated from those of the virtual space by following the formula:

$$\varepsilon' = J\varepsilon J^T/\det(J),\ \mu' = J\mu J^T/\det(J), \tag{2}$$

where the Jacobian matrix $J = \partial(x', y', z')/\partial(x, y, z)$ characterizes the underlying coordinate transformation between the virtual and physical spaces.

TO serves as a powerful tool for the geometrical reshaping of common GRIN lenses as it preserves the electromagnetic properties of the GRIN lens. In the case of the MFEL, TO has been used to flatten the image and feed planes (Smith et al., 2010; Hunt et al., 2011). Moreover, conformal and quasi-conformal transformations have been employed

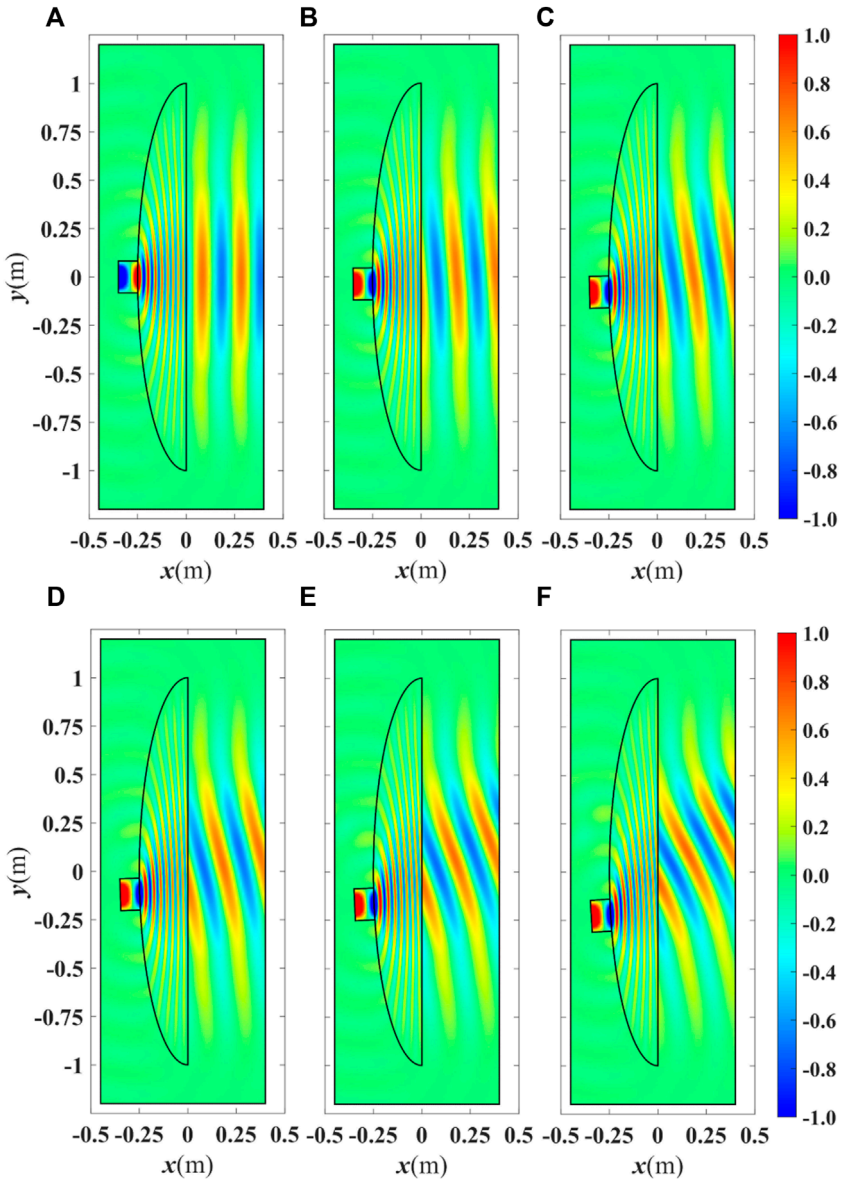

FIGURE 3
Real part of E_z for the EHMFEL excited by a waveguide carrying the TE_1 mode at a frequency of 1.5 GHz for a beam direction θ of **(A)** 0°, **(B)** +4°, **(C)** +8°, **(D)** +12°, **(E)** +16°, and **(F)** +20°. The waveguide is moved across the elliptical boundary to achieve beam scanning.

to transform the circular shape of a two-dimensional (2D) MFEL to a rectangle (Yang et al., 2014; Badri et al., 2020), a square (Tao et al., 2019), and a semi-octagon (Li et al., 2018) for improved integration with photonic devices as a cross-coupler. As a lens reshaping tool, TO can compress the lens in one direction, resulting in a more compact device (Roberts et al., 2009). Numerous studies have employed the Luneburg lens as an example of how to use this concept, either by changing the circular shape into an ellipse (Demetriadou and Hao, 2011b,a; Ebrahimpouri and Quevedo-Teruel, 2019; Liu et al., 2020; Giddens et al., 2021; Chen et al., 2021) or a rectangle (Mateo-Segura et al., 2014; Su and Chen, 2018, 2019; Xu and Chen, 2022). However, reshaping the Luneburg lens has an intrinsic flaw that is not present in the case of MFEL. This topic is expanded upon in the Discussion section. A conformal solution has been proposed to compress a circular MFEL into an elliptical MFEL (EMFEL) (Eskandari et al., 2019a). Slicing the resulting EMFEL in half to achieve directive beams results

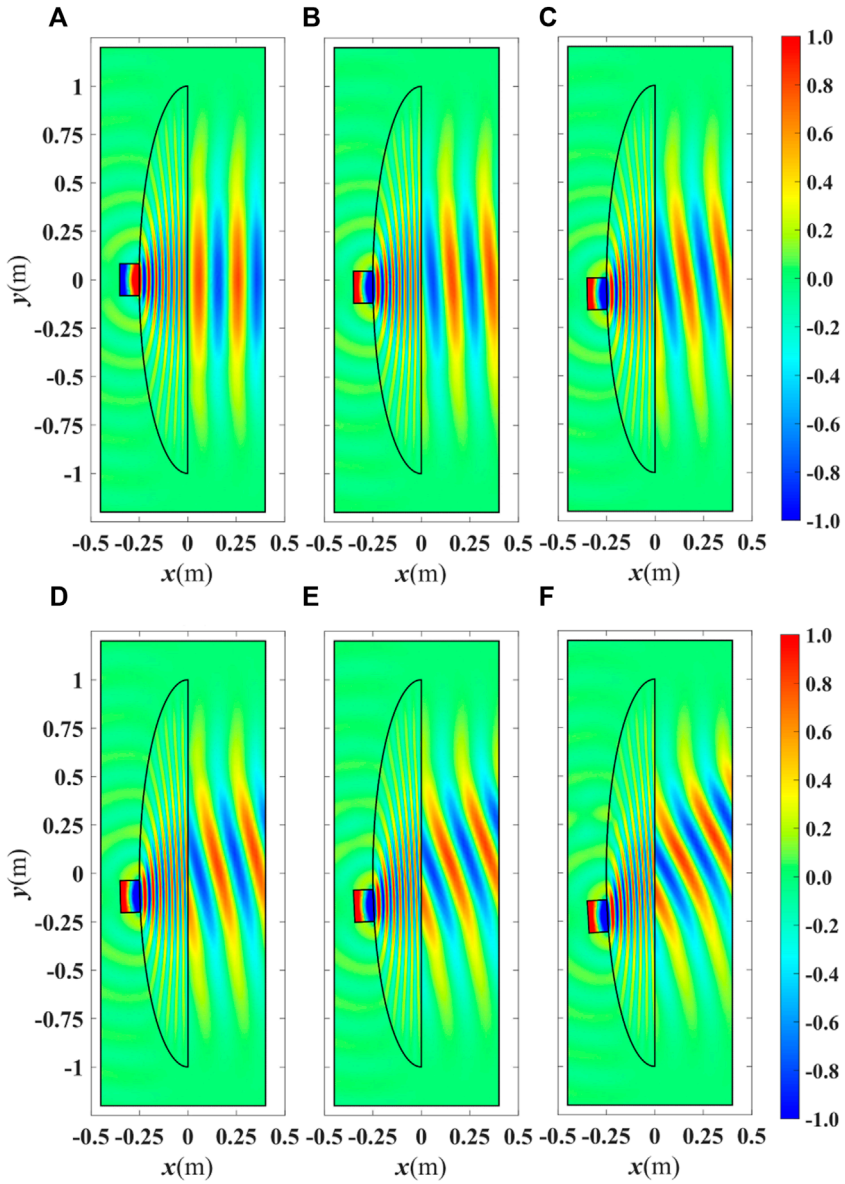

FIGURE 4
Real part of H_z for the EHMFEL excited by a waveguide carrying the TM_0 mode at a frequency of 1.5 GHz for a beam direction θ of **(A)** 0°, **(B)** +4°, **(C)** +8°, **(D)** +12°, **(E)** +16°, and **(F)** +20°. The waveguide is moved across the elliptical boundary to achieve beam scanning.

in significant reflections from the aperture due to the index mismatch.

Here, a 2D HMFEL was compressed using a linear transformation. The conditions that resulted in a reflectionless device were derived and applied. It was shown that the device could provide reasonable scanning as well. The device's performance was evaluated when the electric field was along the z' direction (TE polarization) or the magnetic field was along the z' direction (TM polarization). The design method was validated using COMSOL.

2 Design method

Consider the following linear transformation, which maps a half circle with a radius of one to an ellipse with a semi-major axis of one along the y'-axis and a semi-minor axis of δ ($\delta < 1$) along the x'-axis.

$$x' = \delta x,\ y' = y,\ z' = z. \tag{3}$$

The transformation schematic is shown in Figure 2 for $\delta = 1/2$. The x-constant and y-constant coordinate lines in the

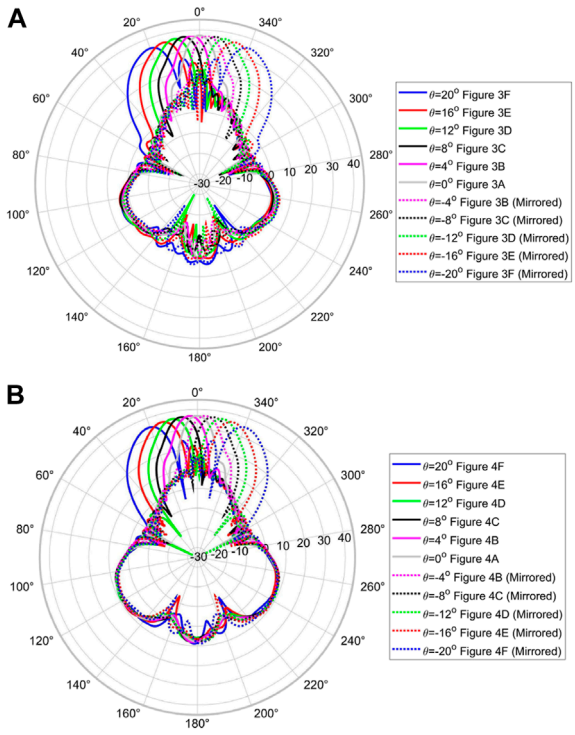

FIGURE 5
Farfield pattern of the EHMFEL in decibels versus θ for **(A)** the TE_1 mode (corresponding to the results depicted in **Figure 3**) and **(B)** the TM_0 mode (corresponding to the results depicted in **Figure 4**). The dotted lines represent the cases where the feed location is mirrored with respect to the x-axis.

virtual space and their mapped counterparts in the physical space are also presented. Because of the 2D nature of the problem, δ, which is the half-ellipse area divided by the half-circle area, quantifies the amount of space occupancy reduction.

It is known that only the $\mu_{x'x'}, \mu_{x'y'} = \mu_{y'x'}, \mu_{y'y'}, \varepsilon_{z'z'}$ and $\varepsilon_{x'x'}, \varepsilon_{x'y'} = \varepsilon_{y'x'}, \varepsilon_{y'y'}, \mu_{z'z'}$ constitutive parameters contribute to the wave propagation for TE and TM polarization, respectively. It is worth noting that TE (TM) polarization occurs when the electric (magnetic) field is polarized along the z-axis. Using the linear coordinate transformation in **Eq. 3**, the TO formula in **Eq. 2**, and the refractive index formula for the HMFEL, the transformation medium of the elliptical HMFEL (EHMFEL) is calculated for the TE and TM polarizations following

$$\text{TE:}\begin{cases}\mu'_{x'x'} = \delta G(r)H(r)\\ \mu'_{y'y'} = \dfrac{G(r)H(r)}{\delta}\\ \varepsilon'_{z'z'} = \dfrac{f(r)}{\delta H(r)}\end{cases}, \text{TM:}\begin{cases}\varepsilon'_{x'x'} = \dfrac{\delta f(r)}{H(r)}\\ \varepsilon'_{y'y'} = \dfrac{f(r)}{\delta H(r)}\\ \mu'_{z'z'} = \dfrac{G(r)H(r)}{\delta}\end{cases}, \quad (4)$$

where the refractive index of the virtual space has been split into two functions $n^2(r) = f(r)G(r)$, in which $\varepsilon(r) = f(r)$ and

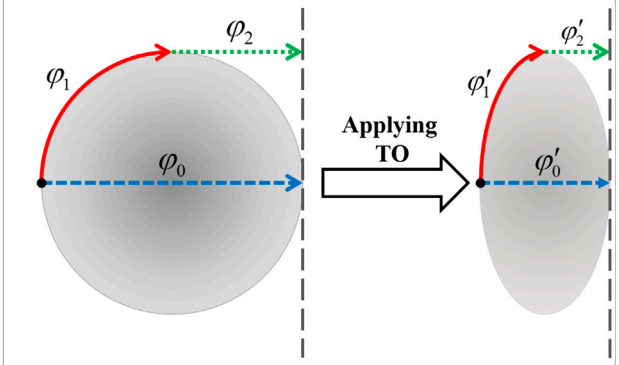

FIGURE 6
Schematics of the Luneburg lens before and after reshaping by TO.

$\mu(r) = G(r)$. As an additional degree of freedom, the scaling function $H(r)$ is introduced. The permeability (permittivity) has been multiplied (divided) by $H(r)$, which would not change the principal refractive indices (the device functionality). The preceding considerations are made to aid in the suppression of reflections.

The constitutive parameters of an anisotropic medium must meet the following conditions for the interface along the y'-axis between the medium and the vacuum to be omnidirectionally reflectionless (Gok and Grbic, 2016; Eskandari et al., 2019b).

$$\text{TE:}\begin{cases}\mu'_{x'x'}\varepsilon'_{z'z'}\big|_{x'=0} = 1\\ \mu'_{x'x'}\mu'_{y'y'}\big|_{x'=0} = 1\end{cases}, \quad \text{TM:}\begin{cases}\varepsilon'_{x'x'}\mu'_{z'z'}\big|_{x'=0} = 1\\ \varepsilon'_{x'x'}\varepsilon'_{y'y'}\big|_{x'=0} = 1\end{cases}. \quad (5)$$

In the instance of EHMFEL, omnidirectionally reflectionless means that the device creates all scanning beams with zero reflections. The above conditions are translated into the following using the transformation medium calculated in **Eq. 4**

$$\text{TE:}\begin{cases}\mu'_{x'x'}\varepsilon'_{z'z'}\big|_{x'=0} = n^2(r)\big|_{x'=0} = 1\\ \mu'_{x'x'}\mu'_{y'y'}\big|_{x'=0} = G^2(r)H^2(r)\big|_{x'=0} = 1\end{cases}, \quad \text{TM:}\begin{cases}\varepsilon'_{x'x'}\mu'_{z'z'}\big|_{x'=0} = n^2(r)\big|_{x'=0} = 1\\ \varepsilon'_{x'x'}\varepsilon'_{y'y'}\big|_{x'=0} = f^2(r)/H^2(r)\big|_{x'=0} = 1\end{cases}. \quad (6)$$

According to the $n(r)$ formula in **Eq. 1**, the first condition cannot be satisfied for any polarizations at $x' = 0$. Hence, it is impossible to have an omnidirectionally reflectionless EHMFEL.

Now we investigate whether the main beam along the optical axis (x'-axis) can be reflectionless. Following a similar approach to that in reference (Eskandari et al., 2017b) and aiming for a derivation of the reflection coefficient at $x' = 0$ for a diagonal

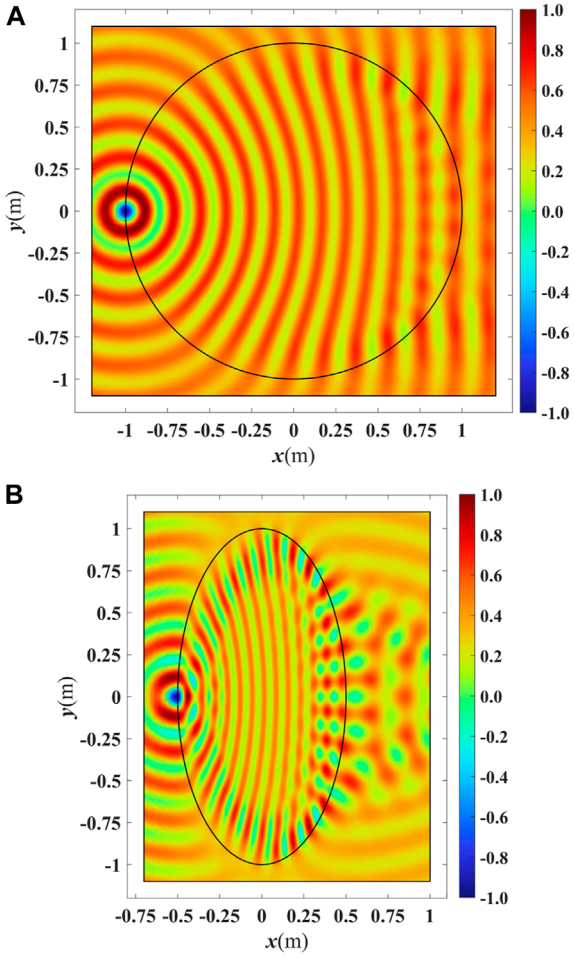

FIGURE 7
Simulation results for **(A)** an uncompressed Luneburg lens and **(B)** a compressed Luneburg lens with a semi-minor axis of $\delta = 0.5$. A point source on the lens rim feeds the lenses with a TE polarized wave.

material, we get the following result for the TM polarization

$$\Gamma = \left| \frac{\cos\theta - \sqrt{\mu'_{z'z'}/\varepsilon'_{y'y'} - \sin^2\theta/\varepsilon'_{x'x'}\varepsilon'_{y'y'}}}{\cos\theta + \sqrt{\mu'_{z'z'}/\varepsilon'_{y'y'} - \sin^2\theta/\varepsilon'_{x'x'}\varepsilon'_{y'y'}}} \right|, \tag{7}$$

where θ is the beam's scan angle, the angle between the beam direction and the x'-axis. Using the duality principle, the reflection coefficient for TE polarization can be easily calculated. Based on Eq. 7, for a diagonal medium to be reflectionless for $\theta = 0$, the impedance terms for TM and TE polarizations should satisfy $Z^{\mathrm{TM}}_{y'}\big|_{x'=0} = \sqrt{\mu'_{z'z'}/\varepsilon'_{y'y'}} = 1$ and $Z^{\mathrm{TE}}_{y'}\big|_{x'=0} = \sqrt{\mu'_{y'y'}/\varepsilon'_{z'z'}} = 1$, respectively. Using Eq. 4, it is seen that the impedance matching is achieved if $G(r)H(r) = n(r)$.

In conclusion, the following transformation medium leads to a reflectionless design for $\theta = 0$

$$\varepsilon'_r = \mu'_r = \begin{bmatrix} n(r)\delta & 0 & 0 \\ 0 & n(r)\delta^{-1} & 0 \\ 0 & 0 & n(r)\delta^{-1} \end{bmatrix}, \tag{8}$$

where subscript r stands for relative values. Note that the term $n(r)$ should be translated into the physical space coordinates using Eq. 3. For $n_0 = 1$ and $R = 1$ we have $n(r) = 2/(1 + x'^2/\delta^2 + y'^2)$. The principal refractive indices also follow the formula below:

$$\begin{aligned} \text{TE:} &\begin{cases} n^{\mathrm{TE}}_{x'} = \sqrt{\mu_{z'z'}\varepsilon_{y'y'}} = \dfrac{n(r)}{\delta^{-1}} \\ n^{\mathrm{TE}}_{y'} = \sqrt{\mu_{z'z'}\varepsilon_{x'x'}} = n(r) \end{cases}, \\ \text{TM:} &\begin{cases} n^{\mathrm{TM}}_{x'} = \sqrt{\varepsilon_{z'z'}\mu_{y'y'}} = \dfrac{n(r)}{\delta^{-1}} \\ n^{\mathrm{TM}}_{y'} = \sqrt{\varepsilon_{z'z'}\mu_{x'x'}} = n(r) \end{cases}. \end{aligned} \tag{9}$$

The anisotropy ratio equals $n'_y/n'_x = \delta$, which means that the refractive index in the direction of compression is $1/\delta$ times larger. The above anisotropic refractive index profile can be realized using glide-symmetric meandered transmission lines and holey ellipse unit cells (Ebrahimpouri and Quevedo-Teruel, 2019), and glide-symmetric substrate-integrated-holey unit cells (Chen et al., 2021).

The reflection coefficient at $x' = 0$ for the transformation medium described in Eq. 8 follows:

$$\Gamma = \left| \frac{\cos\theta - \sqrt{1 - \dfrac{\sin^2\theta}{n^2(r)}}}{\cos\theta + \sqrt{1 - \dfrac{\sin^2\theta}{n^2(r)}}} \right| <= \left| \frac{\cos\theta - \sqrt{1 - \dfrac{\sin^2\theta}{4}}}{\cos\theta + \sqrt{1 - \dfrac{\sin^2\theta}{4}}} \right|, \tag{10}$$

where it assumed that the refractive index along the $x' = 0$ boundary is constant and $n = 2$ (worst case scenario) for the derivation of the maximum possible value. Note that the reflection coefficient is zero for $\theta = 0$; but it is non-zero for other scan angles.

3 Simulation results

Simulations are carried out for TE and TM polarizations at a frequency of 1.5 GHz. The design parameters are $n_0 = 1, R = 1, \delta = 0.25$. The EHMFEL aperture length is 5λ. The standard feeding waveguide WR650 is used with a width of 165 mm. The waveguide is perpendicular to the ellipse's boundary. To simplify the representation, we will no longer use primed coordinates.

Figure 3 depicts the real part of E_z for the TE_1 mode, and Figure 4 illustrates the real part of H_z for the TM_0 mode. Both figures, show results for the cases corresponding to the positive

scan angles of $\theta = 0°$, 4°, 8°, 12°, 16°, and 20°. The waveguide is moved across the surface to examine the device's scanning capacity. Because of the symmetry of the structure, only the cases where the waveguide is moved downward are shown.

The farfield patterns corresponding to **Figures 3**, **4** are illustrated in **Figure 5**. The dotted lines represent the cases where the feed location is mirrored with respect to the *x*-axis. The results are almost identical for both polarizations, as expected.

According to the results in **Figures 3–5**, it is seen that the EHMFEL performs well for both polarizations. The device achieves a scanning range of $-20° \leq \theta \leq 20°$. For a larger scanning angle, an undesirable grating lobe appears. It is practically not expected from HMFEL to provide large scan angles (Fuchs et al., 2007). Furthermore, using **Eq. 10**, the reflection coefficient Γ is less than 0.024 for $-20° \leq \theta \leq 20°$.

4 Discussion

Here we studied the lens compression in the case of a Luneburg lens with a radius of one and a refractive index of $n = \sqrt{2 - x^2 - y^2}$. It is known that when a Luneburg lens is excited from a point on its rim, a flat phase front is formed on the opposite side. **Figure 6** illustrates this case.

The lens works in such a way that $\varphi_0 = \varphi_1 + \varphi_2$. A beam traveling along the optical axis should have the same total phase as a ray traveling along the rim toward the aperture. If the lens is transformed into any shape, such as an ellipse (as shown in **Figure 6**), To ensures that $\varphi_0 = \varphi_0'$, $\varphi_1 = \varphi_1'$. For the phase front to be a straight line after reshaping, $\varphi_2 = \varphi_2'$ equality must be satisfied, which is not the case due to the altered lens geometry. As a result, the phase front will not be a straight line after the reshaping. If the Luneburg lens is reshaped, either the directivity enhancement is significantly degraded or the lens's focus moves outside the lens and becomes non-ideal. The same problem does not occur in the case of HMFEL since the phase front overlaps the lens border, implying that $\varphi_2 = \varphi_2' = 0$. **Figure 7** illustrates the simulation results for an uncompressed Luneburg lens and a compressed Luneburg lens with $\delta = 0.5$. A point source with an out-of-plane current excites the TE polarization. It is clear that the output phase front of the compressed device is not flat, and the lens appears to be focusing the wave.

5 Conclusion

The transformation optics method is employed to reshape the geometry of a HMFEL into an EHMFEL, making the device more compact while preserving its electromagnetic properties. The boundary reflections were studied, and a reflectionless design was proposed for the case where the beam was perpendicular to the EHMFEL aperture. A prototype was designed and simulated for TE and TM polarization using COMSOL. The device provides a scanning range of ±20° with negligible boundary reflections.

Data availability statement

The original contributions presented in the study are included in the article; further inquiries can be directed to the corresponding author.

Author contributions

HE conceived the idea, conducted the simulations, and prepared and revised the manuscript.

Conflict of interest

The author declares that the research was conducted in the absence of any commercial or financial relationships that could be construed as a potential conflict of interest.

Publisher's note

References

Aghanejad, I., Abiri, H., and Yahaghi, A. (2012). Design of high-gain lens antenna by gradient-index metamaterials using transformation optics. *IEEE Trans. Antennas Propag.* 60, 4074–4081. doi:10.1109/tap.2012.2207051

Badri, S. H., Gilarlue, M. M., and Taghipour-Farshi, H. (2020). Rectangular Maxwell's fisheye lens via transformation optics as a crossing medium for dissimilar waveguides. *J. Opt. Soc. Am. B* 37, 2437. doi:10.1364/josab.392644

Chen, Q., Giusti, F., Valerio, G., Mesa, F., and Quevedo-Teruel, O. (2021). Anisotropic glide-symmetric substrate-integrated-holey metasurface for a compressed ultrawideband luneburg lens. *Appl. Phys. Lett.* 118, 084102. doi:10.1063/5.0041586

Demetriadou, A., and Hao, Y. (2011a). A grounded slim luneburg lens antenna based on transformation electromagnetics. *IEEE Antennas Wirel. Propag. Lett.* 10, 1590–1593. doi:10.1109/lawp.2011.2180884

Demetriadou, A., and Hao, Y. (2011b). Slim luneburg lens for antenna applications. *Opt. Express* 19, 19925. doi:10.1364/oe.19.019925

Ebrahimpouri, M., and Quevedo-Teruel, O. (2019). Ultrawideband anisotropic glide-symmetric metasurfaces. *IEEE Antennas Wirel. Propag. Lett.* 18, 1547–1551. doi:10.1109/lawp.2019.2922238

Emiroglu, C. D., and Kwon, D.-H. (2010). Impedance-matched three-dimensional beam expander and compressor designs via transformation optics. *J. Appl. Phys.* 107, 084502. doi:10.1063/1.3383057

Eskandari, H., Albadalejo-Lijarcio, J. L., Zetterstrom, O., Tyc, T., and Quevedo-Teruel, O. (2021a). H-plane horn antenna with enhanced directivity using conformal transformation optics. *Sci. Rep.* 11, 14322. doi:10.1038/s41598-021-93812-6

Eskandari, H., Attari, A. R., and Majedi, M. S. (2018). Design of polarization splitting devices with ideal transmission and anisotropy considerations. *J. Opt. Soc. Am. B* 35, 1585–1595. doi:10.1364/josab.35.001585

Eskandari, H., Attari, A. R., and Majedi, M. S. (2017a). Reflectionless design of a nonmagnetic homogeneous optical waveguide coupler based on transformation optics. *J. Opt. Soc. Am. B* 35, 54–60. doi:10.1364/josab.35.000054

Eskandari, H., Majedi, M. S., Attari, A. R., and Quevedo-Teruel, O. (2019a). Elliptical generalized Maxwell fish-eye lens using conformal mapping. *New J. Phys.* 21, 063010. doi:10.1088/1367-2630/ab2471

Eskandari, H., Majedi, M. S., and Attari, A. R. (2017b). Reflectionless compact nonmagnetic optical waveguide coupler design based on transformation optics. *Appl. Opt.* 56, 5599–5606. doi:10.1364/ao.56.005599

Eskandari, H., Quevedo-Teruel, O., Attari, A. R., and Majedi, M. S. (2019b). Transformation optics for perfect two-dimensional non-magnetic all-mode waveguide couplers. *Opt. Mat. Express* 9, 1320–1332. doi:10.1364/ome.9.001320

Eskandari, H., Saviz, S., and Tyc, T. (2021b). Directivity enhancement of a cylindrical wire antenna by a graded index dielectric shell designed using strictly conformal transformation optics. *Sci. Rep.* 11, 1–11. doi:10.1038/s41598-021-92200-4

Eskandari, H. (2022). Strictly conformal transformation optics for directivity enhancement and unidirectional cloaking of a cylindrical wire antenna. *Sci. Rep.* 12, 16278. doi:10.1038/s41598-022-20503-1

Eskandari, H., and Tyc, T. (2019). Controlling refractive index of transformation-optics devices via optical path rescaling. *Sci. Rep.* 9, 18412–12. doi:10.1038/s41598-019-54516-0

Fuchs, B., Lafond, O., Rondineau, S., Himdi, M., and Coq, L. L. (2007). Off-axis performances of half Maxwell fish-eye lens antennas at 77 GHz. *IEEE Trans. Antennas Propag.* 55, 479–482. doi:10.1109/tap.2006.886576

Fuchs, B., Lafond, O., Rondineau, S., and Himdi, M. (2006). Design and characterization of half Maxwell fish-eye lens antennas in millimeter waves. *IEEE Trans. Microw. Theory Tech.* 54, 2292–2300. doi:10.1109/tmtt.2006.875255

García-Meca, C., Tung, M. M., Galán, J. V., Ortuño, R., Rodríguez-Fortuño, F. J., Martí, J., et al. (2011). Squeezing and expanding light without reflections via transformation optics. *Opt. Express* 19, 3562–3575. doi:10.1364/oe.19.003562

Giddens, H., Andy, A. S., and Hao, Y. (2021). Multimaterial 3-d printed compressed luneburg lens for mm-wave beam steering. *IEEE Antennas Wirel. Propag. Lett.* 20, 2166–2170. doi:10.1109/lawp.2021.3109591

Giddens, H., and Hao, Y. (2020). Multibeam graded dielectric lens antenna from multimaterial 3-d printing. *IEEE Trans. Antennas Propag.* 68, 6832–6837. doi:10.1109/tap.2020.2978949

Gok, G., and Grbic, A. (2016). A physical explanation for the all-angle reflectionless property of transformation optics designs. *J. Opt.* 18, 044020. doi:10.1088/2040-8978/18/4/044020

Gu, C., Yao, K., Lu, W., Lai, Y., Chen, H., Hou, B., et al. (2012). Experimental realization of a broadband conformal mapping lens for directional emission. *Appl. Phys. Lett.* 100, 261907. doi:10.1063/1.4731877

Huang, M., Yang, S., Gao, F., Quarfoth, R., and Sievenpiper, D. (2014). A 2-d multibeam half Maxwell fish-eye lens antenna using high impedance surfaces. *IEEE Antennas Wirel. Propag. Lett.* 13, 365–368. doi:10.1109/lawp.2014.2306207

Hunt, J., Jang, G., and Smith, D. R. (2011). Perfect relay lens at microwave frequencies based on flattening a Maxwell lens. *J. Opt. Soc. Am. B* 28, 2025–2029. doi:10.1364/josab.28.002025

Kadera, P., Sanchez-Pastor, J., Eskandari, H., Tyc, T., Sakaki, M., Schusler, M., et al. (2022). Wide-angle ceramic retroreflective luneburg lens based on quasi-conformal transformation optics for mm-wave indoor localization. *IEEE Access* 10, 41097–41111. doi:10.1109/access.2022.3166509

Kwon, D.-H., and Werner, D. H. (2008). Polarization splitter and polarization rotator designs based on transformation optics. *Opt. Express* 16, 18731–18738. doi:10.1364/oe.16.018731

Leonhardt, U. (2006). Optical conformal mapping. *Science* 312, 1777–1780. doi:10.1126/science.1126493

Li, S., Zhou, Y., Dong, J., Zhang, X., Cassan, E., Hou, J., et al. (2018). Universal multimode waveguide crossing based on transformation optics. *Optica* 5, 1549–1556. doi:10.1364/optica.5.001549

Liu, K., Yang, S., Chen, C., Qu, S.-W., and Chen, Y. (2020). A wide-scanning ellipsoid lens antenna fed by phased array antenna. *Int. J. RF Microw. Comput. Aided. Eng.* 30. doi:10.1002/mmce.22127

Luneberg, R. (1964). *Mathematical theory of optics*. University of California Press.

Markov, P., Valentine, J. G., and Weiss, S. M. (2012). Fiber-to-chip coupler designed using an optical transformation. *Opt. Express* 20, 14705–14713. doi:10.1364/oe.20.014705

Mateo-Segura, C., Dyke, A., Dyke, H., Haq, S., and Hao, Y. (2014). Flat luneburg lens via transformation optics for directive antenna applications. *IEEE Trans. Antennas Propag.* 62, 1945–1953. doi:10.1109/tap.2014.2302004

Maxwell, J. C. (1854). Solutions of problems. *Camb. Dublin Math. J.* 8, 188–195.

Mousavi, S. S. S., Majedi, M. S., and Eskandari, H. (2017). Design and simulation of polarization transformers using transformation electromagnetics. *Optik* 130, 1099–1106. doi:10.1016/j.ijleo.2016.11.129

Nazarzadeh, F., and Heidari, A. A. (2022). Wideband flat reflector antenna based on conformal transformation optics. *Optik* 264, 169429. doi:10.1016/j.ijleo.2022.169429

Pendry, J. B., Schurig, D., and Smith, D. R. (2006). Controlling electromagnetic fields. *Science* 312, 1780–1782. doi:10.1126/science.1125907

Rahm, M., Roberts, D. A., Pendry, J. B., and Smith, D. R. (2008). Transformation-optical design of adaptive beam bends and beam expanders. *Opt. Express* 16, 11555–11567. doi:10.1364/oe.16.011555

Roberts, D. A., Kundtz, N., and Smith, D. R. (2009). Optical lens compression via transformation optics. *Opt. Express* 17, 16535–16542. doi:10.1364/oe.17.016535

Schmiele, M., Varma, V. S., Rockstuhl, C., and Lederer, F. (2010). Designing optical elements from isotropic materials by using transformation optics. *Phys. Rev. A . Coll. Park.* 81, 033837. doi:10.1103/physreva.81.033837

Shi, Y., Li, K., Wang, J., Li, L., and Liang, C.-H. (2015). An etched planar metasurface half Maxwell fish-eye lens antenna. *IEEE Trans. Antennas Propag.* 63, 3742–3747. doi:10.1109/tap.2015.2438337

Smith, D. R., Urzhumov, Y., Kundtz, N. B., and Landy, N. I. (2010). Enhancing imaging systems using transformation optics. *Opt. Express* 18, 21238–21251. doi:10.1364/oe.18.021238

Su, Y., and Chen, Z. N. (2018). A flat dual-polarized transformation-optics beamscanning luneburg lens antenna using PCB-stacked gradient index metamaterials. *IEEE Trans. Antennas Propag.* 66, 5088–5097. doi:10.1109/tap.2018.2858209

Su, Y., and Chen, Z. N. (2019). A radial transformation-optics mapping for flat ultra-wide-angle dual-polarized stacked GRIN MTM luneburg lens antenna. *IEEE Trans. Antennas Propag.* 67, 2961–2970. doi:10.1109/tap.2019.2900346

Tao, S., Zhou, Y., and Chen, H. (2019). Maxwell's fish-eye lenses under schwartz-christoffel mappings. *Phys. Rev. A . Coll. Park.* 99, 013837. doi:10.1103/physreva.99.013837

Tyc, T., Herzánová, L., Šarbort, M., and Bering, K. (2011). Absolute instruments and perfect imaging in geometrical optics. *New J. Phys.* 13, 115004. doi:10.1088/1367-2630/13/11/115004

Wu, Q., Jiang, Z. H., Quevedo-Teruel, O., Turpin, J. P., Tang, W., Hao, Y., et al. (2013). Transformation optics inspired multibeam lens antennas for broadband directive radiation. *IEEE Trans. Antennas Propag.* 61, 5910–5922. doi:10.1109/tap.2013.2282905

Xu, H.-X., Wang, G.-M., Tao, Z., and Cai, T. (2014). An octave-bandwidth half Maxwell fish-eye lens antenna using three-dimensional gradient-index fractal metamaterials. *IEEE Trans. Antennas Propag.* 62, 4823–4828. doi:10.1109/tap.2014.2330615

Xu, R., and Chen, Z. N. (2022). A transformation-optics-based flat metamaterial luneburg lens antenna with zero focal length. *IEEE Trans. Antennas Propag.* 70, 3287–3296. doi:10.1109/tap.2021.3137528

Yang, F., Mei, Z. L., and Cui, T. J. (2014). Design and experiment of perfect relay lens based on the schwarz-christoffel mapping. *Appl. Phys. Lett.* 104, 073510. doi:10.1063/1.4866284

Yao, K., and Jiang, X. (2011). Designing feasible optical devices via conformal mapping. *J. Opt. Soc. Am. B* 28, 1037–1042. doi:10.1364/josab.28.001037

frontiers | Frontiers in Materials

TYPE Original Research
PUBLISHED 25 January 2023
DOI 10.3389/fmats.2022.1048011

OPEN ACCESS

EDITED BY
Yue Li,
Hefei Institutes of Physical Science (CAS), China

REVIEWED BY
Samir Kumar,
Korea University, South Korea
Guangqiang Liu,
Qufu Normal University, China

*CORRESPONDENCE
Xiao Zhang,
changshui@hotmail.com
Liang Wang,
healthscience@foxmail.com

SPECIALTY SECTION
This article was submitted to Colloidal Materials and Interfaces, a section of the journal Frontiers in Materials

RECEIVED 19 September 2022
ACCEPTED 30 November 2022
PUBLISHED 25 January 2023

CITATION
Usman M, Ishafaq MUU, Muhammad Z, Ali W, Dastgeer G, Zhang X and Wang L (2023), Evaporation-induced self-assembly of gold nanorods on a hydrophobic substrate for surface enhanced Raman spectroscopy applications. *Front. Mater.* 9:1048011. doi: 10.3389/fmats.2022.1048011

Evaporation-induced self-assembly of gold nanorods on a hydrophobic substrate for surface enhanced Raman spectroscopy applications

Muhammad Usman[1], M. U. U. Ishafaq[2], Zahir Muhammad[3], Wajid Ali[4], Ghulam Dastgeer[5], Xiao Zhang[1]* and Liang Wang[1,6]*

[1]Department of Bioinformatics, School of Medical Informatics and Engineering, Xuzhou Medical University, Xuzhou, China, [2]Hefei National Laboratory for Physical Sciences at Microscale and Department of Physics, University of Science and Technology of China, Hefei, Anhui, China, [3]Hefei Innovation Research Institute, School of Microelectronics, Beihang University, Hefei, China, [4]Key Laboratory for Micro-Nano Physics and Technology of Hunan Province, College of Materials Science and Engineering, Hunan University, Changsha, Hunan, China, [5]Department of Physics and Astronomy and Graphene Research Institute, Sejong University, Seoul, South Korea, [6]Laboratory Medicine, Guangdong Provincial People's Hospital, Guangdong Academy of Medical Sciences, Guangzhou, China

The controllable assembly of plasmonic nanoparticles has developed as one of the most significant approaches for surface enhanced Raman spectroscopy (SERS) applications. This study developed a simple approach to improve a large-scale ordered assembly of gold nanorods (GNRs) by controlling the droplet evaporation mode on hydrophobic substrates. The hydrophobic substrate was efficiently produced by spin coating the silicone oil onto the glass slides and annealing them. The analyte molecule rhodamine (R6G) was employed as a surface-enhanced Raman scattering probe to demonstrate the potential effects of the synthesized arrays. This hydrophobic platform enables the concentration and delivery of analyte molecules into the surface enhanced Raman spectroscopy sensitive site while suppressing the coffee ring effect generated by the smooth contraction motion of the base contact radius of the droplet without any pinning. Thus, the limit of detection (LOD) of the R6G analyte was lowered to 10^{-10} M and the homogenous dispersion of surface enhanced Raman spectroscopy hotspots within the self-assembly reproducible surface enhanced Raman spectroscopy signal. This new method enables a broad range of packing patterns and mechanisms by changing the host nanoparticles in the dispersion.

KEYWORDS

plasmonic nanoparticles, self-assemblies, hydrophobic surface, coffee ring effect, Raman spectroscopy

1 Introduction

The self-assembly of nanoparticles is becoming a common and effective approach for fabricating controlled colloidal patterns (Jana, 2004; Ko et al., 2008; Prasad et al., 2008; Grzelczak et al., 2010; Dai et al., 2011). Several methods for fabricating GNRs arrays have been developed to compact complicated particle structures with diverse symmetry and assembly configurations at the nanoscale (Zhu et al., 2011; Quan et al., 2014; Li et al., 2015; Wang et al., 2015; Lu and Tang, 2016; Luo et al., 2017a; Luo et al., 2017b). The assembly of anisotropic colloidal nanoparticles into complicated well-arranged structures has long been a hot topic in nanoscience due to their distinct collective optical and electronic properties and incorporation into nanophotonics (Zhu et al., 2011; Lu and Tang, 2016; Luo et al., 2017a; Quan et al., 2014; Li et al., 2015; Wang et al., 2015; Xia et al., 2003; Cho et al., 2010; Wang et al., 2012; Sun, 2013; Wang et al., 2015; Xu et al., 2015; Neretina et al., 2016; Abeyweera et al., 2017; Kim et al., 2017). The successful incorporation of such nanoparticles into efficient optoelectronic devices needs reproducible, highly organized, and macroscopic uniformity of performance from the structure (Zhu et al., 2011; Li et al., 2016; Lu and Tang, 2016).

The droplet evaporation has been intensively examined among the diverse approaches used to produce complicated structures due along with its functionality, cost-effectiveness, and broad applicability to numerous nanomaterials (Zhang et al., 2014; Vogel et al., 2015). Moreover, the drying droplet commonly leaves a non-uniform solid-ring on the substrate known as a coffee ring (Deegan et al., 1997). The configuration of a solid ring structure is strongly related to droplet-controlled dispersion, which is primarily focused on heat and mass loss during evaporation (Deegan, 2000). The heat loss causes evaporative cooling to sufficiently produce a surface tension slope capable of driving Marangoni flow (Larson, 2014). The evaporation process causes capillary flow outward from the center of the drop, bringing the suspension particles to the edges. The particles are significantly concentrated along the initial drop edge after evaporation, resulting in a non-uniform solid ring (Deegan et al., 2000). Recent research has focused on addressing the coffee-ring effect by controlling important configurations including particle size, particle shape, charges and surfactant concentration, to attain large-area arrays of self-assembled particles (Fan et al., 2004; Bigioni et al., 2006; Byun et al., 2010; Alvarez-Puebla et al., 2011; Singh et al., 2012; Chen et al., 2013; Peng et al., 2013; Ye et al., 2013; Peng et al., 2014; Zhang and Lin, 2014; Apte et al., 2015; Hamon et al., 2015; Li et al., 2016; Lu and Tang, 2016; Luo et al., 2017a; Luo et al., 2017b; Kim et al., 2017). The most effective method for overcoming the "diffusion limit" of analytes in highly diluted aqueous solutions is to use super hydrophobic surfaces, which have the dynamic ability to deliver analytes to SERS-active sites (De Angelis et al., 2011; Gentile et al., 2014). Moreover, the disadvantage of super hydrophobic surfaces for these applications is that air pockets among the surface structures can be spoiled by outward wetting pressure and could lose wetting property by destructive the surface structure (Reyssat et al., 2007). Recently, slippery surfaces (hydrophobic surfaces) have evolved into a superior substitute to super hydrophobic as a fluid repellent surface with a very small contact angle hysteresis (Bocquet and Lauga, 2011). To our understanding, only few studies has been accompanied on the controlled evaporation method-based SERS technique for analyte detection on cost-effective hydrophilic substrates.

This study proposed a novel method for fabricating self-assembled GNRs. The hydrophobic surface was fabricated in the first step and then controlled the evaporation rate of droplets in the second step. This method was used to reverse the coffee ring effect during droplet evaporation of an aqueous diffusion of GNRs assembly. The droplet evaporation process revealed GNRs formed at the interface between solvent and air, developing domains that improved in size and density as the solvent evaporated under microscope light. The optical properties of the attained superstructures were experimentally determined. Finally, the promising application of GNRs self-assembly arrays for analytical detection using R6G as a model analyte based on SERS was established.

2 Material and method

2.1 Preparation of GNRs

The study synthesized the GNRs and employed a seed-mediated growth method as described in our previous procedure (Usman et al., 2019). After the seed solution was formed, HAuCl4 (0.1 ml; 0.025 M) and CTAB (5 ml; 0.2 M) were combined at room temperature. The solution of ice-cold $NaBH_4$ (0.01 M, 0.6 ml) was promptly introduced. The color of the solution gradually changed from yellow to brownish-yellow. The solution continues to stirring for 20 min. The solution was cooled down to room temperature for 30 min. The growth solution was prepared by adding hexadecyltrimethyl ammonium bromide (CTAB), 5 ml, 0.2 M, and different amounts of 0.05, 0.10, 0.15, 0.20, and 0.25 ml of 0.16 mM $AgNO_3$ solutions at 30°C, respectively. Then, add 0.2 ml of 0.025 M $HAuCl_4$ to the solution. Following constant stirring, the ascorbic acid (0.08 M, 70 ml) was added and changed the color from dark-yellow to colorless. Lastly, the seed solution of 12 ml was mixed with the growth solution at 30°C. The color of the mixture slowly changes in 15–30 min. The GNRs were well designed at room temperature after rapid growth.

2.2 Silicone oil-based hydrophobic surface preparation

The glass slides were cleaned for 10 min using sonication and plasma cleaning. The silicone oil, with a kinematic viscosity of 370 cSt, was applied to a clean glass slide and spin-coated at 1,000 rpm for 1 min. This method was effective for removing additional lubricating

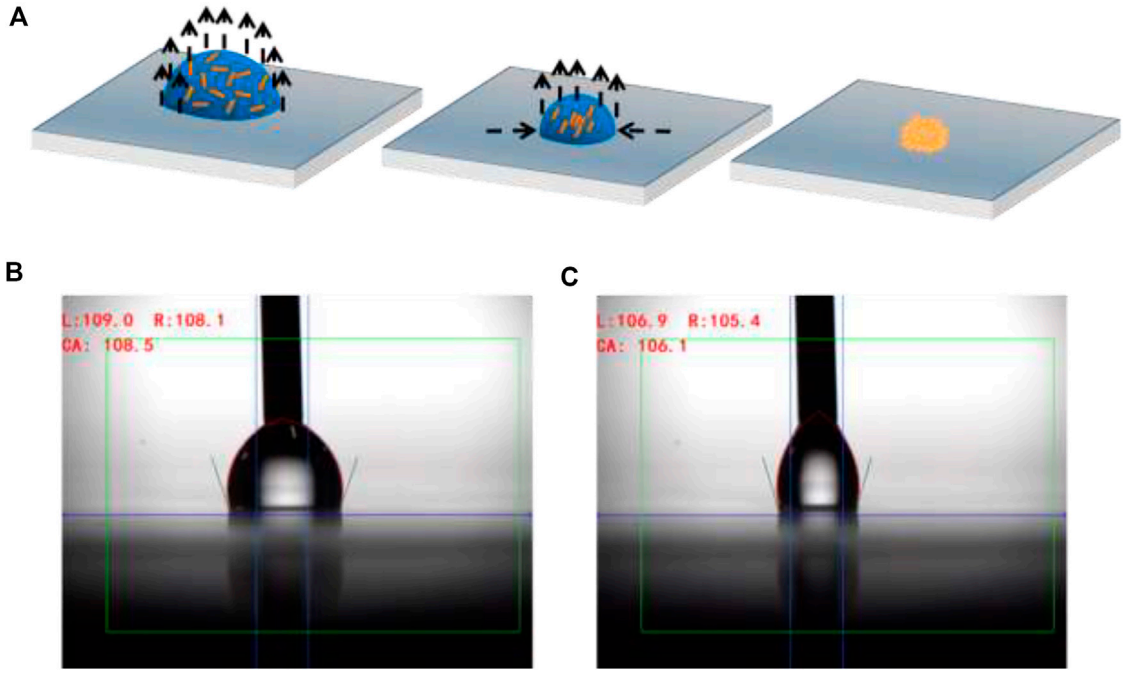

FIGURE 1
(A) A diagram showing the enrichment and self-assembly of GNRs on a hydrophobic surface. **(B)** Contact angles advancing and **(C)** receding on a hydrophobic surface.

oil. The silicone oil-coated glass slide was then annealed at 150°C for 120 min. As a result, the surface chemical property was modified to be hydrophobic and a uniform silicone oil coating was formed on the glass slide.

2.3 Evaporation-induced assembly of aligned GNRs arrays

The GNRs were centrifuged at 7,000 rpm for 20 min to reduce extra CTAB. A 30-μl drop of GNRs was deposited on the hydrophobic substrate. Then the hydrophobic substrate was transferred onto a polystyrene Petri dish plate with dimensions of 94 mm in width and 15 mm in height. After that, add 1 ml of water to the Petri dish to regulate the humidity. The Petri dish was wrapped and put inside an incubator. After the evaporation, the GNRs solution on the hydrophobic substrate contracted into tiny droplets without forming coffee-rings. As a result, the well-arranged assemblies of GNRs were observed on the hydrophobic substrate.

2.4 Raman spectroscopy measurements

For the SERS measurements, R6G dye was working as a Raman probe molecule and was diluted to various concentrations. The concentrated molecules and GNRs solution of 30 μl was placed on the SERS substrate and evaporated at room temperature. All SERS measurements were carried out using a 633 nm laser excitation and a laser power of about 1.5 mW. A confocal Raman microscope (Renishaw PLC., England, United Kingdom) with a 50-microscope objective and a numerical aperture (NA) of 0.6 was used to detect in-elastically scattered radiation.

2.5 FEM simulation

We used the commercial program COMSOL Multiphysics 5.5 for numerical simulation to do electromagnetic analysis. Comsol uses the finite element method (FEM) to solve the following differential form of the Maxwell equation:

$$\nabla \times \frac{1}{\mu_r}(\nabla \times E) - K_0^2\left(\varepsilon_r - \frac{j\sigma}{\omega\varepsilon_0}\right)E = 0 \quad (1)$$

where μ_r and ε_r are the medium's relative permittivity and permeability, respectively, and K is the wave's propagation vector defined for all mediums in the model, ω is the angular frequency, and σ is the medium's conductivity. A 3D frequency-domain model is used to solve the problem in the wave optics module. A perfect matching layer PML is applied at the top and bottom of the model to secure the physical domain from any background fields. Furthermore, periodic boundary conditions

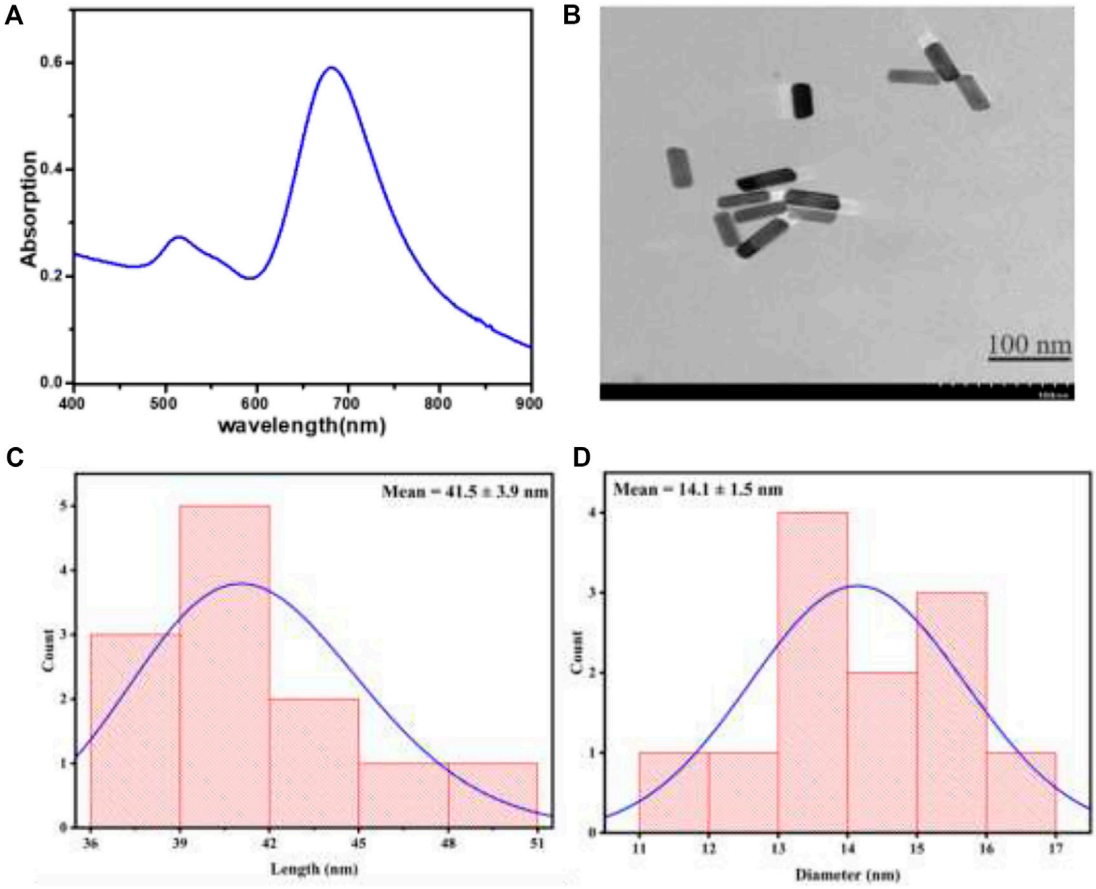

FIGURE 2
(A) The UV-vis spectrum of GNRs in aqueous medium **(B)** TEM image of GNRs demonstrating good size uniformity. The histogram figures show the **(C)** length and **(D)** diameter of GNRs from TEM images.

are applied in the X and Y directions to simulate light propagation through the hexagonal unit cell of the standing GNRs. Physic controlled fine meshing used for GNRs and physical domain. The whole structure is irradiated vertically with a transverse electric polarized light with an electric field intensity of 1V/m. The GNRs array in the simulations has a surface-to-surface separation $p = 7$ nm, diameter D of 17 nm, and a height of 30 nm. P. B. Johnson and R. W. Christy experimentally determined values for gold permittivity was utilized for the model. The dielectric constants of the silicone layer and quartz glass were also sourced from the comsol material library.

3 Results and discussion

The hydrophobic surface and high humidity environment are critical for GNRs self-assembly and enrichment. A lubricated substrate containing a silicon oil-coated glass slide is a simple depiction followed by spin coating and annealing. Hence, this would make the substrate hydrophobic because the high surface energy of silicon dioxide changes the surface energy of the glass through covalent bonding of silicone oil molecules with the glass surface. The hydrophobic surface played an important part in the development and self-assembly of GNRs. It is extremely important to keep droplet evaporation in a steady-state assembly process, which is primarily a thermodynamic procedure, in imperative to produce homogeneous self-assembled particle arrays. As a result, the environmental parameters must be carefully monitored, including the temperature and humidity of the substrates during the evaporation process. When the temperature falls below 25°C, the CTAB surfactant in the droplets crystallizes and precipitates from the solution. This clearly devastates the self-assembly process, resulting in poor quality GNRs arrays. When the temperature rises to 50°C, however, the convection in the droplet intensifies, causing serious damage in large non-uniform accumulations (Ming et al., 2008). The evaporation

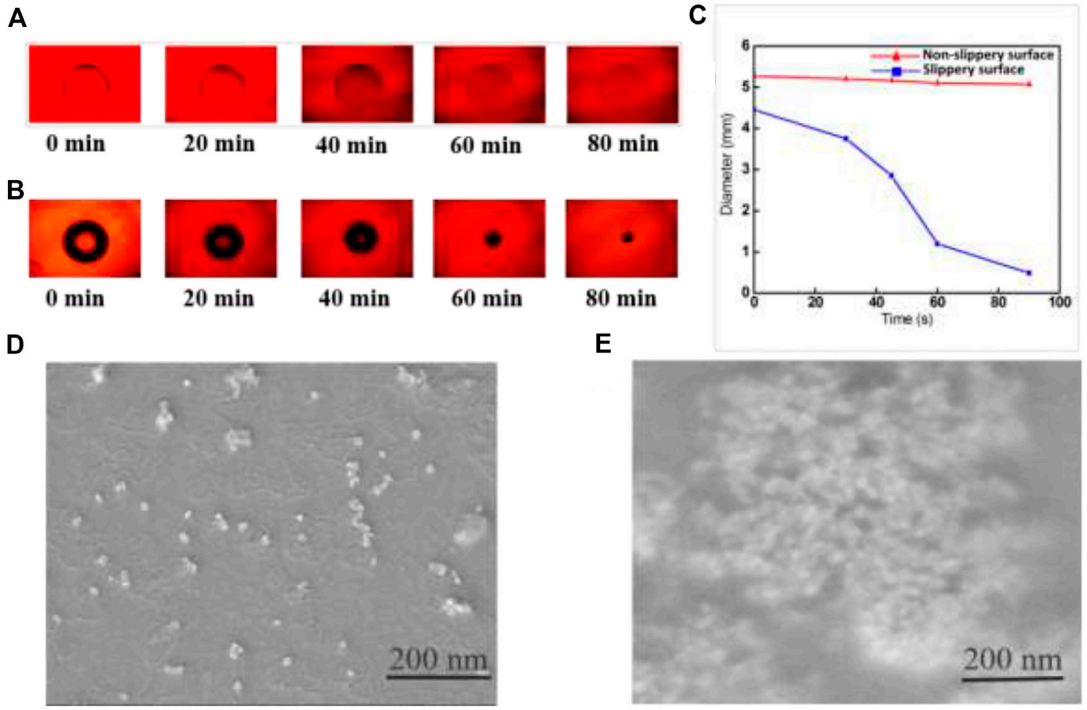

FIGURE 3
(A) Optical microscopy images of droplets evaporating at different times on a hydrophilic **(B)** hydrophobic surface. **(C)** The contact diameter (CD) of a droplet on non-slippery surfaces and slippery surfaces as a function of evaporation time. SEM images of GNRs solution after evaporation **(D)** on the hydrophilic surface and **(E)** lubricated liquid-infused hydrophobic surface.

was carried out in a controlled environment with a high humidity level in maintenance. The high humidity environment slowed the evaporation of the GNRs droplets, allowing the solvent to evaporate at the same rate from the contact line to the droplet centers (Zhang and Lin, 2014). The slow evaporation could reduce the convection and inhibit GNRs from following from the center to the contact line, thus preventing the formation of a coffee-ring structure (Hu and Larson, 2006). The solution contracted into smaller droplets owing to the homogeneous evaporation speed and the absence of a pinned edge across the surface of the droplets. Figure 1A depicts a schematic demonstration of the fabrication method of the hydrophobic platform.

After optimizing the conditions, we investigated the effects of substrate hydrophobicity and repellency by contact angle (θ) and contact angle hysteresis (CAH) ($\Delta\theta = \theta_a - \theta_r$), the difference between the advancing (θ_a) and receding contact angle (θ_r) measured by optical Goniometer (OCA35, Data Physics Germany). Figure 1B showed substrates with GNRs contact angles of 108.5°, indicating the value of the fabricated hydrophobic surface was tremendous. Contact angle hysteresis ($\Delta\theta$) is associated with the pinning of the contact line and characterizes the droplet evaporation process. In the case of contact line pinning, the contact angle decreases as the droplet volume decreases and the contact line starts to withdraw. Contact-angle hysteresis during droplet evaporation reflects the contact line receding in this way. In our case, $\Delta\theta$ on a hydrophobic surface was only 2.4°, as shown in Figure 1C, which demonstrated that the fabricated hydrophobic surface was of high quality. The small contact angle hysteresis of the dispersion of GNRs on the hydrophobic surface helps to reverse the coffee-ring effect. It can be established that Marangoni flow and contact line receding can efficiently control the final configuration of GNRs on the substrate. This process avoids the coffee-ring effect that occurs during nanoparticle evaporation, resulting in uniform deposition and adjacent packing of GNRs.

This study used an evaporation-induced self-assembly approach to obtain GNRs from a liquid drop containing GNRs. The UV-vis absorption spectrum of GNRs dispersed in water is shown in Figure 2A. The transverse and longitudinal modes were assigned to the surface plasmon resonance peaks that were obtained at wavelengths of 510 and 670 nm, respectively. The previous research has shown that the maximum SERS intensity was achieved when the laser excitation wavelength was slightly shorter than LSPR, so the laser excitation wavelength was in resonance with the substrate of the surface plasmon (Hossain et al., 2009; Kumar et al., 2020). Figure 2B depicts a transmission electron microscopy (TEM)

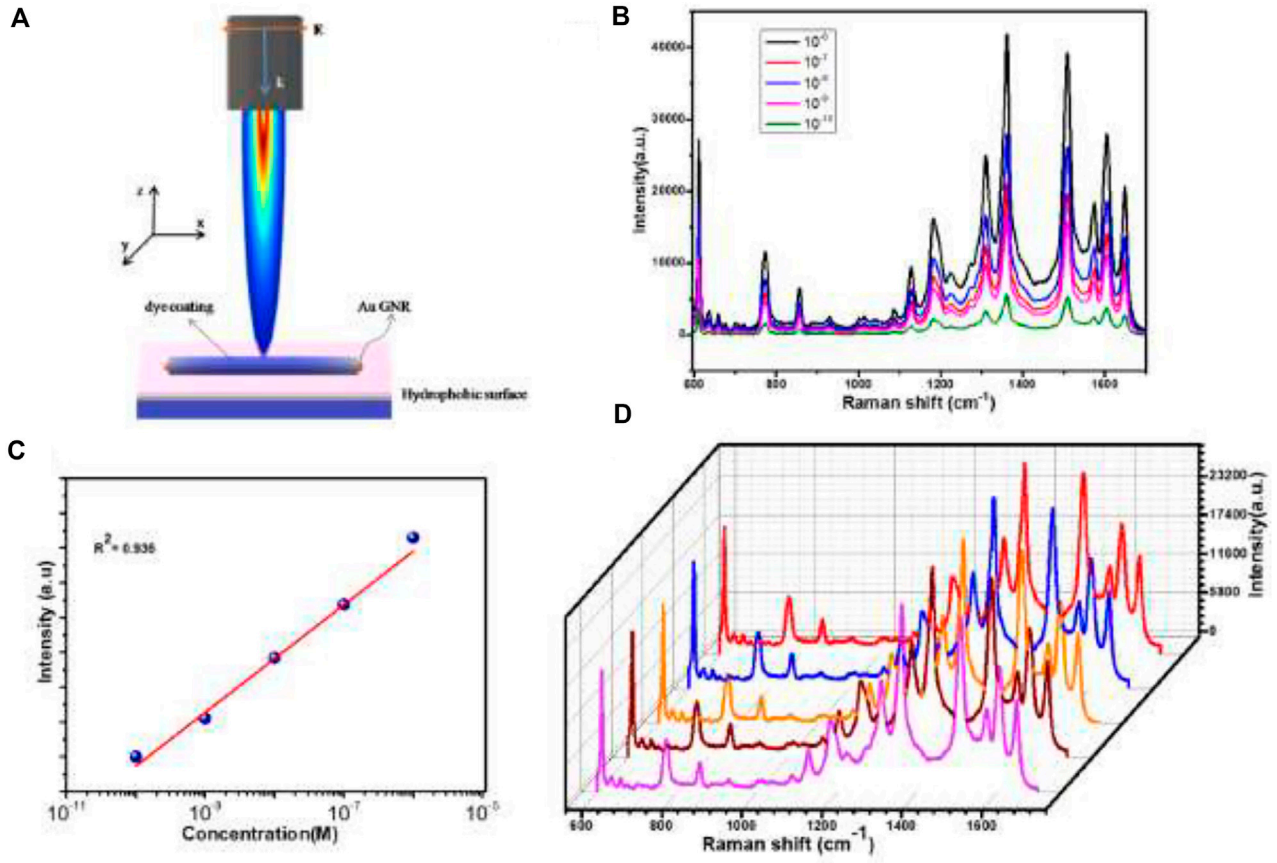

FIGURE 4
(A) Schematic diagram of GNRs coupling with dye analyte on a hydrophobic surface as a strategy to increase the electric field enhancement effect **(B)** Raman scattering spectra of various concentrations of solutions. **(C)** The peak intensities of various concentrations at 1,340 cm^{-1} **(D)** SERS spectra from R6G aqueous solution (10^{-6} M) dried on randomly chosen five spots of the GNRs arrays demonstrate the good reproducibility of the substrate.

representation of GNRs. The distributions of GNRs particle sizes measured in TEM images were plotted in (Figures 2C, D). The length of 41.5 + 3.9 nm and the width of 14.1 + 1.5 nm of the GNRs were obtained from the histogram diagram, and an aspect ratio of about 3. According to this, GNRs had uniform morphology and a narrow size distribution.

We investigated the effects of hydrophobicity on the development of GNRs arrays after optimizing the evaporation conditions, such as temperature at 30°C and humidity at 96%. The GNRs evaporated on the hydrophobic surface in a controlled environment, producing a highly concentrated pattern and repellency. The 20 µl GNRs were measured using an optical microscope at various times on hydrophilic and hydrophobic substrates (see Figure 3).

The droplet of the initial contact diameter (d) on the non-slippery surface (hydrophilic surface) was large (d = 4.47 mm). The contact diameter did not change significantly over the evaporation time due to the hydrophilic nature of the particles and the droplet spread over a large spot with a diameter of 4.27 mm after completely solvent drying (after 55 min), as shown in Figure 3A. On the other hand, the contact diameter of the droplet on the hydrophobic surface was reduced to 0.193 mm from its initial diameter of 3.154 mm after complete drying of the solvent, which was smaller than that of a droplet of the same volume on the hydrophilic surface due to surface hydrophobicity as revealed in Figure 3B. The contact diameter of hydrophilic and hydrophobic surfaces varied with the evaporation time, as shown in Figure 3C. The hydrophobic surface reduced contact area by approximately 98.78% when compared to the hydrophilic surface.

The scanning electron microscopy (SEM) images suggest an exciting effect of the enrichment and the concentration of GNRs particles on hydrophilic and hydrophobic surfaces after evaporation. In Figure 3D, the GNRs particles showed a scattered pattern after complete evaporation on a hydrophilic

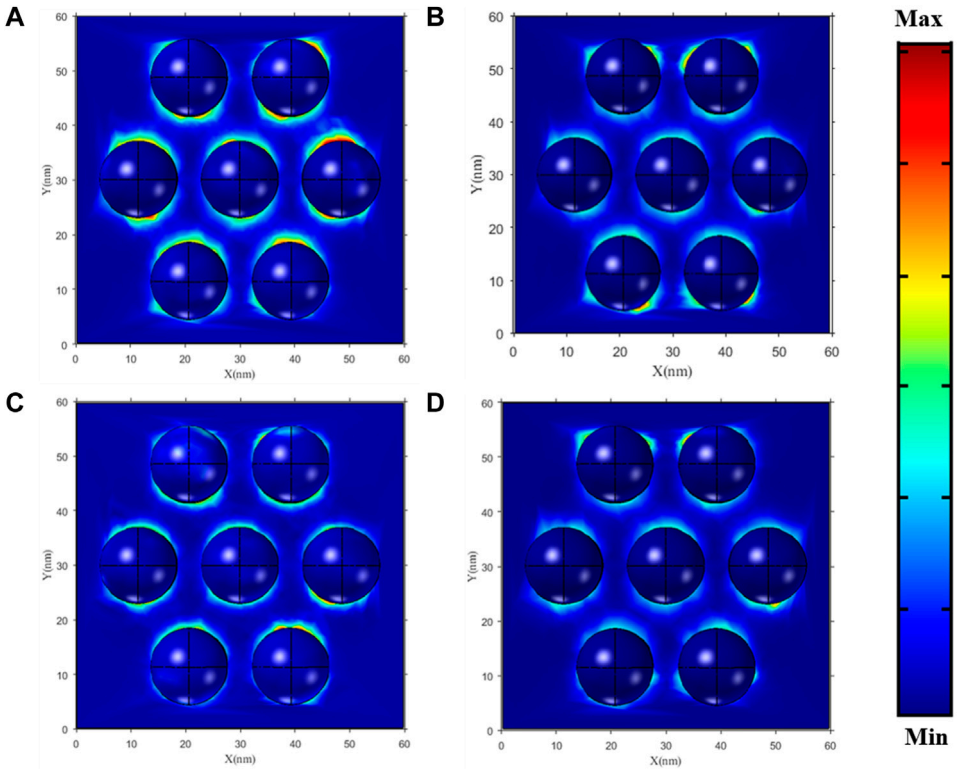

FIGURE 5
The enhancement of the electromagnetic field in GNRs with hydrophobic and hydrophilic substrates with 7-nm gaps **(A,C)** and **(B,D)**, respectively.

surface, with the maximum value at the droplet edge, as described by the "coffee ring effect." This effect is commonly observed at pinning sites on surfaces. As a result, GNRs particles show an extensive configuration over a large area. However, the GNRs solution produced interesting results on the hydrophobic surface. The easy contraction of the droplet without pinning suppressed the coffee ring effect to enrich all the GNRs particles into a very small spot on the hydrophobic surface. The effective compact self-assembly of GNRs *via* droplet evaporation on the hydrophobic surface is shown in Figure 3E.

Furthermore, the condition for a high contact angle and low CAH is critical for improving SERS performance. In former studies has demonstrated that densely compacted metallic nanoparticles have significant SERS enhancement factors (Diebold et al., 2009; Huang et al., 2015). The formation of the hot spots between neighboring particles significantly increases SERS enhancement.

In this study, the fabricated substrate was covered by a closely packed GNRs array, which produced a significant field enhancement effect. The schematically Figure 4A illustrates the encapsulated GNRs on a hydrophobic surface. Here a rounded ends cylindrical GNRs (with orange color) coated with dye (blue color), shined by TE polarized light. The electric field is parallel to the plane of the hydrophobic surface with normal K-propagation vector. The densely-packed GNRs arrays and their uniform structure were able to produce a SERS signal for molecular detection at concentrations as low as 10^{-10} M. SERS measurements on the GNRs arrays were carried out using a Raman spectrometer with a 633 nm excitation. The target molecule was R6G solution, a common dye used in biological research. Figure 4B shows the SERS spectra of R6G at various concentrations ranging from 10^{-6} to 10^{-10} M. The Raman spectra of R6G were attributed to C-C-C ring in plane, out-of-plane being, and C-H in-plane bending vibrations in the sharp peaks at 611 and 776 $cm^{-1,}$ respectively. It also had Raman shift peaks at 1,180, 1,360, 1,509, and 1,650 cm^{-1}, which were ascribed to symmetric modes of C-C stretching vibrations in plane. These R6G Raman peaks are consistent with those previously reported (Lu et al., 2005; Jensen and Schatz, 2006). The Raman spectra clearly showed the characteristic Raman peaks of R6G even when the concentration was as low as 10^{-10} M. The SERS substrates for the GNRs arrays had excellent reusability, enabling multiple detections after plasma etching to clean the previous substrate. The Raman signal

decreased gradually with the decreasing the concentration of R6G. The previous results were also confirmed in the study of Wei et al. (2018) using R6G detection at a concentration was as low as 10^{-10} M. We obtained the calibration curves with this result analyzed as shown in Figure 4C. Notably, it had a relatively good linear correlation relationship (correlation coefficient, R^2 = 0.9928) between the SERS signal ratio and R6G concentration. The suggested approach might, therefore, prove helpful in the quantitative analysis.

In order to study the uniformity and ensure a homogeneous distribution, 10^{-6} M of the analyte R6G aqueous solution was dispersed on the surface of the hydrophobic surface. After that, we observed five random spots on the substrate with the same exciting line and integration time (Figure 4D). The relative signal deviation of R6G was about 10% on the GNRs arrays, revealing the overall reliability and uniformity of such a substrate for SERS detection. The excellent performance of the GNRs arrays could be attributed to a number of factors. For example, the GNRs were arranged in a regular pattern. In periodic structures, photon density redistribution was common, causing an increase in the density of optical modes and an improvement in the Raman scattering of the detected molecules (Gaponenko, 2002).

To effectively understand the physical mechanism underlying the detected SERS response, the electric field intensity enhancement of the GNRs array was investigated employing Comsol multiphysics simulation (see Figure 5), on hydrophobic and hydrophilic substrates, under 540 and 670 nm laser light. The GNRs arrays are assembled with a gap of 7 nm. The GNRs revealed the enhancement of electromagnetic fields in the case of the hydrophobic surface. Figure 5A indicates that at 540 nm of laser excitation, the field is a maximally localized electromagnetic field within the GNRs array in the hydrophobic substrate compared to the hydrophilic substrate in Figure 5B. Similarly, Figure 5C exhibits a similar excellent local field enhancement effect on a hydrophobic substrate as compared to the hydrophilic substrate using 670 nm laser excitation. Hence, when compared with the disordered substrate, the resonance of the local electromagnetic field around the GNRs arrays is relatively strong, and the dense “hot spots” can improve the SERS activity of the substrate. These results further confirm and demonstrate that the hydrophobic substrate can be used to enhance and detect the SERS signals, which is almost consistent with our experimental results.

4 Conclusion

In summary, we used the controlled evaporation process to fabricate large-area ordered self-assembly arrays of GNRs on the hydrophobic surface. The droplet contracts effectively because of the lack of pinning sites and hydrophobicity of the substrate, which prevent the coffee-ring effect and offer a smooth surface. Therefore, this process effectively delivers the molecules inside the droplet to a concentrated hot spot. The resulting arrays had constant structural and efficient homogeneity on a macroscopic scale. We also established that the fabricated GNRs arrays produced a SERS signal for detecting R6G at a concentration of 10^{-10} M. The exceptional results in SERS detection reproducibility are due to the uniformity in large areas. The structure of the GNRs relied solely on the hydrophobicity of substrates in an evaporating environment. The limitation of hydrophobic surfaces is also observed when there are many liquid drops sliding on them, which slowly removes the lubricating oil. In this case, the hydrophobic performance is degraded, but it can be rapidly recovered by coating the silicone oil on the surface again. As a result, this technology could be easily applied to different nanoparticle systems to produce ordered nanoscale arrays for the integration of microscopic devices.

Data availability statement

The original contributions presented in the study are included in the article/Supplementary Material, further inquiries can be directed to the corresponding authors.

Author contributions

MU conceived the core ideas and designed the outlines of the manuscript. MI and ZM contributed to the project administration. WA carried out the theoretical simulation analysis of literature. All authors made significant contributions to write and revise the manuscript. XZ and LW set-up the platforms, provided resources, and secured funding for the study. All authors read and approved the submitted version of the manuscript.

Funding

This work was supported in part by National Natural Science Foundation of China (31900022, 32171281), Young Science and Technology Innovation Team of Xuzhou Medical University (TD202001), and Jiangsu Qinglan Project (2020).

Acknowledgments

We acknowledge the assistance from the scanning electron microscopy analysis.

Conflict of interest

The authors declare that the research was conducted in the absence of any commercial or financial relationships that could be construed as a potential conflict of interest.

Publisher's note

References

Abeyweera, S. C., Rasamani, K. D., and Sun, Y. (2017). Ternary silver halide nanocrystals. *Acc. Chem. Res.* 50, 1754–1761. doi:10.1021/acs.accounts.7b00194

Alvarez-Puebla, R. A., Agarwal, A., Manna, P., Khanal, B. P., Aldeanueva-Potel, P., Carbó-Argibay, E., et al. (2011). Gold nanorods 3D-supercrystals as surface enhanced Raman scattering spectroscopy substrates for the rapid detection of scrambled prions. *Proc. Natl. Acad. Sci.* 108, 8157–8161. doi:10.1073/pnas.1016530108

Apte, A., Bhaskar, P., Das, R., Chaturvedi, S., Poddar, P., and Kulkarni, S. (2015). Self-assembled vertically aligned gold nanorod superlattices for ultra-high sensitive detection of molecules. *Nano Res.* 8, 907–919. doi:10.1007/s12274-014-0572-2

Bigioni, T. P., Lin, X. M., Nguyen, T. T., Corwin, E. I., Witten, T. A., and Jaeger, H. M. (2006). Kinetically driven self-assembly of highly ordered nanoparticle monolayers. *Nat. Mat.* 5, 265–270. doi:10.1038/nmat1611

Bocquet, L., and Lauga, E. (2011). A smooth future? *Nat. Mat.* 10, 334–337. doi:10.1038/nmat2994

Byun, M., Bowden, N. B., and Lin, Z. (2010). Hierarchically organized structures engineered from controlled evaporative self-assembly. *Nano Lett.* 10, 3111–3117. doi:10.1021/nl1018035

Chen, H., Shao, L., Li, Q., and Wang, J. (2013). Gold nanorods and their plasmonic properties. *Chem. Soc. Rev.* 42, 2679–2724. doi:10.1039/c2cs35367a

Cho, E. C., Camargo, P. H., and Xia, Y. (2010). Synthesis and characterization of noble-metal nanostructures containing gold nanorods in the center. *Adv. Mat.* 22, 744–748. doi:10.1002/adma.200903097

Dai, Q., Rettner, C. T., Davis, B., Cheng, J., and Nelson, A. (2011). Topographically directed self-assembly of gold nanoparticles. *J. Mat. Chem.* 42, 16863–16865. doi:10.1039/c1jm11683e

De Angelis, F., Gentile, F., Mecarini, F., Das, G., Moretti, M., Candeloro, P., et al. (2011). Breaking the diffusion limit with super-hydrophobic delivery of molecules to plasmonic nanofocusing SERS structures. *Nat. Photonics* 5, 682–687. doi:10.1038/nphoton.2011.222

Deegan, R. D., Bakajin, O., Dupont, T. F., Huber, G., Nagel, S. R., and Witten, T. A. (1997). Capillary flow as the cause of ring stains from dried liquid drops. *Nature* 389, 827–829. doi:10.1038/39827

Deegan, R. D., Bakajin, O., Dupont, T. F., Huber, G., Nagel, S. R., and Witten, T. A. (2000). Contact line deposits in an evaporating drop. *Phys. Rev. E* 62, 756–765. doi:10.1103/physreve.62.756

Deegan, R. D. (2000). Pattern formation in drying drops. *Phys. Rev. E* 61, 475–485. doi:10.1103/physreve.61.475

Diebold, E. D., Mack, N. H., Doorn, S. K., and Mazur, E. (2009). Femtosecond laser-nanostructured substrates for surface-enhanced Raman scattering. *Langmuir* 25, 1790–1794. doi:10.1021/la803357q

Fan, H., Yang, K., Boye, D. M., Sigmon, T., Malloy, K. J., Xu, H., et al. (2004). Self-assembly of ordered, robust, three-dimensional gold nanocrystal/silica arrays. *Science* 304, 567–571. doi:10.1126/science.1095140

Gaponenko, S. V. (2002). Effects of photon density of states on Raman scattering in mesoscopic structures. *Phys. Rev. B* 65, 140303. doi:10.1103/physrevb.65.140303

Gentile, F., Coluccio, M. L., Zaccaria, R. P., Francardi, M., Cojoc, G., Perozziello, G., et al. (2014). Selective on site separation and detection of molecules in diluted solutions with super-hydrophobic clusters of plasmonic nanoparticles. *Nanoscale* 6, 8208–8225. doi:10.1039/c4nr00796d

Grzelczak, M., Vermant, J., Furst, E. M., and Liz-Marzán, L. M. (2010). Directed self--assembly of nanoparticles. *ACS Nano* 4, 3591–3605. doi:10.1021/nn100869j

Hamon, C., Novikov, S. M., Scarabelli, L., Solís, D. M., Altantzis, T., Bals, S., et al. (2015). Collective plasmonic properties in few-layer gold nanorod supercrystals. *ACS Photonics* 2, 1482–1488. doi:10.1021/acsphotonics.5b00369

Hossain, M. K., Kitahama, Y., Huang, G. G., Han, X., and Ozaki, Y. (2009). Surface-enhanced Raman scattering: Realization of localized surface plasmon resonance using unique substrates and methods. *Anal. Bioanal. Chem.* 394, 1747–1760. doi:10.1007/s00216-009-2762-4

Hu, H., and Larson, R. G. (2006). Marangoni effect reverses coffee-ring depositions. *J. Phys. Chem. B* 110, 7090–7094. doi:10.1021/jp0609232

Huang, L., Mühlenbernd, H., Li, X., Song, X., Bai, B., Wang, Y., et al. (2015). Broadband hybrid holographic multiplexing with geometric metasurfaces. *Adv. Mat.* 27, 6444–6449. doi:10.1002/adma.201502541

Jana, N. R. (2004). Shape effect in nanoparticle self-assembly. *Angew. Chem. Int. Ed.* 43, 1536–1540. doi:10.1002/anie.200352260

Jensen, L., and Schatz, G. C. (2006). Resonance Raman scattering of rhodamine 6G as calculated using time-dependent density functional theory. *J. Phys. Chem. A* 110, 5973–5977. doi:10.1021/jp0610867

Kim, J., Song, X., Ji, F., Luo, B., Ice, N. F., Liu, Q., et al. (2017). Polymorphic assembly from beveled gold triangular nanoprisms. *Nano Lett.* 17, 3270–3275. doi:10.1021/acs.nanolett.7b00958

Ko, H., Singamaneni, S., and Tsukruk, V. V. (2008). Nanostructured surfaces and assemblies as SERS media. *Small* 4, 1576–1599. doi:10.1002/smll.200800337

Kumar, S., Tokunaga, K., Namura, K., Fukuoka, T., and Suzuki, M. (2020). Experimental evidence of a twofold electromagnetic enhancement mechanism of surface-enhanced Raman scattering. *J. Phys. Chem. C* 124, 21215–21222. doi:10.1021/acs.jpcc.0c07930

Larson, R. G. (2014). Transport and deposition patterns in drying sessile droplets. *AIChE J.* 60, 1538–1571. doi:10.1002/aic.14338

Li, P., Li, Y., Zhou, Z. K., Tang, S., Yu, X. F., Xiao, S., et al. (2016). Evaporative self-assembly of gold nanorods into macroscopic 3D plasmonic superlattice arrays. *Adv. Mat.* 28, 2511–2517. doi:10.1002/adma.201505617

Li, R., Bian, K., Wang, Y., Xu, H., Hollingsworth, J. A., Hanrath, T., et al. (2015). An obtuse rhombohedral superlattice assembled by Pt nanocubes. *Nano Lett.* 15, 6254–6260. doi:10.1021/acs.nanolett.5b02879

Lu, C., and Tang, Z. (2016). Advanced inorganic nanoarchitectures from oriented self-assembly. *Adv. Mat.* 28, 1096–1108. doi:10.1002/adma.201502869

Lu, Y., Liu, G. L., and Lee, L. P. (2005). High-density silver nanoparticle film with temperature-controllable interparticle spacing for a tunable surface enhanced Raman scattering substrate. *Nano Lett.* 5, 5–9. doi:10.1021/nl048965u

Luo, B., Smith, J. W., Ou, Z., and Chen, Q. (2017). Quantifying the self-assembly behavior of anisotropic nanoparticles using liquid-phase transmission electron microscopy. *Acc. Chem. Res.* 50, 1125–1133. doi:10.1021/acs.accounts.7b00048

Luo, B., Smith, J. W., Wu, Z., Kim, J., Ou, Z., and Chen, Q. (2017). Polymerization-like co-assembly of silver nanoplates and patchy spheres. *ACS Nano* 11, 7626–7633. doi:10.1021/acsnano.7b02059

Ming, T., Kou, X., Chen, H., Wang, T., Tam, H. L., Cheah, K. W., et al. (2008). Ordered gold nanostructure assemblies formed by droplet evaporation. *Angew. Chem. Int. Ed. Engl.* 47, 9831–9836. doi:10.1002/ange.200803642

Neretina, S., Hughes, R. A., Gilroy, K. D., and Hajfathalian, M. (2016). Noble metal nanostructure synthesis at the liquid–substrate interface: New structures, new insights, and new possibilities. *Acc. Chem. Res.* 49, 2243–2250. doi:10.1021/acs.accounts.6b00393

Peng, B., Li, G., Li, D., Dodson, S., Zhang, Q., Zhang, J., et al. (2013). Vertically aligned gold nanorod monolayer on arbitrary substrates: Self-assembly and femtomolar detection of food contaminants. *ACS Nano* 7, 5993–6000. doi:10.1021/nn401685p

Peng, B., Li, Z., Mutlugun, E., Martínez, P. L. H., Li, D., Zhang, Q., et al. (2014). Quantum dots on vertically aligned gold nanorod monolayer: Plasmon enhanced fluorescence. *Nanoscale* 6, 5592–5598. doi:10.1039/c3nr06341k

Prasad, B. L. V., Sorensen, C. M., and Klabunde, K. J. (2008). Gold nanoparticle superlattices. *Chem. Soc. Rev.* 37, 1871–1883. doi:10.1039/b712175j

Quan, Z., Xu, H., Wang, C., Wen, X., Wang, Y., Zhu, J., et al. (2014). Solvent-mediated self-assembly of nanocube superlattices. *J. Am. Chem. Soc.* 136, 1352–1359. doi:10.1021/ja408250q

Reyssat, M., Yeomans, J. M., and Quéré, D. (2007). Impalement of fakir drops. *Europhys. Lett.* 81, 26006. doi:10.1209/0295-5075/81/26006

Singh, A., Gunning, R. D., Ahmed, S., Barrett, C. A., English, N. J., Garate, J. A., et al. (2012). Controlled semiconductor nanorod assembly from solution: Influence of concentration, charge and solvent nature. *J. Mat. Chem.* 22, 1562–1569. doi:10.1039/c1jm14382d

Sun, Y. (2013). Controlled synthesis of colloidal silver nanoparticles in organic solutions: Empirical rules for nucleation engineering. *Chem. Soc. Rev.* 42, 2497–2511. doi:10.1039/c2cs35289c

Usman, M., Guo, X., Wu, Q., Barman, J., Su, S., Huang, B., et al. (2019). Facile silicone oil-coated hydrophobic surface for surface enhanced Raman spectroscopy of antibiotics. *RSC Adv.* 9, 14109–14115. doi:10.1039/c9ra00817a

Vogel, N., Retsch, M., Fustin, C. A., Del Campo, A., and Jonas, U. (2015). Advances in colloidal assembly: The design of structure and hierarchy in two and three dimensions. *Chem. Rev.* 115, 6265–6311. doi:10.1021/cr400081d

Wang, C., Siu, C., Zhang, J., and Fang, J. (2015). Understanding the forces acting in self-assembly and the implications for constructing three-dimensional (3D) supercrystals. *Nano Res.* 8, 2445–2466. doi:10.1007/s12274-015-0767-1

Wang, T., Zhuang, J., Lynch, J., Chen, O., Wang, Z., Wang, X., et al. (2012). Self-assembled colloidal superparticles from nanorods. *Science* 338, 358–363. doi:10.1126/science.1224221

Wei, W., Wang, Y., Ji, J., Zuo, S., Li, W., Bai, F., et al. (2018). Fabrication of large-area arrays of vertically aligned gold nanorods. *Nano Lett.* 18, 4467–4472. doi:10.1021/acs.nanolett.8b01584

Xia, Y., Yang, P., Sun, Y., Wu, Y., Mayers, B., Gates, B., et al. (2003). One-dimensional nanostructures: Synthesis, characterization, and applications. *Adv. Mat.* 15, 353–389. doi:10.1002/adma.200390087

Xu, H., Xu, Y., Pang, X., He, Y., Jung, J., Xia, H., et al. (2015). A general route to nanocrystal kebabs periodically assembled on stretched flexible polymer shish. *Sci. Adv.* 1, 1500025. doi:10.1126/sciadv.1500025

Ye, X., Millan, J. A., Engel, M., Chen, J., Diroll, B. T., Glotzer, S. C., et al. (2013). Shape alloys of nanorods and nanospheres from self-assembly. *Nano Lett.* 13, 4980–4988. doi:10.1021/nl403149u

Zhang, S. Y., Regulacio, M. D., and Han, M. Y. (2014). Self-assembly of colloidal one-dimensional nanocrystals. *Chem. Soc. Rev.* 43, 2301–2323. doi:10.1039/c3cs60397k

Zhang, Z., and Lin, M. (2014). High-yield preparation of vertically aligned gold nanorod arrays via a controlled evaporation-induced self-assembly method. *J. Mat. Chem. C* 2, 4545–4551. doi:10.1039/c4tc00325j

Zhu, Z., Meng, H., Liu, W., Liu, X., Gong, J., Qiu, X., et al. (2011). Superstructures and SERS properties of gold nanocrystals with different shapes. *Angew. Chem. Int. Ed.* 50, 1593–1596. doi:10.1002/anie.201005493

frontiers | Frontiers in Materials

TYPE Original Research
PUBLISHED 22 March 2023
DOI 10.3389/fmats.2023.1144236

OPEN ACCESS

EDITED BY
Fei Sun,
Taiyuan University of Technology, China

REVIEWED BY
Zhongquan Nie,
Taiyuan University of Technology, China
Chujun Zhao,
Hunan University, China

*CORRESPONDENCE
Yong Yang,
yangy@suda.edu.cn
Junyi Yang,
yjy2010@suda.edu.cn
Yinglin Song,
ylsong@hit.edu.cn

SPECIALTY SECTION
This article was submitted to Metamaterials, a section of the journal Frontiers in Materials

RECEIVED 14 January 2023
ACCEPTED 09 March 2023
PUBLISHED 22 March 2023

CITATION
Shao Z, Yang Y, Yang J, Zhou W, Liu K, Li Z, Fang Y, Wu X and Song Y (2023), Sensitivity optical non-linear measurement based on wide-band phase objects.
Front. Mater. 10:1144236.
doi: 10.3389/fmats.2023.1144236

Sensitivity optical non-linear measurement based on wide-band phase objects

Zhangyang Shao[1], Yong Yang[1]*, Junyi Yang[1]*, Wenfa Zhou[2], Kun Liu[1], Zhongguo Li[3], Yu Fang[4], Xingzhi Wu[4] and Yinglin Song[1,2]*

[1]School of Physical Science and Technology, Soochow University, Suzhou, China, [2]Department of Physics, Harbin Institute of Technology, Harbin, China, [3]School of Electronic and Information Engineering, Changshu Institute of Technology, Suzhou, China, [4]Jiangsu Key Laboratory of Micro and Nano Heat Fluid Flow Technology and Energy Application, School of Physical Science and Technology, Suzhou University of Science and Technology, Suzhou, China

On the basic that the phase object (PO) is the key optical device in the 4f imaging system, a modified high sensitivity optical nonlinear measurement technique with an absorptive homemade phase object (HPO) is reported in order to characterize the value of weak nonlinear refraction material. The absorptive HPO used in this technique is two transparent glass plates on which a liquid film between two pieces of transparent glasses is deposited and added a rotating object at the below HPO to modulate the phase of a PO. The measuring sensitivity can be improved by changing the transmittance of the absorptive HPO. Meanwhile, because the phase retardation of HPO can be continuously adjustable by modulate the rotating object, it makes the sensitivity of measurement at different wavelengths of laser optimal. Results show that the measuring sensitivity is improved 2-4 times compare with the conventional 4f imaging technique. Furthermore, the modified technique can be used to measure the spectrum of nonlinear refraction coefficients of materials at the continuous wavelength. This method further expands the 4f phase coherent imaging measurement technology, not only solves the deficiencies of the conventional phase object, but also improves the accuracy of the measurement. Experiment and theoretical analysis results are presented to validate our technique.

KEYWORDS

non-linear optical, phase object, 4f imaging, non-linear refractive, measure sensitivity, continue wavelength

1 Introduction

In recent years, a large number of non-linear optical (NLO) materials have been investigated for their potential use in photoelectronic devices (Zhang et al., 2022), optical information processing (Wu et al., 2020) and optical communication (SOROKINA et al., 2016). In particular, large attention has been paid to the development of simple and accurate measurement techniques, with emphasis on measurement sensitivity. Highly sensitive measurements play a significant role in characterizing optical non-linearities, especially those of weak NLO materials. The Z-scan technique (Pereira and Correia, 2020) is a popular method to obtain information about third- and higher order non-linearities. The method provides estimate of NLO and is based on the analysis of the distortion of a beam passing through non-linear materials. However, high quality Gaussian beams are not readily available. Hence, Zhao et al. reported that the use of the s-called top-hat (Zhao and Palffy-Muhoray, 1993) beams instead of Gaussian beams in Z-scan

setups improves the measurement sensitivity by a factor of 2.5. However, the technique requires multiple irradiations by strong laser pulses to obtain the complex non-linear NLO of optical materials and involves measurements at focal plane. This may damage the sample, especially for photo-sensitive materials, and suggests the use of single-shot techniques, which would overcome the above difficulties. One powerful technique is based on single-shot 4f coherent imaging system (Cherukulappurath et al., 2004). The method involves a different spatial distribution of beams compared to Z-scan, and allows one to obtains accurate measurements of the intensity when equipped with a charge-coupled device (CCD) camera. The setup is based on the Zernike spatial filtering principle to transform the phase changes caused by non-linear refraction into light intensity changes in the plane. Other advantages of the method include the simplicity of the alignment, and the high measurement sensitivity. Furthermore, as it happens for Z-scan experiments, sensitivity may be improved using top-hat beams instead of Gaussian beams (Cherukulappurath et al., 2004). Boudebs et al. reported a 4f non-linear-imaging technique with improved sensitivity and involving a phase object (NIT-PO) (Boudebs and Cherukulappurath, 2004) to analyze the sign of non-linear index. Later on, the technique has been modified with considerable effort, see e.g., Yang et al. (Yang et al., 2017) about Z-scan technique with absorptive PO. The sensitivity of the technique can be improved by the changing absorption index of PO which, however, cannot be changed arbitrarily. In addition, an important limitation of 4f NIT-PO techniques employed so far, is the impossibility to use the same PO with a continuous spectrum, as the phase retardation of PO cannot be changed arbitrarily. Indeed, it is significant for the 4f imaging technique to modulate phase and there are piezoelectric ceramic and phase modulators to this aim. However, those devices are expensive and their use complex. Therefore, an alternative simple method with high precision would be exceedingly welcome.

In this paper, the use with a homemade phase object (HPO) added to the 4f imaging technique to and put forward a high sensitivity measurement technique. The materials of the HPO are readily available and the manufacturing is simple. Additionally, our HPO may be used with pulses with a continuous spectrum. The non-linearity of CS_2 and absolute ethanol are considered in this new technique in order to assess its sensitivity and verify the enhancement compared to traditional 4f imaging techniques. Our results confirm that the use of a wideband (The phase object is suitable for optical non-linear measurement at multiple wavelengths) HPO improves the sensitivity of 4f imaging systems and may be used with beams characterized by a continuous spectrum.

2 Theoretical analysis and model

Our HPO is composed of two round pieces of transparent glass with a liquid film in between. The liquid film required by the homemade phase object (HPO) in the technique can be any pure absorptive or transparent liquid. The black ink is used to be a liquid film in our method. The radius is L_p, and the HPO is fixed on a rotary table (see Figure 1). The working principle is that a micron space gap may be formed between the two pieces of glass and that changing the thickness of the HPO is possible by controlling the angle of the rotary table (Figure 1C). The technique consists of lenses L_3 and L_4 and is schematically shown Figure 2. The HPO is placed on the object plane of the 4f imaging system. After passing through HPO, the incident beam of light is divided into two beams of light by a beam splitter (BS). One beam is detected by D_1 for the energy of the incident light is monitored, whereas the other beam is focused on the non-linear medium through lens L_3.

In order to analyze the scheme, let us start from a traditional 4f imaging system (see Ref (Cherukulappurath et al., 2004; Boudebs and Cherukulappurath, 2004; Yang et al., 2017; Fedus and Boudebs, 2013). for more details) and assume that we use a top-hat beam and that the HPO is placed on the object plane. Further, we assume for simplicity that a non-linear medium is placed on the focal plane. We refer to Ref (Fedus and Boudebs, 2013). for situations where the non-linear medium is far away from the focus. Finally, we assume that Fourier optics can fully describe the 4f imaging technique. The HPO and the transparent glasses are illuminated at normal incidence by a linearly polarized monochromatic plane wave $E(x, y, t) = E_0(x, y, t)\exp[-\mathrm{j}(\mathrm{wt} - \mathrm{kz})] + \mathrm{c.c.}$, where k is the wave vector, w is angular frequency, and $E_0(x, y, t)$ is amplitude of the electric field containing the temporal envelope of the laser pulse. We use the slowly varying envelope approximation (SVEA) (Bloembergen, 1996; Sutherland, 2003) to investigate the propagation of the electric field in the non-linear sample. Moreover, since we only analyze the intensity of the image, the time term may be omitted. We may also ignore any thermo-optical effect since we are dealing with nanosecond pulses and a low repetition rate (10Hz) (Boudebs and Cherukulappurath, 2004).

The two parts of the HPO, H_1 and H_2, are shown in Figure 1B. The central region H_1 has radius L_p and amplitude transmittance T_{PO} $(0 < T_{PO} \leq 1)$. It induces a uniform shift ϕ and is characterized by a transmittance $t_p = T_{PO}\exp[\mathrm{i} \times \mathrm{cir}(\mathrm{r} - \mathrm{L}_p) \times \phi]$, as a function of the radial coordinate, where $\mathrm{cir}(x) = 1$ if $x < 0$ and $\mathrm{cir}(x) = 0$ otherwise. The transmittance of the annular region H_2 can be expressed as $t_a = cir(\mathrm{r} - \mathrm{R}_a) - \mathrm{cir}(\mathrm{r} - \mathrm{L}_p)$. If we denote the total transmittance of the HPO by $t_{PO}(x, y)$, the electric field on the external surface can be written as $O(x, y) = E(x, y)t_{PO}(x, y)$, whereas the field amplitude on the front surface of the non-linear medium (on the focal plane of L_3) is spatial Fourier transform of the $O(x, y)$:

$$S(u, v) = \frac{1}{\lambda f}\iint o(x, y)\exp[-2\pi j(ux + vy)]dxdy, \tag{1}$$

where f is the focal length of L_3, λ is the wavelength of the exciting wave, $u = \frac{x}{\lambda f}$ and $v = \frac{y}{\lambda f}$ are the spatial frequencies on the focal plane. Taking into account the three main features of the non-linear sample, i.e., the linear absorption a (m^{-1}), the non-linear absorption $ß$ (m/W) and the non-linear index n_2 (m^2/W), the phase shift imposed to the beam by the non-linear sample can be written as

$$\varphi_{NL}(u, v) = \frac{kn_2}{\beta}\ln\left[1 + \beta L_{eff} I(u, v)\right], \tag{2}$$

where $k = 2\pi/\lambda$ is the wave vector, $L_{eff} = \frac{[1-\exp(-\alpha L)]}{\alpha}$ is the effective length of a non-linear medium, L is the actual length of a non-linear medium and $I(u, v) \propto |S(u, v)|^2$ is the intensity of laser beam exciting a non-linear medium. After modulation through the

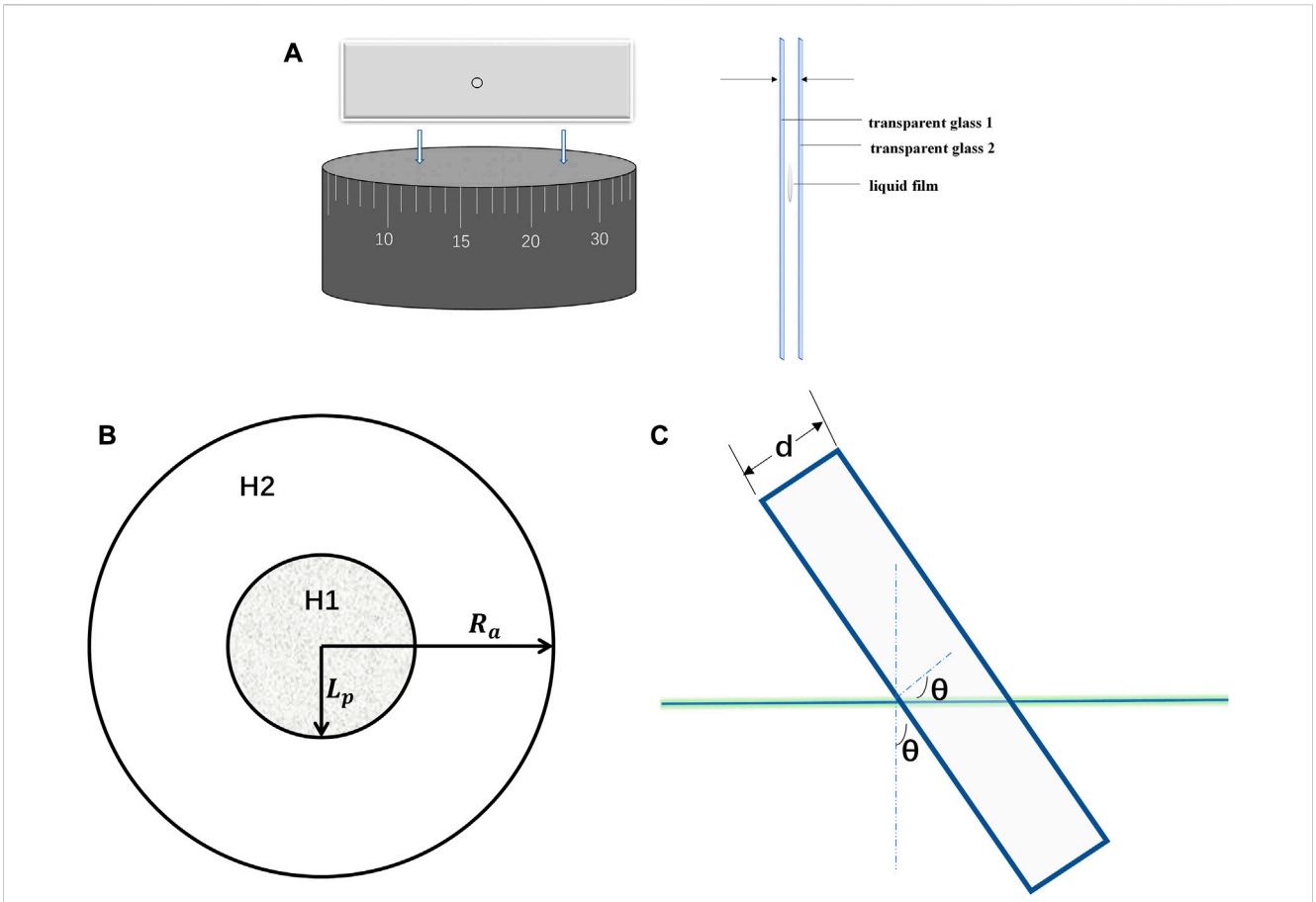

FIGURE 1
(A,B) Schematic of the HPO used in the 4f imaging system. **(C)** Schematic of the HPO changing the angle of the rotating object.

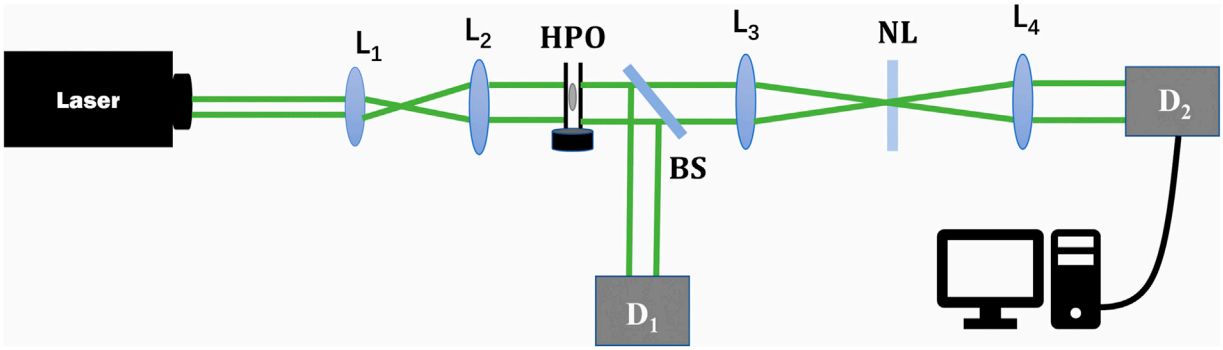

FIGURE 2
Schematic of 4f imaging system with HPO. L_1-L_4, lenses; BS, beam splitter; D_1 is used to detect the reference light, D_2 is used to detect the linear and non-linear images.

sample, the complex electric field at the output surface can be defined as

$$S_L(u,v) = S(u,v)\frac{e^{-\alpha L/2}}{\left[1+\beta L_{eff} I(u,v)\right]^{1/2}} e^{j\varphi_{NL}(u,v)}, \quad (3)$$

where $T(u,v)$ is the complex amplitude response due to non-linearity, i.e.,

$$T(u,v) = \frac{S_L(u,v)}{S(u,v)} = \frac{e^{-\alpha L/2}}{\left[1+\beta L_{eff} I(u,v)\right]^{1/2}} e^{j\varphi_{NL}(u,v)}, \quad (4)$$

where, if the sample is a Kerr medium, a and β are both negligible, and Eqs 2, 3 reduce to:

$$\varphi_{NL}(u,v) = kn_2 LI(u,v), \tag{5}$$

$$S_L(u,v) = S(u,v)e^{j\varphi_{NL}(u,v)}, \tag{6}$$

The technique is described with more details in the following two Subsections.

2.1 Improve sensitivity of 4f imaging system with the absorptive HPO

The non-linear sample in our setup may be regarded as a low-frequency filter. The portion of the incident light passing through the H_2 is spread less than the portion passing through H_1 because R_a is much larger L_P (Shui et al., 2010). Hence, the modulation induced by H_1 may be ignored and we only consider the non-linear modulation induced by H_2. The on-axis field intensity for H_1 is then considered. The complex field amplitude at the output plane of 4f imaging system can be expressed as:

$$E = E_1 + \Delta E_2, \tag{7}$$

The electric field amplitudes coming from the regions H_1 and H_2 of HPO can be written as E_1 and E_2 respectively. The light coming from H_1 is considered a uniform background distribution (regarded as a direct light) because the non-linear modulation is negligible, whereas the light from H_2 is modulated by the non-linear medium at the focal plane and produce a small perturbation of the incident wave (as diffracted light). The second term (ΔE_2) in Eq. 7 results from the diffracted light.

The interference induced by the diffracted light is insensitive to phase changes (φ_{NL}) when $\phi = 0$ and $\varphi_{NL} \ll 1$ (Boudebs and Cherukulappurath, 2004; Yang et al., 2017). However, if $\phi = \pi/2$, the intensity at the output of 4f imaging system is given by

$$I'(u,v) = \frac{1}{n}{E_1}^2 + {\Delta E_2}^2 + 2\frac{1}{\sqrt{n}}E_1\Delta E_2\cos(\pi/2 + \varphi_{NL}), \tag{8}$$

The first term ($\frac{1}{n}{E_1}^2$) in Eq. 8 is the intensity in the linear region on the axis. The transmittance T_{nor} is the normalized peak value of T_{NL}/T_L. The variable ΔT can be defined as an appropriate parameter to estimate the refractive coefficient (n_2) of non-linear samples.

The difference ΔT can be written as:

$$\Delta T = \frac{2\left(\frac{1}{\sqrt{n}}E_1\right)\Delta E_2\cos(\pi/2 + \varphi_{NL}) + {\Delta E_2}^2}{\left(\frac{1}{\sqrt{n}}E_1\right)^2} = -\sqrt{n}\,\frac{2E_1\Delta E_2\sin\varphi_{NL}}{{E_1}^2}, \tag{9}$$

where $\frac{2E_1\Delta E_2}{{E_1}^2}$ is the sensitivity of the system when $n = 1$. If the incident field in the HPO region is reduced by a factor of $\frac{1}{\sqrt{n}}$ ($n > 1$), the sensitivity increased by $\sqrt{n}$ times.

In our measurements, the signal received by CCD on the exit plane of the 4f system has been processed using the above analysis (Eqs. 1–9). The extension of the PO region increases if the non-linear sample has a positive phase shift, whereas it decreases otherwise. Here a non-linear sample producing a positive shift has been simulated. In Figure 3A we show the difference transmittance (ΔT) for various transmittance (T_{PO}). Figure 3B shows the cross-section views of the normalized linear image and non-linear image amplitudes. The black curve denotes the linear image, the green one denotes the non-linear image as measured by conventional transparent PO ($n = 1$), and the others denote the non-linear image measured by HPO ($n < 1$).

The simulation results show that when the electric field amplitude (transmittance) in the PO region is less than 50% of the original, the sensitivity is increased by 2–4 times. For example, for $\sqrt{n} = 10$ and a HPO with $T_{PO} = 0.1$, the sensitivity 4f imaging system is improved by a factor $\sqrt{10}$ compared to that of a conventional transparent PO.

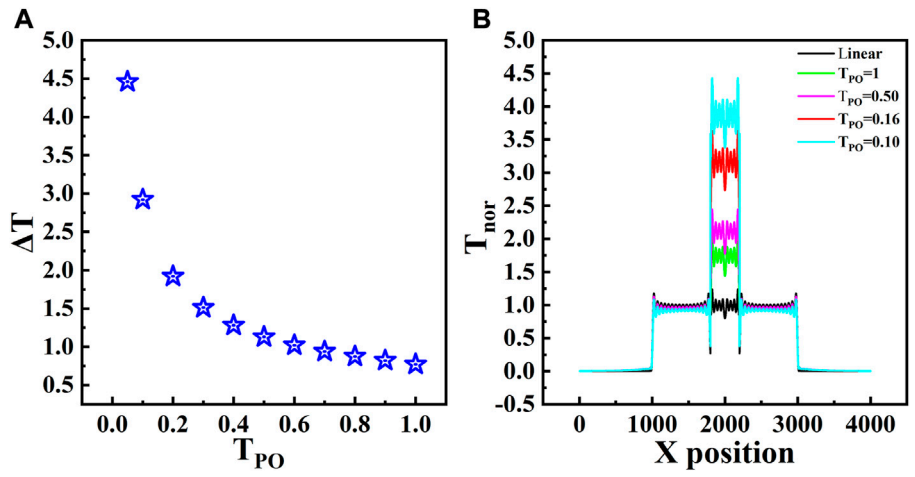

FIGURE 3
(A) Normalized transmittance ΔT as a function of the transmittance of the HPO. **(B)** The non-linear imaging curve for various transmittance values.

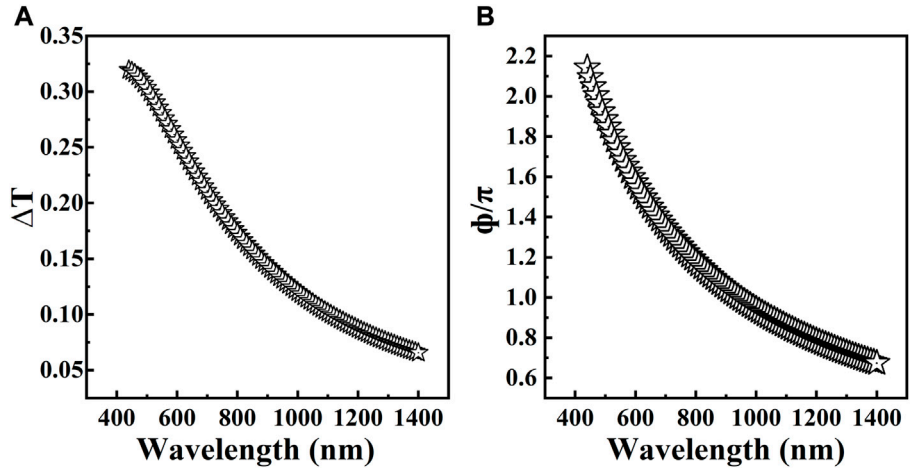

FIGURE 4
(A) Transmittance changes (ΔT) as a function of the wavelength (λ). **(B)** The phase shift in the object as a function of the wavelength (λ).

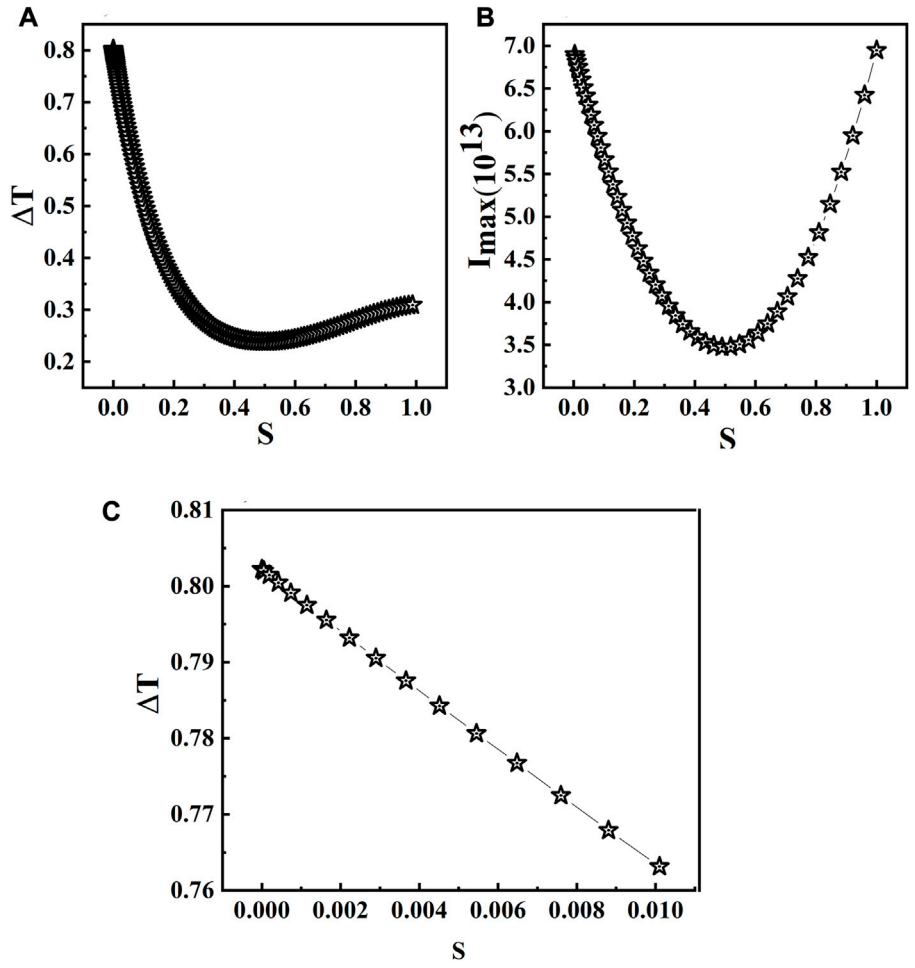

FIGURE 5
(A) Transmittance changes (ΔT) as a function of the area ($S = (L_p/R_a)^2$). **(B)** The intensity I_{max} (given in GW/cm^2 inside) of phase object as a function of the area ($S = (L_p/R_a)^2$). **(C)** Dependence of ΔT on the HPO area when $S \leq 0.01$.

2.2 The use of the HPO in 4f imaging system with light with a continuous spectrum

In Figures 4A, B, we show theoretical results and simulations for the case of the phase shift ϕ of the PO set to $\phi = 2\pi d(n' - 1)/\lambda$. Numerical results show that a traditional PO cannot be used to measure the non-linear index with a continuous spectrum. In order to make the phase object conform to the high sensitivity measurement at different wavelengths, the optical path difference between the two beams needs to be changed with high precision, and the required accuracy is up to nm. There are piezoelectric ceramic and phase modulator to match that accuracy, but the devices are expensive and the process is complex. Therefore, a more simple and convenient method ensuring high precision is needed. We consider the scheme in Figure 1A, where a rotating object is added below the HPO in order to modulate the phase ϕ for use with light with a continuous spectrum, and measure the thickness of the HPO. As a function of the angle (θ) of the rotating object we have

$$\phi = 2\pi \mathrm{d}(n' - 1)/\lambda \cos\theta, \tag{10}$$

And the thickness of the HPO can be expressed as:

$$\mathrm{d} = [(\phi_1 - \phi_2)\lambda] \Big/ \left[2\pi(n' - 1)\left(\frac{1}{\cos\theta_1} - \frac{1}{\cos\theta_2}\right)\right], \tag{11}$$

Where n' is the refractive index of the used slide, θ is the angle of the rotating object and $(\phi_1 - \phi_2)$ is phase aberration accumulated in a cycle. However, the area of the HPO changes with the angle of rotation and this should be considered to assess the sensitivity of this technique. The dependence of the sensitivity on the area has been investigated numerically and results are shown in Figure 5A: the sensitivity of system is higher when the area of a HPO is smaller ($S = (L_p/R_a)^2$) and the sensitivity is minimum for $S \approx 0.5$. In Figure 5B we show how the area influences the light intensity from the HPO. The behaviour is similar to that of FIG, i.e., the light intensity is higher when S is smaller and is minimum when $S \approx 0.5$. Although the light intensity increases when $S > 0.5$, the part of the incident light passing through H_2 (diffracted light) decreases. Therefore, the quantity ΔT increases slowly for $S > 0.5$. We use a HPO L_p equal to 0.1 (i.e., $S \approx 0.01$). Figure 5C shows that the area has little effect on ΔT when the angle is changed ($S < 0.01$).

The sensitivity of 4f phase coherent imaging technology is determined by the phase retardation of PO, and the phase retardation of PO, given a certain thickness, is different at different wavelengths. This means that the sensitivity of the system may be optimized only for a specific wavelength given the

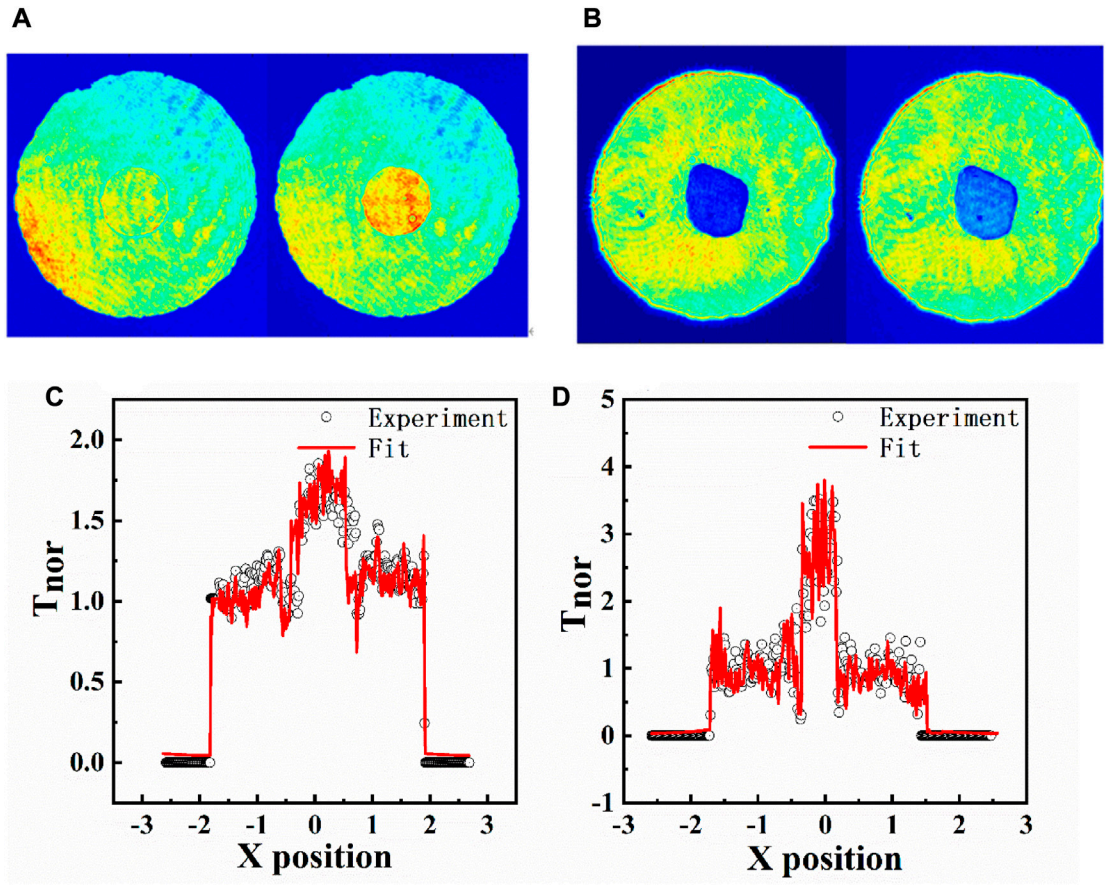

FIGURE 6
(A,B) Linear and non-linear images for CS_2 as acquired by our experimental 4f imaging system with a conventional transparent PO and absorptive ($T_{PO} \approx 16\%$) HPOs. **(C,D)** Profiles of images **(A,B)** by processing T_{NL}/T_L; the red solid lines are theoretical values.

thickness of PO. In order to ensure the optimal measurement sensitivity of the system at different wavelengths, it is necessary to continuously change the optical path difference of PO. This also means that conventional transparent PO cannot be used to perform measurements with a continuous spectrum. For example, a conventional transparent PO using light at 400 nm cannot be used to perform measurements at 905 nm. The simulation results also show that the sensitivity is higher when S is smaller ($S < 0.5$) (Boudebs and Cherukulappurath, 2004). This is due to the fact that the light intensity depends on the area, whereas the area of HPO has little effect for the ΔT when $S < 0.01$.

3 Experimental results and discussion

In order to order to assess the reliability and precision of our technique we have implemented it to measure the third-order non-linear refraction index of Carbon disulfide (CS_2) and absolute ethanol using an absorptive HPO. Among them, CS_2 is a standard sample to verify the validity of characterization techniques. The solvent CS_2 and the absolute ethanol are loaded into a 2 mm glass sell. The excitation source is a Q-switched and mode-locked Nd: YAG laser which provides 21ps output laser pulses, with a wavelength of 532 nm and a repetition rate of 10-Hz. As a benchmark, the solvent is also measured with a HPO and conventional transparent PO at 905 nm (100 mW) with a continuous laser.

Three kinds of imaging data are needed in experiment. i) No sample: The acquisition is reference light. ii) Linear image: The image acquisition is obtained with low intensity by placing high-density neutral filters before the non-linear samples. iii) Non-linear image: The image is acquired with high intensity by placing the same high-density neutral filters after the non-linear samples. The linear and non-linear images are used to calculate the refraction index n_2 using Eqs 1–9. The non-linear signal processing leads to ΔT using the normalized peak value of T_{NL}/T_L.

The absorptive HPO used in our experiments consists in two transparent glass plates with a liquid film in between. The absorption index can be changed by changing the thickness of the liquid film. The phase ϕ can be changed by controlling the rotation, and the HPO can be rotated to produce a $\pi/2$ phase at 532 nm. Figures 6A, B show the results of the non-linear refraction of CS_2 with a conventional PO and an absorptive HPO at an energy of about 1.2 μJ. The transmittance of the HPO is approximately 16%. The solid lines in Figures 6C, D are the fitting curves with $\beta = 0$; $n_2 = 3.2 \times 10^{-18} m^2/W$ (Boudebs and

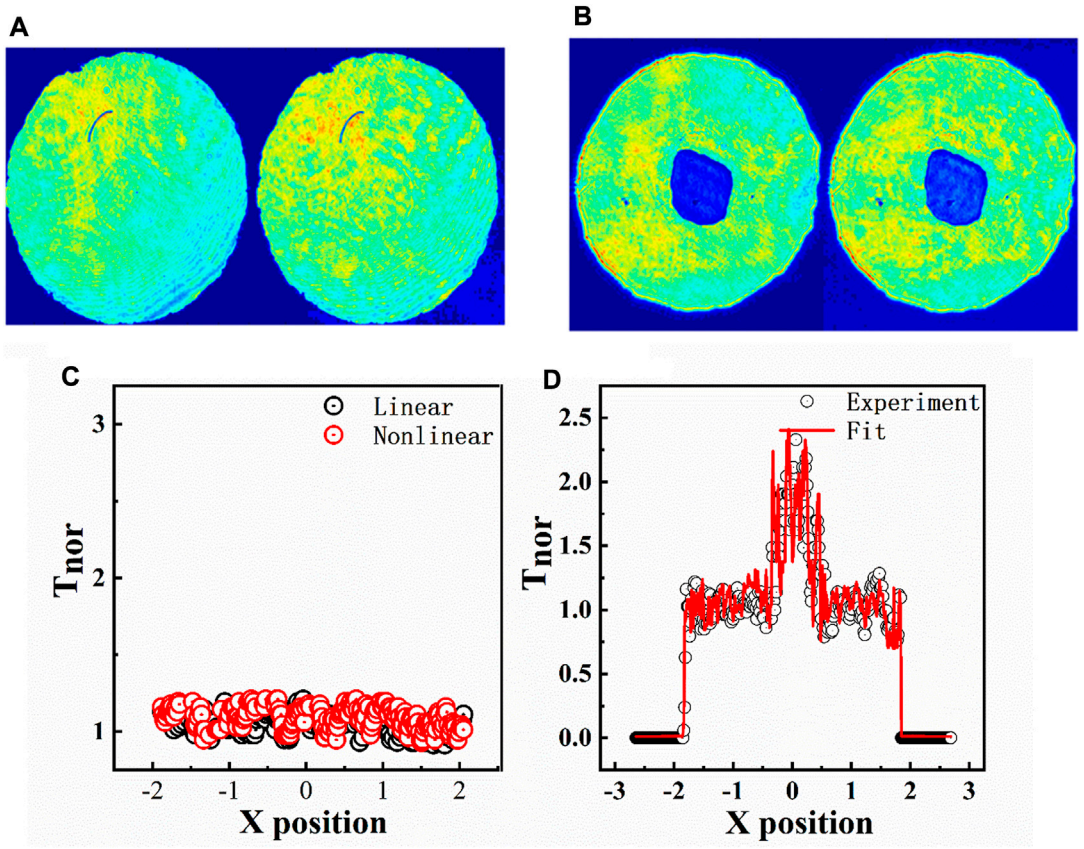

FIGURE 7
(A,B) Linear and non-linear images for ethanol as acquired by our experimental 4f imaging system with a conventional transparent PO and an absorptive ($T_{PO} \approx 16\%$) HPO. **(C,D)** Profiles of images **(A,B)** by processing T_{NL}/T_L; the red solid lines are theoretical values.

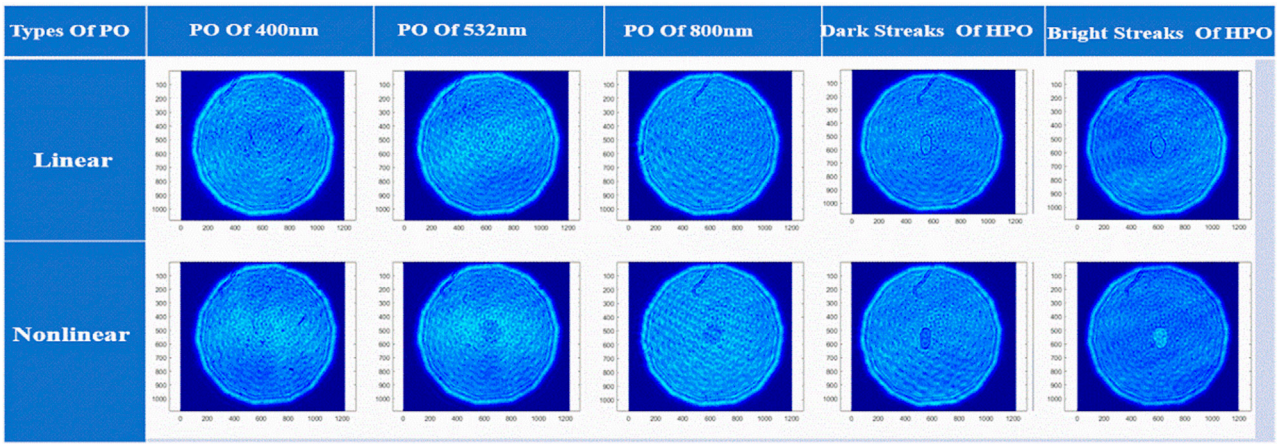

FIGURE 8
Experimental 4f imaging with conventional transparent POs (a conventional transparent PO of 400 nm, a conventional transparent PO of 532 nm and a conventional transparent PO of 800 nm) and linear and non-linear images acquired with a transparent HPO.

Cherukulappurath, 2004; Ganeev et al., 2004). Figures 7A, B show the estimated non-linear refraction of absolute ethanol obtained with a conventional PO and an absorptive HPO at an energy of about 4.5 μJ. The solid line in Figure 7D is the fitting curve with $\beta = 0$; $n_2 = 4.55 \times 10^{-19} m^2/\mathrm{W}$ (Ho and Alfano, 1979; Yi et al., 2020). As it can be seen from Figure 6, the normalized transmittance ΔT measured using this technique with HPO is about 2.5 times higher than that measured using the traditional technique. It shows that the use of absorptive HPO can improve the measure sensitivity in the 4f imaging system. And the experimental results for ΔT are consistent with the theoretical one from Eq. 9. Meanwhile, the non-linear refraction signal of absolute ethanol is not observed by using the conventional PO, but can be clearly observed by using absorptive HPO. It is further explained that the proposed method can effectively improve the sensitivity of the 4f imaging system. Therefore, our technique has a better advantage for some optical materials which have weak non-linear optical coefficients.

Figure 8 is instead the results obtained with conventional transparent POs (a conventional transparent PO of 400 nm, a conventional transparent PO of 532 nm and a conventional transparent PO of 800 nm) and a transparent HPO to measure the solvent using a 905 nm continuous laser at the power of 1 mW. The results shows that the conventional transparent PO cannot be used with a continuous spectrum. The results also shows that the HPO can be modulated to produce a complete cycle and overcome the disadvantage of the conventional transparent PO. Overall, these results confirm the validity of our approach. Furthermore, from our experimental results, the thickness of the HPO is calculated to be approximately 0.634 μm from the Eq. 11. Therefore, if other experimental factors are not considered, it can theoretically be used in a range of about 304 nm–1752 nm by the Eq. 10.

4 Conclusion

In summary, a simple and high-sensitive 4f imaging technique has been suggested and demonstrated to measure the non-linear refractive coefficient. In particular, we have illustrated numerically that the use of the low transmittance HPO lead to a higher sensitivity compared to a conventional transparent PO in a 4f imaging system. The sensitivity improves by a factor of $(1/T_{PO})^{1/2}$ when $0 < T_{PO} < 1$. In addition, by modulating the phase using a rotating object placed below HPO we made it possible the use of light with a continuous spectrum. In order to verify our technique, the non-linear coefficient of CS_2 (a well-known non-linear material) and that of absolute ethanol have been investigated. The value and sign obtained are agreement with the results obtained by other methods. Furthermore, we have used a HPO in 4f imaging system with continuous spectrum, a technique not available with conventional transparent PO. Our technique retains the advantages of the traditional 4f imaging system (optical alignment is easy, single-shot and no displacement of samples, et.,) and show higher sensitivity in measuring non-linearity. Furthermore, it can be used for non-linearity measurement with 4f imaging systems and continuous spectrum sources.

Data availability statement

The original contributions presented in the study are included in the article/supplementary material, further inquiries can be directed to the corresponding authors.

Author contributions

ZS: Investigation, writing—Original draft, writing—Review and editing. YY and JY: Provide ideas. And all authors take part in formal analysis.

Funding

This work was supported by National Natural Science Foundation of China (Nos. 11804244, 11704273), Natural Science Foundation of Jiangsu Province (Nos. BK20180965, BK20170375), the National Safety Academic Fund (Grant No. U1630103).

Acknowledgments

We gratefully acknowledge National Natural Science Foundation of China (11704273, 51607119), National Safety Academic Fund (U1630103).

Conflict of interest

The authors declare that the research was conducted in the absence of any commercial or financial relationships that could be construed as a potential conflict of interest.

Publisher's note

All claims expressed in this article are solely those of the authors and do not necessarily represent those of their affiliated organizations, or those of the publisher, the editors and the reviewers. Any product that may be evaluated in this article, or claim that may be made by its manufacturer, is not guaranteed or endorsed by the publisher.

References

Bloembergen, N. (1996). *Nonlinear optics*. Singapore: World Scientific.

Boudebs, G., and Cherukulappurath, S. (2004). Nonlinear optical measurements using a4fcoherent imaging system with phase objects. *Phys. Rev. A* 69 (5), 053813. doi:10.1103/physreva.69.053813

Cherukulappurath, S., Boudebs, G., and Monteil, A. (2004). 4*f* coherent imager system and its application to nonlinear optical measurements. *J. Opt. Soc. Am. B* 21 (2), 273–279. doi:10.1364/josab.21.000273

Fedus, K., and Boudebs, G. (2013). Experimental techniques using 4f coherent imaging system for measuring nonlinear refraction. *Opt. Commun.* 292, 140–148. doi:10.1016/j.optcom.2012.11.074

Ganeev, R. A., Ryasnyansky, A. I., Baba, M., Suzuki, M., Ishizawa, N., Turu, M., et al. (2004). Nonlinear refraction in CS2. *Appl. Phys. B* 78, 433–438. doi:10.1007/s00340-003-1389-y

Ho, P. P., and Alfano, R. R. (1979). Optical Kerr effect in liquids. *Phys. Rev. A* 20 (5), 2170–2187. doi:10.1103/physreva.20.2170

Pereira, M. K., and Correia, R. R. B. (2020). Z-scan and eclipsing Z-scan analytical expressions for third-order optical nonlinearities. *J. Opt. Soc. Am. B* 37 (2), 478–487. doi:10.1364/josab.376541

Shui, M., Luo, X., Zhang, X., Jin, X., Li, C., Yang, J., et al. (2010). Phase filtering in nonlinear-imaging technique with a phase object. *J. Opt. Soc. Am. A* 27 (11), 2514–2523. doi:10.1364/josaa.27.002514

Sorokina, M., Sygletos, S., and Turitsyn, S. (2016). Sparse identification for nonlinear optical communication systems: SINO method. *Opt. Express* 24 (26), 30433–33044. doi:10.1364/oe.24.030433

Sutherland, R. L. (2003). *Hand book of nonlinear optics*. Boca Raton: CRC Press.

Wu, J., Li, Z., Luo, J., and Jen, A. K. Y. (2020). High-performance organic second- and third-order nonlinear optical materials for ultrafast information processing. *J. Mater. Chem. C* 8, 15009–15026. doi:10.1039/d0tc03224g

Yang, Y., Yang, J. Y., Li, Z. G., Wu, X. Z., and Song, Y. L. (2017). Sensitive measurement of optical nonlinearity using an absorptive phase object. *Appl. Phys. B* 123 (9), 248. doi:10.1007/s00340-017-6825-5

Yi, J., Miao, L., Li, J., Yi, Q., Huang, J., and Zhao, C. (2020). Self-defocusing of light in ethanol around 1550 nm. *IEEE Photonics J.* 12 (1), 1–8. doi:10.1109/jphot.2019.2960392

Zhang, F., Mi, Z., Hao, W., Chen, H., Zhang, Y., Zhao, J., et al. (2022). Tunable engineering of photo- and electro-induced carrier dynamics in perovskite photoelectronic devices. *Sci. China Mater.* 65 (4), 855–875. doi:10.1007/s40843-021-1906-5

Zhao, W., and Palffy-Muhoray, P. (1993). Z-scan technique using top-hat beams. *Appl. Phys. Lett.* 63 (12), 1613–1615. doi:10.1063/1.110712

frontiers | Frontiers in Materials

TYPE Original Research
PUBLISHED 05 June 2023
DOI 10.3389/fmats.2023.1207156

OPEN ACCESS

EDITED BY
Yadong Xu,
Soochow University, China

REVIEWED BY
Zhengyong Song,
Xiamen University, China
Ke Chen,
Nanjing University, China
Fei Sun,
Taiyuan University of Technology, China

*CORRESPONDENCE
Yuancheng Fan,
phyfan@nwpu.edu.cn
Fuli Zhang,
fuli.zhang@nwpu.edu.cn

RECEIVED 17 April 2023
ACCEPTED 24 May 2023
PUBLISHED 05 June 2023

CITATION
Cai W, Xuan L, Fan Y, Yang R, Zhang W, Zhang Q, Chen S, Ye Z, Zhang Y, Fu Q and Zhang F (2023), Coupled magnetic Mie resonances induced extraordinary optical transmission and its non-linear tunability. *Front. Mater.* 10:1207156. doi: 10.3389/fmats.2023.1207156

Coupled magnetic Mie resonances induced extraordinary optical transmission and its non-linear tunability

Weiqi Cai[1,2], Lixin Xuan[2], Yuancheng Fan[1]*, Ruisheng Yang[1], Wenwu Zhang[2], Qing Zhang[2], Songnan Chen[1], Zhehao Ye[1], Yujing Zhang[1], Quanhong Fu[1] and Fuli Zhang[1]*

[1]Key Laboratory of Light Field Manipulation and Information Acquisition, Ministry of Industry and Information Technology and School of Physical Science and Technology, Northwestern Polytechnical University, Xi'an, China, [2]Aviation Key Lab of Science and Technology on High Performance Electromagnetic Windows, AVIC Research Institute for Special Structures of Aeronautical Composites, Tsinan, China

Dielectric metamaterials with low ohmic losses and resonating in the local magnetic mode are preferable for enhancing material non-linearity. Here, we propose and experimentally demonstrate broadband extraordinary electromagnetic transmission (EET) behavior, which is induced by the coupling of magnetic modes of two ceramic cuboids. It is shown that extraordinary electromagnetic transmission behavior through a perforated metal sheet with a subwavelength aperture can be achieved by exciting the first-order magnetic mode Mie resonant coupling of these cuboids. Our findings indicate that the transmission bandwidth and amplitude are dependent on the strength of coupling between the two ceramic cuboids. Additionally, we utilized non-linear effects within the dielectric cuboids to achieve tunable extraordinary electromagnetic transmission behavior. Our results are promising for developing non-linearly tunable microwave devices such as filters and modulators of their strong light-matter interactions.

KEYWORDS

extraordinary optical transmission, non-linear, tunable metamaterials, Mie resonance, dielectric metamaterials

1 Introduction

Metamaterials, and their two-dimensional counterpart metasurfaces, are artificial media made up of subwavelength-sized resonant elements with tremendous potential for modulating wave beams (Pendry, 2000; Shelby et al., 2001; Smith et al., 2004; Chen et al., 2010; Fan et al., 2011; Liu et al., 2011; Soukoulis and Wegener, 2011; Chen et al., 2012; Jahani and Jacob, 2016; Yang et al., 2021a; Liu et al., 2021; He and Song, 2022; Yang et al., 2023a; Yang et al., 2023b; Li and Song, 2023; Nie et al., 2023). These micro and nano elements can be designed to have optical properties that do not exist in nature, such as negative refraction (Smith et al., 2004), electromagnetic clock (Schurig et al., 2006), electromagnetically induced transparency (Yang et al., 2021a), and metalens (Chen et al., 2012). Recently, researchers have combined metamaterials with the structure of single apertures to enhance transmission efficiency for light. This reduces the size of the structure while increasing its transmission efficiency (Guo and Zhou, 2014; Guo et al., 2016).

Similar research has been conducted in Terahertz frequencies (Navarro-Cía et al., 2018; Freer et al., 2020) and optical bands (Jeong et al., 2015; Qin et al., 2018). Extraordinary optical transmission (EOT) has attracted significant attention owing to its unique physical mechanism and potential applications in photodetectors and non-linear optics (Ebbesen et al., 1998; Martín-Moreno et al., 2001; García de Abajo, 2007; Genet and Ebbesen, 2007; Aydin et al., 2009; Chen et al., 2013). Dielectric metamaterials can achieve higher transmission efficiency than conventional EOT apertures (Hajian et al., 2017a). In the early stages, it was mainly based on periodic array structures to enhance the transmission efficiency of light through subwavelength diaphragms. In 2009, Aydin et al. (2009) achieved strongly localized electromagnetic field coupling and transmission enhancement by applying a single SRR at the near field of the aperture, which initiated the research on extraordinary optical transparency in terahertz band (Chen et al., 2013). Later, this idea was also employed in microwaves to realize high-efficiency extraordinary electromagnetic transmission (EET).

Epsilon-near-zero metamaterials can also achieve efficient EOT/EET behavior (Kurs et al., 2007; Hajian et al., 2017b). However, metamaterials operating in a single resonant mode can only achieve EOT/EET behavior near their resonant frequency. Obtaining EOT/EET behavior within a certain bandwidth range requires introducing more resonant modes and coupling. Andre Kurs et al. proposed the use of strongly coupled self-resonant coils and experimentally demonstrated effective non-radiative power transmission over a distance of up to 8 times the coil radius in Science in 2007 (Zhang et al., 2012; Jonah and Georgakopoulos, 2013). Researchers also found that the first-order Mie resonance of two magnetic mode resonance units will split into two modes: in-phase resonance and reverse resonance (Hao et al., 2008). However, research on broadband EET/EOT is relatively sparse, which is due to the sharp resonance of meta-atoms.

In this work, we have demonstrated the EET behavior of a perforated metal sheet with subwavelength apertures by utilizing near-field coupling of the first-order magnetic mode Mie resonance between two identical ceramic cuboids. The bandwidth of EET was extended by combining the splitting of resonant modes and coupling behavior between ceramic cuboids and metal sheets. Dielectric materials were chosen as resonators to enhance transmission efficiency. By introducing perforated metal sheets to suppress coupling between ceramic cuboids, we increased transmittance in the original transmission dips, achieving broadband transmission instead of double-frequency point transmission. Modulation of transmission amplitude and the frequency band is achieved by varying spacing between two ceramic cuboids to change coupling strength and mode resonance. Further modulation is possible based on non-linear effects in dielectric material for tunable EET frequency. These tunable non-linear EET metamaterials can play an important role in designing new sensor devices and filter devices due to their wider operating frequency range, greater functionality, and lower costs (Hao et al., 2008; Ju et al., 2011; He et al., 2019; Bao and Cui, 2020; Yang et al., 2021b; Zhu et al., 2022).

2 Results and discussion

Figure 1A shows the schematic diagram of double ceramic cuboids placed on a Teflon substrate. The Teflon substrate is with a dimension of 22.86 × 10.16 × 1 mm^3, and the two ceramic cuboids are made of low-loss material calcium titanate ($CaTiO_3$) doped with 1wt% ZrO_2, having a relative permittivity of approximately 121 (Zhao et al., 2008; Zhao et al., 2009; Luo et al., 2015). The $CaTiO_3$ ceramic was synthesized through the conventional solid-state method. All the raw powders of $CaTiO_3$ and ZrO_2 were mixed by ball milling in deionized water for 30 h. After dried, the powders were pestled in agate mortar and sieved through 50 or 60-mesh sieve. Then, the PVA solution (polyvinyl alcohol, 5 wt %) was added to the sieved powders as organic binder. The cylinders were formed by uniaxial compression at the pressure of 4 MPa with a customized mould. Finally, the cylinders were sintered at the temperature ranging from 1,250°C to 1,400°C (Luo et al., 2015). Each ceramic cuboid has dimensions of 3.5 × 3.5 × 1 mm^3. We employed a finite-difference time-domain (FDTD) method to calculate the transmission spectra of the EET metamaterial. In the simulations, electric boundary conditions were set along the *x*- and *y*-directions

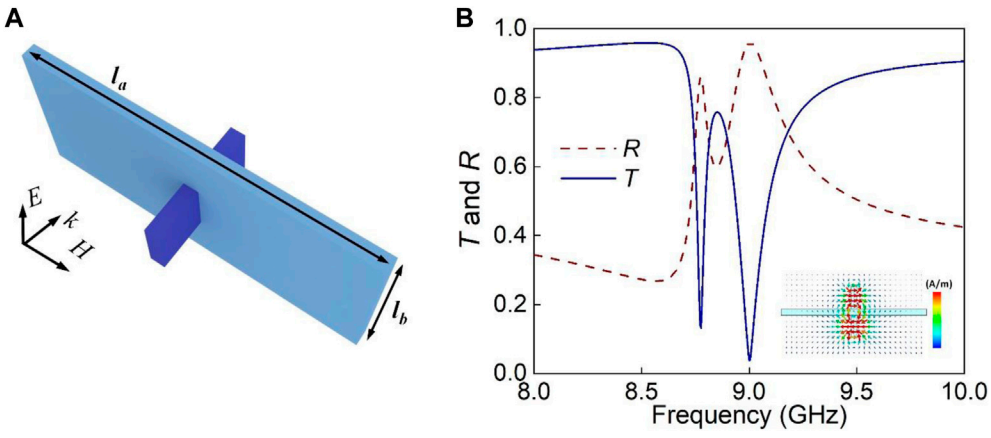

FIGURE 1
(A) Schematic diagram of our design with two ceramic cuboids on opposite sides of the Teflon substrate and **(B)** its reflection and transmission spectra in waveguide WR90, the insert shows the magnetic field distribution with a frequency of 8.776 GHz.

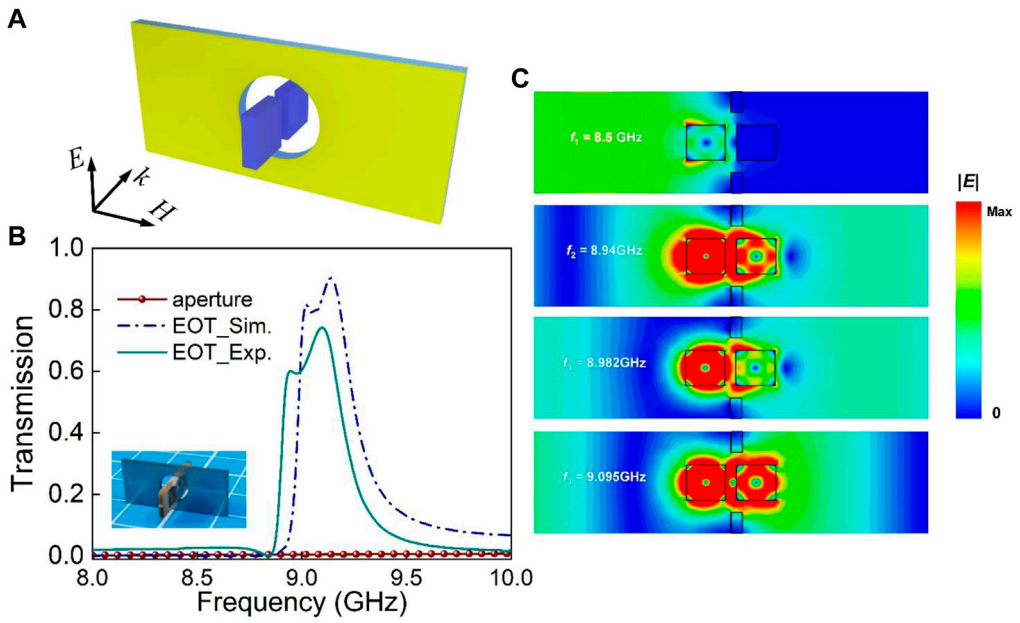

FIGURE 2
(A) Schematic diagram of the EET metamaterial with double cuboids placed in the center of a perforated metal sheet. **(B)** Transmission spectra of the metamaterial with only aperture and with double ceramic cuboids. **(C)** Calculated electric field distribution of EET metamaterial with double ceramic cuboids placed in the center of an aperture inside a waveguide at frequencies of 8.5, 8.94, 8.982, and 9.095 GHz.

to simulate a standard waveguide of WR90, and perfect match layers (PMLs) were set along the *z*-direction. The transmission and reflection spectra were calculated for two ceramic cuboids in the WR90 waveguide, and the results are shown in Figure 1B. For the transmission spectrum, two resonance dips appear at 8.776, and 9 GHz with a transmittance of 0.132, and 0.038 respectively, and a transmission peak appears at 8.852 GHz with a transmittance of 0.758. A typical first-order magnetic mode Mie resonance may be seen in the circular distribution of the magnetic field in the ceramic block as shown in the insert magnetic field distribution with a frequency of 8.776 GHz, which confirms that the ceramic cuboid is a magnetic dipole resonance.

Figure 2A shows that when two ceramic cuboids are placed on opposite sides of a small hole, there is a distinct peak in dual-frequency transmission, where the small hole diameter is 6 mm. The red dotted line in Figure 2B shows the transmittance when only the perforated metal sheet is inserted in the waveguide. Simulated results reveal two transmission peaks at frequencies of 9.02 and 9.14 GHz, while experimental findings show transmission maxima at 8.94 and 9.095 GHz with respective transmittances of 0.6 and 0.742. Note that the experimental EET results have slightly lower frequency and peak values than those from the simulation. This may be attributed to the uniformity doping of the samples during manufacture and small offset in the position of the samples during the experimental operation. However, the general features of the measured spectra agree well with the numerical simulations. Unlike coupling just one ceramic cuboid and a metal aperture (Cai et al., 2022), double ceramic cuboids' EET behavior has no specific frequency restriction but instead has a specified bandwidth. The mechanism behind this enhancement is examined together with local field distribution to achieve amplitude and frequency band modulation of EET behavior by varying coupling mode and strength between the two ceramic cuboids.

Figure 2C displays the calculated local electric field distribution for four frequency points: 8.5, 8.94, 8.982, and 9.095 GHz. The reference pair is set at a frequency of 8.5 GHz since almost no energy can pass through the subwavelength aperture at 8.5 GHz. At frequencies 8.94 and 9.095 GHz, the resonant phase of both ceramic cuboids was similar, allowing energy to couple from one cuboid to another with improved transmission efficiency when interacting with the perforated metal sheet. At 8.982 GHz, the resonant phase of both ceramic cuboids was opposite but still allowed successful coupling and normal energy transmission as if there were only ceramic cuboids in front. In general, the mutual coupling of magnetic modes between ceramic cuboids can make the energy transfer from one ceramic cuboid to another, and the perforated metal sheet can effectively inhibit the energy transfer back. It can also be understood that when the coupling energy passes through the metal sheet again, the phase change of the electric field occurs so that the originally reflected electromagnetic wave is reflected port in 2 again. Therefore, the coupling behavior between two ceramic cuboids is the key to realizing EET behavior. Can we change the coupling strength between two ceramic cuboids or change the coupling mode between ceramics to modulate the realized EET behavior? Based on this idea, we continue the work in the following parts.

For wireless energy transmission using the magnetic mode, distance is the most critical factor affecting efficiency. Therefore, the relationship between the spacing (g) between two ceramic cuboids and coupling efficiency has been investigated. Figure 3 shows that there are two transmission peaks when g = 0.5 mm and g = 1 mm due to a mode generated by the coupling of two

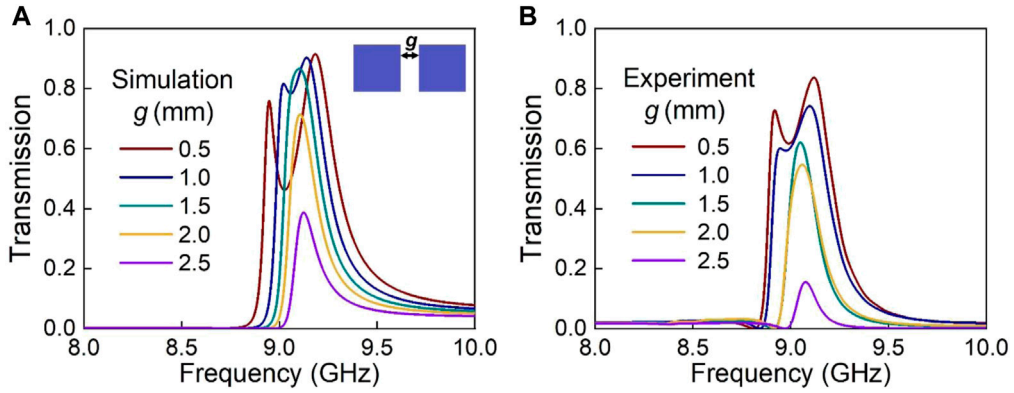

FIGURE 3
(A) Simulated and **(B)** measured transmission spectra with different spacing parameter *g* from 0.5 to 2.5 mm.

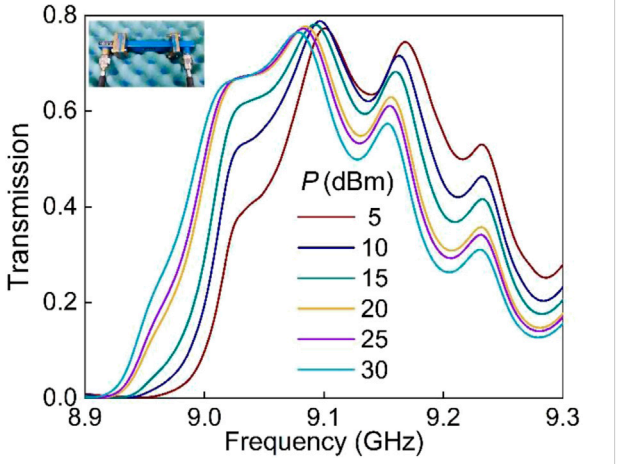

FIGURE 4
Measured transmission spectra with different input power levels *P* from 5 to 30 dBm, the insert shows the waveguide WR90 where the sample was located during the experiment.

ceramic cuboids. This results in broadband transmission as we can observe this mode when the spacing is close. However, increasing the spacing to g = 1.5 mm suppresses this resonance due to a perforated metal plate, resulting in only one transmission peak at a frequency corresponding to the first-order Mie resonance of each ceramic cuboid (f = 9.045 GHz with a transmission rate of 0.62). Further increasing the spacing between ceramic cuboids leads to f = 9.07 GHz and a lower transmission rate of 0.15 for g = 2.5 mm. By changing the coupling between these two ceramic cuboids, we can modulate both the bandwidth and amplitude of transmissions from broadband (g = 0.5 mm, double transmission peak, 8.91–9.12 GHz) to a single band (9.045 GHz), and from an amplitude range of 0.835 to 0.15 by changing spacings from 0.5 to 2.5 mm, respectively.

The transmission amplitude spectra of the sample with different in output power are measured through a Vector Network Analyzer (VNA) combined with a power amplifier. By adjusting the power of the incident electromagnetic field, we may control the transmission frequency by taking use of the thermal expansion effect. Figure 4 shows measured transmission spectra with various electromagnetic wave incident power P, and the insert shows the waveguide WR90 where the sample was located during the experiment. With P increasing from 5 to 30 dBm, the EET operating frequency shows a red shift of 60 MHz. Thanks to the Mie resonance inside the ceramic cuboid, the accompanying strong local field raises the internal temperature changes its dielectric constant, which is responsible for the red shift of the resonant frequency (Guo et al., 2016). In other words, as incident power increases, the temperature in the cuboid will increase accordingly, and the real and imaginary part of the permittivity of $CaTiO_3$ will also increase, which leads to red shift and larger energy dissipation of the EET effect. The effect could be interpreted as a third-order Kerr non-linearity with the relative permittivity ceramic following the expression (Makarov et al., 2017):

$$\varepsilon = \varepsilon' - 2i(\sigma/f)c^2 \times 10^{-7} - \chi|E|^2 \quad (1)$$

where ε' is a real part of the relative permittivity of cuboid ceramics at linear regime, σ is a ceramics conductivity, f is the frequency, c is a speed of light in free space, χ is a coefficient of Kerr non-linearity.

The transmission of metamaterial is dependent on the power of the incident wave, which allows for a mechanism to achieve non-linearly tunable electromagnetic metamaterial (Fan et al., 2021). The measured results indicate that our metamaterials can be employed for a frequency-agile device with high transmittance.

3 Conclusion

In summary, we have theoretically and experimentally demonstrated the EET behavior by using the first-order magnetic mode Mie resonant coupling of two ceramic cuboids. Initially, we analyze the coupling behavior of two identical titanate ($CaTiO_3$) doped with 1wt% ZrO_2 cuboids at their resonant frequency. Subsequently, we position these cuboids on either side of a perforated metal sheet to leverage their local field coupling for achieving EET with a bandwidth exceeding 100 MHz. We then

employ the spacing between these ceramic cuboids to modulate the strength of magnetic mode resonance coupling while controlling transmission amplitude and bandwidth. Finally, by exploiting nonlinear effects in ceramic materials, we achieve EET frequency control above 60 MHz via incident power modulation. This study enhances our comprehension of light-matter interactions and provides valuable insights into research on tunable electromagnetic anomaly transmission microwave devices.

Data availability statement

The raw data supporting the conclusion of this article will be made available by the authors, without undue reservation.

Author contributions

YF and FZ conceived the idea and guided the research. WC designed the metasurface, characterized the samples, and wrote the manuscript. RY, SC, ZY, YZ, QF, LX, WZ, and QZ contributed to the final version of the manuscript. All authors contributed to the article and approved the submitted version.

Funding

The authors would like to acknowledge financial support from the National Key R&D Program of China (Grant Nos. 2022YFB3806002 and 2022YFB3806000), the Natural Science Foundation of China (NSFC) (Grants Nos. 12074314 and 61771402), and the Science and Technology New Star Program of Shaanxi Province (No. 2023KJXX-148).

Conflict of interest

The authors declare that the research was conducted in the absence of any commercial or financial relationships that could be construed as a potential conflict of interest.

Publisher's note

All claims expressed in this article are solely those of the authors and do not necessarily represent those of their affiliated organizations, or those of the publisher, the editors and the reviewers. Any product that may be evaluated in this article, or claim that may be made by its manufacturer, is not guaranteed or endorsed by the publisher.

References

Aydin, K., Cakmak, A. O., Sahin, L., Li, Z., Bilotti, F., Vegni, L., et al. (2009). Split-ring-resonator-coupled enhanced transmission through a single subwavelength aperture. *Phys. Rev. Lett.* 102, 013904. doi:10.1103/PhysRevLett.102.013904

Bao, L., and Cui, T. J. (2020). Tunable, reconfigurable, and programmable metamaterials. *Microw. Opt. Technol. Lett.* 62, 9–32. doi:10.1002/mop.32164

Cai, W., Fan, Y., Fu, Q., Yang, R., Zhu, W., Zhang, Y., et al. (2022). Nonlinearly tunable extraordinary optical transmission in a hybird metamaterial. *J. Phys. D.* 55, 195106. doi:10.1088/1361-6463/ac5082

Chen, H., Chan, C. T., and Sheng, P. (2010). Transformation optics and metamaterials. *Nat. Mat.* 9, 387–396. doi:10.1038/nmat2743

Chen, W. C., Landy, N. I., Kempa, K., and Padilla, W. J. (2013). A subwavelength extraordinary-optical-transmission channel in babinet metamaterials. *Adv. Opt. Mat.* 1, 221–226. doi:10.1002/adom.201200016

Chen, X., Huang, L., Mühlenbernd, H., Li, G., Bai, B., Tan, Q., et al. (2012). Dual-polarity plasmonic metalens for visible light. *Nat. Commun.* 3, 1198. doi:10.1038/ncomms2207

Ebbesen, T. W., Lezec, H. J., Ghaemi, H. F., Thio, T., and Wolff, P. A. (1998). Extraordinary optical transmission through sub-wavelength hole arrays. *Nature* 391, 667–669. doi:10.1038/35570

Fan, Y., Han, J., Wei, Z., Wu, C., Cao, Y., Yu, X., et al. (2011). Subwavelength electromagnetic diode: One-way response of cascading nonlinear meta-atoms. *Appl. Phys. Lett.* 98, 151903. doi:10.1063/1.3579241

Fan, Y., He, X., Zhang, F., Cai, W., Li, C., Fu, Q., et al. (2021). Fano-resonant hybrid metamaterial for enhanced nonlinear tunability and hysteresis behavior. *Research* 2021, 9754083. doi:10.34133/2021/9754083

Freer, S., Camacho, M., Kuznetsov, S. A., Boix, R. R., Beruete, M., and Navarro-Cía, M. (2020). Revealing the underlying mechanisms behind TE extraordinary THz transmission. *Photonics Res.* 8, 430. doi:10.1364/prj.8.000430

García de Abajo, F. J. (2007). Colloquium: Light scattering by particle and hole arrays. *Rev. Mod. Phys.* 79, 1267–1290. doi:10.1103/RevModPhys.79.1267

Genet, C., and Ebbesen, T. W. (2007). Light in tiny holes. *Nature* 445, 39–46. doi:10.1038/nature05350

Guo, Y., Liang, H., Hou, X., Lv, X., Li, L., Li, J., et al. (2016). Thermally tunable enhanced transmission of microwaves through a subwavelength aperture by a dielectric metamaterial resonator. *Appl. Phys. Lett.* 108, 051906. doi:10.1063/1.4941406

Guo, Y., and Zhou, J. (2014). Total broadband transmission of microwaves through a subwavelength aperture by localized E-field coupling of split-ring resonators. *Opt. Express.* 22, 27136. doi:10.1364/OE.22.027136

Hajian, H., Caglayan, H., and Ozbay, E. (2017). Long-range Tamm surface plasmons supported by graphene-dielectric metamaterials. *J. Appl. Phys.* 121, 033101. doi:10.1063/1.4973900

Hajian, H., Ozbay, E., and Caglayan, H. (2017). Beaming and enhanced transmission through a subwavelength aperture via epsilon-near-zero media. *Sci. Rep.* 7, 4741. doi:10.1038/s41598-017-04680-y

Hao, F., Sonnefraud, Y., Van Dorpe, P., Maier, S. A., Halas, N. J., and Nordlander, P. (2008). Symmetry breaking in plasmonic nanocavities: Subradiant LSPR sensing and a tunable fano resonance. *Nano Lett.* 8, 3983–3988. doi:10.1021/nl802509r

He, C., and Song, Z. (2022). Terahertz graphene metasurfaces for cross-polarized deflection, focusing, and orbital angular momentum. *Opt. Express.* 30, 25498. doi:10.1364/OE.462330

He, Q., Sun, S., and Zhou, L. (2019). Tunable/reconfigurable metasurfaces: Physics and applications. *Research* 2019, 1849272. doi:10.34133/2019/1849272

Jahani, S., and Jacob, Z. (2016). All-dielectric metamaterials. *Nat. Nanotechnol.* 11, 23–36. doi:10.1038/nnano.2015.304

Jeong, J., Joushaghani, A., Paradis, S., Alain, D., and Poon, J. K. S. (2015). Electrically controllable extraordinary optical transmission in gold gratings on vanadium dioxide. *Opt. Lett.* 40, 4408. doi:10.1364/ol.40.004408

Jonah, O., and Georgakopoulos, S. V. (2013). Wireless power transfer in concrete via strongly coupled magnetic resonance. *IEEE Trans. Antennas Propag.* 61, 1378–1384. doi:10.1109/TAP.2012.2227924

Ju, L., Geng, B., Horng, J., Girit, C., Martin, M., Hao, Z., et al. (2011). Graphene plasmonics for tunable terahertz metamaterials. *Nat. Nanotechnol.* 6, 630–634. doi:10.1038/nnano.2011.146

Kurs, A., Karalis, A., Moffatt, R., Joannopoulos, J. D., Fisher, P., and Soljačić, M. (2007). Wireless power transfer via strongly coupled magnetic resonances. *Science* 317, 83–86. doi:10.1126/science.1143254

Li, C., and Song, Z. (2023). Tailoring terahertz wavefront with state switching in VO2 Pancharatnam-Berry metasurfaces. *Opt. Laser Technol.* 157, 108764. doi:10.1016/j.optlastec.2022.108764

Liu, N., Hentschel, M., Weiss, T., Alivisatos, A. P., and Giessen, H. (2011). Three-dimensional plasmon rulers. *Science* 332, 1407–1410. doi:10.1126/science.1199958

Liu, W., Xu, J., and Song, Z. (2021). Bifunctional terahertz modulator for beam steering and broadband absorption based on a hybrid structure of graphene and vanadium dioxide. *Opt. Express.* 29, 23331. doi:10.1364/OE.433364

Luo, T., Li, B., Zhao, Q., and Zhou, J. (2015). Dielectric behavior of low microwave loss unit cell for all dielectric metamaterial. *Int. J. Antenn Propag.* 2015, 1–6. doi:10.1155/2015/291234

Makarov, S. V., Zalogina, A. S., Tajik, M., Zuev, D. A., Rybin, M. V., Kuchmizhak, A. A., et al. (2017). Light-Induced tuning and reconfiguration of nanophotonic structures. *Laser Photonics Rev.* 11, 1700108. doi:10.1002/lpor.201700108

Martín-Moreno, L., García-Vidal, F. J., Lezec, H. J., Pellerin, K. M., Thio, T., Pendry, J. B., et al. (2001). Theory of extraordinary optical transmission through subwavelength hole arrays. *Phys. Rev. Lett.* 86, 1114–1117. doi:10.1103/PhysRevLett.86.1114

Navarro-Cía, M., Pacheco-Peña, V., Kuznetsov, S. A., and Beruete, M. (2018). Extraordinary THz transmission with a small beam spot: The leaky wave mechanism. *Adv. Opt. Mat.* 6, 1701312. doi:10.1002/adom.201701312

Nie, R., He, C., Zhang, R., and Song, Z. (2023). Vanadium dioxide-based terahertz metasurfaces for manipulating wavefronts with switchable polarization. *Opt. Laser Technol.* 159, 109010. doi:10.1016/j.optlastec.2022.109010

Pendry, J. B. (2000). Negative refraction makes a perfect lens. *Phys. Rev. Lett.* 85, 3966–3969. doi:10.1103/PhysRevLett.85.3966

Qin, Y., He, J., Yang, F., Zhang, Z., Yuan, Z., and Wu, M. (2018). Extraordinary optical transmission properties of a novel Bi-layered plasmonic nanostructure array. *Optik* 174, 684–691. doi:10.1016/j.ijleo.2018.08.073

Schurig, D., Mock, J. J., Justice, B. J., Cummer, S. A., Pendry, J. B., Starr, A. F., et al. (2006). Metamaterial electromagnetic cloak at microwave frequencies. *Science* 314, 977–980. doi:10.1126/science.1133628

Shelby, R. A., Smith, D. R., and Schultz, S. (2001). Experimental verification of a negative index of refraction. *Science* 292, 77–79. doi:10.1126/science.1058847

Smith, D. R., Pendry, J. B., and Wiltshire, M. C. K. (2004). Metamaterials and negative refractive Index. *Science* 305, 788–792. doi:10.1126/science.1096796

Soukoulis, C. M., and Wegener, M. (2011). Past achievements and future challenges in the development of three-dimensional photonic metamaterials. *Nat. Photonics.* 5, 523–530. doi:10.1038/nphoton.2011.154

Yang, R., Fan, Y., Zhu, W., Hu, C., Chen, S., Wei, H., et al. (2023). Terahertz silicon metagratings: High-efficiency dispersive beam manipulation above diffraction cone. *Laser Photonics Rev.* 2023, 2200975. doi:10.1002/lpor.202200975

Yang, R., Lou, J., Zhang, F., Zhu, W., Xu, J., Cai, T., et al. (2021). Active control of terahertz toroidal excitations in a hybrid metasurface with an electrically biased silicon layer. *Adv. Photonics Res.* 2, 2100103. doi:10.1002/adpr.202100103

Yang, R., Xu, J., Shen, N.-H., Zhang, F., Fu, Q., Li, J., et al. (2021). Subwavelength optical localization with toroidal excitations in plasmonic and Mie metamaterials. *InfoMat* 3, 577–597. doi:10.1002/inf2.12174

Yang, R., Zhang, F., Li, Z., Fu, Q., and Fan, Y. (2023). Controllable electromagnetically induced transparency in an electrically tunable terahertz hybrid metasurface. *Opt. Laser Technol.* 163, 109380. doi:10.1016/j.optlastec.2023.109380

Zhang, F., Kang, L., Zhao, Q., Zhou, J., and Lippens, D. (2012). Magnetic and electric coupling effects of dielectric metamaterial. *New J. Phys.* 14, 033031. doi:10.1088/1367-2630/14/3/033031

Zhao, Q., Kang, L., Du, B., Zhao, H., Xie, Q., Huang, X., et al. (2008). Experimental demonstration of Isotropic negative permeability in a three-dimensional dielectric composite. *Phys. Rev. Lett.* 101, 027402. doi:10.1103/PhysRevLett.101.027402

Zhao, Q., Zhou, J., Zhang, F., and Lippens, D. (2009). Mie resonance-based dielectric metamaterials. *Mat. Today.* 12, 60–69. doi:10.1016/S1369-7021(09)70318-9

Zhu, W., Fan, Y., Yang, R., Geng, G., Fu, Q., Gu, C., et al. (2022). Polarization-multiplexed silicon metasurfaces for multi-channel visible light modulation. *Adv. Funct.* 32, 2200013. doi:10.1002/adfm.202200013

frontiers | Frontiers in Materials

TYPE Original Research
PUBLISHED 02 August 2023
DOI 10.3389/fmats.2023.1229164

OPEN ACCESS

EDITED BY
Fuyin Ma,
Xi'an Jiaotong University, China

REVIEWED BY
Jianping Xia,
Duke University, United States
Nansha Gao,
Northwestern Polytechnical University, China
Yan-Feng Wang,
Tianjin University, China

*CORRESPONDENCE
Fei Sun,
sunfei@tyut.edu.cn
Bingjie Wang,
wangbingjie@tyut.edu.cn

†These authors have contributed equally to this work

RECEIVED 26 May 2023
ACCEPTED 25 July 2023
PUBLISHED 02 August 2023

CITATION
Wu B, Sun F, Liu Y, Liu X, Zhao X, Fei H, Yang Y, Chen Z, Liang S, Wang Z and Wang B (2023), Simultaneously focusing electromagnetic and acoustic waves by double-physical-fields null medium. *Front. Mater.* 10:1229164. doi: 10.3389/fmats.2023.1229164

Simultaneously focusing electromagnetic and acoustic waves by double-physical-fields null medium

Boyang Wu[1†], Fei Sun[1*†], Yichao Liu[1], Xin Liu[1], Xiaodan Zhao[1], Hongming Fei[1], Yibiao Yang[1], Zhihui Chen[1], Shaowei Liang[2], Zheng Wang[2] and Bingjie Wang[1*]

[1]Key Lab of Advanced Transducers and Intelligent Control System, Ministry of Education and Shanxi Province, College of Electronic Information and Optical Engineering, Taiyuan University of Technology, Taiyuan, China, [2]China-Blarus Belt and Road Joint Laboratory on Electromagnetic Environment Effect, Taiyuan, China

A novel double-physical-fields lens that can simultaneously focus acoustic and electromagnetic waves into a given region is designed based on double-physical-fields null medium, which can be realized by metal plates with subwavelength separations/thicknesses and precisely designed lengths. Numerical simulations show the proposed double-physical-fields lens can create exactly the same focusing effect for both electromagnetic and acoustic waves, i.e., the same focal spot size and efficiency at the same focal length. Four typical lens with different output surfaces are studied, which shows different focusing characteristics, e.g., noodle-shaped focal spot, tiny focal spot, and capsule-shaped focal spot. With the help of the designed double-physical-fields lens, an additional degree of freedom for control can be provided by simultaneously focusing acoustic and electromagnetic waves, which may lead to wider range of applications than single-field focusing.

KEYWORDS

null medium, double-physical-fields lens, double-physical-fields focusing, surface transformation, transformation optics

1 Introduction

The focusing of acoustic wave or electromagnetic wave alone has already been applied in various important application. For example, it is an effective non-invasive way of treating tumors by focusing ultrasound/microwave onto the tumor area, where focused high ultrasound/electromagnetic energy can raise the temperature of the tumor cells to produce thermal coagulation or ablation (Sato et al., 1996; Fan et al., 2013; Shi et al., 2015; Xia and Sun, 2015). Usually, tumour treatment by focused ultrasound is more accurate than the treatment by focused microwave. However, some tissues (e.g., esophagus and rectum) cannot be penetrated by ultrasound and can only be treated by focused microwave. Acoustic/electromagnetic tweezers, which can capture the target particles noninvasively by forces and torques generated from the focused acoustic/electromagnetic fields, have been widely used to manipulate the movement of micro-nano particles (e.g., biological molecules and living cells) (Janssen et al., 2012; Ozcelik et al., 2018; Vidiasheva et al., 2018; Marzo and Drinkwater, 2019). Currently, the focused acoustic beam can be achieved by acoustic metasurfaces/metamaterials (Zhang et al., 2009; Qi et al., 2017; Xia et al., 2018), negative or zero refractive index lenses (Fang et al., 2006; Gao et al., 2016), acoustic

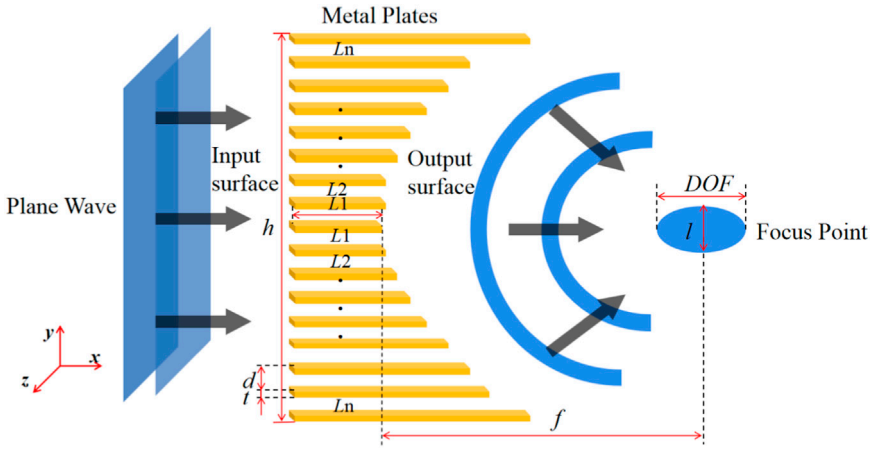

FIGURE 1
Schematic diagram of the DPFL by sub-wavelength air channels enclosed by metal plates.

crystal lens (Yang et al., 2004), graded index lens (Li et al., 2012), anisotropic material lens (Li et al., 2017), and etc. Common methods of focusing electromagnetic waves include various electromagnetic lenses (Kwon and Werner, 2009; Kundtz and Smith, 2010; Roy et al., 2013; Khorasaninejad et al., 2016; Chen et al., 2018), time reversal mirrors (Lerosey et al., 2004; de Rosny et al., 2010), structures designed by deep learning methods (Rivenson et al., 2017; Ma et al., 2021), and etc.

Compared with single-physical-field focusing, focusing acoustic and electromagnetic waves simultaneously has better application value. If the simultaneous focus of acoustic and electromagnetic waves can be achieved, the advantages of the two focused physical fields can complement each other. In tumor therapy, simultaneous focused ultrasound and microwave will provide both the high precision of focused acoustic waves for tumour treatment (Kohrmann et al., 2002) and the high penetration of focused microwaves for tumour treatment (Leggio et al., 2015; Lim and Yoon, 2021). Double-physical-fields tweezers by simultaneous focused ultrasound and microwave can provide additional degrees of freedom in the manipulation of captured targets, e.g., the focused acoustic beam can capture targets in the given region while the focused electromagnetic beam can rotate them at the same time. In industrial inspection, the focused acoustic wave can be used to locate cracks in pipes and castings, while the focused electromagnetic beam can help to repair these cracks (e.g., the thermal effect of focused infrared waves can help repair cracks by dissolving the material at the crack). In double-field focusing, the focused acoustic waves may image/capture/locate the target, and the focused electromagnetic waves may simultaneously perform an additional manipulation (e.g., destruction/rotation/repairment) on the same target. In recent years, various structures have been designed to simultaneously manipulate electromagnetic and acoustic waves, such as electromagnetic-acoustic cloaking (Sun et al., 2020), electromagnetic shielding and sound absorption (Gao et al., 2022), and electromagnetic-acoustic splitter (Chen et al., 2023). However, there is little research on how to achieve simultaneous focusing of electromagnetic and acoustic waves with the same structure.

In order to focus acoustic and electromagnetic waves simultaneously, a novel double-physical-fields lens (DPFL) is proposed in Figure 1. The designed DPFL can be realized by metal plates with subwavelength separations/thicknesses and precisely designed lengths, which performs as a reduced double-physical-fields null medium that can convert the incident electromagnetic/acoustic wavefront on the input surface of the lens into the desired electromagnetic/acoustic wavefront on the output surface of the lens (Sun et al., 2020). Note that the 'subwavelength' means the size of the separation and thickness of the metal plates are smaller than the wavelength of the electromagnetic/acoustic wave, e.g., one-third of the working wavelength.

2 Design method

Double-physical-fields null medium, which performs as a perfect endoscope for electromagnetic waves and acoustic waves simultaneously, has been theoretically studied (Sun et al., 2020). Based on the perfect directional projection properties of the double-physical-fields null medium, double-physical-fields surface transformation has been proposed in our previous study (Sun et al., 2020), which is a graphical method to design double-physical-fields devices. In this study, we use double-physical-fields surface transformation to design DPFL that can focus both electromagnetic waves and acoustic waves into the same focal point. The parameters of the ideal double-physical-fields null medium can be obtained from the extreme space compression transform by transformation optics and transformation acoustics, which can be summarized as (Sun et al., 2020):

$$\begin{cases} \varepsilon = \mu = \mathrm{diag}\left(\frac{1}{\Delta}, \Delta, \Delta\right) \\ \rho = \mathrm{diag}\left(\Delta, \frac{1}{\Delta}, \frac{1}{\Delta}\right) \\ \kappa = \frac{1}{\Delta} \end{cases}, \Delta \to 0. \tag{1}$$

From Eq. 1, the permittivity, permeability and modulus of the ideal double-physical-fields null medium are extremely anisotropic, whose values approach infinity along their main axis and are close to zero in other orthogonal directions. After some theoretical calculations (Sun

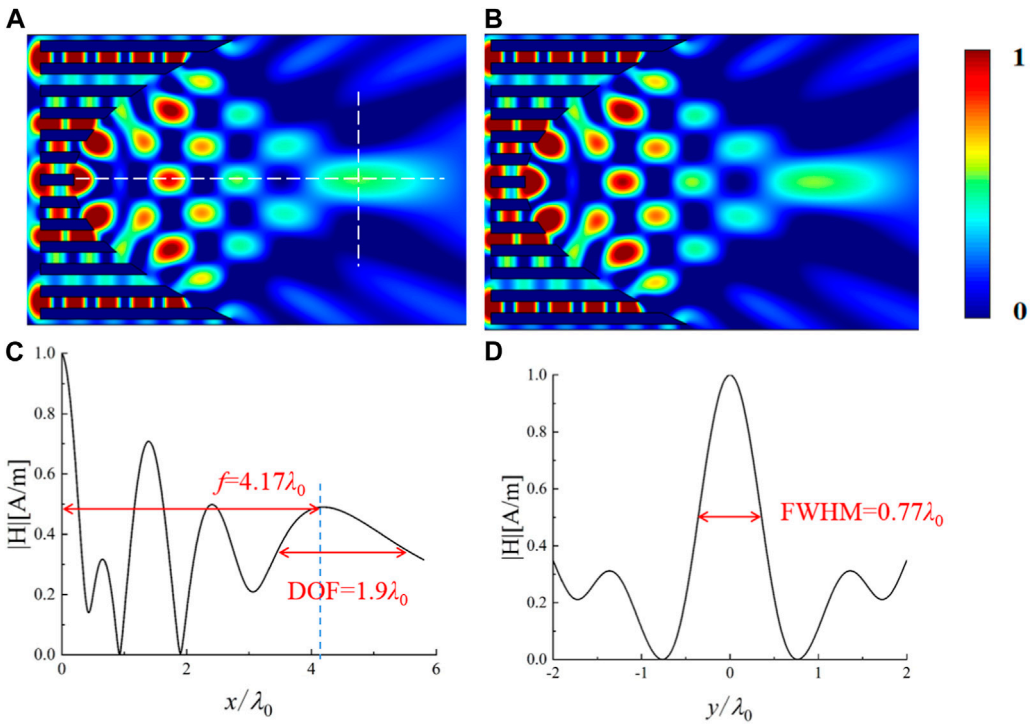

FIGURE 2
Simulated normalized magnetic field distribution **(A)** and normalized acoustic pressure distribution **(B)**, respectively, when a TM-polarized plane electromagnetic wave and a plane acoustic wave are incident onto the designed DPFL with a parabolic output surface $f(x) = \sqrt{55x}$. In this design, $N = 6$, $d = \lambda_0/3$, $t = \lambda_0/6$, $L_1 = 0.5\lambda_0$, $L_2 = 0.58\lambda_0$, $L_3 = 0.78\lambda_0$, $L_4 = 1.14\lambda_0$, $L_5 = 1.6\lambda_0$, $L_6 = 2.17\lambda_0$, and $\lambda_0 = 30$ mm. **(C, D)** show the normalized magnetic field (the same as acoustic pressure) distribution along the x and y directions [marked by white dashed lines in **(A)**], respectively.

et al., 2020), it shows that the metallic plates with subwavelength separations and thicknesses, whose lengths satisfy the Fabry-Perot resonance condition, can perform as a reduced double-physical-fields null medium. The reduced double-physical-fields null medium can still project TM-polarized electromagnetic waves and acoustic waves simultaneously along the orientations of metallic plates.

As shown in Figure 1, the input and output surfaces of the DPFL are designed as a plane and a curved surface (described by the equation $y = f(x)$), respectively. The DPFL is composed by an array structure of $2N + 1$ parallel metal plates with equally subwavelength separation d and thickness t. $2N$ air channels are formed between two adjacent metal plates, which are labeled from the centre of the lens outwards as channel 1, channel 2, . . . and channel N. The size of the input surface of the DPFL is $h = 2Nd + t$, which can be adjusted by increasing or decreasing the number of metal plates for matching the width of the incident wave. The length of the k-th air channel approximately satisfying the Fabry-Perot resonance condition (i.e., $L_k = m\lambda_0$, $m = 1, 2, 3. . .$, where λ_0 is the working wavelength) to obtain the best transmittance, which is defined as the efficiency of the DPFL for electromagnetic waves (Xia et al., 2018):

$$\eta = \frac{\int_l \bar{S} \cdot d\bar{A}}{\int_h \bar{S} \cdot d\bar{A}}, \tag{2}$$

where S is the Poynting vector (i.e., the energy flow density vector), l and h are the transverse sizes of the focusing spot and input surface along the y-axis, respectively (see Figure 1). Although there is no concept of Poynting's vector for acoustic waves, the z component of magnetic field H_z field for TM polarized electromagnetic waves and the acoustic pressure for acoustic waves satisfy the same Heimholtz equation, and the subsequent simulation results show that the designed structure has exactly the same focusing effect on both magnetic field and acoustic pressure, therefore the efficiency defined by Eq. 2 is also suitable for the focusing efficiency of acoustic wave.

In this study, the efficiency of the lens is calculated as follows: we first remove the DPFL and calculate the integration of the incident energy flow over the air surface with the same size of the DPFL's input surface, which gives the denominator of Eq. 2, i.e., the total incident energy. Then, we add the DPFL and calculate the integration of energy flow density over the width of the focused spot, which gives the numerator of Eq. 2, i.e., the energy at the focused spot. Since all simulations show that the lens produces exactly the same field distribution for both electromagnetic wave and acoustic wave, the simulated results for electromagnetic waves are used to calculate the lens efficiency in the subsequent optimization calculations.

The designed DPFL by metal plates in Figure 1 performs as reduced double-physical-fields null medium for TM-polarized electromagnetic and acoustic waves, whose function is to simultaneously project the electromagnetic/acoustic field distributions from the input surface along the direction of the air channel onto the output surface (Sun et al., 2020). When the wavefront of the incident EM wave/acoustic wave coincides with the shape of the DPFL's input surface (e.g., plane wave), the wavefront of the outgoing wave can be converted to coincide

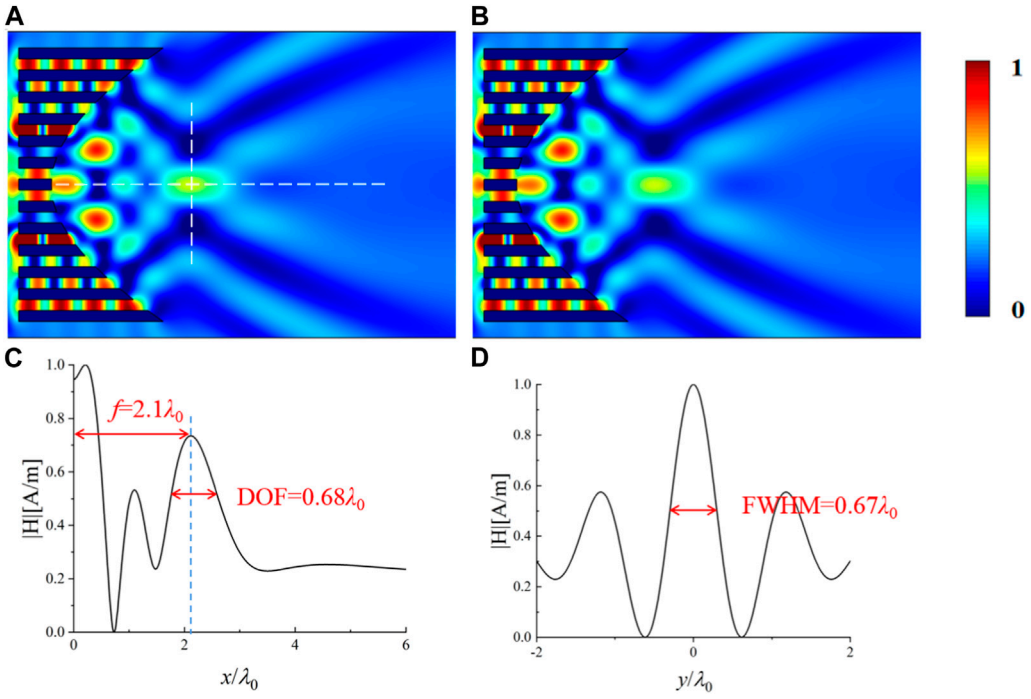

FIGURE 3
Simulated normalized magnetic field distribution **(A)** and normalized acoustic pressure distribution **(B)**, respectively, when a TM-polarized plane electromagnetic wave and a plane acoustic wave are incident onto the designed DPFL with a hyperbolic output surface equation $f(x) = 70\sqrt{-1+x^2/22500}$. In this design, $N = 6$, $d = \lambda_0/3$, $t = \lambda_0/6$, $L_1 = 0.5\lambda_0$, $L_2 = 0.58\lambda_0$, $L_3 = 0.75\lambda_0$, $L_4 = 1.01\lambda_0$, $L_5 = 1.35\lambda_0$, $L_6 = 1.75\lambda_0$, and $\lambda_0 = 30$ mm. **(C, D)** show the normalized magnetic field (the same as acoustic pressure) distribution along the x and y directions [marked by white dashed lines in **(A)**], respectively.

with the shape of the DPFL's output surface after passing through the DPFL. Therefore, a double-physical-field focusing effect can be obtained by designing various geometrical shapes of output surfaces.

3 Simulation results for various DPFLs

The double-physical-fields focusing effect of various DPFLs with different output surfaces are studied numerically. All numerical simulations in this study are carried out by COMSOL Multiphysics 5.6 (license number 9406999). All numerical simulations are 2D simulations in this study, which means that the metal plates are infinite along the z direction. The radio frequency module and the acoustic module are utilized to calculate electromagnetic field distribution and acoustic pressure distribution, respectively. The working wavelength is designed as $\lambda_0 = 30$ mm, which corresponds to the working frequencies 10 GHz for electromagnetic wave and 11.4 kHz for acoustic wave, respectively. The metal is modeled as perfect electric conductor and hard wall boundary condition for electromagnetic simulation and acoustic simulation, respectively. Note that metallic plates can perform as reduced null medium for only TM-polarized electromagnetic waves, we only simulate the DPFLs for TM-polarized electromagnetic waves in this study. The double-physical-fields focusing effect of DPFLs with four different shapes of the output surface are studied, which include the parabolic surface in Figure 2, the hyperbolic surface in Figure 3, the elliptical surface in Figure 4, and the circular surface in Figure 5.

The designed working wavelength ($\lambda_0 = 30$ mm) and corresponding frequencies (11.4 kHz and 10 GHz for acoustic and electromagnetic waves, respectively) is used as one example in this study, which can be changed to other values according to different applications. For example, we can first determine the required acoustic frequency for a specific application (e.g., ultrasonic detection), and then the new working wavelength can be calculated accordingly, thereafter the parameters of the DPELs can be redesigned by using Fabry-Perot resonance condition $L_n = m\lambda_0$, $m = 1, 2, 3\ldots$, where λ_0 is the new working wavelength.

The lens designed in this study involves metal and air. For air, it can be considered a loss-free material for both electromagnetic and acoustic waves. Considering the conductivities of metals are extremely high (e.g., the conductivity of the copper is $6*10^7$ [S/m]) in the microwave band (the designed working frequency 10 GHz), whose skin depth can be treated as zero (modeled as perfect electric conductor), the material loss of the metal has essentially no effect on the focusing effect of the electromagnetic waves in the designed working frequency. Similarly, metals can usually be treated as a hard wall boundary condition for acoustic waves (Yang et al., 2016), i.e., acoustic waves cannot enter. Therefore, the material loss of the metal has no effect on the focusing effect of the acoustic waves.

The simulated results verify the designed DPFL with a parabolic output surface (i.e., the equation of the output surface is chosen as a parabolic equation $f(x) = \sqrt{55x}$) can focus both TM-polarized electromagnetic plane wave in Figure 2A and acoustic plane wave in Figure 2B, respectively. When a planar electromagnetic wave and

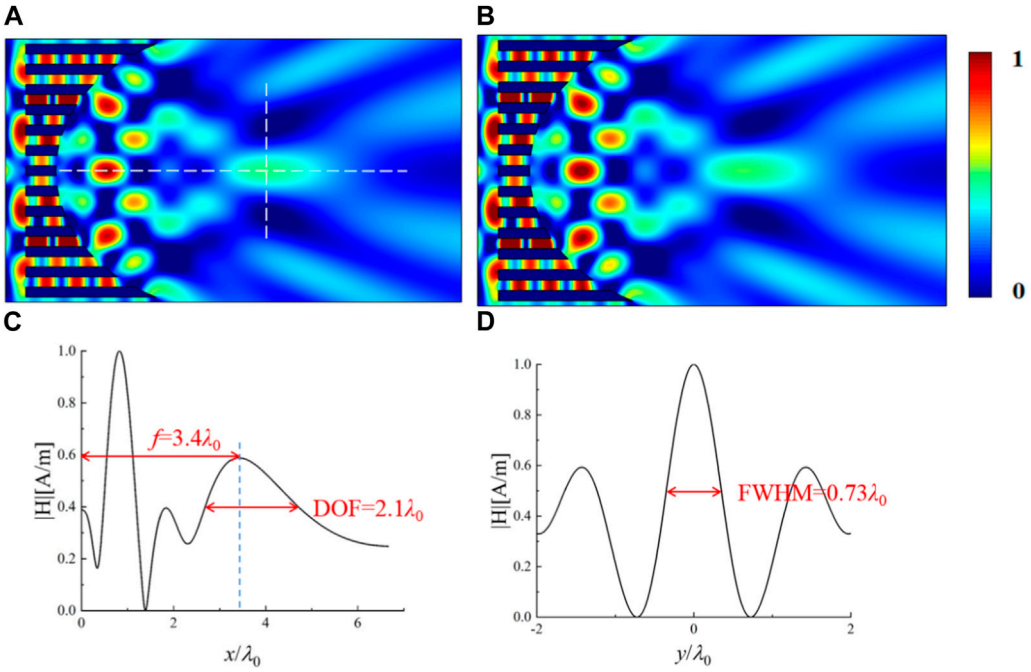

FIGURE 4
Simulated normalized magnetic field distribution **(A)** and normalized acoustic pressure distribution **(B)**, respectively, when a TM-polarized plane electromagnetic wave and a plane acoustic wave are incident onto the designed DPFL with an elliptical output surface equation $f(x) = 70\sqrt{1 - x^2/8100}$. In this design, $N = 6$, $d = \lambda_0/3$, $t = \lambda_0/6$, $L_1 = 0.5\lambda_0$, $L_2 = 0.55\lambda_0$, $L_3 = 0.66\lambda_0$, $L_4 = 0.84\lambda_0$, $L_5 = 1.12\lambda_0$, $L_6 = 1.52\lambda_0$, and $\lambda_0 = 30$ mm. **(C, D)** show the normalized magnetic field (the same as acoustic pressure) distribution along the *x* and *y* directions [marked by white dashed lines in **(A)**], respectively.

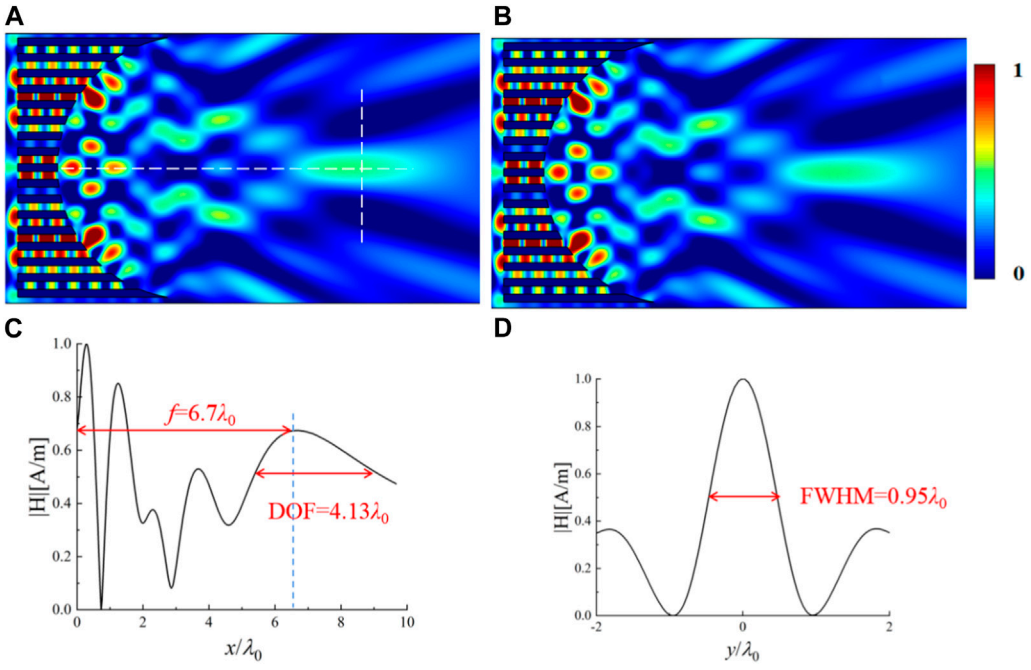

FIGURE 5
Simulated normalized magnetic field distribution **(A)** and normalized acoustic pressure distribution **(B)**, respectively, when a TM-polarized plane electromagnetic wave and a plane acoustic wave are incident onto the designed DPFL with a circular output surface equation $f(x) = \sqrt{8464 - x^2}$. In this design, $N = 8$, $d = 11\lambda_0/30$, $t = 11\lambda_0/60$, $L_1 = 0.93\lambda_0$, $L_2 = 0.97\lambda_0$, $L_3 = 1.05\lambda_0$, $L_4 = 1.17\lambda_0$, $L_5 = 1.36\lambda_0$, $L_6 = 1.61\lambda_0$, $L_7 = 1.96\lambda_0$, $L_8 = 2.47\lambda_0$, and $\lambda_0 = 30$ mm. **(C, D)** show the normalized magnetic field (the same as acoustic pressure) distribution along the *x* and *y* directions [marked by white dashed lines in **(A)**], respectively.

10.3389/fmats.2023.1229164

TABLE 1 Key parameters of the DPFLs with different output surfaces.

Surface	f	DOF	FWHM	Efficiency (%)
Parabola	$4.17\lambda_0$	$1.9\lambda_0$	$0.77\lambda_0$	31.42
Hyperbola	$2.1\lambda_0$	$0.68\lambda_0$	$0.67\lambda_0$	26.86
Ellipse	$3.4\lambda_0$	$2.1\lambda_0$	$0.73\lambda_0$	22.37
Circle	$6.7\lambda_0$	$4.13\lambda_0$	$0.95\lambda_0$	37.71

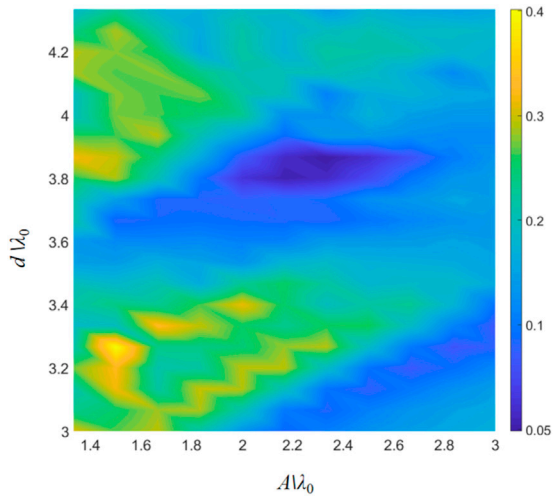

FIGURE 6
Efficiency of the parabolic DPFL when parameters *d* and *A* are scanned.

a planar acoustic wave are incident onto the designed DPFL, the normalized magnetic/acoustic field distributions are identical in Figures 2A, B, which show exactly the same focusing spots for both fields can be created at the same distance f (i.e., the focal length) from the output surface of the DPFL. The depth of focus (DOF) is the distance range measured normal to the lens over which the spot remains tightly focused (Banerji et al., 2020). In this study, DOF is used to describe longitudinal scale of focal spot. The simulated results show that the parabolic DPFL simultaneously focus electromagnetic waves and acoustic waves into a capsule-shaped spot with a relatively moderate size, which is often described by full width at half maxima (FWHM = $0.77\lambda_0$) and depth of focus DOF = $1.9\lambda_0$, at relatively long focal length $f = 4.17\lambda_0$ with efficiency η = 31.42% (see Figures 2C, D).

Please note that the amplitudes of magnetic field and acoustic pressure are normalized, which leads to a range of values between 0 (minimum) and 1 (maximum), and the color bars in all figures are in the range 0–1. In this case, the blue regions in the color bar indicate that the amplitude of magnetic field or acoustic pressure at these positions are zero '0', the red regions in the color bar indicate that the amplitude of magnetic field or acoustic pressure at these positions are the maximum '1', and the other colors mean that the amplitude of magnetic field or acoustic pressure are between the zero '0' and the maximum "1".

The hyperbolic DPFL, whose output surface satisfy a hyperbolic equation $f(x) = 70\sqrt{-1 + x^2/22500}$, can also focus both TM-polarized electromagnetic plane wave in Figure 3A and acoustic plane wave in Figure 3B, respectively. The simulated results in Figure 3 show that the hyperbolic DPFL can produce a tiny focal spot with smaller size FWHM = $0.67\lambda_0$ and depth of focus DOF = $0.68\lambda_0$ for both fields at short focal length $f = 2.1\lambda_0$ with efficiency η = 26.86% (see Figures 3C, D), which is more suitable for the double-fields manipulation of small particles.

The elliptical DPFL, whose output surface satisfy a elliptical equation $f(x) = 70\sqrt{1 - x^2/8100}$, can simultaneously focus TM-polarized electromagnetic plane wave in Figure 4A and acoustic plane wave in Figure 4B, respectively. The simulated results in Figure 4 show that the parameters of the focal spot created by the elliptical DPFL are FWHM = $0.73\lambda_0$, DOF = $2.1\lambda_0$, and $f = 3.4\lambda_0$, which are close to the parameters of the focal spot created by the parabolic DPFL in Figure 2. Compared the parabolic DPFL in Figure 2, the elliptical DPFL has significant side spots around the focal spot, which leads to a small efficiency η = 22.37%.

The circular DPFL, whose output surface satisfy a circular equation $f(x) = \sqrt{8464 - x^2}$, can simultaneously focus TM-polarized electromagnetic plane wave in Figure 5A and acoustic plane wave in Figure 5B, respectively. The simulated results in Figure 5 show that the circular DPFL can produce a noodle-shaped focal spot with the size FWHM = $0.95\lambda_0$ and depth of focus DOF = $4.13\lambda_0$ for both fields at long focal length $f = 6.7\lambda_0$ with efficiency η = 37.71% (see Figures 5C, D), which is more suitable for the double-physical-fields noninvasive processing/treatment.

Theoretically, according to the double-physical-fields surface transformation theory, when the output surface of the lens is chosen to be of different geometrical shapes, the wave front of the output wave will be modulated to that shape accordingly. In this design, the output surfaces are designed as parabola, hyperbola, ellipse and circle, respectively, and according to the nature of perfect projection of null medium, the wave fronts of the output waves are modulated into these four surfaces accordingly. In these four cases, the output wave is focused at the focal point of the parabola/hyperbola/ellipse and at the centre of the circle, and the position of the focal point can be adjusted by changing the geometrical parameters of the corresponding output surface.

The key parameters of the DFPL with four different output surfaces are given in Tab. 1, which can be a guidance for different applications. For the parabolic DPFL, the energy of the sidelobe is concentrated before the focal point, and the energy distribution of the sidelobe is weaker after the focal point and the focal plane, which leads to a relatively high efficiency (~31.42%). The focal spot of the parabolic DPFL is capsule-like spot with a relatively moderate size (FWHM~$0.77\lambda_0$ and DOF~$1.9\lambda_0$), and the long focal length is relatively long ($f \sim 4.17\lambda_0$). For the hyperbolic DPFL, the energy of the sidelobe is distributed before and after focusing plane, which in turn leads to lower efficiency (~26.86%). The hyperbolic DPFL can produce the smallest focal spot with very compact sizes in both horizontal direction (DOF = $0.68\lambda_0$) and vertical direction (FWHM = $0.67\lambda_0$) at the shortest focal length $f = 2.1\lambda_0$, which is very suitable for precisely confining tiny objects to small area. For the elliptical DPFL, the energy of the sidelobe is distributed before and after focusing plane, which has the lowest efficiency (~22.37%). The elliptical DPFL can create a capsule-shaped spot with a relatively

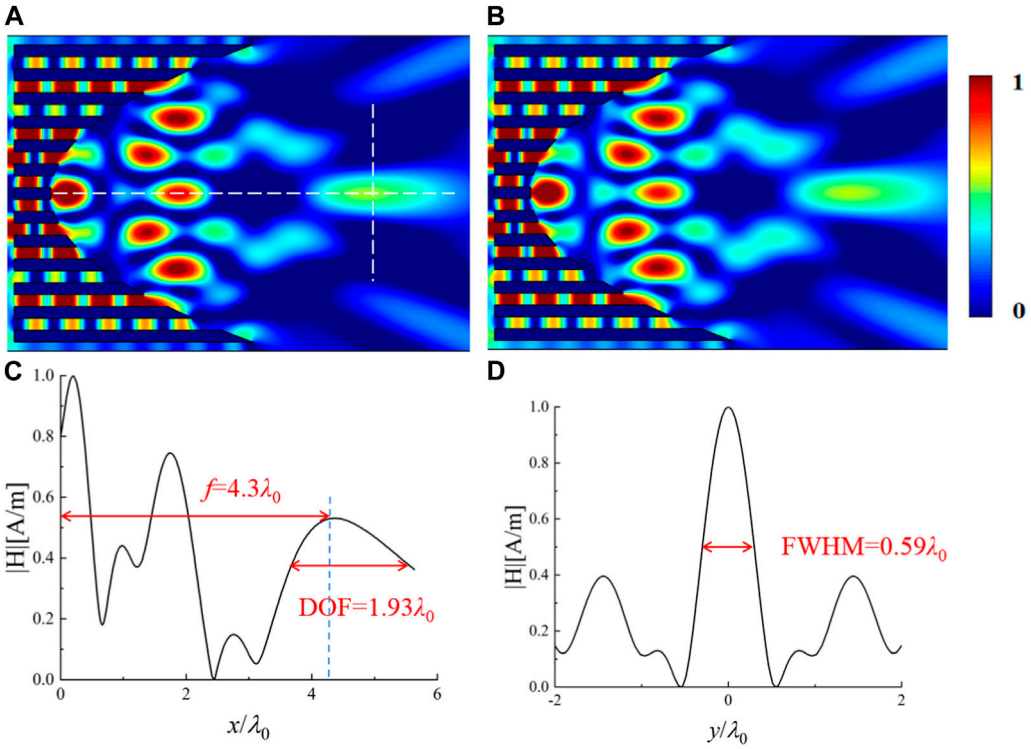

FIGURE 7
Simulated normalized magnetic field distribution **(A)** and normalized acoustic pressure distribution **(B)**, respectively, when a TM-polarized plane electromagnetic wave and a plane acoustic wave are incident onto the optimized parabolic DPFL with a output surface $f(x) = \sqrt{45x}$. In this design, $N = 6$, $d = 3.27\lambda_0$, $t = d/2$, $L_1 = 0.5\lambda_0$, $L_2 = 0.61\lambda_0$, $L_3 = 0.86\lambda_0$, $L_4 = 1.25\lambda_0$, $L_5 = 1.78\lambda_0$, $L_6 = 2.46\lambda_0$, and $\lambda_0 = 30$ mm. **(C, D)** show the normalized magnetic field (the same as acoustic pressure) distribution along the x and y directions [indicated by white dashed lines in **(A)**], respectively.

moderate size (FWHM~$0.73\lambda_0$ and DOF~$2.1\lambda_0$) and moderate focal length ($f \sim 3.4\lambda_0$). For the circular DPFL, the energy of the sidelobe is concentrated before the focal point, and the energy distribution of the sidelobe is weaker after the focal point and the focal plane, which has the highest efficiency (~37.71%). The circular DPFL can produce a noodle-shaped focal spot at the longest focal length ($f \sim 6.7\lambda_0$), which can be used for noninvasive processing/treatment that requires penetration of surfaces (e.g., inside pipes and human bones). In summary, elliptical/parabolic DPFLs are moderate-focal-length lenses with moderate focal spot sizes, hyperbolic DPFL is short-focal-length lens with smallest focal spot size, and circular DPFL is long-focal-length lens with noodle-shaped focal spot.

4 Parameters scanning

From the above analysis, the parabolic DPFL has relatively moderate parameters, which is chosen as an example to study how to further improve the efficiency of the DPFL by choosing suitable structural parameters. Simulation results show separation distance d in Figure 1 and surface parameter A ($f(x) = \sqrt{Ax}$) both affect the focusing efficiency of the parabolic DPFL. As show in Figure 6, both d and A has a significant impact on the efficiency of the parabolic DPFL.

If d is too large, then the metal plates in Figure 1 will no longer behave as an effective medium for double fields; while if d is too small, it is difficult to ensure that each channel approximately meets the Fabry-Perot resonance condition, thus the scan range of d is limited to $d = 3\lambda_0 \sim 4.3\lambda_0$ in Figure 6. If A is too small, the shape of the output surface will be reduced to a plane, and the focusing effect will disappear; while if A is too large, more number of metal plates are required to mimic the sharp curvature variation at the output surface, which is difficult to ensure that each channel approximately meets the Fabry-Perot resonance condition, thus the scanning range of A is limited to $A = 1.4\lambda_0 \sim 3\lambda_0$ in Figure 6.

During the scanning, the number of air channels $2N = 12$, the thickness of the metal plate $t = d/2$, and the working wavelength $\lambda_0 = 30$ mm are kept unchanged. As shown in Figure 6, the best efficiency $\eta = 37.59\%$ can be obtained when $d = 3.27\lambda_0$ and $A = 1.5\lambda_0$ for the optimized parabolic DPFL. The optimized parabolic DPFL with a higher energy utilization can still focus both electromagnetic and acoustic waves simultaneously with a relatively moderate size (FWHM = $0.59\lambda_0$ and DOF = $1.93\lambda_0$) and focal length ($f = 4.3\lambda_0$), which is verified by numerical simulations in Figure 7.

For a perfect DPFL realized by ideal double-physical-fields null medium, the shape of the outgoing wave should be exactly the same as the shape of the output surface. However, for the reduced null medium by metallic array, the length of each air channel must be an integer multiple of the wavelength to obtain the best transmittance,

which leads to the shape of the outgoing wave is not exactly the same as the output surface. In this case, the focal point is the result of the interference of the outgoing waves from multiple air channels, which results in a non-peak energy at the focal point along the x axis. To solve this problem, the waveguide metamaterials (Zheng et al., 2019), instead of an array of metal plates, can be used to realize the reduced null medium, where the FP condition does not need to be satisfied for each channel. In this case, the energy at the focal point can be a peak along the x axis. However, such a lens based on waveguide metamaterials would only be effective for electromagnetic waves and cannot be able to focus both electromagnetic and acoustic waves.

Our design principle is different from the current method on designing metasurfaces, which often needs to numerically calculate the phase shift and transmittance of each metasurface, and then adjust the geometric parameters of each unit to make its transmittance phase satisfy a specific distribution (on the premise of ensuring that the transmittance of each unit is close to 1) to achieve the focusing or other desired effect (Liu et al., 2020; Cai et al., 2021). In our design method, metal channels are used to mimic null medium for both electromagnetic wave and acoustic wave, which perform as the reduced null medium (Sun et al., 2020; Chen et al., 2023). For the ideal null medium, the transmittance should be 100% and the transmission phase should be zero. In this case, the wavefront of the output wave can be directly modulated by changing the geometry of the output surface. To achieve the ideal null medium, the length of each metallic channel needs to be close to an integer multiple of the operating wavelength (i.e., the FP condition) to ensure that the transmittance is close to 1 while the transmission phase is almost 0. Therefore, we do not plot the phase shift and transmittance of each metallic channel. From the simulation results in Figures 2–5, it can be seen that a stable integer number of half standing waves are generated in each metal channel, i.e., the desired FP resonance conditions are met.

In this study, the sound and electromagnetic waves are focused at the same wavelength by the designed DPFL. If we want to simultaneously focus acoustic and electromagnetic waves at individually different wavelengths rather than the same one, some gas [e.g., hydrogen (Li et al., 2017)] may be filled in each metallic channel instead of air. In this case, the effective optical path and acoustic path are different in each metallic channel, which will lead to different wavelengths that satisfy the FP resonance condition for electromagnetic wave and acoustic wave. As the FP resonance condition should be satisfied for each metal channel to mimic null medium for both electromagnetic wave and acoustic wave, the focusing performance of the designed lens is not broadband. The focusing efficiency of the designed lens may be improved by adding some internal structures inside of each metallic channel (see arXiv:2305.00910). The proposed lens is a bulk lens, which has the curved output surface. To achieve a flat lens, metasurface may be a good choice (Liu et al., 2020; Cai et al., 2021). However, the current metasurface can only work for single-physical-field (i.e., electromagnetic wave or acoustic wave). Many prior groundwork are still needed to achieve metasurface-based flat lens for double-physical-field focusing.

5 Conclusion

By designing sub-wavelength air channels surrounded by metal plates, which performs as reduced double-physical-fields null medium, a DPFL lens that can simultaneously focus both electromagnetic and acoustic waves is designed. By adjusting the geometrical shape of the output surface, the focal spot size and focal length for both fields can be modified. Four typical DPFL lenses with different output surfaces are numerically studied, which shows different focusing characteristics and key parameters, e.g., long focal length and noodle-shaped spot for circular DPFL, short focal length and tiny spot for hyperbolic DPFL, and capsule-shaped spot with a moderate size for parabolic/elliptical DPFLs. As an example, the relationship between the key parameters of the parabolic DPFL and its efficiency is studied. This study provides a new way to focus electromagnetic and acoustic waves simultaneously, which may provide an additional degree of freedom for modulation than single-field focusing and have potential applications in medical therapy, sensors/detectors and tweezers.

Data availability statement

The original contributions presented in the study are included in the article/supplementary material, further inquiries can be directed to the corresponding authors.

Author contributions

BW and FS contributed equally to this work. BW and FS wrote and edited the manuscript together. BW performed theoretical analysis and numerical simulations. FS conceived this work, made conceptualization and supervised the work. YL, XL, and XZ helped on simulations. YY, ZC, SL, ZW, and BW helped on revising of the manuscript. FS and BW provide funding support. All authors contributed to the article and approved the submitted version.

Funding

This study is supported by the National Natural Science Foundation of China (Grant Nos. 61971300 and 12274317), Open Foundation of China-Belarus Belt and Road Joint Laboratory on Electromagnetic Environment Effect (No. ZBKF2022031202), 2022 University Outstanding Youth Foundation of Taiyuan University of Technology, and Scientific and Technological Innovation Programs (STIP) of Higher Education Institutions in Shanxi (Nos. 2019L0159 and 2019L0146).

Conflict of interest

The authors declare that the research was conducted in the absence of any commercial or financial relationships that could be construed as a potential conflict of interest.

Publisher's note

References

Banerji, S., Meem, M., Majumder, A., Sensale-Rodriguez, B., and Menon, R. (2020). Extreme-depth-of-focus imaging with a flat lens. *Optica* 7, 214–217. doi:10.1364/optica.384164

Cai, T., Tang, S., Zheng, B., Wang, G., Ji, W., Qian, C., et al. (2021). Ultrawideband chromatic aberration-free meta-mirrors. *Adv. Photonics* 3, 016001. doi:10.1117/1.ap.3.1.016001

Chen, W. T., Zhu, A. Y., Sanjeev, V., Khorasaninejad, M., Shi, Z., Lee, E., et al. (2018). A broadband achromatic metalens for focusing and imaging in the visible. *Nat. Nanotechnol.* 13, 220–226. doi:10.1038/s41565-017-0034-6

Chen, Z., Sun, F., Ma, X., Chen, H., Chao, K., Liu, Y., et al. (2023). Electromagnetic-acoustic splitter with a tunable splitting ratio based on copper plates. *Opt. Lett.* 48, 3407–3410. doi:10.1364/ol.492941

de Rosny, J., Lerosey, G., and Fink, M. (2010). Theory of electromagnetic time-reversal mirrors. *Ieee. Trans. Biomed. Eng.* 58, 3139–3149. doi:10.1109/tap.2010.2052567

Fan, T., Liu, Z., Zhang, D., and Tang, M. (2013). Comparative study of lesions created by high-intensity focused ultrasound using sequential discrete and continuous scanning strategies. *Ieee. Trans. Biomed. Eng.* 60, 763–769. doi:10.1109/tbme.2011.2167719

Fang, N., Xi, D., Xu, J., Ambati, M., Srituravanich, W., Sun, C., et al. (2006). Ultrasonic metamaterials with negative modulus. *Nat. Mat.* 5, 452–456. doi:10.1038/nmat1644

Gao, H., Gu, Z., Liang, B., Zou, X., Yang, J., Yang, J., et al. (2016). Acoustic focusing by symmetrical self-bending beams with phase modulations. *Appl. Phys. Lett.* 108, 073501. doi:10.1063/1.4941992

Gao, N., Guo, X., Deng, J., and Cheng, B. (2022). Design and study of a hybrid composite structure that improves electromagnetic shielding and sound absorption simultaneously. *Compos. Struct.* 280, 114924. doi:10.1016/j.compstruct.2021.114924

Janssen, X. J. A., Lipfert, J., Jager, T., Daudey, R., Beekman, J., and Dekker, N. H. (2012). Electromagnetic torque tweezers: A versatile approach for measurement of single-molecule twist and torque. *Nano Lett.* 12, 3634–3639. doi:10.1021/nl301330h

Khorasaninejad, M., Chen, W. T., Devlin, R. C., Oh, J., Zhu, A. Y., and Capasso, F. (2016). Metalenses at visible wavelengths: Diffraction-limited focusing and subwavelength resolution imaging. *Science* 352, 1190–1194. doi:10.1126/science.aaf6644

Kohrmann, K. U., Michel, M. S., Gaa, J., Marlinghaus, E., and Alken, P. (2002). High intensity focused ultrasound as noninvasive therapy for multilocal renal cell carcinoma: Case study and review of the literature. *J. Urol.* 167, 2397–2403. doi:10.1016/s0022-5347(05)64992-0

Kundtz, N., and Smith, D. R. (2010). Extreme-angle broadband metamaterial lens. *Nat. Mat.* 9, 129–132. doi:10.1038/nmat2610

Kwon, D., and Werner, D. (2009). Beam scanning using flat transformation electromagnetic focusing lenses. *IEEE Antennas Wirel. Propag. Lett.* 8, 1115–1118. doi:10.1109/lawp.2009.2033619

Leggio, L., de Varona, O., and Dadrasnia, E. (2015). A comparison between different schemes of microwave cancer hyperthermia treatment by means of left-handed metamaterial lenses. *Prog. Electromagn. Res.* 150, 73–87. doi:10.2528/pier14101408

Lerosey, G., de Rosny, J., Tourin, A., Derode, A., Montaldo, G., and Fink, M. (2004). Time reversal of electromagnetic waves. *Phys. Rev. Lett.* 92, 193904. doi:10.1103/physrevlett.92.193904

Li, B., Sun, F., and He, S. (2017). Acoustic surface transformation realized by acoustic-null materials using bilayer natural materials. *Appl. Phys. Express* 10, 114001. doi:10.7567/apex.10.114001

Li, Y., Liang, B., Tao, X., Zhu, X., Zou, X., and Cheng, J. (2012). Acoustic focusing by coiling up space. *Appl. Phys. Lett.* 101, 233508. doi:10.1063/1.4769984

Lim, S., and Yoon, Y. J. (2021). Phase compensation technique for effective heat focusing in microwave hyperthermia systems. *Appl. Sci. Basel* 11, 5972. doi:10.3390/app11135972

Liu, Y., Fu, J., Dong, H., Gong, C., Sun, F., and He, S. (2020). Extending the scanning angle of a phased-array antenna using a thin radome of curved metasurface. *Phys. Status Solidi-R* 14, 1900624. doi:10.1002/pssr.201900624

Ma, W., Liu, Z., Kudyshev, Z. A., Boltasseva, A., Cai, W., and Liu, Y. (2021). Deep learning for the design of photonic structures. *Nat. Photonics* 15, 77–90. doi:10.1038/s41566-020-0685-y

Marzo, A., and Drinkwater, B. W. (2019). Holographic acoustic tweezers. *Pnas* 116, 84–89. doi:10.1073/pnas.1813047115

Ozcelik, A., Rufo, J., Guo, F., Gu, Y., Li, P., Lata, J., et al. (2018). Acoustic tweezers for the life sciences. *Nat. Methods* 15, 1021–1028. doi:10.1038/s41592-018-0222-9

Qi, S., Li, Y., and Assouar, B. (2017). Acoustic focusing and energy confinement based on multilateral metasurfaces. *Phys. Rev. Appl.* 7, 054006. doi:10.1103/physrevapplied.7.054006

Rivenson, Y., Gorocs, Z., Gunaydin, H., Zhang, Y., Wang, H., and Ozcan, A. (2017). Deep learning microscopy. *Optica* 4, 1437–1443. doi:10.1364/optica.4.001437

Roy, T., Rogers, E. T. F., and Zheludev, N. I. (2013). Sub-wavelength focusing meta-lens. *Opt. Express* 21, 7577–7582. doi:10.1364/oe.21.007577

Sato, M., Watanabe, Y., Ueda, S., Iseki, S., Abe, Y., Sato, N., et al. (1996). Microwave coagulation therapy for hepatocellular carcinoma. *Gastroenterology* 110, 1507–1514. doi:10.1053/gast.1996.v110.pm8613057

Shi, H., Liu, T., Fu, C., Li, L., Tan, L., Wang, J., et al. (2015). Insights into a microwave susceptible agent for minimally invasive microwave tumor thermal therapy. *Biomaterials* 44, 91–102. doi:10.1016/j.biomaterials.2014.12.035

Sun, F., Liu, Y., and He, S. (2020). Surface transformation multi-physics for controlling electromagnetic and acoustic waves simultaneously. *Opt. Express* 28, 94–106. doi:10.1364/oe.379817

Vidiasheva, I. V., Abalymov, A. A., Kurochkin, M. A., Mayorova, O. A., Lomova, M. V., German, S. V., et al. (2018). Transfer of cells with uptaken nanocomposite, magnetite-nanoparticle functionalized capsules with electromagnetic tweezers. *Biomater. Sci.* 6, 2219–2229. doi:10.1039/c8bm00479j

Xia, J. P., and Sun, H. X. (2015). Acoustic focusing by metal circular ring structure. *Appl. Phys. Lett.* 106, 392–396. doi:10.1063/1.4908117

Xia, J., Zhang, X., Sun, H., Yuan, S., Qian, J., and Ge, Y. (2018). Broadband tunable acoustic asymmetric focusing lens from dual-layer metasurfaces. *Phys. Rev. Appl.* 10, 014016. doi:10.1103/physrevapplied.10.014016

Yang, S., Page, J. H., Liu, Z., Cowan, M. L., Chan, C. T., and Sheng, P. (2004). Focusing of sound in a 3d phononic crystal. *Phys. Rev. Lett.* 93, 024301. doi:10.1103/physrevlett.93.024301

Yang, Y., Wang, H., Yu, F., Xu, Z., and Chen, H. (2016). A metasurface carpet cloak for electromagnetic, acoustic and water waves. *Sci. Rep.* 6, 20219. doi:10.1038/srep20219

Zhang, S., Yin, L., and Fang, N. (2009). Focusing ultrasound with an acoustic metamaterial network. *Phys. Rev.Lett.* 102 (19), 194301. doi:10.1103/physrevlett.102.194301

Zheng, B., Yang, Y., Shao, Z., Yan, Q., Shen, N., Shen, L., et al. (2019). Experimental realization of an extreme-parameter omnidirectional cloak. *Research* 2019, 8282641. doi:10.34133/2019/8282641

frontiers | Frontiers in Materials

TYPE Original Research
PUBLISHED 03 October 2023
DOI 10.3389/fmats.2023.1289250

OPEN ACCESS

EDITED BY
Shuomin Zhong,
Ningbo University, China

REVIEWED BY
Yunbo Li,
Southeast University, China
Cai Tong,
Zhejiang University, China
Yichao Liu,
Taiyuan University of Technology, China

*CORRESPONDENCE
Hao Wu,
12130001@zju.edu.cn
Huan Lu,
luhuan123@zju.edu.cn

RECEIVED 05 September 2023
ACCEPTED 22 September 2023
PUBLISHED 03 October 2023

CITATION
Zhu R, Chen T, Wang K, Wu H and Lu H (2023), Metasurface-enabled electromagnetic illusion with generic algorithm.
Front. Mater. 10:1289250.
doi: 10.3389/fmats.2023.1289250

Metasurface-enabled electromagnetic illusion with generic algorithm

Rongrong Zhu[1,2], Tianhang Chen[3], Kai Wang[2], Hao Wu[1]* and Huan Lu[2,4]*

[1]School of Information and Electrical Engineering, Hangzhou City University, Zhejiang, China, [2]Interdisciplinary Center for Quantum Information, State Key Laboratory of Extreme Photonics and Instrumentation, ZJU-Hangzhou Global Scientific and Technological Innovation Center, Zhejiang University, Hangzhou, China, [3]China Aeronautical Establishment, Beijing, China, [4]Key Laboratory of Advanced Micro/Nano Electronic Devices and Smart Systems of Zhejiang, Jinhua Institute of Zhejiang University, Zhejiang University, Jinhua, China

Electromagnetic cloak or illusion, which can interfere with device detection and provide superior self-protection capabilities for animals or humans, has received much attention. The proposal of transformation optics provides a generalized strategy for realizing electromagnetic illusion. However, the complex parameter composition causes a substantial computational cost, which is not conducive to practical applications. To overcome these challenges, we report an intelligent illusory metasurface optimized by a genetic algorithm, which not only presents predefined illusory effects but also reduces the parameter space in physics. By designing a high-performance tunable metasurface, a high-fidelity inverse design is performed in simulation. Near-field and far field results show that the metasurface can generate virtual targets in different scenarios and realize electromagnetic illusion. This work is helpful in facilitating the practical application of electromagnetic illusion strategies.

KEYWORDS

tunable metasurface, electromagnetic illusion, genetic algorithm, global optimization, inverse design

1 Introduction

Electromagnetic (EM) illusion technology is one of the most promising applications (Jiang et al., 2010; Jiang and Cui, 2011; Schittny et al., 2014; Xu et al., 2015; Yang et al., 2016; Huang et al., 2018; Cai et al., 2022; Liang et al., 2023), which can visually produce virtual objects that do not exist or transform an object into other forms, interfering with EM detection and ultimately achieving camouflage for active attack or passive defense. In traditional methods, optical illusions can be realized with the theory of transformation optics (Pendry et al., 2006; Schurig et al., 2006; Lai et al., 2009a; Lai et al., 2009b; Luo et al., 2009; Landy and Smith, 2013; Zheng et al., 2019), such as using complementary media to eliminate the original object and release the illusion of another object. However, this design is very complicated, and the extreme materials with anisotropy and inhomogeneity also make its practical application face a bottleneck. At the same time, a critical prerequisite for the realization of EM illusions is the acquisition of high-performance metamaterials/metasurfaces with the desired EM response.

Traditionally, this process of designing metasurfaces needs to be accomplished by time-consuming, inefficient, empirically guided numerical simulations or physically based

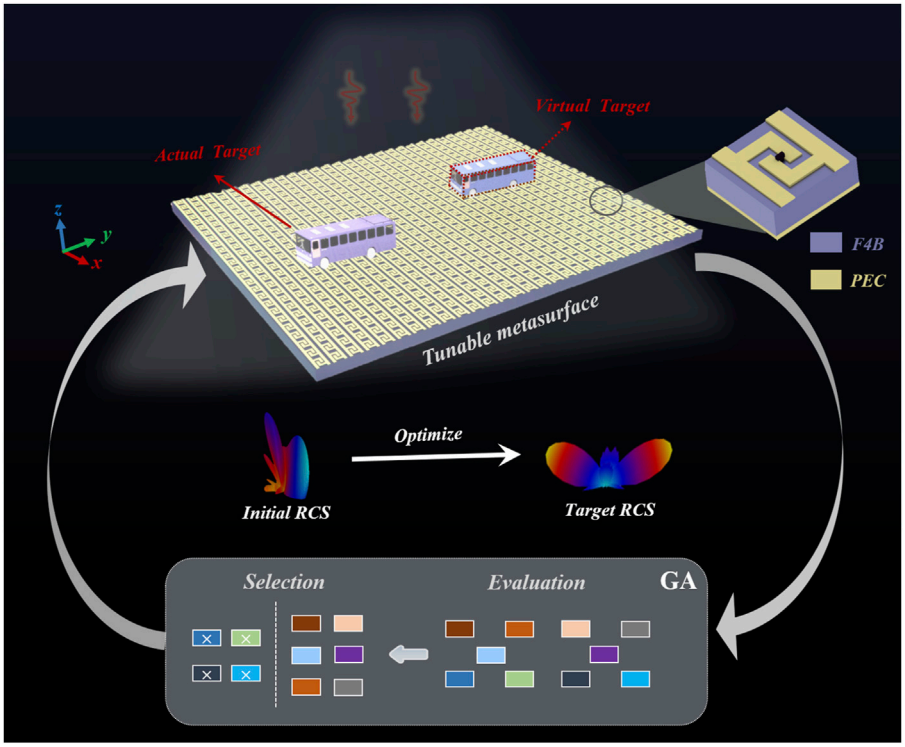

FIGURE 1
The conceptual diagram of GA-driven EM illusion.

methods; and theoretical methods will fail when the shape of the object is irregular (Chen et al., 2007; Li and Pendry, 2008; Hao et al., 2021; Shan et al., 2021; Hao et al., 2022). In recent years, intelligent optimization algorithms have emerged, strongly contributing to the study of metasurfaces (Goodfellow et al., 2016; Vaswani et al., 2017; Li et al., 2019; Qian et al., 2020; Shlezinger et al., 2021; Keeley et al., 2022; Ma et al., 2022; Shao et al., 2022; Lu et al., 2023; Zhong et al., 2023). Such as intelligent scattering and cloak (Qian et al., 2020), adaptive focusing (Lu et al., 2023), *etc*., which provide guidance for the inverse design of metasurfaces, and also provide the basis for realizing the EM illusion of false targets.

This study proposes an illusionary metasurface optimized using genetic algorithm (GA) (Lecun et al., 1998; Shakya, 2002; Pierro et al., 2004; Hinton et al., 2012; Lingaraj, 2016; Krizhevsky et al., 2017; Katoch et al., 2021) that can produce false targets in different scenarios. Firstly, the metasurface with high reflectivity and wide phase coverage is designed, and an adaptive regulation model of GA and metasurface is constructed. Different objective functions are selected according to the requirements in different environments, and the tunable metasurface satisfying the predefined objectives is reverse-designed after global optimization and iteration of the algorithm. Ultimately, illusory scattering that produces false vehicle targets is achieved using the metasurface in both the absence of objects and the presence of a single object. Despite the operating frequency being 5 GHz, the optimization method has no restriction on the frequency, and false scattering can be achieved at other arbitrary frequencies by simply modifying the appropriate objective function. This work eliminates the need for theoretical computation of complex parameters and allows iterative generation of spurious scattering given only the optimization objective. It has a wide range of promising applications in various aspects, such as metasurface inverse design and intelligent tuning.

2 Methods

Figure 1 illustrates the conceptual diagram of an EM illusion using the tunable metasurface to generate the virtual target. The intelligent metasurface consists of a series of tunable unit cells (as shown in the inset at the top right), and it is independently tunable in one-dimensional direction (*y*-direction) for each cell to produce a rich EM response. When an object exists on the metasurface (actual target), initial radar cross section (RCS) is generated under the effect of EM waves. The observer can recognize the target by judging the approximate shape of the object based on the RCS. If other types of far-field RCS can be generated, the detection device will be interfered with to realize EM illusion. As shown in Figure 1, using the target RCS as the objective function, after the global optimization of the GA and the modulation of the metasurface, the system finally produces the RCS that is generated only when two targets exist, i.e., the virtual target is generated.

A high-performance tunable reflection unit cell is designed to generate the false targets. Figure 2A shows the designed structure, consisting of a dielectric substrate and a metal with a relative permittivity $\varepsilon_r = 2.65$, a loss angle tangent of 0.002, a thickness of 2.5 mm, and a size of 10×10 mm^2. The backside of this structure is an all-reflective metal layer, which ensures a high reflectivity of the incident EM wave. The metal on the front side of the unit cell is

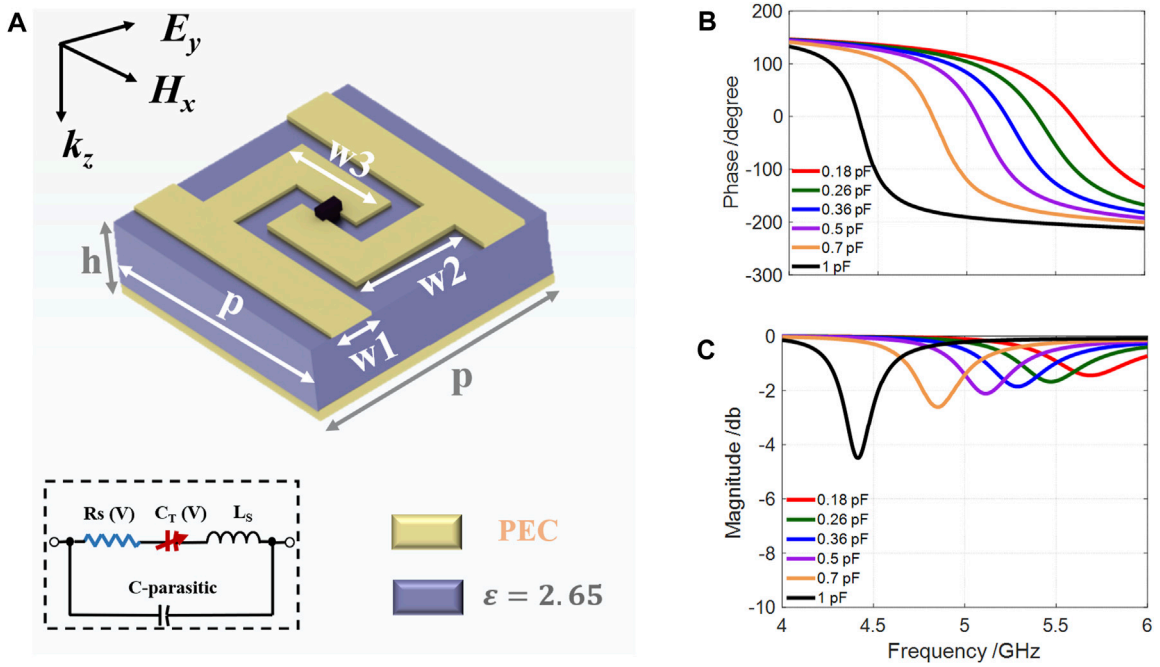

FIGURE 2
The unit cell and S-parameters. **(A)** Schematic diagram of the unit cell, where $p = 10\,mm$, $w1 = 1.5\,mm$, $w2 = 4.2\,mm$, $w3 = 4.5\,mm$, and $h = 2.5\,mm$. **(B)** The phase response of the unit cell. **(C)** The magnitude response of the unit cell.

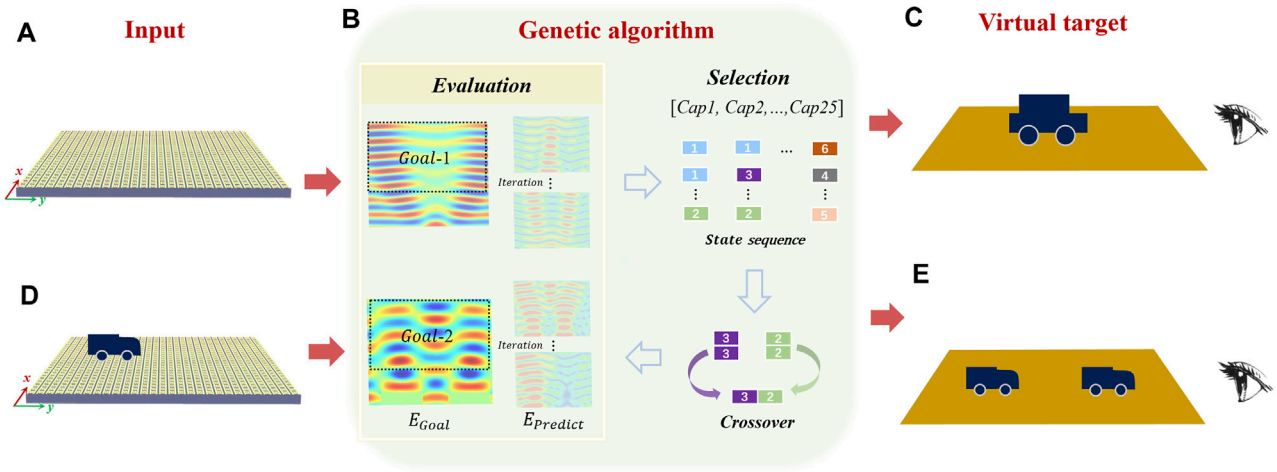

FIGURE 3
The process for generating false targets in different scenarios using GA and metasurface. **(A)** Input data for the first scenario. **(B)** Genetic algorithm process. **(C)** The first illusion scene. **(D)** Input data or the second scenario. **(E)** The second illusion scene.

centrosymmetric in which a varactor diode is embedded in the middle. The diode model is a MAVR-000120-14110P varactor manufactured by MACOM, which has an adjustable capacitance between 0.14 pF and 1.1 pF with a parasitic resistance of 2.5 Ω. The equivalent circuit diagram of the capacitive diode is shown in the inset portion of Figure 2A. In the actual simulation, the RC model is used as the equivalent circuit, and the characteristics of the diode can be changed by adjusting the capacitance. We analyze the S-parameters using the CST2021 in the frequency domain mode. For simulation, both the x and y directions are set as unit cell boundaries, the electric field along the y direction, and the magnetic field along the x direction.

The S-parameter characteristics are shown in Figures 2B, C. The horizontal coordinate represents the frequency change. It can be seen that the reflection phase varies continuously up to 330° at $f = 5\,GHz$ (Figure 2B), and the reflection amplitude is better

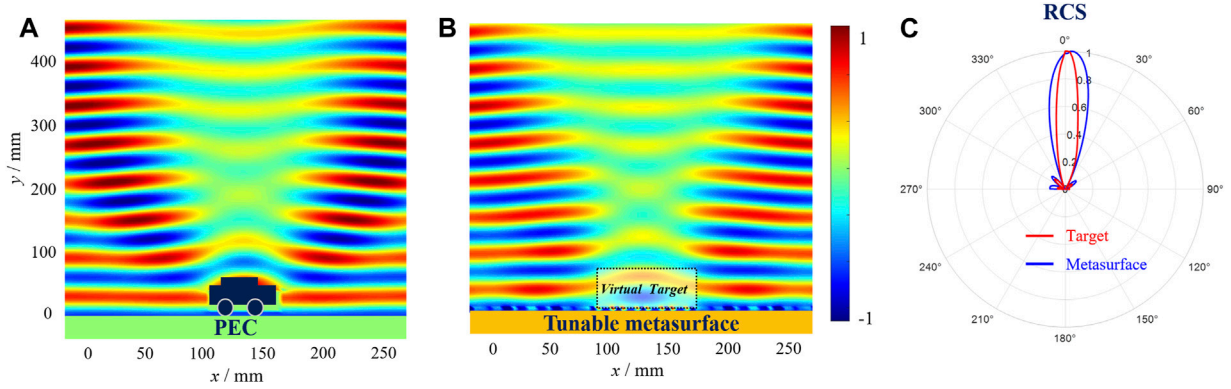

FIGURE 4
Metasurface generates the false vehicle target. **(A)** Scattering of the object. **(B)** Scattering of the metasurface. **(C)** The results of the RCS.

than −2 dB (Figure 2C). The unit cell can achieve continuous phase by adjustment the capacitance. In order to increase the speed of the global optimization, we chose six capacitors as feature with capacitance values of 0.18, 0.26, 0.36, 0.5, 0.7, and 1 pF, respectively. The corresponding phases are 130°, 100°, 70°, 40°, −110°, and −200°, respectively. They are also used for the subsequent iterations of the algorithm. Even if the phase response of a single structure does not reach 360°, rich EM modulation can be realized by global tuning of the metasurface.

The virtual target is then generated using GA and the metasurface, the progress is illustrated in Figure 3. The metasurface is composed of a set of tunable unit cells, the state is independently along the y-direction, and it is periodically arranged along the x-direction. The size of the metasurface is $200mm \times 250mm$, as shown in Figure 3A. Figure 3B shows the iterative flow of the GA. In general, the algorithm includes evaluation, selection, and crossover/mutation. The "evaluation" means the loss between predicted and actual results, also known as the objective function; the "selection" is to select different state sequences, and the "crossover" is an update strategy. Defining the loss function using mean absolute error (MAE):

$$MAE = \frac{1}{m}\sum_{i=1}^{m}\left|E_{Theory} - E_{Test}\right| \tag{1}$$

where E_{Theory} is the target electric field, and the E_{Test} is the electric field generated during the iteration. If the iteration termination condition is not satisfied at the moment t, the algorithm re-selects the state sequence (i.e., capacitance $[Cap1, Cap2, ..., Cap25]$) at the moment $t+1$ according to the loss function. After that, the metasurface state changes and will generate the new electric field. The GA re-judges the error at this time, and terminates the iteration if the condition is satisfied. Otherwise, the next update is performed.

In the first case, we take the electric field generated by the metasurface as the input (Figure 3A) and take the single-vehicle scattering data as the target (Goal-1 in Figure 3B). After global optimization by the GA, we can eventually generate the scattering field similar to one vehicle target, thus confusing the observer, as shown in Figure 3C.

In the second case, the electric field generated by the metasurface and the vehicle together is used as the input (Figure 3D). Taking it as the goal data (Goal-2 of Figure 3B), the system can generate the electric field that similar to two vehicle targets after global optimization, thus creating a false target (as shown in Figure 3E). After being driven and guided by the GA, the various virtual target can be generated in different scenarios, interfering with the detection and realizing the EM illusion.

The results of generating one false vehicle target are shown in Figure 4. Figure 4A shows the results of the real part of the electric field of the vehicle model on a metal ground, where it can be seen that there is strong backward scattering. The vehicle model has a height of about 60 mm and a length of about 70 mm. The electric field is used as the target data. Using GA to optimize and adjust the metasurface, and the final iteration electric field is shown in Figure 4B. In Figure 4, the horizontal coordinate x denotes the length of the metasurface, and the vertical coordinate y denotes the distance from the metasurface, and all data are normalized. A comparison of Figs a and b shows that there is a high similarity, which means the metasurface produces a false target that approximates the vehicle model. The MAE loss is 0.15.

Figure 4C shows the comparison results of the far-field RCS, where the red solid line is the RCS produced by the target (Figure 4A) and the blue solid line is the RCS produced by the metasurface (Figure 4B). The RCS was defined as:

$$\sigma = 2\pi\rho\left|H_y^o - H_y^g\right|^2 \tag{2}$$

where H_y^o and H_y^g are the electric field in the object and background cases respectively. Calculating the correlation coefficient $r(E_{Theory}, E_{Test})$ for Figure 4C, which is defined as:

$$r\left(E_{Theory}, E_{Test}\right) = \frac{C\left(E_{Theory}, E_{Test}\right)}{\sqrt{Var\left[E_{Theory}\right]Var\left[E_{Test}\right]}} \tag{3}$$

$$\begin{aligned} C\left(E_{Theory}, E_{Test}\right) &= \mathbf{E}\left[\left(E_{Theory} - \mathbf{E}\left[E_{Theory}\right]\right)\left(E_{Test} - \mathbf{E}\left[E_{Test}\right]\right)\right] \\ &= \mathbf{E}\left[E_{Theory}E_{Test}\right] - 2\mathbf{E}\left[E_{Test}\right]\mathbf{E}\left[E_{Theory}\right] + \mathbf{E}\left[E_{Theory}\right]\mathbf{E}\left[E_{Test}\right] \\ &= \mathbf{E}\left[E_{Theory}E_{Test}\right] - \mathbf{E}\left[E_{Theory}\right]\mathbf{E}\left[E_{Test}\right] \end{aligned} \tag{4}$$

where $C(E_{Theory}, E_{Test})$ is the covariance of E_{Theory} and E_{Test}, $Var[E_{Theory}]$ is the variance of E_{Theory}, and $Var[E_{Test}]$ is the variance of E_{Test}. $\mathbf{E}$ is the mathematical expectation. The correlation between the two curves in Figure 4 was calculated to be 96.2%. Thus, the

10.3389/fmats.2023.1289250

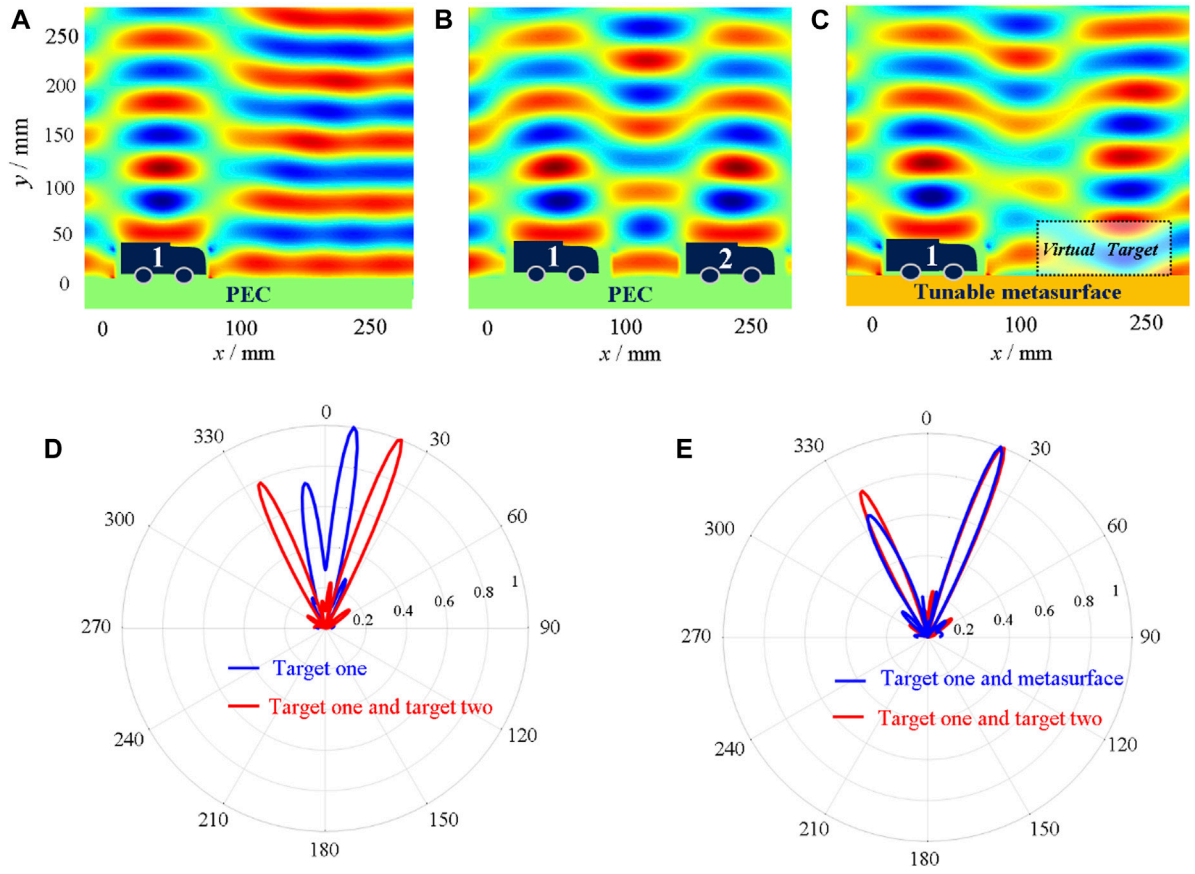

FIGURE 5
Metasurface generates the false vehicle target in another scenario. **(A)** Scattering of the target one. **(B)** Scattering of targets one and two. **(C)** Scattering from metasurface and target one. **(D,E)** Comparison of RCS in different scenarios.

ability of the metasurface to generate false targets is demonstrated in both the near and far fields.

Figure 5 shows the results of the metasurface generating a virtual target in another scenario. In Figure 5A, a vehicle target made of PEC is placed above a metallic ground and generates scattering, labeling the object as target one. In Figure 5, the horizontal coordinate x denotes the length of the metasurface and the vertical coordinate y denotes the distance from the metasurface. Two identical vehicles (target one and target two) were placed above the PEC, and their near-field scattering is shown in Figure 5B. The effect of the metal object results in inhomogeneity across the real part of the electric field. Using the data in Figure 5B as the goal function, and the final iteration electric field is shown in Figure 5C. The comparative results of Figures 5B, C reveal the consistency of the electric field, at which point the MAE loss is 0.18.

Figures 5D, E show the far-field RCS results. In Figure 5D, the blue solid line is the RCS generated by target one (i.e., Figure 5A). The red solid line is the RCS generated by target one and target two together (i.e., Figure 5B), and the correlation of the curves is only 20%. After global optimization, the far-field RCS generated by the metasurface and target one has a high similarity with the two targets, as shown in Figure 5E, and the correlation coefficient is 97.3%.

3 Conclusion

In conclusion, we implement a joint GA and metasurface to realize an EM phantom for false target generation, and this joint modulation model is validated to be effective in different scenarios. High-performance and reliable tunable reflective hypersurface structures are designed, which can achieve a continuous phase change of about 330° at the operating frequency while the amplitude is better than −2 db. The metasurface arrays designed with the assistance of genetic algorithms can generate scattering from vehicle targets in both scenarios with no objects or in the presence of a single object, and both near-field and far-field data validate the effectiveness of the simulations. Compared to traditional deep learning algorithms, GA can achieve global optimization with unlabeled data and explore more parsing solutions to the problem. In scenarios with more targets, only the optimization objective function is modified to achieve false scattering for different scenarios. This work provides new ideas for EM metasurface inverse design and can be used to decode richer structures.

Data availability statement

Data can be obtained from the corresponding author (HL).

Author contributions

RZ: Investigation, Validation, Writing–original draft. TC: Writing–review and editing, Supervision. KW: Writing–review and editing, Supervision. HW: Investigation, Methodology, Supervision, Writing–review and editing. HL: Conceptualization, Methodology, Writing–review and editing.

Funding

The authors declare financial support was received for the research, authorship, and/or publication of this article. This work was sponsored by the Natural Science Foundation of Zhejiang Province under Grant No. LQ21F050002.

Conflict of interest

The authors declare that the research was conducted in the absence of any commercial or financial relationships that could be construed as a potential conflict of interest.

The reviewer CT declared a shared affiliation with the author HL to the handling editor at time of review.

Publisher's note

References

Cai, T., Zheng, B., Lou, J., Shen, L., Yang, Y., Tang, S., et al. (2022). Experimental realization of a superdispersion-enabled ultrabroadband terahertz cloak. *Adv. Mat.* 34 (38), 2205053. doi:10.1002/adma.202205053

Chen, H., Wu, B.-I., Zhang, B., and Kong, J. A. (2007). Electromagnetic wave interactions with a metamaterial cloak. *Phys. Rev. Lett.* 99 (6), 063903. doi:10.1103/physrevlett.99.063903

Goodfellow, I., Bengio, Y., and Courville, A. (2016). *Deep learning*. Cambridge, MA, USA, MIT Press.

Hao, H., Ran, X., Tang, Y., Zheng, S., and Ruan, W. (2021). A single-layer focusing metasurface bassed on induced magnetism. *Prog. Electromagn. Res.* 172, 77–88. doi:10.2528/pier21111601

Hao, H., Tang, Y., Zheng, S., Ran, X., and Ruan, W. (2022). Design of circular polarization multiplexing beam splitter based on transmission metasurface. *Prog. Electromagn. Res. M.* 109, 125–136. doi:10.2528/pierm22010408

Hinton, G., Deng, L., Yu, D., Dahl, G. E., Mohamed, A., Jaitly, N., et al. (2012). Deep neural networks for acoustic modeling in speech recognition:the shared views of four research groups. *IEEE Signal Proc. Mag.* 29 (6), 82–97. doi:10.1109/msp.2012.2205597

Huang, C., Yang, J., Wu, X., Song, J., Pu, M., Wang, C., et al. (2018). Reconfigurable metasurface cloak for dynamical electromagnetic illusions. *ACS Photonics* 5 (5), 1718–1725. doi:10.1021/acsphotonics.7b01114

Jiang, W. X., and Cui, T. J. (2011). Radar illusion via metamaterials. *Phys. Rev. E* 83 (2), 026601. doi:10.1103/physreve.83.026601

Jiang, W. X., Ma, H. F., Cheng, Q., and Cui, T. J. (2010). Illusion media:generating virtual objects using realizable metamaterials. *Appl. Phys. Lett.* 96 (12), 121910. doi:10.1063/1.3371716

Katoch, S., Chauhan, S. S., and Kumar, V. (2021). A review on genetic algorithm:past, present, and future. *Multimed. Tools Appl.* 80 (5), 8091–8126. doi:10.1007/s11042-020-10139-6

Keeley, E., Joe, L., Colin, G., and Ian, J. (2022). Machine-learning-enabled recovery of prior information from experimental breast microwave imaging data. *Prog. Electromagn. Res.* 175, 1–11. doi:10.2528/pier22051601

Krizhevsky, A., Sutskever, I., and Hinton, G. E. (2017). ImageNet classification with deep convolutional neural networks. *Commun. ACM* 60 (6), 84–90. doi:10.1145/3065386

Lai, Y., Chen, H., Zhang, Z.-Q., and Chan, C. T. (2009b). Complementary media invisibility cloak that cloaks objects at a distance outside the cloaking shell. *Phys. Rev. Lett.* 102 (9), 093901. doi:10.1103/physrevlett.102.093901

Lai, Y., Ng, J., Chen, H., Han, D., Xiao, J., Zhang, Z.-Q., et al. (2009a). Illusion optics: the optical transformation of an object into another object. *Phys. Rev. Lett.* 102 (25), 253902. doi:10.1103/physrevlett.102.253902

Landy, N., and Smith, D. R. (2013). A full-parameter unidirectional metamaterial cloak for microwaves. *Nat. Mat.* 12 (1), 25–28. doi:10.1038/nmat3476

Lecun, Y., Bottou, L., Bengio, Y., and Haffner, P. (1998). Gradient-based learning applied to document recognition. *Proc. IEEE* 86 (11), 2278–2324. doi:10.1109/5.726791

Li, J., and Pendry, J. B. (2008). Hiding under the carpet: A new strategy for cloaking. *Phys. Rev. Lett.* 101 (20), 203901. doi:10.1103/physrevlett.101.203901

Li, L., Shuang, Y., Ma, Q., Li, H., Zhao, H., Wei, M., et al. (2019). Intelligent metasurface imager and recognizer. *Light. Sci. Appl.* 8 (1), 97. doi:10.1038/s41377-019-0209-z

Liang, Q., Li, Z., Xu, J., Duan, Y., Yang, Z., and Li, D. (2023). A 4D-printed electromagnetic cloaking and illusion function convertible metasurface. *Adv. Mat. Technol.* 2202020. doi:10.1002/admt.202202020

Lingaraj, H. (2016). A study on genetic algorithm and its applications. *Int. J. Comput. Sci. Eng.* 4, 139–143.

Lu, H., Zhao, J., Zheng, B., Qian, C., Cai, T., Li, E., et al. (2023). Eye accommodation-inspired neuro-metasurface focusing. *Nat. Commun.* 14 (1), 3301. doi:10.1038/s41467-023-39070-8

Luo, Y., Zhang, J., Chen, H., Ran, L., Wu, B.-I., and Kong, J. A. (2009). A rigorous analysis of plane-transformed invisibility cloaks. *IEEE Trans. Antenn. Propag.* 57 (12), 3926–3933. doi:10.1109/tap.2009.2027824

Ma, W., Xu, Y., Xiong, B., Deng, L., Peng, R. W., Wang, M., et al. (2022). Pushing the limits of functionality-multiplexing capability in metasurface design based on statistical machine learning. *Adv. Mater* 34 (16), 2110022. doi:10.1002/adma.202110022

Pendry, J. B., Schurig, D., and Smith, D. R. (2006). Controlling electromagnetic fields. *Science* 312 (5781), 1780–1782. doi:10.1126/science.1125907

Pierro, D.-F., Khu, S.-T., and Djordjevi, S. (2004). *A new genetic algorithm to solve effectively highly multi- objective problems: POGA, report nr*. Center for WaterSystems, University of Exeter., London, UK ,

Qian, C., Zheng, B., Shen, Y., Jing, L., Li, E., Shen, L., et al. (2020). Deep-learning-enabled self-adaptive microwave cloak without human intervention. *Nat. Photonics* 14 (6), 383–390. doi:10.1038/s41566-020-0604-2

Schittny, R., Kadic, M., Bückmann, T., and Wegener, M. (2014). Invisibility cloaking in a diffusive light scattering medium. *Science* 345 (6195), 427–429. doi:10.1126/science.1254524

Schurig, D., Mock, J. J., Justice, B. J., Cummer, S. A., Pendry, J. B., Starr, A. F., et al. (2006). Metamaterial electromagnetic cloak at microwave frequencies. *Science* 314 (5801), 977–980. doi:10.1126/science.1133628

Shakya, S. K. (October 2002). "Probabilistic model building genetic algorithm (pmbga): A survey," in Proceedings of the 7th international conference, granada, Spain.

Shan, T., Li, M., Xu, S., and Yang, F. (2021). Phase synthesis of beam-scanning reflectarray antenna based on deep learning technique. *Prog. Electromagn. Res.* 172, 41–49. doi:10.2528/pier21091307

Shao, S., Fan, M., Yu, C., Li, Y., Xu, X., Wang, H., et al. (2022). Machine learning-assisted sensing techniques for integrated communications and sensing in WLANs:current status and future directions. *Prog. Electromagn. Res.* 175, 45–79. doi:10.2528/pier22042903

Shlezinger, N., Alexandropoulos, G. C., Imani, M. F., Eldar, Y. C., and Smith, D. R. (2021). Dynamic metasurface antennas for 6G extreme massive MIMO communications. *IEEE Wirel. Commun.* 28 (2), 106–113. doi:10.1109/mwc.001.2000267

Vaswani, A., Shazeer, N., Parmar, N., Uszkoreit, J., Jones, L., Gomez, A. N., et al. (January 2017). "Attention is all you need," in Proceedings of the neural information processing systems (Long Beach, CA, USA:).

Xu, S., Xu, H., Gao, H., Jiang, Y., Yu, F., Joannopoulos, J. D., et al. (2015). Broadband surface-wave transformation cloak. *Proc. Nat. Acad. Sci.* 112 (25), 7635–7638. doi:10.1073/pnas.1508777112

Yang, Y., Jing, L., Zheng, B., Hao, R., Yin, W., Li, E., et al. (2016). Full-polarization 3D metasurface cloak with preserved amplitude and phase. *Adv. Mat.* 28 (32), 6866–6871. doi:10.1002/adma.201600625

Zheng, B., Yang, Y., Shao, Z., Yan, Q., Shen, N.-H., Shen, L., et al. (2019). Experimental realization of an extreme-parameter omnidirectional cloak. *Research* 2019 (8282641), 8282641. doi:10.34133/2019/8282641

Zhong, S., Wang, X., and Tretyakov, S. (2023). Coherent control of wave beams via unidirectional evanescent modes excitation. *Adv. Funct. Mater*, 15, 2304300. doi:10.1002/adfm.202304300

Frontiers in Materials

Investigates the discovery and design of materials for future application

A multidisciplinary journal that explores the breadth of materials science, engineering and mechanics - from carbon-based materials to smart materials.

Discover the latest Research Topics

See more →

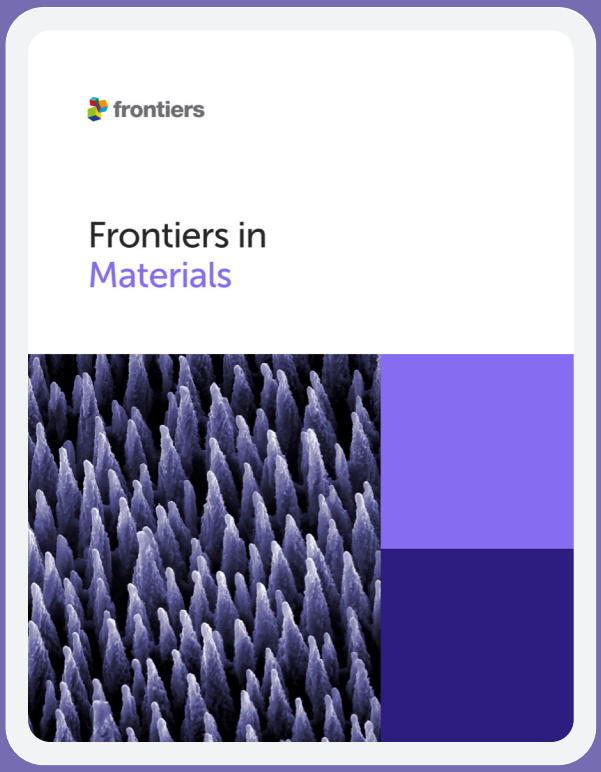

Frontiers

Avenue du Tribunal-Fédéral 34
1005 Lausanne, Switzerland
frontiersin.org

Contact us

+41 (0)21 510 17 00
frontiersin.org/about/contact